ABSTRACT

Title of Dissertation: INFLUENCE OF NOISE ON RESPONSE LOCALIZATIONS IN MECHANICAL OSCILLATOR ARRAYS

Lautaro D. Cilenti, 2022

Dissertation Directed by: Professor Balakumar Balachandran
Department of Mechanical Engineering

Associate Professor Maria Cameron
Department of Mathematics

The dynamics of mechanical systems such as turbomachinery and vibration energy harvesting systems (VEH) consisting of one or multiple cantilever structures is often modeled by arrays of periodically driven coupled nonlinear oscillators. It is known that such systems may have multiple stable vibration steady states. Some of these steady states are localized vibrations that are characterized by high amplitude vibrations of a subset of the system, with the rest of the system being in a state of either low amplitude vibrations or no vibrations. On one hand, these localized vibrations can be detrimental to mechanical integrity of turbomachinery, while on the other hand, the vibrations can be potentially desirable for increasing energy yield in VEHs. Transitions into or out of localized vibrations may occur under the influence of random factors.

A combination of experimental and numerical studies has been performed in this dissertation to study the associated transition times and probability of transitions in these mechanical systems. The developments reported here include the following: (i) a numerical methodology based on the Path Integral Method to quantify the probability of transitions due to noise, (ii) a numerical methodology based on the Action Plot Method to quantify the quasipotential and most probable transition paths in nonlinear systems with periodic external excitations, and (iii) experimental evidence and stochastic simulations of the influence of noise on response localizations of rotating macro-scale cantilever structures. The methodology and results discussed in this dissertation provide insights relevant to the stochastic nonlinear dynamics community, and more broadly, designers of mechanical systems to avoid potentially undesirable stochastic nonlinear behavior.

INFLUENCE OF NOISE ON RESPONSE LOCALIZATIONS IN MECHANICAL OSCILLATOR ARRAYS

by

Lautaro Daniel Cilenti

Dissertation submitted to the Faculty of the Graduate School of the
University of Maryland, College Park in partial fulfillment
of the requirements for the degree of
Doctor of Philosophy
2022

Advisory Committee:
Professor Balakumar Balachandran, Mechanical Engineering, Chair/Advisor
Associate Professor Maria Cameron, Mathematics, Co-Chair/Advisor
Professor Eyad Abed, Electrical and Computer Engineering
Professor Amr Baz, Mechanical Engineering
Associate Professor Jin-Oh Hahn, Mechanical Engineering
Assistant Professor Eleonora Tubaldi, Mechanical Engineering

© Copyright by
Lautaro Daniel Cilenti
2022

Dedication

To the love of my life, Yeming Hao,
and
to my niece and nephews: Mateo, Bruno, Victoria, Jeremiah, and Alejandro.

Acknowledgments

This endeavor would not have been possible without the support of the chair of my committee, Professor Balakumar Balachandran. He opened a door for me to a field in which I had limited prior experience, was patient and supportive through my learnings, provided expert technical advice, and has been an exceptional mentor as I grew to love this research. I would also like to express my deepest gratitude to my co-chair and advisor, Professor Maria Cameron. Her invaluable insight into the field of stochastic nonlinear dynamics has fueled my research with interesting ideas, inspired me to be curious about so many more, and has in general shaped me into a better researcher and technical writer. Furthermore, words cannot express my gratitude to my dissertation committee who generously provided their time, knowledge, and expertise.

I am also extremely grateful to the Clark Doctoral Fellowship, and through Professor Balachandran, the Minta Martin Professorship and NSF grant CMMI-1760366 for the financial support that made this all possible. I wish to acknowledge the University of Maryland supercomputing resources (http://hpcc.umd.edu) made available for conducting a part of the research reported in this dissertation.

I am grateful to my lab mates over the course of the last four years. They have shared their research with me, taught me, learned with me, and helped me succeed. Many thanks to Jonathan Deboer for joining me as an undergrad in the design and prototyping of the experiment during my last year, and to Majid Aroom and the UMD Dept. of Mechanical Engineering machine shop for the prototyping resources and expertise. Special thanks as well to my former mentors, Dan Yeaw, Professor Erik Andersen, Professor David Gatchell, Dr. Bruce Lindvall, and Dr. Ako Chijioke for their teachings in general and support with graduate school and fellowship applications that made this possible.

I want to also acknowledge the support of my family. It goes without saying that the lifelong support from my parents, Daniel and Jaquelina, is impossible to fully acknowledge. Over the last four years, and especially during the pandemic, it has been a special pleasure to have their cheerful attitudes, love, and warmth close by.

Last, but not least, my heartfelt thanks to my wife, Yeming, for her unwavering patience and support, especially during the most stressful times, and for challenging me and motivating me to do my best and make the most of my PhD journey. Thank *you*, Yeming, also, for all the fun times that have made the past four years the best so far.

Table of Contents

Dedication ii

Acknowledgements iii

Table of Contents iv

List of Tables vii

List of Figures viii

List of Abbreviations xix

Chapter 1: Introduction and Research Objectives 1
- 1.1 Systems and Phenomena of Interest . . . 2
  - 1.1.1 Turbomachinery . . . 2
  - 1.1.2 Vibration Energy Harvesters . . . 4
  - 1.1.3 Response Localizations . . . 4
- 1.2 Objectives and Structure . . . 5

Chapter 2: Literature Review 9
- 2.1 Prior Experimental Work . . . 9
  - 2.1.1 In-line Macro-scale Cantilever Arrays . . . 12
  - 2.1.2 Circular Macro-scale Cantilever Arrays . . . 13
  - 2.1.3 Alternative Oscillator Arrays . . . 14
  - 2.1.4 Stochastic Experiments on Single Cantilevers . . . 15
  - 2.1.5 Summary of Experimental Work . . . 16
- 2.2 System Model . . . 16
  - 2.2.1 Localized Modes of the Deterministic System . . . 19
- 2.3 Noise Influenced System . . . 22
  - 2.3.1 Solving Stationary Fokker Planck Equation . . . 24
  - 2.3.2 Integrating Moment Differential Equations . . . 25
  - 2.3.3 Euler Maruyama Scheme . . . 27
  - 2.3.4 Other Relevant Low Dimensional Studies ($N = 1$) . . . 29
- 2.4 Transition Events in the Weak Noise Limit . . . 30

Chapter 3: Transient Probability in Basins of Noise-Influenced Responses of Mono and Coupled Duffing Oscillators 36

3.1 Background and Methods . . . 36
3.1.1 Path Integral Method Formulation . . . 37
3.1.2 Transient Probability in Basins . . . 45
3.2 Forced Duffing Oscillator: Results . . . 47
3.3 Two Coupled Duffing Oscillators: Results . . . 61
3.4 Conclusion . . . 69

Chapter 4: Most Probable Escape paths in Periodically Driven Nonlinear Oscillators 72
4.1 Introduction . . . 73
4.2 Objectives and Structure . . . 78
4.3 Background . . . 83
4.3.1 Large Deviations Theory . . . 83
4.3.2 Definitions for periodically driven nonlinear oscillators . . . 85
4.3.3 Pontryagin's Maximum Principle . . . 87
4.4 Methodology . . . 92
4.4.1 The Lagrangian Manifold . . . 93
4.4.2 The Escape Time . . . 97
4.4.3 Optimization and Implementation . . . 98
4.5 Forced Duffing Oscillator . . . 107
4.6 Two Coupled Oscillators . . . 123
4.7 Circular Oscillator Arrays . . . 133
4.8 Discussion . . . 141
4.9 Notes on Computational Cost and Nomenclature . . . 143

Chapter 5: Influence of Noise on a Rotating Cantilever Beam 149
5.1 Introduction . . . 149
5.2 Experimental Arrangement and Experiments . . . 150
5.3 Frequency Response . . . 154
5.4 System Identification . . . 158
5.4.1 System Model . . . 158
5.4.2 Parametric System Identification . . . 162
5.5 Experimental Results . . . 166
5.6 Simulation Results . . . 177
5.7 Discussion . . . 192

Chapter 6: Influence of Noise on Response Localizations of a Circular Cantilever Beam Array 195
6.1 Introduction . . . 195
6.2 Experimental Arrangement and Experiments . . . 197
6.2.1 Real-time Stiffness Detuning System . . . 200
6.3 Influence of Noise on Two Coupled Cantilever Beams . . . 202
6.3.1 Frequency Response . . . 203
6.3.2 System Identification . . . 208
6.3.3 Experimental Results . . . 217
6.3.4 Simulation Results . . . 224

6.4 Influence of Noise on Four Coupled Cantilever Beams 228
6.4.1 Frequency Response 229
6.4.2 System Identification 231
6.4.3 Experimental Results 236
6.4.4 Simulation Results 241
6.5 Eight Coupled Cantilever Beams 249
6.6 Discussion 251

Chapter 7: Contributions and Future Work 256
7.1 Summary of Contributions 256
7.2 Future Work 259

Bibliography 262

List of Tables

4.1 The quasipotential barriers for the escapes from localized modes at which only one oscillator has high amplitude for $N = 1, 2, 3, 5$ and from all modes for $N = 2$ at the frequency of $\omega = 1.4$ with $\nu = 0.01$. 140
4.2 Parameters and computational cost 146
4.3 Chapter 4 nomenclature 147
4.4 Chapter 4 nomenclature (continued) 148

List of Figures

1.1 Pratt & Whitney PW4000-112 engine [11]. 3
1.2 Underwater vibration energy harvester from research by Taylor *et al.* [17]. 4
1.3 Experimental circular array of macro-scale cantilevers. Each cantilever is approximately 16.5 cm (6.5 inches) long. Additional details of the components of the prototype are available in Chapter 5 and 6. 8

2.1 Summary of related experimental work. All reference works here are described in the following sections and are limited in scope to experiments that have identified nonlinear vibration modes including but not exclusive to response localizations. The work in the center circle focuses on noise induced transitions between nonlinear modes. Chapter 5 expands on some prior work on noise induced transitions in single cantilever beam vibrations. Chapter 6 addresses an unexplored research space by demonstrating experimentally the existence and statistics of noise induced transitions between nonlinear modes of circular cantilever beam arrays. . 11
2.2 Schematic of nonlinear spring mass damper system. 18
2.3 Schematic of a cyclically arranged array of linearly coupled nonlinear spring mass damper systems. 19
2.4 Overview of analytical and numerical methods used to find and study response localizations in arrays of coupled nonlinear oscillators subjected to a periodic excitation. The numerical continuations package AUTO2007 [51] is used to find localized modes in Chapters 3 and 4. COCO [52] is used to find localized modes numerically in Chapters 5 and 6. 20
2.5 Prior work summary of some methods that can be used to solve for the approximate stochastic response of nonlinear oscillators. 23
2.6 Prior work summary of methods that can be used to solve for the MPEP and the quasipotential. 32

3.1 Example of the transition probability density function for the forced Duffing oscillator. The white dots are the Gauss Legendre integration points in phase space. The white X marks the initial point $\boldsymbol{q}_o$ at time t_i. The contour plot shows the probability density function. The system has the highest probability of moving to region in yellow from the white X between time t_i and t_{i+1}. The orange-yellow circle surrounds the mapping subset around the mean for this $\boldsymbol{q}_o$ with a radius of 2. Note that the most important part of the TPDF is inside this circle. The entire space considered is $-4 \leq x \leq 4$ and $-4 \leq \frac{dx}{dt} \leq 4$. 49
3.2 Frequency response diagram for the deterministic harmonically forced Duffing oscillator. The presence of a hysteresis region with two stable branches (depicted with solid lines) and one unstable branch (depicted with dashed lines) is noted. This response diagram has been generated by using AUTO2007 [51]. 50
3.3 Contour of the probability density function after 1500 periods of the harmonically forced Duffing oscillator with additive noise intensity: (a) $\sigma = 0.1$ and (b) $\sigma = 0.2$. The probability density function in this figure has been normalized so that the integral over the domain (total probability) is equal to 1. In color are PDF level sets denser than 0.01 to highlight the regions of phase space with dense probability. The initial probability density corresponds to a deterministic point on the high amplitude attractor. It is noted that in (a), the probability is dense only near the high amplitude attractor, and in (b), the probability is dense near both attractors. 52
3.4 Basins of attraction of the harmonically excited deterministic Duffing oscillator. 53
3.5 Probability in each basin of attraction at each period for $\sigma = 0.2$. P_1 corresponds to basin of the low amplitude attractor (A_1) and P_2 corresponds to the high amplitude attractor (A_2). These probabilities are calculated by integrating the PDF in Fig. 3.3 (b) over the basins of attraction of the deterministic system. 54
3.6 Probability in the high amplitude basin of attraction at each period for different noise intensity. 55
3.7 Maximum density sets that with probability greater or equal to 95% contain solutions of the noise influenced forced Duffing oscillator in the first 1000 periods of noise influence with an initial deterministic initial condition at the high amplitude attractor. 57
3.8 L_2 Norm of maximum density sets of phase space, which with probability greater or equal to 95% contain solutions of the noise influenced forced Duffing oscillator in the first 1000 periods of noise influence. The initial deterministic initial condition is on the high amplitude attractor. 58
3.9 Transient probability in each basin generated by using Euler-Maruyama simulations compared with the results of the PIM method. 59

3.10 Root mean squared error (RMSE) of the PDF of forced Duffing oscillator for different grid resolutions defined by number of points N and different mapping resolutions specified by $N * N_\mu$ and $N * N_o$. There are N_μ points R distance from the forward mapped means and N_o points R distance from the initial point $\boldsymbol{x}_o$. Reference resolution is N = 6400 and R = 7. 60
3.11 Frequency response for system (3.30) of two coupled forced Duffing oscillators. It is noted that at $\omega = 1.4$. one has a stable synchronous high amplitude mode, a stable synchronous low amplitude mode, and two overlapping stable localized modes. The results are generated by using AUTO2007 [51]. 62
3.12 Probability density at each integration point normalized to a maximum density of 1 projected into the L_2 norm, for $\kappa = 0.1$ and $\sigma = 0.2$. 64
3.13 Probability in each basin of attraction at each period. Each $\tilde{p}_k$ corresponds to a basin of an attracting mode. $\kappa = 0.1$ and $\sigma = 0.2$. 65
3.14 Probability density at each integration point normalized to a maximum density of 1 projected into the L_2 Norm, for $\kappa = 0.01$ and $\sigma = 0.2$. 66
3.15 Probability in each basin of attraction at each period. Each $\tilde{p}_k$ corresponds to a basin of an attracting mode. The parameter values are $\kappa = 0.01$ and $\sigma = 0.2$. 67
3.16 Probability in the initial localized mode's basin of attraction at each period for varying coupling coefficients. $\sigma = 0.2$. 68
3.17 Probability in the initial localized mode's basin of attraction at each period for varying noise intensities. $k_c = 0.01$. 69

4.1 Schematic of linearly coupled nonlinear spring– mass-damper systems arranged in a cyclical array. 74
4.2 Frequency response of a circular array of $N = 5$ coupled forced Duffing oscillators as a function of excitation frequency, ω. At the frequency $\omega = 1.4$, unique attractors of the array are highlighted. This figure is generated by using the continuation package AUTO2007 [51]. The parameters in the ODE system (4.3) are set to $\alpha = 1$, $\beta = 0.3$, $\delta = 0.1$, $\nu = 0.01$, and the periodic excitation is of the form $f(t) = 0.4\cos(\omega t)$. Solid (dotted) lines in the figure correspond to stable (unstable) periodic solutions of the system (4.3). Here, it is of interest to examine how random perturbations influence the transition from one stable solution to another. 76
4.3 A flowchart overview of the main concepts in this chapter. Background is presented on a noise influenced system model, large deviation theory, and optimal control theory. A methodology built on the action plot method combined with the Floquet theory and numerical optimization is used to compute most probable escape paths and the quasipotential barriers of escapes from attractors of the system model. 81

4.4 An illustration for the origin of discontinuities in the cost function (4.37) on the example of a single bistable Duffing oscillator $\ddot{x} + \dot{x} - x + x^3 = \sqrt{\epsilon}\eta(t)$. This oscillator has stable equilibria at $(\pm 1, 0)$ and a saddle at the origin. The basin of $(-1, 0)$ is shaded cyan. The optimal Hamiltonian escape path and a collection of other Hamiltonian paths with close initial conditions are shown in red and black, respectively. It is apparent that overshooting initial conditions results in a much longer escape route and a sharp increase of escape cost. 100
4.5 A flow chart of the process of evaluating the cost function given an input $\boldsymbol{q}_\gamma$ and θ_0. A detailed version of the process shown here is described in the pseudocode of Algorithm 2. 104
4.6 Frequency response of a forced Duffing oscillator as a function of excitation frequency, ω. Attractor and saddle locations are highlighted at the frequency of $\omega = 1.4$. This figure is generated by using the continuation package AUTO2007 [51]. 108
4.7 Poincaré Map of the Basins of Attraction at the frequency of $\omega = 1.4$. . . 109
4.8 The cost (4.39) to escape from the high amplitude attractor as a function of ζ and the initial time $\theta_0 = t_0 \bmod T$. The variable ζ is the angle around a circle that completely surrounds the initial attractor at time θ_0. Three lowest local minima at $\theta_0 = 0$ are marked with red stars. They correspond to the minimum escape cost up to numerical errors. 112
4.9 The cost to escape from the high amplitude attractor as a function of ζ for fixed phase $\theta_0 = 0$. The variable ζ is the angle around a circle that completely surrounds the initial attractor at θ_0. Note that the minimizers of the cost function arise immediately next to discontinuities. 113
4.10 The escape action from the high amplitude attractor is minimized with respect to ζ at each initial phase θ_0. Notice that with some small error tolerance, the minimum action does not change with θ_0. 114
4.11 The Poincaré section of one MPEP that escapes the high amplitude attractor. This escape path begins at the attractor, rotates clockwise in the Poincaré section, and ends at the saddle. 116
4.12 The Poincaré sections of three MPEPs, which escape the high amplitude attractor with $\theta_0 = 0$, are plotted on top of each other. Notice that these escape paths all overlap in phase space, but cross the Poincaré section at different times. These MPEPs and all other MPEPs of this system share the same quasipotential, share this same characteristic in phase space, and have the same probability of occurrence. 117
4.13 The Poincaré section of a MPEP that escapes the low amplitude attractor. This escape path begins at the attractor, rotates counter-clockwise in the Poincaré section, and ends at the saddle. 118

4.14 The Poincaré section of a trajectory of equation (3) for $N = 1$ that is drawn to the saddle cycle as $t \to -\infty$, is rotated clockwise in the Poincaré section, and is drawn to the high amplitude attractor as $t \to \infty$. The rotation of the trajectory in phase space matches the rotation of the escape path of that same basin; this is common in lower dimensional systems such as the bistable unforced Duffing oscillator shown in Fig. 4.4, and is noteworthy because one could naively expect the most probable escape paths to move along the space of a trajectory but in the opposite direction, and this is not the case. 119
4.15 Euclidean norm, $|\boldsymbol{q}(t)| = \sqrt{\sum_i^{2N} q_i(t)^2}$, at all time steps of a MPEP that escapes the high amplitude attractor (solid) and of an unperturbed trajectory that descends from the saddle to the low amplitude attractor (dotted). 121
4.16 Euclidean norm of a MPEP that escapes the low amplitude attractor (solid) and of an unperturbed trajectory that ascends from the saddle to the high amplitude attractor (dotted). 121
4.17 (top) L_2 norm of the frequency response of the forced Duffing oscillator with attractor branches highlighted in color in the hysteresis region. (bottom) The quasipotential as a function of excitation frequency; action values corresponding to escapes from the low and high amplitude attractors are shown in blue and red, respectively. 123
4.18 Frequency response of two coupled forced Duffing oscillators as a function of excitation frequency, ω. Attractor and saddle locations are shown at the frequency $\omega = 1.4$. This figure is generated by using the continuation package AUTO2007 [51]. 124
4.19 Hyperplanes of a Poincaré map of a MAP that escapes the HH attractor. . 126
4.20 Euclidean norm of a MAP that escapes the HH attractor (solid) and of an unperturbed trajectory that from the SH saddle to the LH attractor (dotted). 127
4.21 Hyperplanes of a Poincaré map of a MPEP that escapes the LL attractor. . 128
4.22 Euclidean norm of a MPEP that escapes the LL attractor (solid) and of an unperturbed trajectory that ascends from the LS saddle to the LH attractor (dotted). 129
4.23 Hyperplanes of a Poincaré map of a MPEP that escapes the HL attractor. 130
4.24 Euclidean norm of a MPEP that escapes the HL attractor (solid) and of an unperturbed trajectory that descends from the SL saddle to the LL attractor (dotted). 131
4.25 (top) L_2 norm of the frequency response of the $N = 2$ system with attractor branches highlighted in color in the hysteresis region. (bottom) The quasipotential as a function of excitation frequency; action values corresponding to escapes from the LL, HL, HH attractors are shown in blue, yellow, and red respectively. 133

4.26 Frequency response of a circular array of $N = 3$ coupled forced Duffing oscillators as a function of excitation frequency, ω. Unique attractors are shown at the frequency $\omega = 1.4$. This figure is generated by using the continuation package AUTO2007 [51]. 135
4.27 Euclidean norm of a MPEP that escapes the LHL attractor (solid) and of an unperturbed trajectory that descends from the LSL saddle to the LLL attractor (dotted). 136
4.28 Euclidean norm of a MPEP that escapes the $LHLLL$ attractor (solid) and of an unperturbed trajectory that descends from the $LSLLL$ saddle to the $LLLLL$ attractor (dotted). 137
4.29 (top) The L_2-norm (4.4) of the frequency response of the $N = 3$ system with attractor branches highlighted in color in the hysteresis region. (bottom) The quasipotential corresponding to escapes from the LHL attractor as a function of excitation frequency. 138
4.30 The quasipotential barriers as a function of coupling coefficient ν that correspond to the following: (a) escapes from the H attractor of the single Duffing oscillator, (b) escapes from the localized mode of the single side coupling ($N = 2$) system, and (c) and (d) escapes from the localized mode with a single oscillator being at high amplitude in circular arrays ($N = 3$) and ($N = 5$), respectively. 139

5.1 Schematic of the data and energy flow in the experiment. 150
5.2 Experimental prototype with one cantilever beam. 151
5.3 Test piece prototype with one cantilever beam. 153
5.4 Time series response example with (top) the voltage signal read from the strain gauge and (bottom) a voltage signal proportional to the motor current read from a current sensor in the Kollmorgen AKD motor drive. . 153
5.5 Time series response of the beam near resonance when slowly increasing the excitation frequency. 155
5.6 Time series response of the beam near resonance when slowly decreasing the excitation frequency. 155
5.7 First harmonic amplitude of the response, a, as a function of frequency, f. 157
5.8 Top side visualization of the test piece, including the cantilever beam with a tip mass and a tip magnet, and a rigid base with a secondary magnet. The structure rotates following the angle θ with axis centered at the shaft mount. The beam tip displaces with coordinate s. This coordinate would be an arc length if the system was a rigid structure, and is a more complicated lateral displacement in the flexible structure. . . 159
5.9 Geometry of the beam tip displacement relative to the base magnet, assuming small displacements. 161
5.10 The experimental frequency response in nondimensionalized form, compared to the analytical approximation to the frequency response of the Duffing oscillator with parameters that minimize (5.13). Here, $\beta = -0.48$, $\hat{F}_0 = \eta = 0.0104$. 164

5.11 The experimental frequency response in nondimensionalized form compared to the frequency response of the Duffing oscillator computed via numerical continuation. Here, $\beta = -0.48$, $\hat{F}_0 = 0.007$, and $\eta = 0.009$. 165
5.12 An example noise trial of the experiment. Each trial began with a gradual decrease of the frequency of excitation, f_i, which leads the strain response to a high amplitude stable mode. At $t \approx 70$, noise is added to the control signal. After some time, the random perturbations induced a transition from the high amplitude strain response to a low amplitude strain response. 166
5.13 The power spectrum of the noisy control signal averaged over 500 trials for $\sigma_E = 100$. Notice a sharp peak at 18Hz corresponding to the deterministic cosine excitation and attenuation of the signal at higher frequencies that occurs due to the low pass behavior of the motor. 168
5.14 Box plots of the noise trials. Each box plot consists of 500 experimental trials for a different value of the noise multiplier. Here the excitation frequency is 18 Hz. 169
5.15 Histogram of the natural log of experimental escape times for $\sigma_E = 100$. . 170
5.16 Histogram of the natural log of experimental escape times for $\sigma_E = 80$. . 171
5.17 Estimate of the probability of remaining in the high amplitude attractor as a function of time and noise intensity, σ_E. Here, the excitation frequency is fixed to $f_i = 18$ Hz. These curves are created by using (5.14) on the experimental escape times. 173
5.18 Box plots of the noise trials. Each box plot consists of 500 experimental trials for a different value of the excitation frequency, f_i. Here $\sigma_E = 100$. 174
5.19 Estimate of the probability of remaining in the high amplitude attractor as a function of time and excitation frequency. Here, the noise intensity is fixed to $\sigma_E = 100$. These curves are created by using (5.14) on the experimental escape times. 175
5.20 Experimental escape paths of trial 1 and 2 of 500 for $\sigma_E = 60$ and $f_i = 18Hz$. The paths are visualized via a stroboscopic map sampled once a period of displacement and velocity. The velocities are calculated by using a first order central difference scheme on the displacement. The path includes the state of the system 200 periods before and after the transition. 176
5.21 Basins of attraction of the system model at $\Omega = 0.9$ or equivalently $f_i = 18$Hz. The basin of the high amplitude attractor and the low amplitude attractor are shown in red and green, respectively. An unstable basin in which the response blows up to infinity is shown in blue. 178
5.22 The Euclidean norm of the Poincaré section of the stochastic response of the system model simulated using the Euler-Maruyama scheme. The transition time between a high amplitude response and the low amplitude response is highlighted with the dashed line. 180

5.23 The median escape time for sets of Euler-Maruyama simulations that begin at the high amplitude attractor as a function of the noise intensity σ. Each data point is calculated using 200 Euler-Maruyama simulations. Each simulation used $\Omega = 0.9$ that is equivalent to $f_i = 18$Hz. The experimental escape times are fit to the natural log simulated escape times for comparison. 181
5.24 Estimates of the probability of remaining in the high amplitude attractor of the experiment (left) and simulation (right) data as a function of time and noise intensity. Here, $f_i = 18$Hz. 182
5.25 Estimates of the quasipotential U extracted from the slope of $\log(\lambda(\sigma))$ and $1/\sigma^2$. 184
5.26 Basins of attraction of the system model for different excitation frequencies, f_i. Notice that the domain of the high amplitude basin of attraction increases in area with excitation frequency. 185
5.27 Box plots of the escape times of the experiment (left) and the Euler-Maruyama simulations (right) as a function of excitation frequency. . . . 186
5.28 Estimates of the probability of remaining in the high amplitude attractor of the experiment (left) and simulation (right) data as a function of time and frequency. 187
5.29 The most probable escape paths out of the high amplitude attractor of the system model for different excitation frequencies. 189
5.30 The quasipotential as a function of frequency for escapes out of the high amplitude and low amplitude attractors, shown in red and blue, respectively. Notice that the quasipotential to escape the high amplitude attractor is lower in magnitude than the quasipotential to escape the low amplitude attractor for the majorities, except for those very close to the jump up frequency. This suggests the probability of transitioning from high amplitude response to low amplitude response far exceeds the probability of transitioning from low amplitude response to high amplitude response for the majority of frequencies of excitation. 191

6.1 Picture of the experimental system with the excitation system consisting of motors, drivers, controllers, and the circular oscillator array. 197
6.2 Picture of the circular oscillator array consisting of eight cantilever beams. The depicted 120Ω strain gauges are used for data acquisitions. The linear actuators are used for nonlinear mode manipulation. The permanent magnets and the calibration screws are used to calibrate the linear stiffness and nonlinear stiffness of the beams. 198
6.3 Top view schematic of the circular cantilever beam array with tuned beams of interest 3 and 7 highlighted in black. 203
6.4 Response time histories for Beams 3 and 7 near resonance when slowly decreasing the excitation frequency. 204
6.5 Response time histories for Beams 3 and 7 near resonance when slowly increasing the excitation frequency. 205

6.6 Response time histories for Beams 3 and 7 near resonance when slowly decreasing the excitation frequency. At a time of approximately 390 seconds, the linear actuator corresponding to Beam 7 is powered to displace the base magnet temporarily; this is labeled as the *Magnet Movement Event*. After the magnet movement event, the linear actuator returned the magnet to the original position and the frequency sweep continued in the HL mode. 206
6.7 The sum of the first harmonic amplitudes of Beam 3 and Beam 7 for different excitation frequencies. A total of four frequency sweeps with different initial conditions are performed to acquire the data in this figure. The sweeps are conducted in a manner to record the steady-state response at each frequency. 208
6.8 Best fit of the analytical approximation of the sum of the frequency response of four Duffing oscillators to the experimental data. The minimizing parameters are $\beta_L = -0.2605$, $\hat{F}_{0L} = 0.0059$, $\eta_L = 0.0059$. . 211
6.9 The experimental phase response of the LL, HL, and HH modes for each beam as a function of nondimensionalized excitation frequency. The phase angle, ϕ, is in radians. 214
6.10 The phase cost (6.6) as a function of coupling force coefficient h. 215
6.11 The phase response of the HL mode from experimental data and from the $N = 2$ system model of (6.5) for four different h values. In the legend, a high amplitude oscillator is denoted as "High oscillator", and a low amplitude oscillator is denoted as "Low oscillator". The phase angle, ϕ, is in radians. 216
6.12 Numerical continuation frequency amplitude response of the stable modes of (6.5) with parameters $\alpha = 1, \beta = -0.2605, \eta = 0.0069, h = -0.0045, F = 0.0059$ shown with the experimental data. 217
6.13 Time series representation of a single noise trial. (1-2) strain response of cantilevers 3 and 7. (3) Runtime experimental parameters including the excitation frequency, the displacement of the Beam 7 base magnet, and the noise multiplier. Notice that the strain response increases in both cantilevers into the HH mode with decreases in the excitation frequency, the cantilevers transition in the HL mode with the magnet movement event, and then the cantilevers transition to the LL mode due to the influence of noise. 219
6.14 Box plots of transitions times out of the HL mode for varying noise intensity and constant excitation frequency, $f_i = 18$Hz. 220
6.15 Average probability of remaining in the HL mode. Each curve corresponds to a different noise intensity and is made up of 10 bins of 50 trials each. The dashed lines indicate $\pm$ one standard deviation bound as an estimate of the error. All curves correspond to the excitation frequency of 18Hz. 222
6.16 Box plots of transitions times out of the HL mode for varying excitation frequency and constant noise intensity, $\sigma_E = 175$. 223

6.17 The median transition times of transitions out of the HL mode for different noise intensities, σ. Each point of the red curve is the median from 200 numerical trials. The experimental points are shown alongside the numerical data. The location of the experimental data with respect to σ is determined by finding a scalar multiplier for σ_E and an offset that best fits the numerical data. 225
6.18 The probability of remaining in the HL mode for both the experiments and the simulations for different noise intensities. Here the excitation frequency is 18Hz. 226
6.19 Box plots of the transition times from the HL mode to the LL mode for both the experimental and simulation results for different excitation frequencies, f_i and constant noise intensity. 227
6.20 Top view schematic of the circular cantilever beam array with tuned beams of interest 1, 3, 5, and 7 highlighted in black. 229
6.21 The sum of the first harmonic amplitude responses of the four beam system as a function of excitation frequency. Notice 6 unique nonlinear modes labeled in this figure. Additional symmetric modes are also observed but not shown here. 230
6.22 Best fit of the analytical approximation of the sum of the frequency response of four Duffing oscillators to the experimental data. The minimizing parameters are $\beta = -0.2989$, $F = 0.0068$, and $\eta = 0.0068$. . 231
6.23 The experimental phase response of the $LLLL$, $LHLL$, and $HHHH$ modes for each beam as a function of nondimensionalized excitation frequency. The phase angle, ϕ, is in radians. 233
6.24 The phase cost (6.6) as a function of coupling force coefficient h. 234
6.25 The phase response of the $LHLL$ mode from experimental data and from the $N = 4$ system model of (6.5) for four different h values. In the legend, a high amplitude oscillator is denoted as "High Oscillator", and a low amplitude oscillator is denoted as "Low Oscillator". The phase angle, ϕ, is in radians. 235
6.26 Numerical continuation frequency amplitude response of the stable modes of (6.5) with parameters $\alpha = 1, \beta = -.2989, \eta = 0.0078, h = -0.0023$, and $F = 0.0068$ shown with the experimental data. 236
6.27 Time series representation of a single noise trial. (1-4) strain response of cantilevers 1,3,5,7. (5) Runtime experimental parameters including the excitation frequency, the displacement of magnets, and the noise multiplier. Notice that the strain response increases in all cantilevers into the $HHHH$ mode with decreases in the excitation frequency, the cantilevers transition in the $LHLL$ mode with the magnet movement event, and then the cantilevers transition to the $LLLL$ mode due to the influence of noise. 238
6.28 Box plots of transitions times out of the $LHLL$ mode for different noise intensities and constant excitation frequency, $f_i = 23$Hz. 239

6.29 Average probability of remaining in the $LHLL$ mode. Each curve corresponds to a different noise intensity and is made up of 10 bins of 50 trials each. The dashed lines indicate $\pm$ one standard deviation bound as an estimate of the error. All curves correspond to the excitation frequency of 23Hz. 240
6.30 Box plots of transitions times out of the $LHLL$ mode for different excitation frequencies and constant noise intensity, $\sigma_E = 200$. 241
6.31 The median transition times of transitions out of the $LHLL$ mode for different noise intensities, σ. Each point of the red and yellow curves is the median from 200 numerical results. The experimental points are shown alongside the numerical data. The location of the experimental data with respect to σ is determined by finding a scalar multiplier for σ_E and an offset that best fits the numerical data resulting from (6.11). . . . 243
6.32 The probability of remaining in the $LHLL$ mode for both the experiments and the simulations for different noise intensities. 244
6.33 (left) The escape rate, λ, estimated from the results in Fig. 6.32 as a function of time. Note it approaches a constant after an initial transient and terminates (no more data) after all trials have transitioned out of the $LHLL$ mode. (right) The slope of the $\log(\lambda)$ and $1/\sigma^2$ that can be used to estimate the quasipotential from simulation results. At the excitation frequency of 23Hz the estimate of the quasipotential is $3.6 * 10^{-5}$. 245
6.34 Box plots of the transition times from the $LHLL$ mode to the $LLLL$ mode for both the experimental and simulation results for different excitation frequencies, f_i and a constant noise intensity. 246
6.35 (top) L_2 norm of the frequency response of the stable modes of the Four Beam system as a function of excitation frequency. (bottom) The quasipotential (min. action) of escapes from the $LHLL$ mode to as a function of excitation frequency. At $\Omega = 0.92$, the excitation frequency is equivalent to $f_i = 23Hz$, and the corresponding quasipotential value is $3.1 * 10^{-5}$. 248
6.36 Top view schematic of the circular cantilever beam array with all eight beams as tuned beams of interest. 249
6.37 The sum of the first harmonic amplitude responses of the eight beam system as a function of frequency. Notice only two unique nonlinear modes labeled in this figure. 250

List of Abbreviations

AMAM	Adaptive Minimum Action Method
BA	Basin of attraction
DOF	Degree of freedom
EM	Euler-Maruyama
FPGA	Field Programmable Gate Arrays
GMAM	Geometric Minimum Action Method
IC	Integrated circuits
ILM	Isolated localized modes
JPDF	Joint probability density function
MAP	Minimum action path
MAM	Minimum action method
MEMS	Micro-electromechanical system
MPEP	Most probable escape path
ODE	Ordinary differential equation
PDE	Partial differential equation
PDF	Probability density function
PIM	Path integral method
RMSE	Root mean squared error
SDE	Stochastic differential equation
TPDF	Transition probability density function
VEH	Vibration energy harvester

Chapter 1: Introduction and Research Objectives

Mechanical vibrations influence the structural integrity and performance of mechanical systems to the extent they can create undesirable operating conditions or even catastrophic failures. Often, studies of these systems resort to deterministic linear models that are simple and powerful first-approach tools, but can in certain situations not adequately capture the behavior of a system. In reality, mechanical systems experience both seemingly random and nonlinear forces; stochastic nonlinear models can be better suited to explain the resulting behavior, but they give rise to challenging mathematical problems.

In this dissertation, the effect of random forces on systems with inherently nonlinear behavior is studied via a combination of experimental and simulation work. In particular, the systems of interest, including turbomachinery, micro-electromechanical systems (MEMS), and vibration energy harvesters (VEH), consist of multiple beam-like and plate-like structures that can exhibit stable periodic mechanical oscillations that are best explained via nonlinear analysis [1–3]. Furthermore, it is known that random factors can induce transitions into and out of these vibration modes [4, 5]. In this dissertation, experiments are developed to demonstrate the effect of random perturbation on these mechanical systems. These developments include automatic control of electromechanical

components to produce thousands of trials of noise induced transitions out of undesired vibration modes of rotating macro-scale cantilever structures *(Chapters 5 and 6)*. They also include the first experiments of a circular oscillator array of mechanical macro-scale cantilevers developed and used to study the influence of noise on nonlinear modes of the structure *(Chapter 6)*. Additionally, new computational methodologies, physics-based models, and observations are explained for quantifying and understanding the stochastic nonlinear behavior that arises in the considered systems. These include adding post processing steps to numerical results that can be obtained using the Path Integral Method [6] to quantify probability of transitions *(Chapter 3)*, promoting the Action Plot Method [7] to quantify quasipotentials and transition paths for high dimensional systems with periodic external excitations *(Chapter 4)*, and comparisons of Monte Carlo simulations of system models to experimental results *(Chapters 5 and 6)*. The selected modeling approach consists of coupled single degree of freedom nonlinear oscillators. The resulting governing equations are high dimensional, nonlinear, lightly damped, non-autonomous, and non-deterministic. These equations can be difficult to solve as there are no generalized solutions for these system models, and numerical approximations of solutions are an active area of research [3, 8, 9].

1.1 Systems and Phenomena of Interest

1.1.1 Turbomachinery

Turbomachinery refers to devices through which energy is transferred between a fluid or gas and a rotor [10]. The energy transfer is often performed by a bladed disk

mounted on a rotor. When the energy is transferred from a fluid or gas to the rotor, the machine is known as a turbine. There are steam, gas, and hydraulic turbines, and common applications of these machines include wind turbines and power plants. When the energy is transferred from the rotor to the fluid or gas by increasing its pressure, the machine is known as a compressor. Compressors are used for example in rockets and jet engines by the aerospace industry. A picture of a Pratt & Whitney PW4000-112 engine is included as an example of turbomachinery in Fig. 1.1 [11]. The competitive and growing nature of the energy and aerospace markets creates a need for lower cost, increased efficiency and safety, which has led to proposals for new products that rely on lightweight designs or materials [12]. Resulting slender, lightweight, or under-damped structures from new designs may lead to higher deflections of vibrating components that can lead to undesired nonlinear behavior [3].



Figure 1.1: Pratt & Whitney PW4000-112 engine [11].

1.1.2 Vibration Energy Harvesters

Vibration energy harvesters (VEH) are another type of mechanical system of interest that convert ambient vibration energy into primarily electrical energy [13, 14]. These systems can be integrated into micro scale devices such as micro-electromechanical systems (MEMS) or integrated circuits (IC) when they are used to power wireless sensors in biomedical applications and remote tracking and positioning applications [15, 16]. There are also macro-scale VEHs such as those that harvest energy from underwater motion, as shown in Fig. 1.2 [17]. Nonlinear behavior in some designs of VEHs can increase the frequency bandwidth over which the system response yields a high energy output [18].

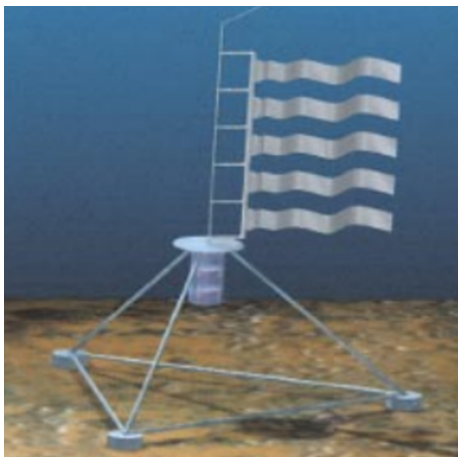


Figure 1.2: Underwater vibration energy harvester from research by Taylor *et al.* [17].

1.1.3 Response Localizations

A response localization consists of a subset or component of the system vibrating at a high energy level while the rest of the system vibrates with less energy. In

turbomachinery, this can take the form of one or more blades vibrating at a high amplitude while the rest of the blades vibrate at low amplitudes. Localization can occur when the blades of the bladed disk are mistuned; that is, in-homogeneous due to manufacturing errors or wear. Severs [19] developed an experimental study of mistuning in turbomachinery and has cited many experimental studies of the effect in turbomachinery in his dissertation. Others have studied mistuning in turbomachinery by developing Finite Element models [20] or other models [21–23]. Likewise, response localizations can occur in designs of VEHs, in which coupled in-homogeneous blades are used; Gardonio *et al.* [24] studied localized modes in a system of coupled in-homogeneous linear oscillators; they discussed how localizations can be utilized to maximize energy yield by properly placing a piezoelectric generator where the energy is localized. In these studies of mistuning, the systems are studied and modeled in the linear regime. In newer slender or lightweight system designs, by design or as a bi-product, systems can exhibit nonlinear behavior to the extent these linear approximations are inadequate; a system with nonlinear behavior even when perfectly homogeneous (well-tuned) can exhibit response localizations [1–3, 25–27]. These localized high amplitude oscillations can on one hand be destructive in turbomachinery [3, 19, 20, 22, 28] and on the other hand be beneficial for energy harvesting systems [24, 29].

1.2 Objectives and Structure

The overarching goal behind this work is to understand how response localizations that arise due to nonlinear behavior are influenced by random perturbations. Random

perturbations can be representative of the cumulative external excitations from a complicated surrounding environment. That is, random perturbations arise naturally from the environment and influence these systems. Additionally, random perturbations could be used in a simplified control strategy to transition into or out of response localizations. The tools and knowledge developed in this work can be used by designers of systems that consist of vibrating cantilever structures to understand, design for, and control potentially undesirable stochastic nonlinear behavior. The following research objectives are addressed in this work:

1. Generate experimental evidence of the effect of noise on a cyclically arranged macro-scale mechanical oscillator array

2. Quantify the probability of transitions into and out of nonlinear modes of nonlinear oscillator arrays influenced by harmonic excitations and noise

3. Quantify the quasipotential to transition into and out of nonlinear modes of nonlinear oscillator arrays subjected to periodic excitations

4. Identify the most probable transition paths between stable nonlinear modes in the weak noise limit

Through work towards the first objective the undesired nonlinear vibration modes and the noise influenced transitions are demonstrated in a controlled environment. Experimental evidence is invaluable to the validation of theoretical and computational work modeling noise induced transitions out of nonlinear modes. The second, third, and fourth objective address the development of theoretical and computational tools that can

be used to understand and design for the problem of interest.

Prior research and contributions relevant to these objectives are described via a literature review in Chapter 2.

Original work in Chapter 3 expands on prior work by defining a methodology to quantify the probability of transitions in a forced Duffing oscillator system and a system of two coupled Duffing oscillators. This chapter primarily addresses challenges in quantifying probabilities of transitions in non-autonomous systems with more than one potential well due to large noise intensities, and uses the developed methodology on a case study of Duffing oscillators representative of the mechanical system. The results of the case study are approximations of the probability with respect to time of transitioning out of stable periodic solutions; these can be practically useful in understanding how likely transitions will occur in the short term due to random perturbations.

While Chapter 3 addresses large noise intensities, Chapter 4 is focused on systems subjected to very small noise intensities. Chapter 4 includes a case study on noise induced transitions between nonlinear modes that occur with the highest probability in the weak noise limit. The chapter improves on an existing methodology allowing it to work with higher dimensional systems subjected to periodic excitations. The improved methodology is then used to determine the most probable transitions paths and the quasipotential, a system specific quantifier of the difficulty of a system transitioning due to noise.

Experimental results are described in Chapters 5 and 6 for a single cantilever and a circular array of cantilevers, respectively. The array, developed in this work, consists of eight cantilevers arranged as shown in Fig. 1.3. The array is designed so that the cantilevers resonate at low frequencies, the cantilevers could be calibrated to a

desired natural frequency, nonlinear modes could be generated programmatically, and the effect of long duration, low intensity noise could be observed. In addition to producing experimental evidence of transitions, the design is used to explore a system identification approach and the statistics of noise induced transitions.

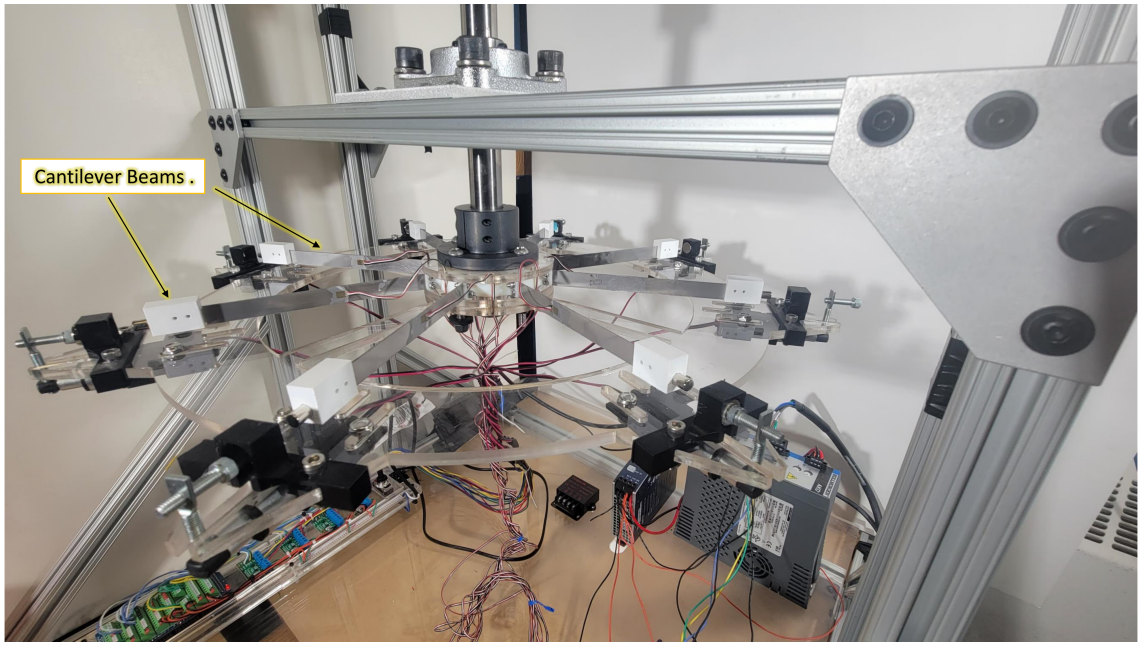


Figure 1.3: Experimental circular array of macro-scale cantilevers. Each cantilever is approximately 16.5 cm (6.5 inches) long. Additional details of the components of the prototype are available in Chapter 5 and 6.

A summary of the key contributions of this work is provided in Chapter 7, along with suggestions for future work.

Chapter 2: Literature Review

This chapter discusses relevant prior work. Experimental efforts related to nonlinear response localizations or noise induced transitions in mechanical systems are summarized in Section 2.1. The most common lumped mass deterministic system model for these cantilever structures and the study of response localizations due to nonlinearity in these systems is discussed in Section 2.2. Prior studies of the influence of noise on this system model for finite (not infinitesimal) noise intensities are discussed in Section 2.3. Finally, literature relevant to the study of noise induced transitions for systems subjected to infinitesimally weak noise is reviewed in Section 2.4.

2.1 Prior Experimental Work

Nonlinear response localizations have been demonstrated in controlled experiments in systems that are representative of turbomachinery and Vibration Energy Harvesters (VEHs). This has most commonly took the form of experimental arrays of cantilevers that represent the blades of turbomachinery or VEHs, wherein the cantilevers were designed and manufactured with tight enough tolerances that the system could be considered as a set of coupled homogeneous oscillators. Furthermore, cantilevers that are excited into large displacements exhibit nonlinear behavior. As an alternative to large high frequency

excitations that generate large displacements, the nonlinear behavior is in some cases enhanced through other means; some examples are explained throughout this section. Given the dimensions of the cantilever structures considered, cantilever, cantilever beams, and beams are used interchangeably to describe a cantilever structure. This section includes a review of this prior experimental work.

A visual overview and categorization of the work discussed in this section is given in Fig. 2.1. In Fig. 2.1, relevant experimental literature is categorized as circular cantilever arrays studies, in-line cantilever arrays studies, individual cantilever studies, and other array studies. These categories are subdivided further into works that studies noise influenced transitions and works that did not. The categorization in Fig. 2.1 is designed to highlight relevant work, but is not a comprehensive overview of all available literature in these categories.

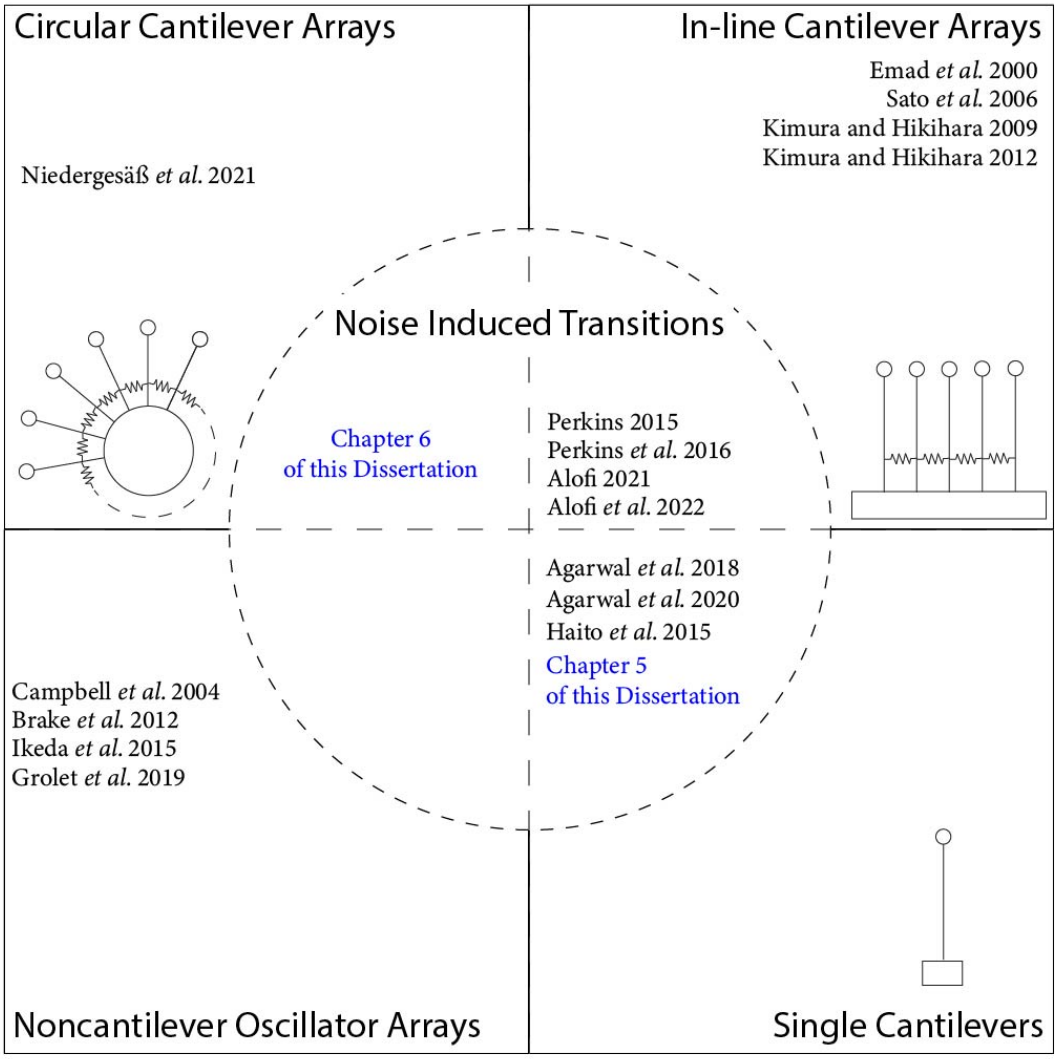


Figure 2.1: Summary of related experimental work. All reference works here are described in the following sections and are limited in scope to experiments that have identified nonlinear vibration modes including but not exclusive to response localizations. The work in the center circle focuses on noise induced transitions between nonlinear modes. Chapter 5 expands on some prior work on noise induced transitions in single cantilever beam vibrations. Chapter 6 addresses an unexplored research space by demonstrating experimentally the existence and statistics of noise induced transitions between nonlinear modes of circular cantilever beam arrays.

2.1.1 In-line Macro-scale Cantilever Arrays

Emad *et al.* [30] were the first to design an array of in-line arranged macro-scale cantilever beams hanging from a base. Nonlinearity was enhanced in their experiment via the addition of permanent magnets that generate a nonlinear restoring force. These magnetic restoring forces are not always representative of real applications, but allow the nonlinear behavior to be observed without needing a large high frequency excitation system to generate large displacements. A shaker was used to excite the system harmonically near resonance. Due to the in-line arrangement, each cantilever beam was most strongly coupled to its nearest neighbors. The cantilever beams at each end of the array are free. Response localization and the hysteresis region near resonance of the cantilever beams were observed. Kimura and Hikihara [31, 32] took this work a step further by designing an array of in-line arranged cantilever beams also hanging from a base that use electromagnets instead of permanent magnets. With the electromagnets they were able to explore creation and destruction of the localized modes by changing the on site nonlinear restoring force at each beam. Perkins *et al.* [4, 33] studied this system to demonstrate that noise could create or destroy the localized modes in a model of this experiment.

Perkins *et al.* [4] also designed a similar array of in-line arranged cantilever beams. These beams had permanent magnets to enhance the nonlinear behavior, and the beams were supported upright on the base instead of hanging down from a base. Perkins *et al.* [4] used this experiment to create empirical evidence that additive random perturbations to the excitation system could be used to destroy response localizations. Alofi *et al.* [5, 9]

continued with the Perkins *et al.* [4] experimental setup and studied the effect of noise on two beams. They demonstrated that the average transition time out of a localized mode due to random perturbations depends on a relationship between the frequency of an external excitation and the hysteresis region; modeling the experimental results they found that at different frequencies of excitation, the model's stable responses have differences in the size of the basins of attraction that can be correlated to transition times.

2.1.2 Circular Macro-scale Cantilever Arrays

In Chapter 6 of this dissertation, the effect of noise in an array of cyclically arranged macro-cantilever beams is explored. This arrangement can be modeled with boundary conditions that are periodic, and the experiment can be considered representative of the bladed disk of a turbine. In the explored literature space, there is only one experimental study where nearly homogeneous cantilever beams are arranged in a cyclical manner to study the effect of nonlinearity on localized modes. Niedergesäß *et al.* [34] developed an experimental circular oscillator array where they used discontinuous contact to generate the nonlinear behavior. They created a model of the system with the piece-wise linear stiffness and demonstrate numerically localized modes and also experimentally localized modes. In the experiments, these nonlinear stable modes were found near resonance. They used undefined external perturbations to create the initial conditions in the experiment prior to beginning the frequency sweep, and they showed the effect of changing frequency on the response. Unlike the work in this dissertation, Niedergesäß *et al.* [34] explored contact nonlinearities, and did not study noise induced transitions.

2.1.3 Alternative Oscillator Arrays

Others have studied localization in experiments that do not use macro-cantilever beams fixed at one end; for example, Campbell *et al.* [35] discussed localized energy in other systems including charge-transfer solids, Josephson Junctions, photonic structures, and micro-mechanical oscillator arrays. The cause of localized energy in these systems is due to nonlinearity and discreteness in the systems. Sato *et al.* [36] developed a micro-cantilever array representative of MEMS applications by using silicon deposition and etching. They forced the micro-cantilever array using a piezoelectric transducer to generate response localizations and used optical lasers to measure the displacement of the cantilever's tip. Brake *et al.* [37] presented an experimental example of localized modes in crystalline pillars for sensing applications in the nano-scale; The existence of localizations depend on the properties of the crystalline pillars. Ikeda *et al.* [38] experimentally studied localization in an array of two pendulum oscillators. By changing the coupling springs, they found Hopf bifurcations, amplitude modulated motions, and chaotic vibrations. Grolet *et al.* [39] designed an arrangement of two coupled fixed-fixed beams and observed response localizations. The beams in this experiment were cut from a supporting base plate except for at ends to yield fixed-fixed boundary conditions; the coupling was achieved through the base plate which was excited by a magnet and a coil carrying electric current. Other forms of response localization have been widely studied in other research areas as well, where they are also known as "Discrete Breathers" or "Anderson Localization," from a Nobel Prize winning discovery by Anderson [40] in the context of a diffusion wave problem.

2.1.4 Stochastic Experiments on Single Cantilevers

A few notable mentions of experimental studies of noise in individual macro-scale cantilever beams are presented here. Focusing on only one beam can be considered a simplification wherein a subset of the array that consists of one cantilever beam is uncoupled to the array and can be studied separately. Agarwal *et al.* [41] examined how the region of multi-stability in the frequency response of a softening, nonlinear oscillator can be influenced by noise. They did this by running an experiment with a cantilever with a magnet at the tip and found the hysteresis region is smaller when the system is influenced by noise. In this work, Agarwal *et al.* also described a parametric system identification approach for the cantilever beam that involves normalizing the highest amplitude of the frequency response curve and by using analytically derived frequency response approximations for the Duffing oscillator. The system identification approach of Chapter 5 and 6 is based on the method of Agarwal *et al.* [41]. In a separate study, Agarwal *et al.* [42] studied a cantilever beam operating in a chaotic regime and showed that noise additions induced crisis, as a consequence of which the system followed an escape path from a chaotic attractor to a stable attractor. Haitao *et al.* [43] presented a tri-stable energy harvesting experiment where a cantilever beam is subjected to forces from three magnets, one at the tip, and two at specially selected locations to create the triple stability. The dynamic responses of the system subjected to harmonic excitation and random perturbations are explored by a numerical method and validated by experiments. They conclude the tri-stable configuration with a low depth, low amplitude potential well yields maximum output voltage for an energy harvester of this type.

2.1.5 Summary of Experimental Work

The reviewed experimental work reveals an unexplored research space: Except for the work by Perkins *et al.* [4] and Alofi *et al.* [9], noise induced transitions out of response localizations have not been studied. Furthermore, in the work by Perkins and the Balachandran group, the design included free-free boundary conditions with the in-line arranged cantilever array, whereas in Chapter 6, the influence of noise is explored in experiments representative of turbo machinery with a cyclical arrangement.

2.2 System Model

In the prior section, examples were discussed of experimental representation of turbomachinery and VEHs as arrays of macro-cantilever beams where each beam is often fixed on one end and free at the other end. The first vibration mode of a fixed-free beam can be modeled as a lumped mass single degree of freedom (DOF) spring mass damper system with the discretized mass and response coordinate being at the tip of the beam [44]. In addition, when a beam is subjected to large displacements or magnetic restoring forces, it can be desirable to include nonlinear stiffness terms in the model. Hochrainer and Puhwein [45] described the magnetic restoring force in a cantilever beam with a permanent magnet at the tip, and Kimura and Hikihara described the same using electromagnets [31]. For these beam oscillators, a prototypical single degree of freedom model in nonlinear vibrations is the Duffing oscillator.

The Duffing equation [46],

$$\ddot{x} + \eta\dot{x} + \alpha x + \beta x^3 = F(t), \tag{2.1}$$

is a second order differential equation with a linear stiffness term and a nonlinear cubic stiffness term. Here x is a coordinate that models the displacement of the beam tip, η is a parameter representative of the system damping coefficient, α is a parameter representative of the squared natural frequency term, β is a parameter that scales the nonlinear restoring force, and $F(t)$ is a time varying external excitation. Abstract parameters are used in equation (2.1) because the actual system parameters may be nondimensionalized as is convenient. One may think of this oscillator as a mass attached to a nonlinear spring as shown in Fig. 2.2. Depending on the nonlinear stiffness parameter value, β, the corresponding oscillator can exhibit hardening or softening characteristics. The response of the forced Duffing oscillator can be approximated analytically or numerically by using methods described in nonlinear vibration textbooks [47–49]. When excited near the primary resonance, the Duffing oscillator can exhibit multiple stable responses and hysteresis. In certain configurations, the Duffing oscillator can also exhibit chaos [50].

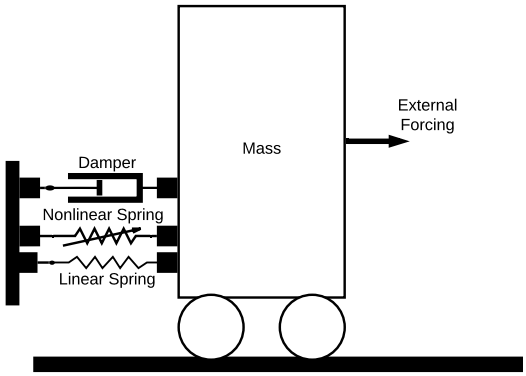


Figure 2.2: Schematic of nonlinear spring mass damper system.

The system model for an array of $N \geq 3$ cyclically arranged Duffing oscillators is shown in equation (2.2).

$$\begin{aligned} &\ddot{x}_i + \eta\dot{x}_i + \alpha x_i + \beta x_i^3 + \nu\left(2x_i - x_{i-1} + x_{i+1}\right) = F(t) \\ &i = [1, 2, ..., N], \quad x_{N+1} = x_1, \quad x_{(1-1)} = x_N \end{aligned} \tag{2.2}$$

In equation (2.2), each oscillator is index by i and is linearly coupled with coupling stiffness ν to neighboring oscillators as shown in the Fig. 2.3 schematic.

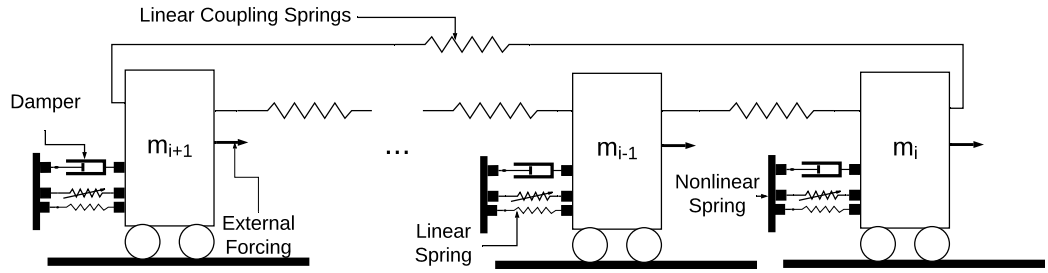


Figure 2.3: Schematic of a cyclically arranged array of linearly coupled nonlinear spring mass damper systems.

2.2.1 Localized Modes of the Deterministic System

Arrays of coupled, Duffing oscillators have been studied to understand localization and special structures such as localized modes using both analytical and numerical approaches. Methods that have been used in prior work are summarized in Fig. 2.4.

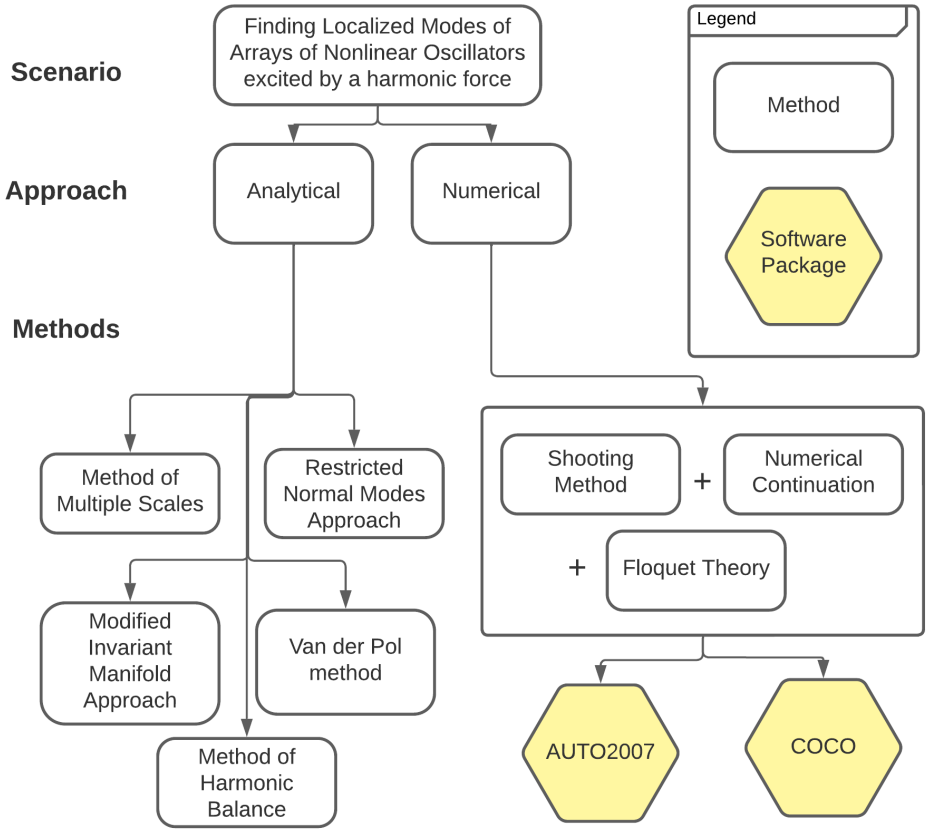


Figure 2.4: Overview of analytical and numerical methods used to find and study response localizations in arrays of coupled nonlinear oscillators subjected to a periodic excitation. The numerical continuations package AUTO2007 [51] is used to find localized modes in Chapters 3 and 4. COCO [52] is used to find localized modes numerically in Chapters 5 and 6.

Vakakis and Cetinkaya [53] demonstrated that nonlinear localized modes occur in homogeneous, perfectly symmetric, weakly coupled structures. They used an asymptotic

approximation up to first order to find the modes and numerical methods are used for validation. A recent study of the localized modes for a cyclic homogeneous Duffing oscillator array was carried out by Papangelo *et al*. [3]. They found that nonlinear modes of the conservative system, and used the continuation package, AUTO [51], to find the frequency response diagram for the periodic solutions of the corresponding harmonically forced damped system. Kerschen *et al.* [54] and Peeters *et al.* [55] describe the numerical shooting method and continuation procedures that can be used in finding the nonlinear modes of mechanical systems. These references also describe the use of Floquet theory to find the stability of the identified modes.

In some studies of localized modes researchers have used analytical approaches. Dick *et al.* [25] studied localization in micro-resonator arrays modeled with cubic nonlinearities. They used multiple analytical methods including the method of multiple scales, the restricted normal modes approach, and a modified invariant manifold approach to identify intrinsic localized modes. In another study, Dick *et al.* [56] studied frequency tuning in nonlinear systems of Duffing oscillators using the Van der Pol method, and they tuned the frequency of neighboring oscillators from one to one and three to one ratios. They observed that the special frequency tuning itself does not have an effect of increasing the number of localized modes but that the parameter values that increase the effect of the coupling term can lead to more localized modes. Grolet and Thouverez [1] used the harmonic balance method and studied free and forced nonlinear vibrations of an undamped structure with cyclic symmetry. Ikeda *et al.* [27] explored the behavior of a coupled Duffing oscillator array forced by a harmonic excitation. The Van der Pol method was applied to determine the approximate steady state solutions of the system and the

frequency response curves are generated showing the hysteresis region for a system with two Duffing oscillators. They show how certain initial conditions lead to the localized modes by plotting the basins of attraction (BA) for the two degree of freedom system and also by plotting time series examples for ten oscillators.

2.3 Noise Influenced System

In the prior section, examples of system models of turbomachinery and VEHs as arrays of coupled Duffing oscillators were shown. In most of that prior work, the systems are subjected to harmonic excitations near primary resonance in response to which the system exhibits multiple stability including localized modes. The work in this dissertation focuses on the effect of noise by including an additive noise term in addition to the harmonic excitation:

$$\ddot{x}_i + \eta\dot{x}_i + \alpha x_i + \beta x_i^3 + \nu\left(2x_i - x_{i-1} + x_{i+1}\right) = Fcos(\omega t) + \sqrt{\varepsilon}\dot{W}(t), \quad i = [1, 2, ..., N] \tag{2.3}$$

In equation (2.3), ω is the forcing frequency, ε is a parameter that scales noise intensity, and $\dot{W}(t)$ is white noise that influences each oscillator equally. Methods used in prior work to analyze systems like (2.3) with finite ε are summarized in Fig. 2.5. Note that the colors highlight prior use cases and limitations for each method, but the methods could possibly be adapted for other use cases in the future. In particular the Euler-Maruyama method is used throughout Chapters 3, 5, and 6, and the Path Integral Method is a focus of the methodology in Chapter 3. Euler-Maruyama is computationally expensive (slow) but

works in high dimensions, and the Path Integral Method yields fast approximations, but only works in low dimensions with systems that have large noise relative to the system dynamics.

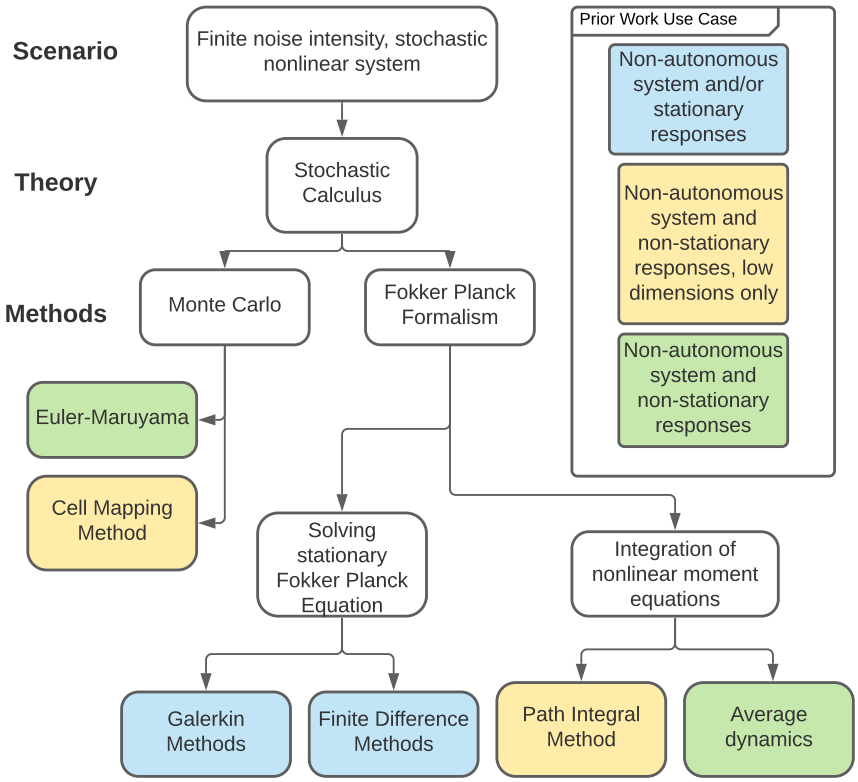


Figure 2.5: Prior work summary of some methods that can be used to solve for the approximate stochastic response of nonlinear oscillators.

The following section focuses on methods applied to case studies of systems very similar to (2.3) and is not a comprehensive review of methods in the field of stochastic nonlinear dynamics.

2.3.1 Solving Stationary Fokker Planck Equation

Von Wagner and Wedig [57] studied a Duffing oscillator excited only by white noise, a set of coupled Duffing oscillators excited only by white noise, and a single Duffing oscillator excited by white noise and harmonic excitation. They converted their stochastic differential equations (SDE) first into polar coordinates, and then used the stochastic averaging method to create an approximate probability density function (PDF). They then used the Fokker Planck equation and a Galerkin method to solve for weights of polynomials that scale the approximate solution into a more accurate stationary PDF. Their methodology is useful in understanding the steady state behavior of these systems, though notably they did not solve for the high dimensional non-autonomous system. Martens *et al.* [58] expanded on this approach by calculating the stationary probability density function of high dimensional arrays of coupled mono-stable Duffing oscillators with up to ten oscillators. Their novel contribution is the use of orthogonal polynomials with the Galerkin method which yielded faster results making higher dimensional studies feasible. They validated results with Euler-Maruyama (EM) simulations. Förster *et al.* [59] also used a similar Galerkin method approach to calculate the stationary response for a system representative of a bladed disk only under random perturbations. The model in this work is high-dimensional with a cubic nonlinearity and also includes a special damping attributed to friction. These efforts yielded results for the unforced autonomous system in the steady state, but could potentially be explored in studying the non-autonomous system.

2.3.2 Integrating Moment Differential Equations

2.3.2.1 Average Dynamics

Ramakrishnan and Balachandran [60] and Perkins and Balachandran [61] studied non-autonomous nonlinear systems with a harmonic excitation and additive noise using a different approach. Ramakrishnan and Balachandran [60] studied a non-homogeneous system with cubic on site nonlinearity and cubic inter-site (coupling) nonlinearities. The system is non-homogeneous in that neighboring oscillators alternated between two stiffness parameter sets representative of a micro-cantilever array that has alternating long and short cantilevers. Perkins and Balachandran [61] used the same approach but for a homogeneous system with only onsite cubic nonlinearities. In both studies, they derived the differential equations for the moments of the probability density function from the Fokker Planck equation. In both of the efforts, assumptions were made that higher order moments are negligible and that neighboring oscillators are independent. Both studies demonstrate results for the mean displacements of the oscillators due to the effect of noise and conclude that a level of noise in these systems can generate or destroy localized modes. Validation of their approach is also included using EM simulations. Learnings from this work are instrumental in that this methodology yields results for the high dimensional non-autonomous system in the transient as opposed to previously mentioned work that focused on the stationary probability density functions. Further illustrating the methodology using the moment equations in a transient example, Perkins *et al.* [62] demonstrated the effect of noise on travelling energy localizations in an array of Duffing

oscillators influenced by noise. The localization is created with a sinc pulse exciting the first oscillator and travelling through 16 oscillators via energy transfer through the coupling springs. They find the probability distribution of the solutions and demonstrate an attenuation of the traveling wave when noise is present. In another effort explaining experimental results, Perkins *et al.* [4] used the shooting method to numerically find localized modes of an array of weakly coupled Duffing oscillators that modeled a macro-cantilever array. They carried out simulations with the EM scheme to integrate an SDE governing the array influenced by white noise and showed that the response localizations could be destroyed and other localized modes could be created by using noise in the system representative of the mechanical experiment.

2.3.2.2 Path Integral Method

Another useful approach, a discretized Path Integral Method (PIM), was first described by Yu *et al.* [6]. In the PIM used by them, the nonlinear moment differential equations were derived from the Fokker Planck equation and Gauss-Legendre integration of the PDFs was performed over phase space. The approach integrates moment differential equations forward in time, generates transition probability density functions (TPDF) using the resulting moments, and maps an initial probability density function forward in time through a convolution over a discretized phase space with the transition probability density function. This approach is described in more detail in Chapter 3. In demonstrating the methodology, Yu and Lin [63] generated the probability density functions of the forced Duffing oscillator. Kumar and Narayanan [64] and Narayanan

and Kumar [65] also generated the probability density functions of the forced Duffing oscillator while demonstrating a new developments in the Path Integral Method that uses Hermite polynomial expansions to generate non-Gaussian transition probability density functions that yield more accurate results with reduced computational cost. Cui *et al.* [66] also used the PIM to study the non-stationary response of variable-mass Duffing oscillators. Xie *et al.* [67] used PIM to study a Duffing -Rayleigh oscillator with harmonic and stochastic excitations. In another work, Ren *et al.* [68] proposed a faster local averaged alternative to the traditional PIM but used a different nonlinear system as the example. PIM is affected by the curse of dimensionality and existing prior work is limited to low dimensional examples. Furthermore, the discretized PIM works better when the noise intensity is sufficiently large such that the transition probability density functions are non-singular in the discretized phase space. As a trade-off, as the noise intensity decreases, the resolution of the phase space and the number of integration time-steps to reach the stationary response must increase.

2.3.3 Euler Maruyama Scheme

The Euler-Maruyama (EM) scheme is a popular simulation methodology of the response systems like (2.3). The methodology based on stochastic calculus extends the Euler method to integrate with respect to additional Brownian motion increments. Here a Brownian motion increment is a random variable from a Gaussian distribution with mean zero and variance proportional to the time-step of integration. The Brownian motion itself is the random path generated from the cumulative Brownian motion increments.

Higham [69] provides a concise summary of the relevant theory and a description of the simulation methodology. Because this stochastic integration scheme is widely used, the majority of the literature in this section uses it standalone or as for validations of other methodologies. Monte-Carlo analysis of the simulations that result from the Euler-Maruyama scheme are useful because this methodology is less limited than others by the curse of dimensionality. Nevertheless, the approach can be computationally time intensive since a small time-step of integration and a large quantity of EM simulations are necessary for accurate results; if the noise intensity is too small or the time span of interest is too long, this approach may not be practical.

Balachandran *et al.* [2] studied a system of linearly arranged oscillators with cubic nonlinearities and coupling cubic nonlinearity representative of a di-element micro-cantilever array influenced by noise. In the forced and damped case, they use a EM scheme and integrate the SDEs with and without noise, with and without cubic coupling, noting that noise can destroy the localization with and without cubic coupling, cubic coupling attenuates the localization by giving more energy to the neighboring oscillators, and that noise more easily destroys the localization with the presence of cubic coupling.

Balachandran *et al.* [8] studied the effect of coupling and frequency parameters on noise induced transitions out of response localizations in circular oscillator arrays using EM stochastic simulations. A similar Monte Carlo stochastic simulation approach is used in Chapter 5 and 6, but in this work the analysis is focused on explaining the behavior of the experimental system.

2.3.4 Other Relevant Low Dimensional Studies ($N = 1$)

In considering weakly coupled Duffing oscillator arrays, it is of interest to explore the simpler anti-continuum limit. In this limit, the coupling term vanishes and each oscillator behaves as an individual single degree of freedom Duffing oscillator. As a result, it is useful to review prior work on the effect of noise on a individual Duffing oscillator excited by a harmonic force and additive white noise.

Von Wagner [70] discussed a relationship between noise and the size of the potentials in generating an analytical approximation to the stationary probability density function of the noise influenced, harmonically forced Duffing oscillator. He used a set of zeroth order approximations of the probability density functions assumed to be Gaussian in each basin of attraction and then scaled the approximations by the size of the basin of attraction in which they reside. This approximation was compared to probability density functions generated using EM simulations.

Xu *et al.* [71, 72] studying the forced Duffing oscillator defined a set of points in the phase space as stochastic attractors, stochastic basins, and stochastic saddles, and they used the cell mapping method to demonstrate the evolution of these sets with noise intensity. Furthermore, they characterized significant qualitative changes in the structure of the stochastic solutions with respect to variation in the noise intensity as stochastic bifurcations. Agarwal *et al.* [41] examined how the region of multi-stability in the frequency response of a softening, nonlinear oscillator can be influenced by noise. In another study, Agarwal *et al.* [42] numerically studied noise induced crisis and trajectory escape from a chaotic attractor when noise is added to a harmonically forced

Duffing oscillator. Zhang *et al.* [73] studied a similar oscillator, and used Monte Carlo schemes and stochastic averaging methods to study P-bifurcation and D-bifurcation of the responses of oscillators with quintic stiffness, wherein a D-bifurcation is associated with a sign change in the largest Lyapunov exponent and P-bifurcations are associated with changes in the qualitative structure of the joint probability density function (JPDF). Kumar *et al.* [74] analyzed the influence of Gaussian noise on a VEH that is modeled as a Duffing oscillator coupled to a first order model for the generator. He used a finite element approach to solve the Fokker Planck Equation and EM simulations to validate the resulting stationary PDF.

2.4 Transition Events in the Weak Noise Limit

The previous section reviews prior work on the noise influenced responses of forced Duffing oscillators excited by noise of finite intensity. This section focuses on prior work related to the study of stochastic nonlinear systems in the weak noise limit. Consider the following SDE:

$$d\boldsymbol{q} = \boldsymbol{b}(\boldsymbol{q}, t)dt + \sqrt{\varepsilon}\,\boldsymbol{g}(\boldsymbol{q})\,d\boldsymbol{W}(t) \tag{2.4}$$

Here, $\boldsymbol{q}$ is a vector of states, $\boldsymbol{b}$ is the drift vector and $\boldsymbol{g}(\boldsymbol{q})$ is a matrix function of $\boldsymbol{q}$. $\boldsymbol{Q}(\boldsymbol{q}) = \boldsymbol{g}\boldsymbol{g}^{\top}$ is the diffusion matrix; when $\boldsymbol{Q}$ is invertible, the noise in equation (2.4) is non-degenerate. The state space representation of an SDE like (2.3) is defined with a non-invertible matrix $\boldsymbol{Q}$; as a result, the systems studied in this dissertation are considered to be influenced by degenerate noise. In equation (2.4), $d\boldsymbol{W}(t)$ is the differential representation of a Wiener process that discretizes into Gaussian random

variables with mean zero and variance proportional to a discrete time-step. The parameter, ε, scales the contribution of noise to the system. The magnitude of this parameter either depends on the nature of the environment or on the desired magnitude of a noise control strategy and could be as small as zero or larger than deterministic excitation forces. When this parameter is zero, the system is deterministic; however, in the limit that noise intensity approaches zero, the system is still non-deterministic. This weak noise limit is of interest in nonlinear systems with multiple attractors because however small, the probability of a transition between one attractor to another is non-zero [75]. The possibility of these rare events is interesting when the timescale of deterministic dynamics are different from another timescale of interest. For example, in an illustrative example for turbomachinery, one can imagine blades may vibrate with sub second periods, but the timescale of continuous operation of the system could range from hours to years such that rare transitions are relevant. Moreover, studying the weak noise limit can provide insight into how a system behaves at higher noise intensities. Freidlin and Wentzell demonstrated that in the weak noise limit when a transition between attractors occurs, with overwhelming probability it will occur through a specific path, the Most Probable Escape Path (MPEP) [75]. Furthermore, for autonomous systems with degenerate noise, they demonstrated that the MPEP is the path with action equal to the quasipotential, a system specific coefficient that quantifies the difficulty of a transition occurring due to random perturbations.

A graphical summary of the methods that have been used in related work to find the MPEP and the quasipotential are included in Fig. 2.6. As highlighted in Fig. 2.6, the action plot method is capable of handling the degenerate noise in the system studied

in this dissertation. An original methodology that promotes the Action Plot Method with optimization for higher dimensional systems with periodic external excitations is presented in Chapter 4.

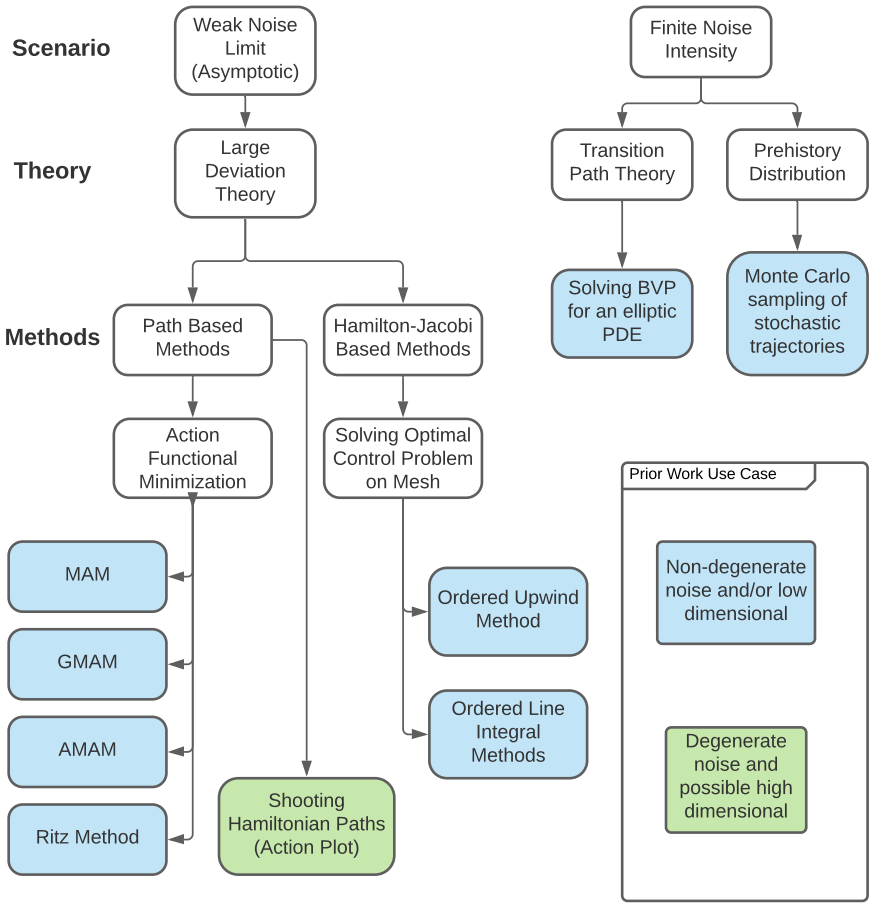


Figure 2.6: Prior work summary of methods that can be used to solve for the MPEP and the quasipotential.

In general, the MPEP cannot be found analytically. Numerical methods have been developed to find the MPEP in autonomous gradient and non-gradient systems. Weinan E *et al.* [76] developed the Minimum Action Method (MAM) which is a generalization of some prior methods that solved for the path by minimizing action in paths of finite

time. Heymann and Vanden-Eijnden [77, 78] developed the Geometric Minimum Action Method (GMAM) where the time is removed from the action functional and replaced by the path arc-length. GMAM can solve for minimum action paths of infinite time durations such as paths that begin and end at fixed points. Zhou *et al.* [79] presented an adaptive MAM (AMAM) algorithm that modifies the mesh of the paths in improving efficiency of MAM. By using MAM, Zhou and E [80] found the transition paths in the Lorenz system with parameters for both chaotic attractors and limit cycles. In more recent work, Kikuchi *et al.* [81] used a Ritz method. They defined the minimum action path as a linear combination of functions and developed an optimization problem to find coefficients to the functions such that the linear combination minimizes the action functional. Lin *et al.* [82] proposed a new computational strategy of MAM to compute the minimum action path from a limit cycle. Since the initial attractor is a limit cycle, the path is infinitely long and this imposes a numerical challenge in using MAM. They solve for the quasipotential near the limit cycle first and then using a local approximation of the quasipotential as a starting point that truncates the infinitely long path. These path based methods work in any dimension and are relatively simple to implement, but they have some disadvantages; the methods can only handle cases with non-singular diffusion matrices (non-degenerate noise) and are biased by initial guesses for the minimum action path. Furthermore, GMAM was designed only for autonomous systems.

Other related work has used Hamilton-Jacobi based methods. Cameron [83] used a variation of the Ordered Upwind Method to find level sets of quasipotential and the minimum action path for a two dimensional system. Dahiya and Cameron [84] developed the more efficient Ordered Line Integral Method for computing the quasipotential. In

another work, Dahiya and Cameron [85] extend the Ordered Line Integral Methods for the case of variable and an-isotropic diffusion. Yang *et al.* [86] used an upgrade of the Ordered Line Integral Method to solve for the quasipotential in rectangular meshes in three dimensions. Because using these methods yields results that approximate the value of the quasipotential at all points, these methods do not require a biased initial guess and are guaranteed to yield the global minimum of the quasipotential. Nevertheless, these methods have disadvantages including that they are designed for non-degenerate noise, autonomous systems, and are limited to low dimensional (less than or equal to three dimensions) efforts.

There are also some notable mentions of methods that have been used to find MPEP in small but finite (not in the asymptotic limit) noise scenarios. Dykman and McClintock [87] describe a Monte Carlo approach to solve for prehistory distributions. They define a prehistory probability density function $\boldsymbol{p}_h(\boldsymbol{q}, t, \boldsymbol{q_f}, t_f)$, that describes the distribution of paths that end at $\boldsymbol{q_f}$ at time t_f having been at $\boldsymbol{q}$ at time t, with $t < t_f$. This method allows for degenerate noise, but is limited to low dimensional analysis with long run times. E and Vanden-Eijnden [88] describe the method used in Transition Path Theory. One can create accurate estimates for transition paths and transition rates when a Markov process transitions from a set A of states to a set B of states. When using transition path theory, one defines and solves an elliptic PDE for the committor function, where the committor function is the probability that a process first reaches B rather than A. Solving the PDE is limited to low dimensional (two dimensional) systems.

Lingala *et al.* [89] studied the quasipotential and most probable transition paths of nonlinear oscillators excited by periodic excitation. Their approach is based on a

perturbation method that assumes weak nonlinearities and small external excitations.

Chapter 4 is devoted to the study of quasipotential barriers and the most probable escape paths (MPEPs) from basins of various attractors of arrays of periodically forced Duffing oscillators in the limit of the white noise intensity tending to zero. The work in Chapter 4 does not assume weak nonlinearity or weak forcing. Central to the developed methodology in Chapter 4 is the *action plot method* introduced in the work of Beri *et al.* [7] for finding MPEPs in two-dimensional non-gradient SDEs. An important advantage of the action plot method is that it is suitable for systems with inertia and external forcing. For example, Chen *et al.* [90] used this method to find a MPEP for a chaotic oscillator [91] and validated it by matching it with the computed prehistory probability distribution. The action plot method implies a graphical solution to the optimization problem that arises – this is the reason for its name – and hence this approach in its original form [7] is limited to low dimensional systems (single oscillator). The main methodological contributions of Chapter 4 are the extension of the action plot method to high dimensional systems with periodic forcing and the development of a minimization technique for solving the optimization problem for initial conditions for the MPEP.

Chapter 3: Transient Probability in Basins of Noise-Influenced Responses of Mono and Coupled Duffing Oscillators

In this chapter, the Path Integral Method (PIM) is explained and used in a new way to calculate the probability of transitions between nonlinear stable modes under the influence of short-duration noise of large intensity. A modified methodology is proposed that decreases the computational cost of the original method and makes it possible to expand the study to a four dimensional system of two coupled Duffing oscillators. The original work in this chapter was peer reviewed and published [92] in *Chaos: An Interdisciplinary Journal of Nonlinear Science*.

3.1 Background and Methods

In this section, the original Path Integral Method (PIM) is described generalized for systems with attractors that are subjected to additive noise excitation. The attractors of the systems and the associated basins of attractions (BAs) are found numerically. For each simulation, the initial condition is approximated as a deterministic point located on an attractor. The approach can be summarized in the following steps:

1. Define a set of governing equations that can be used to describe the evolution of the system's moments.

2. Map the moment equations forward in time.

3. Define a transition probability density function (TPDF) using the system's moments.

4. Map an initial probability density function (PDF) forward in time using the TPDF.

5. Acquire the probability in each basin by integrating the new PDF over the domain of each basin of attraction.

The numerical approach to using PIM is based on the PIM scheme of Yu *et al.* [6]; that is, discretizing the domain of interest into Gauss Legendre integration points.

3.1.1 Path Integral Method Formulation

This analysis is applicable to a system that can be described by an SDE of the form (2.4). $\boldsymbol{q}$ is a random variable governed by (2.4). With $\boldsymbol{B} = \frac{1}{2}\boldsymbol{g}\boldsymbol{g}^{\top}$, the Fokker-Planck equation governing the transition probability density function (TPDF), $L(\boldsymbol{q}, t \,|\, \boldsymbol{q}_0, t_0)$, is the following:

$$\frac{\partial L(\boldsymbol{q}, t \,|\, \boldsymbol{q}_0, t_0)}{\partial t} = -\sum_{i=1}^{d} \frac{\partial (b_i \, L(\boldsymbol{q}, t \,|\, \boldsymbol{q}_0, t_0))}{\partial q_i} + \frac{1}{2} \sum_{i=1}^{d} \sum_{j=1}^{d} \frac{\partial^2 (B_{ij} L(\boldsymbol{q}, t \,|\, \boldsymbol{q}_0, t_0))}{\partial q_i \partial q_j} \tag{3.1}$$

In (3.1), $L(\boldsymbol{q}, t \,|\, \boldsymbol{q}_0, t_0)$ denotes the transition probability from an initial condition $(\boldsymbol{q}_0, t_0)$ to $\boldsymbol{q}$ at time t. Here d is the dimension of $\boldsymbol{q}$. Equation (3.1) is used to obtain moment differential equations that can be integrated numerically to create a transition

probability density function. All moments of the random variable $\boldsymbol{q}$ are defined by the corresponding expectation operation and indexed by the bookkeeping parameter j:

$$m^{(j)} = E[\prod_{i=1}^{d} q_i^{\phi_i^{(j)}}] = \int_{\mathbb{R}^d} \prod_{i=1}^{d} q_i^{\phi_i^{(j)}} L(\boldsymbol{q}, t \mid \boldsymbol{q}_0, t_0) d\boldsymbol{q} \tag{3.2}$$

Here $\boldsymbol{\phi}^{(j)}$ is a vector containing the powers of the random variable in the expectation operators to indicate different orders of moments and correlated moments. In order to evaluate the evolution of the moments in time, the time derivative of the moment equations is defined as the following:

$$\dot{m}^{(j)} = \dot{E}[\prod_{i=1}^{d} \boldsymbol{q}_i^{\phi_i^{(j)}}] = \int_{\mathbb{R}^d} \prod_{i=1}^{d} \boldsymbol{q}_i^{\phi_i^{(j)}} \frac{\partial L(\boldsymbol{q}, t \mid \boldsymbol{q}_0, t_0)}{\partial t} d\boldsymbol{q} \tag{3.3}$$

After substituting (3.1) into (3.3), and then integrating by parts, one can derive a set of ordinary differential equations (ODEs) where the time derivatives of the moments are a function of moments. For example, consider the system:

$$\dot{x} + \alpha x + \beta x^3 = \sigma \dot{W}(t) \tag{3.4}$$

The state space SDE of this system with $q = x$ is:

$$dq = \left(-\alpha q - \beta q^3\right) dt + \sigma dW(t) \tag{3.5}$$

The Fokker-Planck equation for this system takes the form:

$$\frac{\partial L(q,t \mid q_0,t_0)}{\partial t} = (\alpha + 3\beta q^2) + \frac{\sigma^2}{2}\frac{\partial^2 L(q,t \mid q_0,t_0)}{\partial^2 q} \tag{3.6}$$

Therefore the time derivatives of the first two moment are given as:

$$\begin{aligned}
\dot{m}^{(1)} = \dot{E}[q^1] &= \int_{-\infty}^{\infty} q\frac{\partial L}{\partial t}dq \\
&= \int_{-\infty}^{\infty} q(\alpha + 3\beta q^2)Ldq + \int_{-\infty}^{\infty} \frac{\sigma^2 q}{2}\frac{\partial^2 L}{\partial^2 q}dq \\
&= \int_{-\infty}^{\infty} q(\alpha + 3\beta q^2)Ldq + \int_{-\infty}^{\infty} \frac{\sigma^2 q}{2}\frac{\partial^2 L}{\partial^2 q}dq \\
&= \alpha E[q] + 3\beta E[q^3] + \int_{-\infty}^{\infty} \frac{\sigma^2 q}{2}\frac{\partial^2 L}{\partial^2 q}dq \\
&\quad \text{Integration by parts with the assumptions } L(q,t \mid q_0,t_0) \text{ approaches 0 at } q = \pm\infty \\
&= \alpha E[q] + 3\beta E[q^3] \\
\dot{m}^{(2)} = \dot{E}[q^2] &= \alpha E[q^2] + 3\beta E[q^4] + \sigma^2
\end{aligned} \tag{3.7}$$

For concise notation L is used in place of $L(\boldsymbol{q}, t \mid \boldsymbol{q}_0, t_0)$. The algebra for $\dot{m}^{(2)}$ is not shown in (3.7). Notice in (3.7) that the resulting integral is simplified by substituting definitions for other higher order moments. For nonlinear systems, in general, one generates an infinite number of moment equations with this procedure because the time derivative of a moment depends on higher moments. A non-Gaussian moment closure technique is used to limit the number of moments in the procedure to a finite set. Socha provides a concise summary of multiple moment closure techniques in [93]. A cumulant moment closure

technique first proposed by Cramer [94] and later by Stratonovich [95] was employed by Yu *et al.* [6] and also throughout this chapter. This procedure is used to close the set of ODEs to a set of desired moments, $M(t, \boldsymbol{x}_o, t_o)$, defined by a set of moment powers Φ:

$$\Phi = \left\{ \boldsymbol{\phi}^{(j)} \in \mathbb{W}^d : \sum_{i=1}^{d} \phi_i^{(j)} \leq 2 \right\} \tag{3.8}$$

With this procedure, one defines the higher order moments not included in Φ in terms of the lower order moments that are included in Φ. For the purpose of approximating the TPDFs, this chapter assumes Gaussian TPDFs as in the method used by Yu *et al.* [6]. As a result the derivation and calculation of the moment equations to the minimum number of moments required to generate a multivariate Gaussian distribution with corresponding means, variances, and co-variances. Φ from (3.8) is the set of all these moment powers of interest and is defined in (3.8) as the set of all permutations of d whole numbers where the sum of the d numbers is smaller or equal to 2. The moment equations are defined and evaluated for each $\boldsymbol{\phi}^{(j)}$ in Φ.

$$M = \{m^{(j)}\} \quad \forall\, j = 1, 2, ..., |\Phi| \tag{3.9}$$

Here, $|\Phi|$ is the cardinality of Φ which is also equal to the total number of moments. Applying moment closure for example (3.4), the moment ODE's in (3.7) can be closed

to:

$$\begin{aligned} \dot{m}^{(1)} &= \dot{E}[q^1] = \alpha E[q] + 3\beta E[q]E[q^2] + 2\beta E[q]^3 \\ \dot{m}^{(2)} &= \dot{E}[q^2] = 2\alpha E[q^2] + 6\beta E[q^2]^2 - 4\beta E[q]^4 + \sigma^2 \end{aligned} \tag{3.10}$$

which for simplicity can be written as

$$\begin{aligned} \dot{m}_1 &= \alpha m_1 + 3\beta m_1 m_2 + 2\beta m_1^3 \\ \dot{m}_2 &= 2\alpha m_2 + 6\beta m_2^2 - 4\beta m_1^4 + \sigma^2 \end{aligned} \tag{3.11}$$

This example is provided for illustration and follows [6]. Numerical integration of a system of moment ODEs can be performed to calculate a set of desired moments $M(t, \boldsymbol{q}_o, t_o)$. Then the TPDF takes the following form:

$$L(\boldsymbol{q}, t \,|\, \boldsymbol{q}_o, t_o) = G\left(\boldsymbol{q}, M(t, \boldsymbol{q}_o, t_o)\right) \tag{3.12}$$

Here, G represents a multivariate Gaussian distribution that can be generated by using a covariance matrix and means derived from the moments as shown in equation (3.13).

$$L(\boldsymbol{q}, t \,|\, \boldsymbol{q}_o, t_o) = \frac{1}{(2\pi)^{d/2}\sqrt{\left|\boldsymbol{K}\right|}} \exp\left(\frac{1}{2}(\boldsymbol{q} - \boldsymbol{\mu}) * \boldsymbol{K^{-1}} * (\boldsymbol{q} - \boldsymbol{\mu})^T\right) \tag{3.13}$$

Here, $\boldsymbol{K} = \boldsymbol{K}(t, \boldsymbol{q}_o, t_o)$ is the covariance matrix derived from M, $|\boldsymbol{K}|$ is the determinant of the covariance matrix, and $\boldsymbol{\mu} \in M(t, \boldsymbol{q}_o, t_o)$ are the mean quantities.

The path integral method is the integration of an initial probability density function

acted upon by the transition probability density function:

$$p(\boldsymbol{q}^{(i+1)}, t^{(i+1)}) = \int_{\mathbb{R}^d} p(\boldsymbol{q}^{(i)}, t^{(i)})\, L(\boldsymbol{q}^{(i+1)}, t^{(i+1)} \,|\, \boldsymbol{q}^{(i)}, t^{(i)})\, d\boldsymbol{q} \tag{3.14}$$

The integration is carried out over the d dimensional phase space with a transition probability density function that may be different for each $\boldsymbol{q}^{(i)}$, $t^{(i)}$, and $t^{(i+1)}$. Note that if the discretized phase space is the same at time step i and step $i+1$ then the index on $\boldsymbol{q}$ is not necessary. In this study, the systems are time periodic and the periodicity of the TPDF means that the values of the TPDF need to be computed over just one period. By using (3.14) recursively, one can compute the PDF of the d dimensional system forward in time, providing an initial PDF, $p(\boldsymbol{q}, t^{(0)})$.

As described by Yu *et al.* [6], for numerical implementation, phase space can be discretized into sub intervals and Gauss Legendre integration points:

$$\begin{gathered} p(\boldsymbol{q}_{mn}^{(i+1)}, t^{(i+1)}) = \sum_{k=1}^{K_s} \frac{\delta_k}{2} \sum_{l=1}^{\hat{L}_k} c_{kl}\, p(\boldsymbol{q}_{kl}^{(i)}, t^{(i)})\, L(\boldsymbol{q}_{mn}^{(i+1)}, t^{(i+1)} \,|\, \boldsymbol{q}_{kl}^{(i)}, t^{(i)}) \\ m = 1, 2, ..., K_s \quad and \quad n = 1, 2, ..., \hat{L}_m \end{gathered} \tag{3.15}$$

In (3.15), K_s represents the number of sub-intervals in phase space, $\hat{L}_m$ represents the number of Gauss Legendre integration points in each sub-interval, δ_k scales by the size of the sub-interval, and c_{kl} is the weight that corresponds to each integration point. The total number of integration points is

$$N \equiv \sum_{k=1}^{K_s} \hat{L}_k \tag{3.16}$$

In mapping all N points $\boldsymbol{q}_{kl}^{(i)}$ to all N points $\boldsymbol{q}_{mn}^{(i+1)}$, the method has an $O(N^2)$

computational cost as described in (3.15). Yu *et al.* [6] and Yu and Lin [63] proposed that for a short duration integration, $L(\boldsymbol{q}_{mn}^{(i+1)}, t^{(i+1)} \mid \boldsymbol{q}_{kl}^{(i)}, t^{(i)})$ can be evaluated for points, $\boldsymbol{q}_{mn}^{(i+1)}$, near $\boldsymbol{q}_{kl}^{(i)}$ with little loss in accuracy. Though they did not explicitly describe it, in determining the nearby points, they may have created a reduction from $O(N^2)$ cost to $O(N * N_o)$ with some selection of $N_o < N$, $\boldsymbol{q}_{mn}^{(i+1)}$ points near all $\boldsymbol{q}_{kl}^{(i)}$ points. In this chapter, the methodology is adapted to further reduce the cost to $O(N * N_\mu)$ with $N_\mu < N_o < N$. The proposal here is that the selection of N_μ points can yield similar accuracy as a selection of N_o or N points. This is later demonstrated to be true with convergence analysis. Consider the means $\boldsymbol{\mu}$,

$$\boldsymbol{\mu} \equiv \boldsymbol{\mu}(\boldsymbol{q}_{kl}^{(i)}) \equiv \boldsymbol{\mu}(t^{(i+1)}, \boldsymbol{q}_{kl}^{(i)}, t^{(i)}) \in \boldsymbol{M}(t^{(i+1)}, \boldsymbol{q}_{kl}^{(i)}, t^{(i)}) \tag{3.17}$$

A subset of points a parameter R distance from $\boldsymbol{\mu}$ can be defined as $X_\mu \subset X_N$ and N_μ is the number of X_μ points. The logic for this new implementation is as follows: the TPDF is Gaussian and nearly zero far from the mean. R can therefore be estimated from variance of the TPDF or fixed at the start for constant time-steps. Since $\boldsymbol{\mu}$ is already available from other necessary logic in the formulation, and it is an improved center for finding the reduced range of $\boldsymbol{q}_{mn}^{(i+1)}$ points as opposed to the location of $\boldsymbol{q}_{kl}^{(i)}$, a smaller radius R yields a higher accuracy and lower computational cost. First one must define X_μ:

$$\begin{aligned} X_N &= \{\boldsymbol{q}_{mn}\} \quad \forall\, (m = 1, 2, ..., K_s\,,\, n = 1, 2, ..., \hat{L}_m) \\ X_\mu(\boldsymbol{q}_j^{(i)}) &= \{\boldsymbol{q} \in X_N : \left\| \boldsymbol{q} - \boldsymbol{\mu}(\boldsymbol{q}_j^{(i)}) \right\| \leq R\} \quad \forall\, \boldsymbol{q}_j \in X_N \end{aligned} \tag{3.18}$$

This is the subset of mapped points near the mean position of the Gaussian TPDF after mapping. One can use this to redefine (3.15) as follows:

$$
\begin{aligned}
& p(\boldsymbol{q}_m^{(i+1)},\, t^{(i+1)}) = \\
& \sum_{j=1}^{N} \begin{cases} \frac{\delta_j}{2} c_j\, p(\boldsymbol{q}_j^{(i)}, t^{(i)})\, L(\boldsymbol{q}_m^{(i+1)}, t^{(i+1)} \mid \boldsymbol{q}_j^{(i)}, t^{(i)}), & \boldsymbol{q}_m^{(i+1)} \in X_\mu(\boldsymbol{q}_j^{(i)}) \\ 0, & \boldsymbol{q}_m^{(i+1)} \notin X_\mu(\boldsymbol{q}_j^{(i)}) \end{cases} \\
& \forall\, m = 1, 2, ..., N
\end{aligned}
\tag{3.19}
$$

Here the summation is redefined in terms of N, whereas previously it was defined in terms of the sub-interval and Gauss-Legendre integration indices, and then it is assumed the added term is non-zero only when $\boldsymbol{q}_m^{(i+1)}$ is in the mapping subset, $X_\mu(\boldsymbol{q}_j^{(i)})$. This method is found to work efficiently when the TPDFs and the mapping subsets are calculated prior to performing the path integration. The approach can be summarized by using the pseudocode in Algorithm 1. A visual example of the space discretization and a TPDF is given in Fig. 3.1.

Algorithm 1: Pseudocode for the methodology

Initialization

i: Define initial condition $p(\boldsymbol{q}, t_0)$

ii: Define the moment ODEs $\dot{\boldsymbol{m}}$

iii: Define the Gauss Legendre integration points X_N

iv: Define dT, a subdivision of the excitation period T such that $dT = T/h$ and $h \in \mathbb{N}$

Create the TPDFs and the Mapping Subset

For $j = 1, 2, ..., h$**,** sub-period timesteps

For $k = 1, 2, ..., N$**,** integration points

1: Moments: $M(t_{i+1} = jdT, \boldsymbol{q_0} = X_{Nk}, t_i = (j-1)dT) = \int_{t_i}^{t_{i+1}} \dot{\boldsymbol{m}}\left(\boldsymbol{m}(t)\right) dt$

2: Means: $\boldsymbol{\mu} \in M(t_{i+1}, \boldsymbol{q_0}, t_i)$

3: Mapping Subset: $X_{\mu,k} = \{\boldsymbol{q} \in X_N : ||\boldsymbol{q} - \boldsymbol{\mu}|| \leq R\}$

4: TPDF: $L_{jk}(\boldsymbol{q}) = G\left(\boldsymbol{q}, M(t_{i+1}, \boldsymbol{q_0}, t_i)\right)$

Path Integration

For $iT = 1, 2, ..., n$**,** number of periods

For $j = 1, 2, ..., h$**,** sub-period timesteps

For $k = 1, 2, ..., N$**,** integration points

For $m = 1, 2, ..., |X_{\mu,k}|$**,** mapping subset points

1: $t_i = iT * T + (j-1) * dT$

2: $t_{i+1} = t_i + dT$

3: $p(\boldsymbol{q}_m, t_{i+1}) = p(\boldsymbol{q}_m, t_{i+1}) + \frac{\delta_k c_k}{2} p(\boldsymbol{q}_m, t_i) L_{jk}(\boldsymbol{q_m})$

3.1.2 Transient Probability in Basins

The probability of creation or destruction of stable modes is calculated by integrating the PDFs in each basin of attraction (BA). In this section it is assumed the system described by (2.4) is forced by excitations with period T and has attracting periodic solutions indexed by k located at $\boldsymbol{q}(t) = \boldsymbol{A}_k(t)$. Each $\boldsymbol{A}_k(t)$ has domain of attraction D_k and smooth boundaries of the domains ∂D_k. The basins of attraction are

defined for attractor $\boldsymbol{A}_k(t)$ as:

$$D_k(t) \equiv \{\boldsymbol{q}(t) \in \mathbb{R}^d : \lim_{m\to\infty} \boldsymbol{q}(t+Tm) = \boldsymbol{A_k}(t)\} \tag{3.20}$$

To approximate the basins of attraction a set of cells is defined in a grid in phase space and each cell is allocated to the domain of an attractor as described by the following procedure. Each of the J cells has the geometry of a d dimensional box which consists of a small subset of phase space, $C^{(j)} \subset \mathbb{R}^d$, and has a set of S vertices. The vertices and the cell surface overlap on an infinitesimally thin space with the neighboring cells. Each vertex, $\boldsymbol{q}_v^{(s)}$, is assigned a basin number corresponding to its attractor:

$$b^{(s,t_o)} \equiv b(\boldsymbol{q}_v^{(s)}, t_o) \equiv k \quad \text{s.t.} \quad \lim_{m\to\infty} \boldsymbol{q}_v^{(s)}(t_o+Tm) = \boldsymbol{A}_k(t) \tag{3.21}$$

Each cell with index j is assigned a basin number corresponding to the mode of the basin number of the vertices:

$$B^{(j,t_o)} \equiv B(C^{(j)}, t_o) \equiv \text{mode}(\{b^{(1,t_o)}, b^{(2,t_o)}, ...b^{(S,t_o)}\}) \tag{3.22}$$

Each approximated basin $\tilde{D}_k^{(i)}$ is defined as the set of points inside all J cells with the same basin number:

$$\tilde{D}_k^{(t_o)} \equiv \{\boldsymbol{q} \in C^{(1)} : B^{(1,t_o)} = k\} \cup ... \cup \{\boldsymbol{q} \in C^{(J)} : B^{(J,t_o)} = k\} \tag{3.23}$$

The basin boundary can be approximated as the intersection of basin k with other basins:

$$\partial \tilde{D}_k^{(t_o)} \equiv \{\boldsymbol{q} \in \mathbb{R}^d : \tilde{D}_k^{(t_o)} \cap \tilde{D}_m^{(t_o)}, \forall m \neq k\} \tag{3.24}$$

For time periodic systems, the basin sets $\tilde{D}_k^{(t_o)}$ need to be calculated for each t_o. For this study, it suffices to limit the integration in the BAs of the PDF to once a period, and only one initial phase of the time periodic BAs is used.

The probability in each BA is integrated by discretizing space. Each cell is defined as a sub-interval with Gauss-Legendre integration points inside each sub interval. The PDF is interpolated to the Gauss-Legendre integration points, and then integration is carried out via the following weighted summation:

$$\tilde{p}_k(t^{(i)}) = \sum_{j=1}^{J_k} \frac{\delta_k}{2} \sum_{l=1}^{L_j} c_{jl}\, \tilde{p}(\boldsymbol{q}_{jl}^{(i)}, t^{(i)}) \tag{3.25}$$

Here, $\tilde{p}_k(t^{(i)})$ is the probability of a solution in basin k, $\tilde{p}(\boldsymbol{q}_{jl}^{(i)}, t^{(i)})$ is the interpolated probability to the new Gauss-Legendre points, J_k is the number of cells of each basin number, and $\tilde{L}_j$ is the number of Gauss-Legendre integration points in each cell.

3.2 Forced Duffing Oscillator: Results

The harmonically excited Duffing oscillator

$$\ddot{x} + \delta\dot{x} + \alpha x + \beta x^3 = Fcos(\omega t) + \sigma\dot{W}(t) \tag{3.26}$$

can be expressed as the stochastic differential equation:

$$\begin{pmatrix} dx_1 \\ dx_2 \end{pmatrix} = \begin{pmatrix} x_2 \\ -\beta\, {x_1}^3 - \alpha\, x_1 - \delta\, x_2 + F\, \cos(\omega\, t) \end{pmatrix} dt + \begin{pmatrix} 0 \\ \sigma \end{pmatrix} dW(t) \tag{3.27}$$

when also excited by noise. This system has the following moment ODEs:

$$\begin{pmatrix} \dot{m}_{10} \\ \dot{m}_{01} \\ \\ \dot{m}_{20} \\ \dot{m}_{11} \\ \\ \dot{m}_{02} \\ \\ \end{pmatrix} = \begin{pmatrix} m_{01} \\ F cos(\omega t) - \alpha\, m_{10} - \delta\, m_{01} \\ +2\, \beta\, {m_{10}}^3 - 3\, \beta\, m_{10}\, m_{20} \\ 2\, m_{11} \\ 2\, \beta\, {m_{10}}^4 + F cos(\omega t)\, m_{10} \\ -3\, \beta\, {m_{20}}^2 - \alpha\, m_{20} + m_{02} - \delta\, m_{11} \\ 4\, \beta\, m_{01}\, {m_{10}}^3 + \sigma^2 + 2\, F cos(\omega t)\, m_{01} \\ -2\, \alpha\, m_{11} - 2\, \delta\, m_{02} \; - 6\, \beta\, m_{11}\, m_{20} \end{pmatrix} \tag{3.28}$$

These moment equations can be used as described in Algorithm 1 to create the TPDF. An example of a resulting TPDF is shown in Fig. 3.1

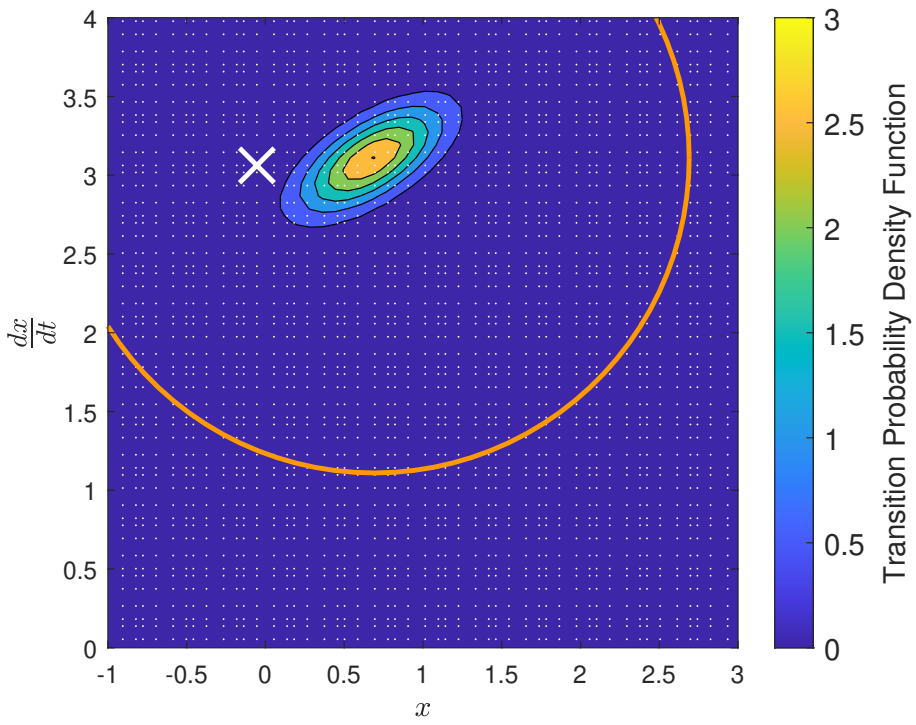


Figure 3.1: Example of the transition probability density function for the forced Duffing oscillator. The white dots are the Gauss Legendre integration points in phase space. The white X marks the initial point $\boldsymbol{q}_o$ at time t_i. The contour plot shows the probability density function. The system has the highest probability of moving to region in yellow from the white X between time t_i and t_{i+1}. The orange-yellow circle surrounds the mapping subset around the mean for this $\boldsymbol{q}_o$ with a radius of 2. Note that the most important part of the TPDF is inside this circle. The entire space considered is $-4 \leq x \leq 4$ and $-4 \leq \frac{dx}{dt} \leq 4$.

The parameters $\alpha = 1$, $\beta = 0.3$, $\delta = 0.1$, and $F = 0.4$ have been selected for this system to exhibit a multistable response on a hardening oscillator. The frequency response diagram is shown in Fig. 3.2. This is obtained for the deterministic system by using AUTO2007 [51] continuation.

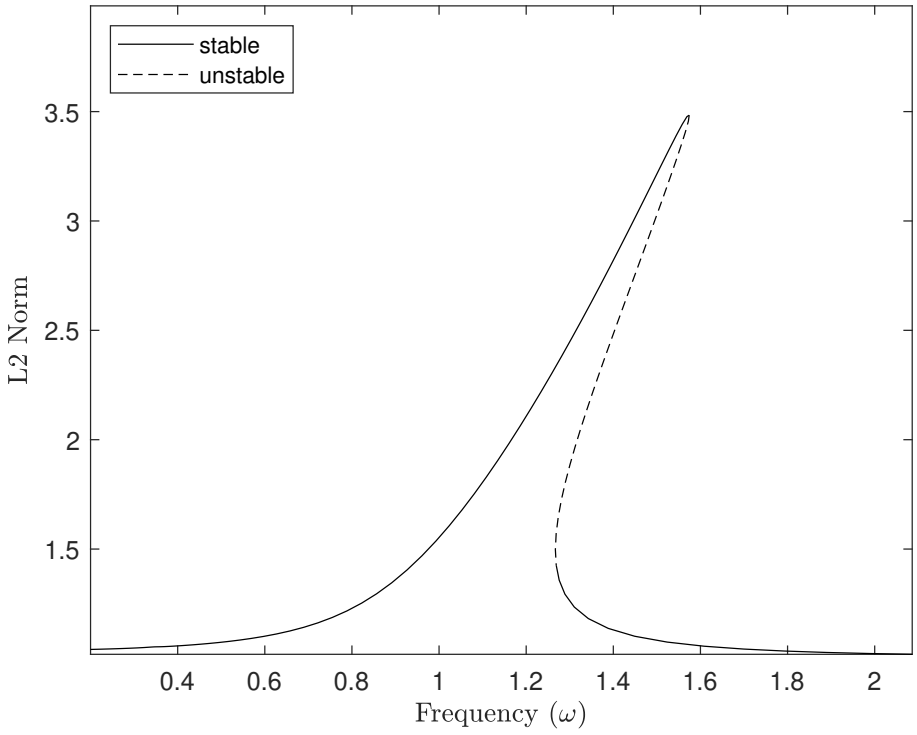


Figure 3.2: Frequency response diagram for the deterministic harmonically forced Duffing oscillator. The presence of a hysteresis region with two stable branches (depicted with solid lines) and one unstable branch (depicted with dashed lines) is noted. This response diagram has been generated by using AUTO2007 [51].

As shown in Fig. 3.2, there is a region of multistability or hysteresis in the frequency range $1.27 \leq \omega \leq 1.57$. In this region, there are two branches of stable periodic solutions and one unstable branch of periodic solutions. The excitation frequency $\omega = 1.4$ is selected to explore the system in the parameter space with two BAs, with each of them corresponding to one of the stable periodic solutions. The initial probability density function is chosen to be nearly singular near the deterministic high amplitude steady state solution $\boldsymbol{x}_H$:

$$p(\boldsymbol{x}, t^{(0)}) = \hat{\delta}(\boldsymbol{x} - \boldsymbol{x}_H) \tag{3.29}$$

Here, $\hat{\delta}(.)$ is the Dirac delta function such that the initial probability density function is 1 at $\boldsymbol{x}_H$ and 0 at all other points in phase space. Note that in practice the initial probability density function is close to being singular but not singular, as limited by the resolution of the simulation.

The PDFs of the single Duffing oscillator with an initial condition at the high amplitude attractor are shown in Fig. 3.3 for noise intensities of $\sigma = 0.1$ units and $\sigma = 0.2$. These PDFs are the distribution of the states after 1500 periods. It is remarked that the states for $\sigma = 0.1$ with high probability stay near the high amplitude attractor while the states for $\sigma = 0.2$ with higher probability escape towards the low amplitude attractor.

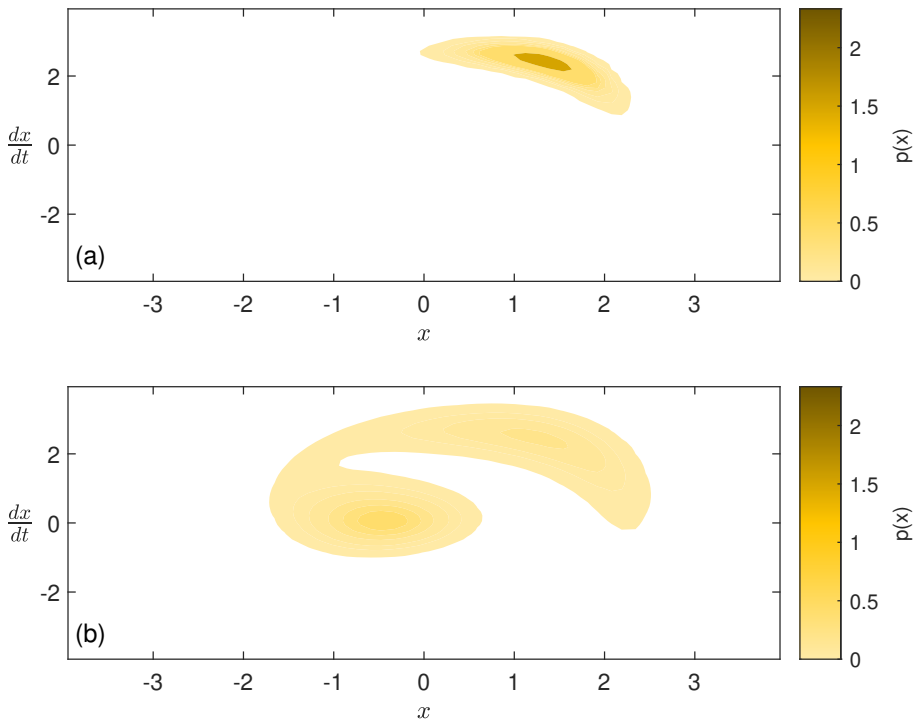


Figure 3.3: Contour of the probability density function after 1500 periods of the harmonically forced Duffing oscillator with additive noise intensity: (a) $\sigma = 0.1$ and (b) $\sigma = 0.2$. The probability density function in this figure has been normalized so that the integral over the domain (total probability) is equal to 1. In color are PDF level sets denser than 0.01 to highlight the regions of phase space with dense probability. The initial probability density corresponds to a deterministic point on the high amplitude attractor. It is noted that in (a), the probability is dense only near the high amplitude attractor, and in (b), the probability is dense near both attractors.

The basins of attraction for the stable solutions of the deterministic forced Duffing oscillator are shown in Fig. 3.4.

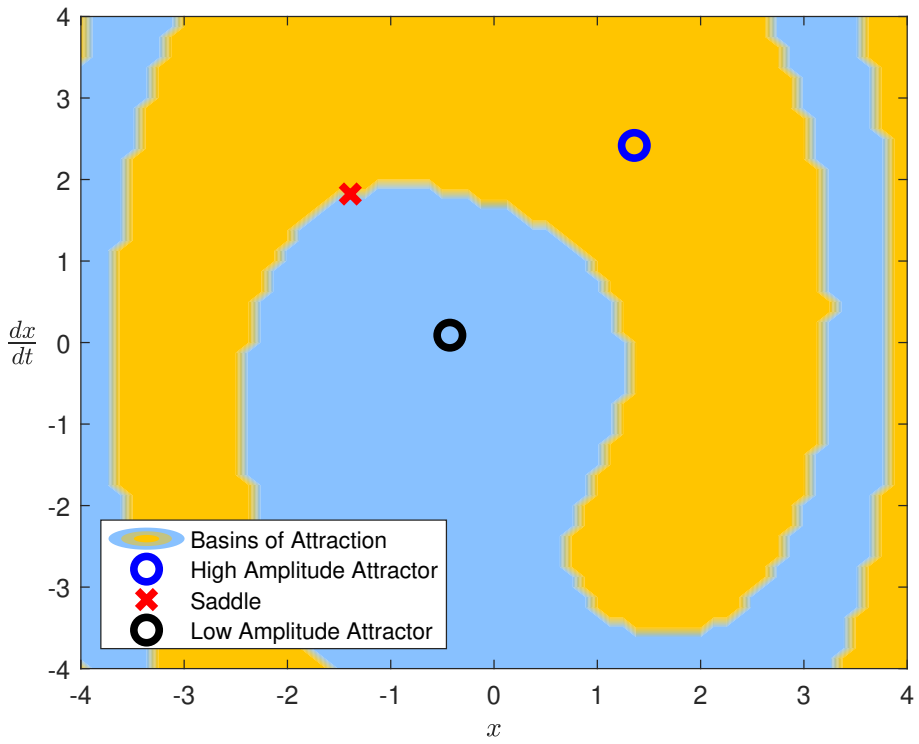


Figure 3.4: Basins of attraction of the harmonically excited deterministic Duffing oscillator.

The transient probability of solutions in each basin are generated by integrating the PDFs over the domains of the basins of attraction at all time steps as described in Section 3.1.2. The transient probability over time for the noise intensity of $\sigma = 0.2$ is shown in Fig. 3.5.

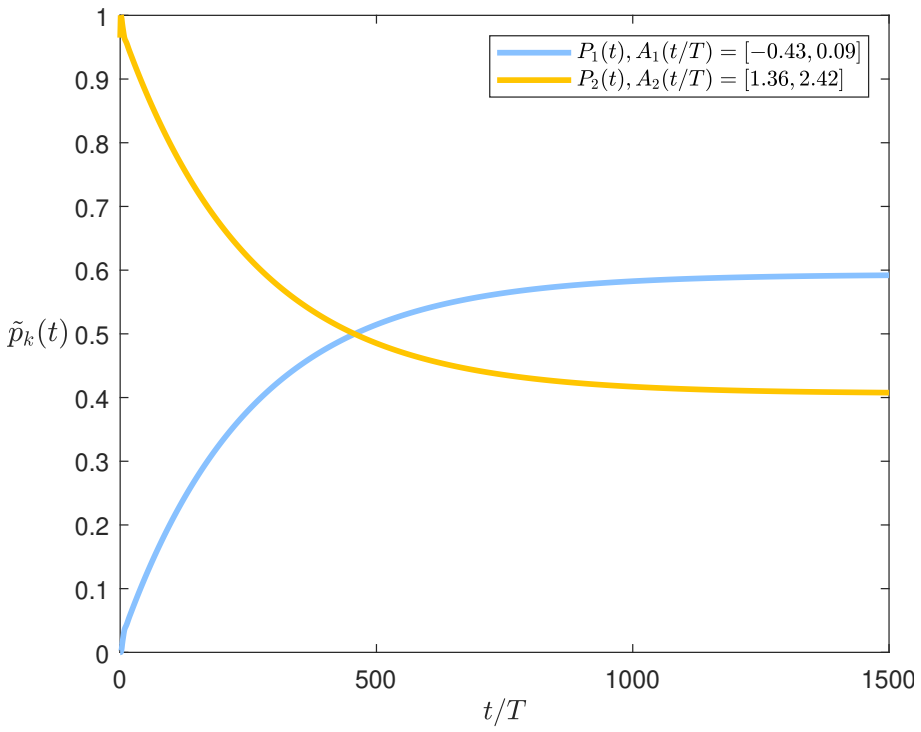


Figure 3.5: Probability in each basin of attraction at each period for $\sigma = 0.2$. P_1 corresponds to basin of the low amplitude attractor (A_1) and P_2 corresponds to the high amplitude attractor (A_2). These probabilities are calculated by integrating the PDF in Fig. 3.3 (b) over the basins of attraction of the deterministic system.

This analysis quantifies the probability of destruction of the high amplitude solution with a short duration additive noise. That is, when the noise is removed, the solution moves deterministically towards the attractor of the basin in which it resides with this quantified probability. This is applicable for those interested in preventing the jump between basins that can cause a change in the stable mode, and also useful for those interested in understanding how effective noise can be used as a control strategy through examination of the probability of noise having an effect in a short duration control effort.

The transient probability in the high amplitude basin is shown in Fig. 3.6 as a

function of noise intensity. Note that the probability in the high amplitude basin drops faster for higher noise intensities. From Fig. 3.5 and Fig. 3.6, it can be inferred that for the high noise intensity case, by 1500 periods, the probability density function represents the stationary probability density function since there is a near zero slope indicating no change in the probability. However, this cannot be similarly inferred for the lower noise intensity of 0.1, at which the curve is still dropping in probability at the end of the simulation.

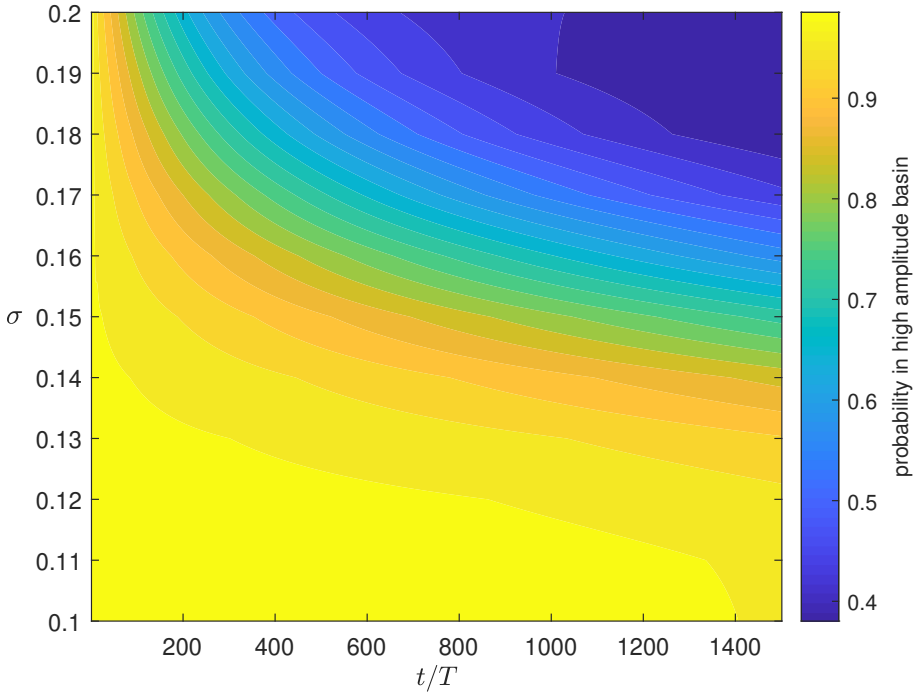


Figure 3.6: Probability in the high amplitude basin of attraction at each period for different noise intensity.

As shown in Fig. 3.6, even when the noise intensity is lower, the probability that solutions will transition from the high amplitude basin to the low amplitude basin is non-zero, and eventually after long enough time, a drop in probability in the high amplitude

basin is noticeable. It makes sense that since this system is excited by unbounded white noise, there is a non-zero probability of large enough random values for which a solution in the high amplitude basin will be pushed into the low amplitude basin. In the current model, these low probabilities show up in the tails of the Gaussian transition probability density function. As a result, by defining a probability parameter ρ, and a time parameter τ, where $0 < \rho < 1$ and $0 < \tau < \infty$, one can define sets of constrained spaces in which a solution may exist with some probability and observe how these sets vary with noise intensity. For uniqueness, these sets are also defined as the sets with the highest probability density that meets all other conditions; that is, the smallest set with at least ρ probability.

The parameter values $\rho = 95\%$ and $\tau = 1000T$ are chosen; these values constrain a set of x_ρ points where a solution may exist with probability greater than or equal to 95% within the first 1000 periods. Fig. 3.7 illustrates how these sets vary with σ.

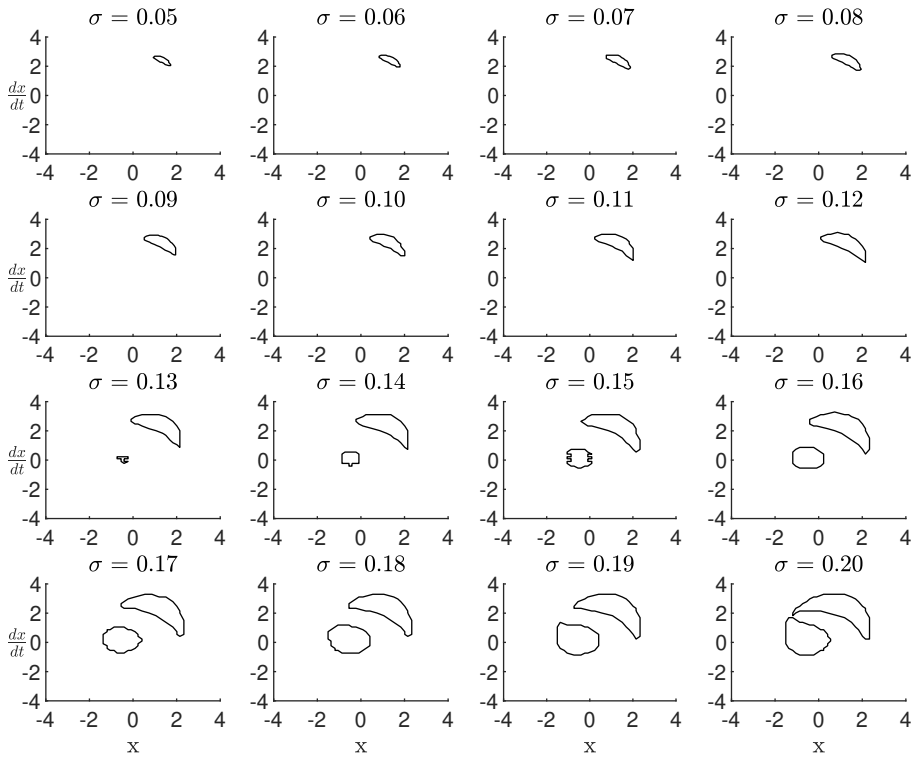


Figure 3.7: Maximum density sets that with probability greater or equal to 95% contain solutions of the noise influenced forced Duffing oscillator in the first 1000 periods of noise influence with an initial deterministic initial condition at the high amplitude attractor.

For a noise intensity $\sigma \leq 0.12$, the sets are constrained inside the high amplitude deterministic basin of attraction, and for a noise intensity, $\sigma \geq 0.13$, the sets exists in both basins. The qualitative change in shape of the PDF indicates that a type of stochastic bifurcation occurs in between the two noise intensities. Existing definitions for stochastic bifurcations are reserved for the stationary probability density function, and not, as is the case here, parameterized by a probability constant ($\rho = 95\%$) and a time constant ($\tau = 1000$). Nevertheless, in the spirit of bifurcation analysis for this transient case, the L_2 norm of the sets plotted with the noise intensity are depicts in Fig. 3.8.

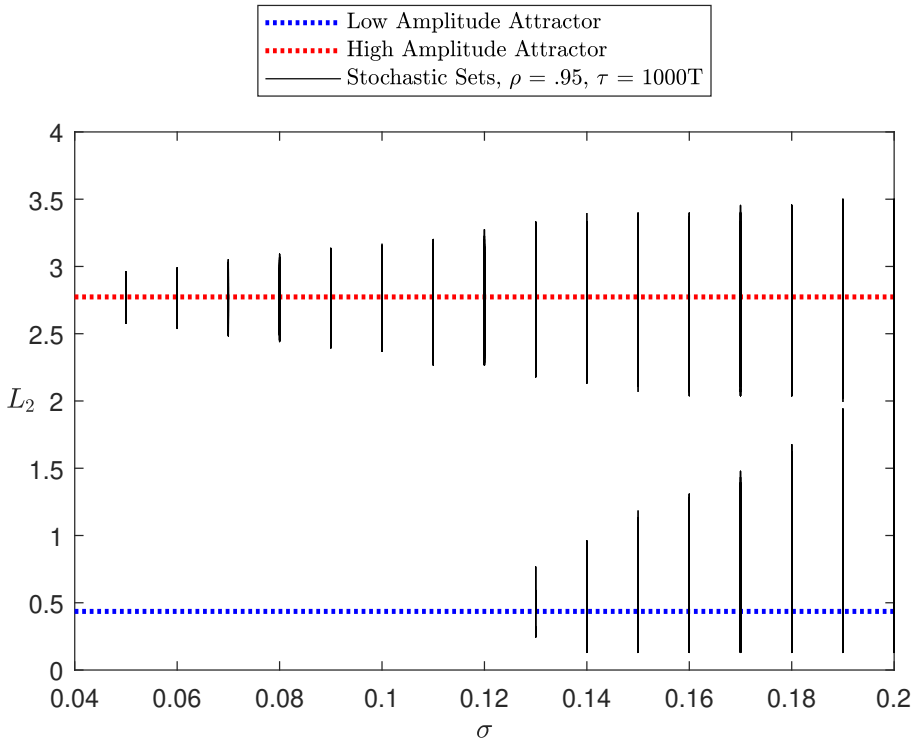


Figure 3.8: L_2 Norm of maximum density sets of phase space, which with probability greater or equal to 95% contain solutions of the noise influenced forced Duffing oscillator in the first 1000 periods of noise influence. The initial deterministic initial condition is on the high amplitude attractor.

The simulations here agree qualitatively with the results from Euler-Maruyama simulations [69] in both the probability density shapes and the probability a solution will be in each basin. Monte Carlo simulations results are shown in Fig. 3.9. Note that it is a different process to generate a representation of the PDF with the Euler-Maruyama scheme, and that errors in this generation include the size of the boxes used to generate a probability density from individual Euler-Maruyama simulations and the number of simulations. Note the probability curves are qualitatively alike to the results shown in Fig. 3.5 in the decay rate of the probability and the steady state response.

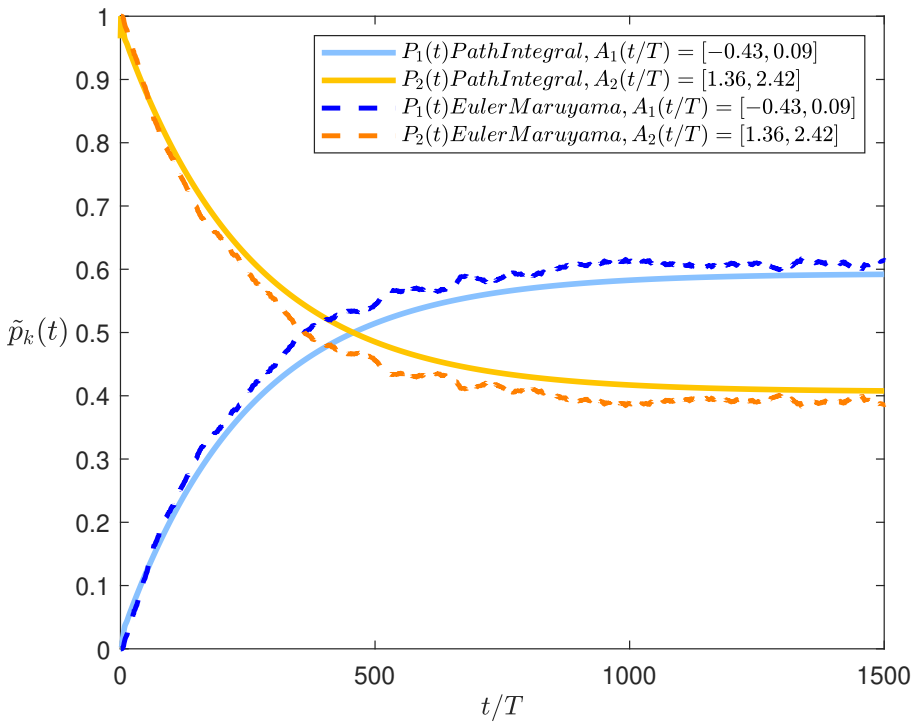


Figure 3.9: Transient probability in each basin generated by using Euler-Maruyama simulations compared with the results of the PIM method.

The effect of the reduced radius method is validated via convergence analysis in Fig. 3.10. Note that both the method suggested by Yu *et al.* [6], and the mean centered radius method described in Section 3.1.1 converge as the radius is increased and the number of Gauss Legendre integration points is increased. Furthermore, it can be seen in Fig. 3.10 that the new radius method centered at the means converges at lower radius values and can therefore be used to lower computational costs.

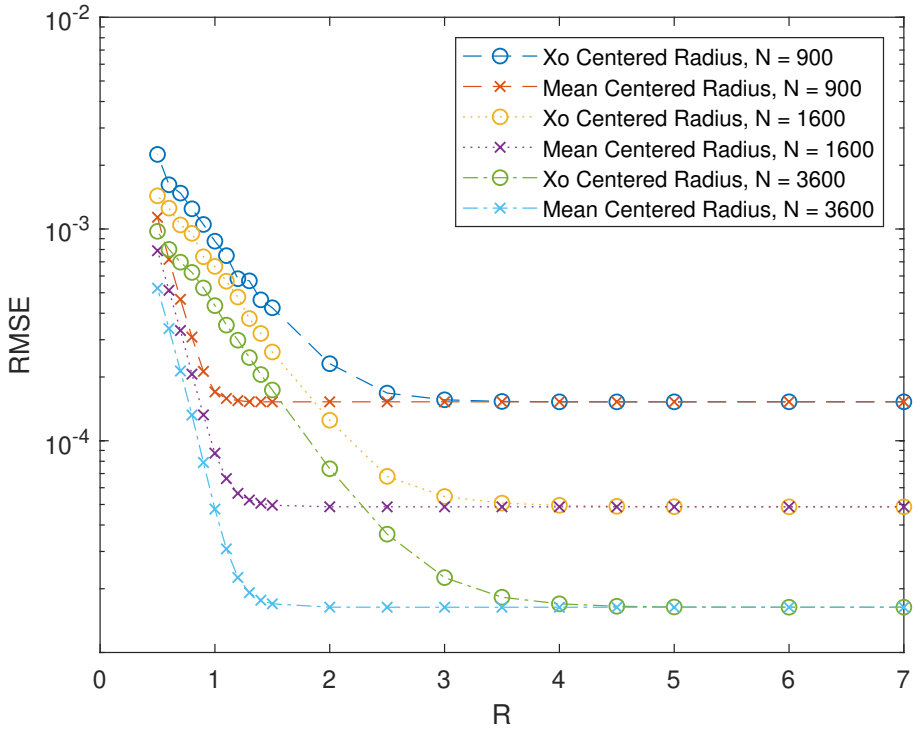


Figure 3.10: Root mean squared error (RMSE) of the PDF of forced Duffing oscillator for different grid resolutions defined by number of points N and different mapping resolutions specified by $N * N_\mu$ and $N * N_o$. There are N_μ points R distance from the forward mapped means and N_o points R distance from the initial point $\boldsymbol{x}_o$. Reference resolution is N = 6400 and R = 7.

For this system and a fixed constant PIM timestep, the maximum standard deviation from all TPDFs is 1.024. From a visual inspection of Fig. 3.10, for $R > 3$ both reduced radius approaches have converged. For the mean centered radius approach, from a visual inspection for $R > 1.5$ the method has converged. As an example, at $R \approx 3$, there is truncation of the TPDFs at three maximum standard deviations from the mean.

The probabilities could be calculated for infinite radius if contributions of the TPDF far from the mean (deterministic dynamics) are desired. However, for sufficiently large R,

these contributions are negligible in the sense that errors from grid resolution are orders of magnitude larger than errors from integrating over a reduced space. This can be observed in Fig. 3.10, where changing the grid resolution (number of integration points) has a large influence on the root mean squared error (RMSE) while extending R beyond $R > 3$ has negligible influence on the RMSE error.

3.3 Two Coupled Duffing Oscillators: Results

In this section, a system of two coupled Duffing oscillators forced by a common harmonic excitation and additive noise is considered:

$$\begin{aligned} \ddot{x_1} + \delta\dot{x_1} + \alpha x_1 + \beta x_1^3 + \kappa(x_1 - x_2) &= F cos(\omega t) + \sigma\dot{W}(t) \\ \ddot{x_2} + \delta\dot{x_2} + \alpha x_2 + \beta x_2^3 + \kappa(x_2 - x_1) &= F cos(\omega t) + \sigma\dot{W}(t) \end{aligned} \tag{3.30}$$

The corresponding state space SDE is:

$$\begin{pmatrix} dx_1 \\ dx_2 \\ dx_3 \\ dx_4 \end{pmatrix} = \begin{pmatrix} x_2 \\ -\beta\, {x_1}^3 - \alpha\, x_1 - \delta\, x_2 - \kappa(x_1 - x_3) + F\, \cos(\omega\, t) \\ x_4 \\ -\beta\, {x_3}^3 - \alpha\, x_3 - \delta\, x_4 - \kappa(x_3 - x_1) + F\, \cos(\omega\, t) \end{pmatrix} dt + \begin{pmatrix} 0 \\ \sigma \\ 0 \\ \sigma \end{pmatrix} dW \tag{3.31}$$

By using the same parameters as in Section 3.2, and a coupling parameter $\kappa = 0.1$, the system is found to have the FED shown in Fig. 3.11.

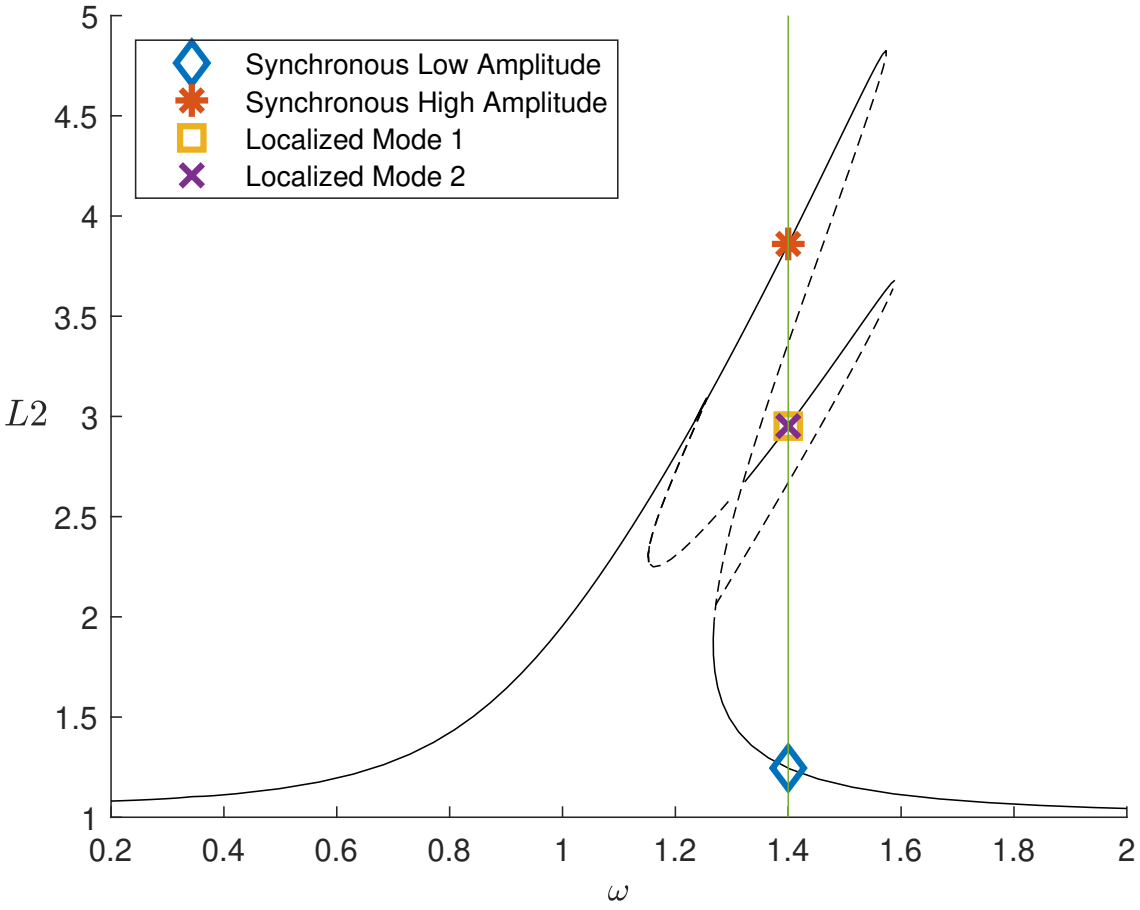


Figure 3.11: Frequency Energy Diagram for system (3.30) of two coupled forced Duffing oscillators. It is noted that at $\omega = 1.4$. one has a stable synchronous high amplitude mode, a stable synchronous low amplitude mode, and two overlapping stable localized modes. The results are generated by using AUTO2007 [51]. Solid lines are used for stable solutions and dashed lines are used for unstable solutions.

At the frequency $\omega = 1.4$, there are seven branch points, two of which are not visible because they overlap with others in this reduced dimensional figure. The highest point at $\omega = 1.4$ corresponds to the stable synchronous motion of both oscillators with high amplitudes. The lowest L_2 norm corresponds to the stable synchronous motion of both oscillators in which both are at a low amplitude. In between, two overlapping points

indicate stable modes at which one oscillator oscillates at a high amplitude while the other oscillates at a low amplitude; this is a localized mode or an energy localization. Localized mode 1 is the stable mode where oscillator 1 oscillates at a high amplitude while oscillator 2 oscillates at a low amplitude. Likewise, localized mode 2 is the symmetric mode. All other branch points at $\omega = 1.4$, are unstable solutions of saddle type.

The objective of this section is to quantify how noise affects the localized modes. The probability density function over four snapshots of time is shown in Fig. 3.12. The initial condition for Fig. 3.12 is a nearly singular PDF at the localized mode 1 position in phase space. The four dimensional space is projected into the L_2 norm axes and the L_2 norm of the attracting solutions of the deterministic system are highlighted for reference. It is noted that initially, with probability 1, the PDF is at one of the localized attractors. As time goes forward, the support of the probability density function expands. Eventually, the probability value begins to increase at the high amplitude and low amplitude attractor energy levels, and decrease in the localized mode. After enough time, the probability that solutions will remain near the localized mode has decreased significantly. Effectively, if sustained for sufficient duration, the white noise intensity of $\sigma = 0.2$ has a high probability of destroying the localization. This effect can be quantified specifically by integrating the PDF over the basins of attractions of the coupled system.

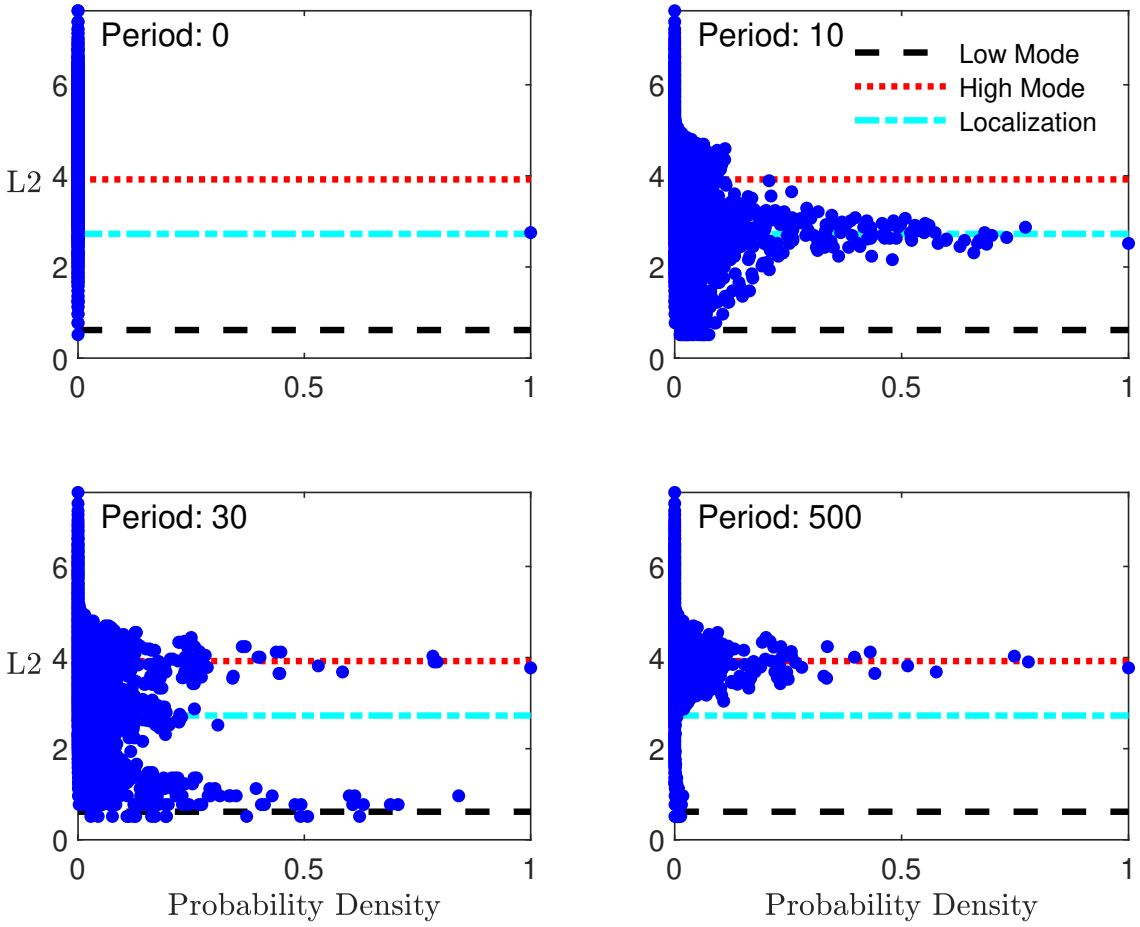


Figure 3.12: Probability density at each integration point normalized to a maximum density of 1 projected into the L_2 norm, for $\kappa = 0.1$ and $\sigma = 0.2$.

In Fig. 3.13, the probability varies in each basin with time until it approaches the stationary probability.

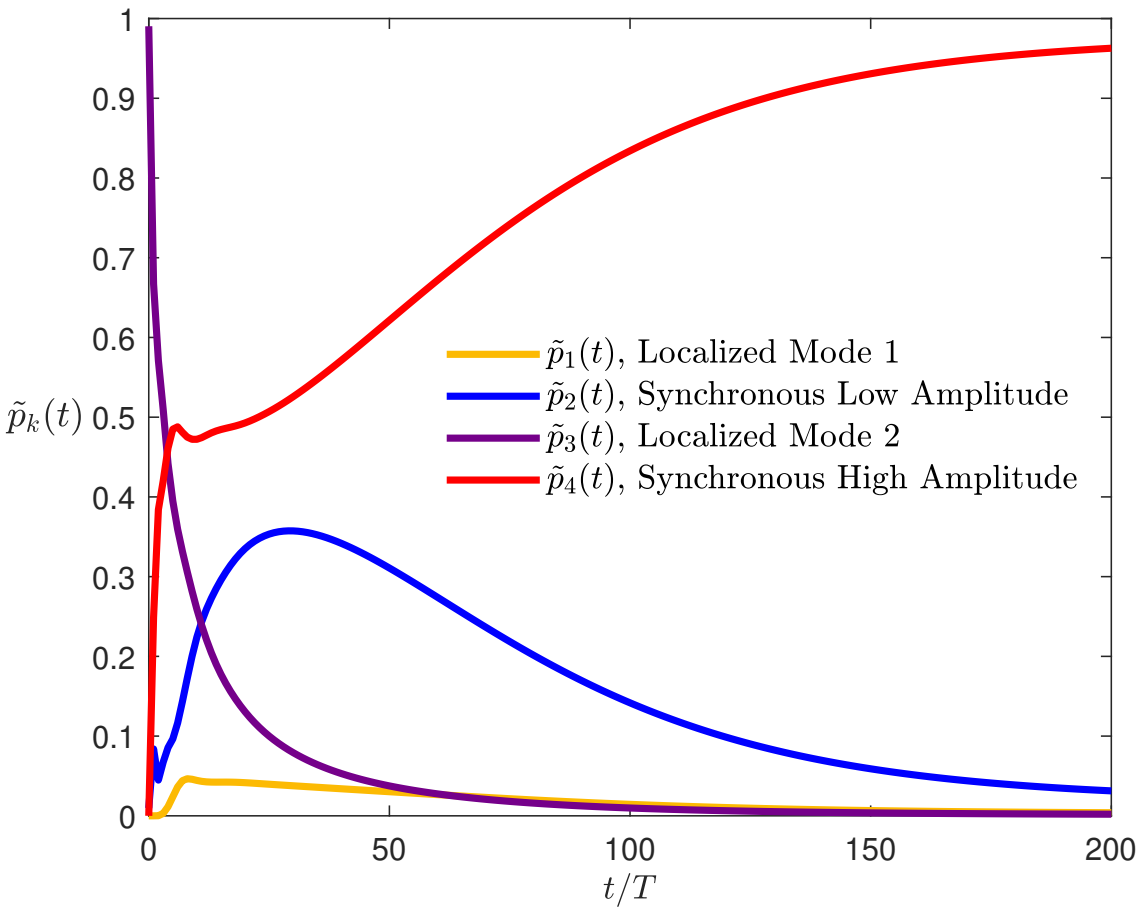


Figure 3.13: Probability in each basin of attraction at each period. Each $\tilde{p}_k$ corresponds to a basin of an attracting mode. $\kappa = 0.1$ and $\sigma = 0.2$.

It is remarked that initially the probability increases in the low amplitude BA, meaning some solutions transition from the localized mode to the synchronous low amplitude mode's basin. This generates a competing rate of increase in the probability density between the low amplitude basin and the high amplitude basin. Eventually the probability density is predominately in the high amplitude basin. This density is found to approach the stationary solution not shown in this figure and indeed the same for alternative initial conditions. Notably, this is a system with relatively large coupling, so

the basins of the localized modes are small, and the probability of generating or keeping these modes in the presence of noise is low. Keeping the noise intensity constant, a representative case is shown for a smaller coupling constant, $\kappa = 0.01$, in Fig. 3.14 and Fig. 3.15.

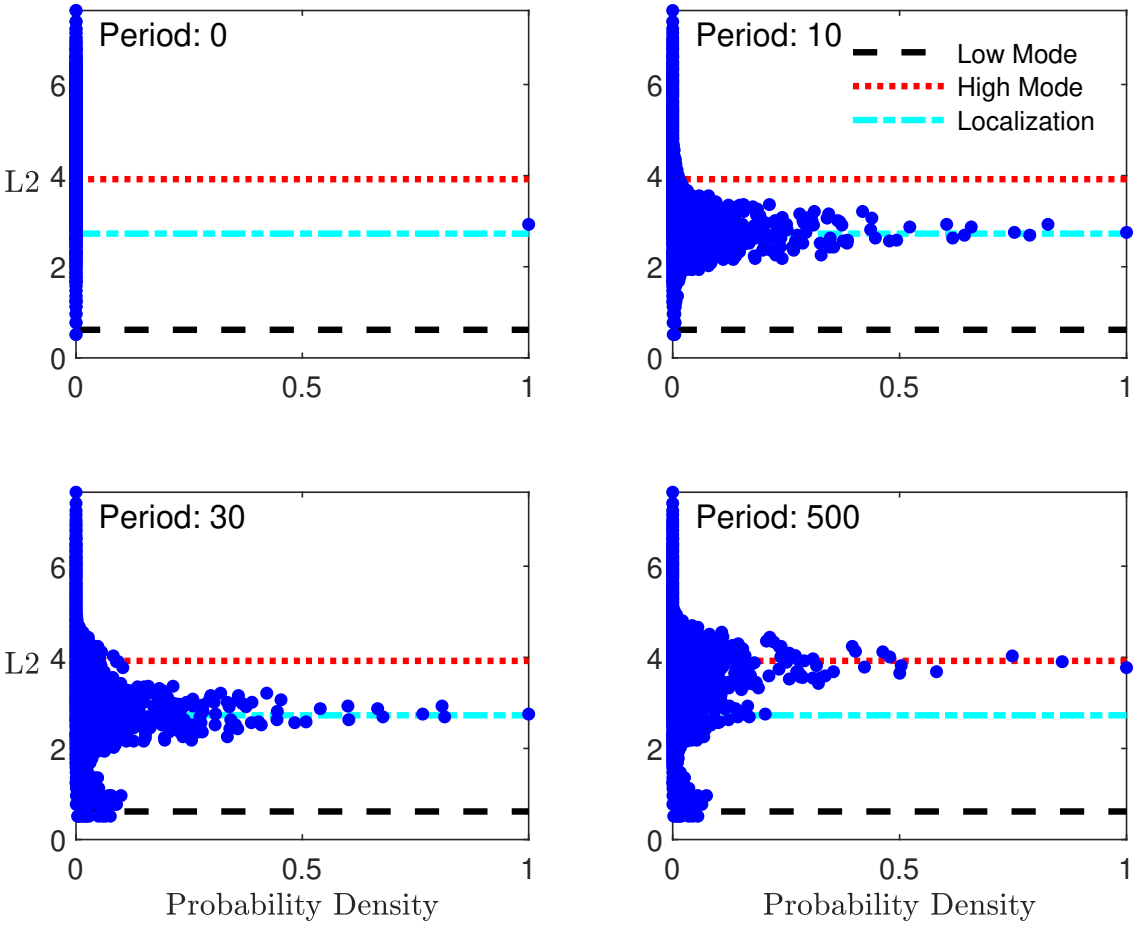


Figure 3.14: Probability density at each integration point normalized to a maximum density of 1 projected into the L_2 Norm, for $\kappa = 0.01$ and $\sigma = 0.2$.

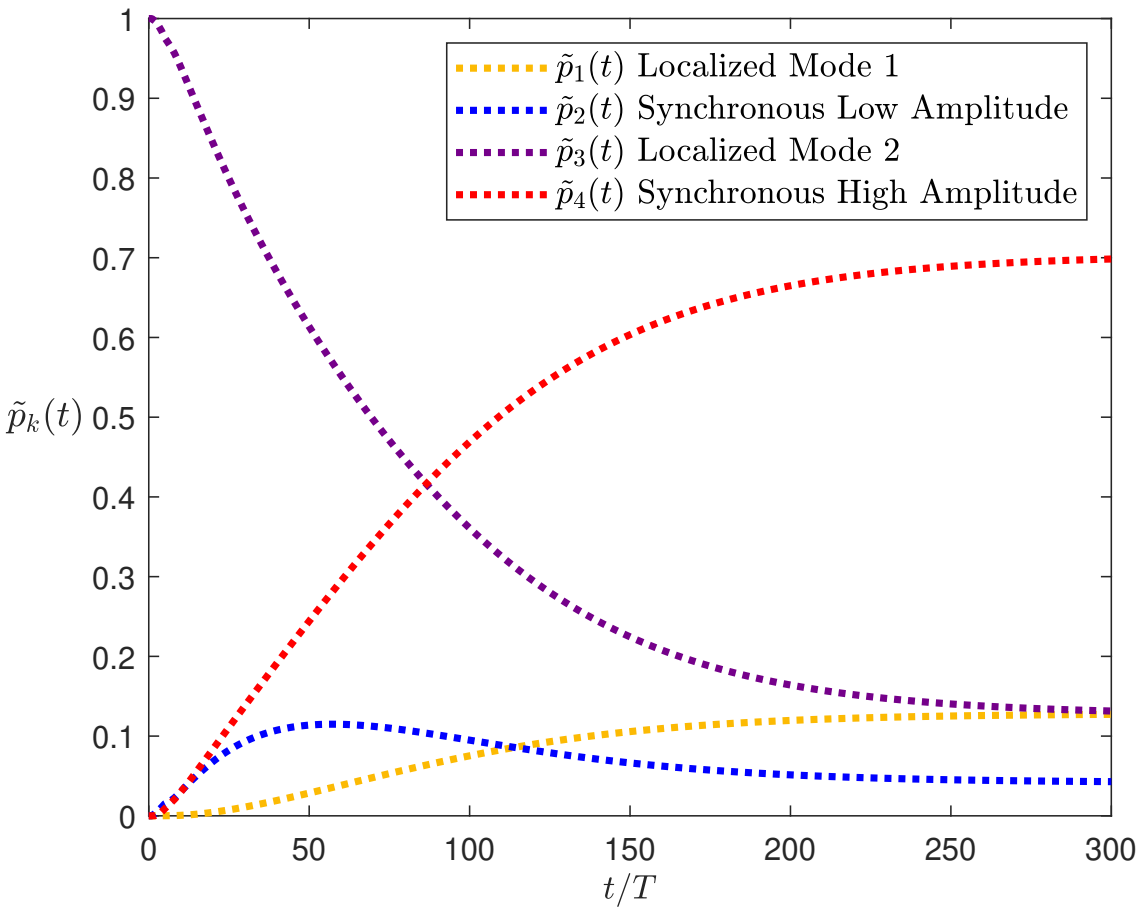


Figure 3.15: Probability in each basin of attraction at each period. Each $\tilde{p}_k$ corresponds to a basin of an attracting mode. The parameter values are $\kappa = 0.01$ and $\sigma = 0.2$.

The probability in the initial localized mode for varying coupling coefficients is shown in Fig. 3.16. One can discern from Fig. 3.16 that for the lower coupling constant, at the same noise intensity, the probability of remaining in the localized mode is higher. This result is the expected result since oscillator arrays with high coupling are less likely to form localizations because of higher energy transfer from the localized oscillator to neighboring oscillators.

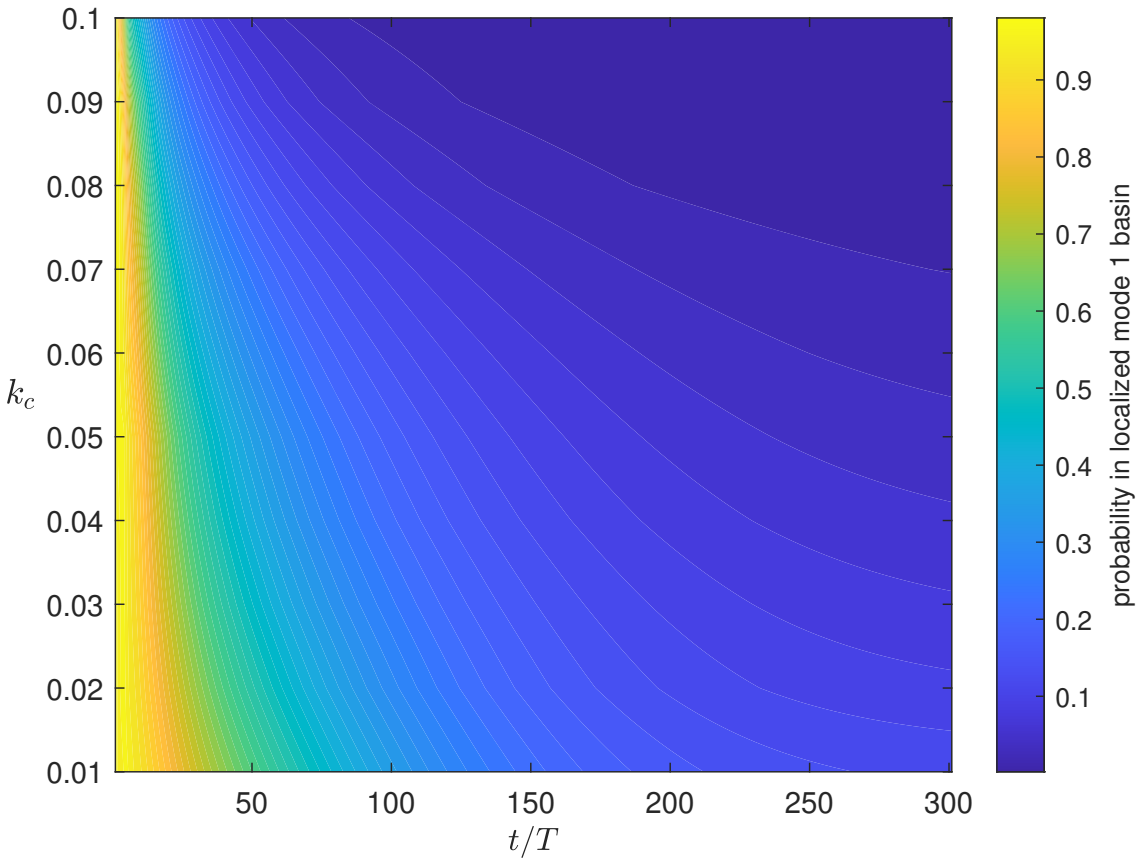


Figure 3.16: Probability in the initial localized mode's basin of attraction at each period for varying coupling coefficients. $\sigma = 0.2$.

The effect on probability in a parameter space of noise intensities is shown in Fig. 3.17. Similar to the analysis for the single Duffing oscillator, one can observe the probabilities in the initial basin are higher for longer period in the initial basin when the noise intensity is lower.

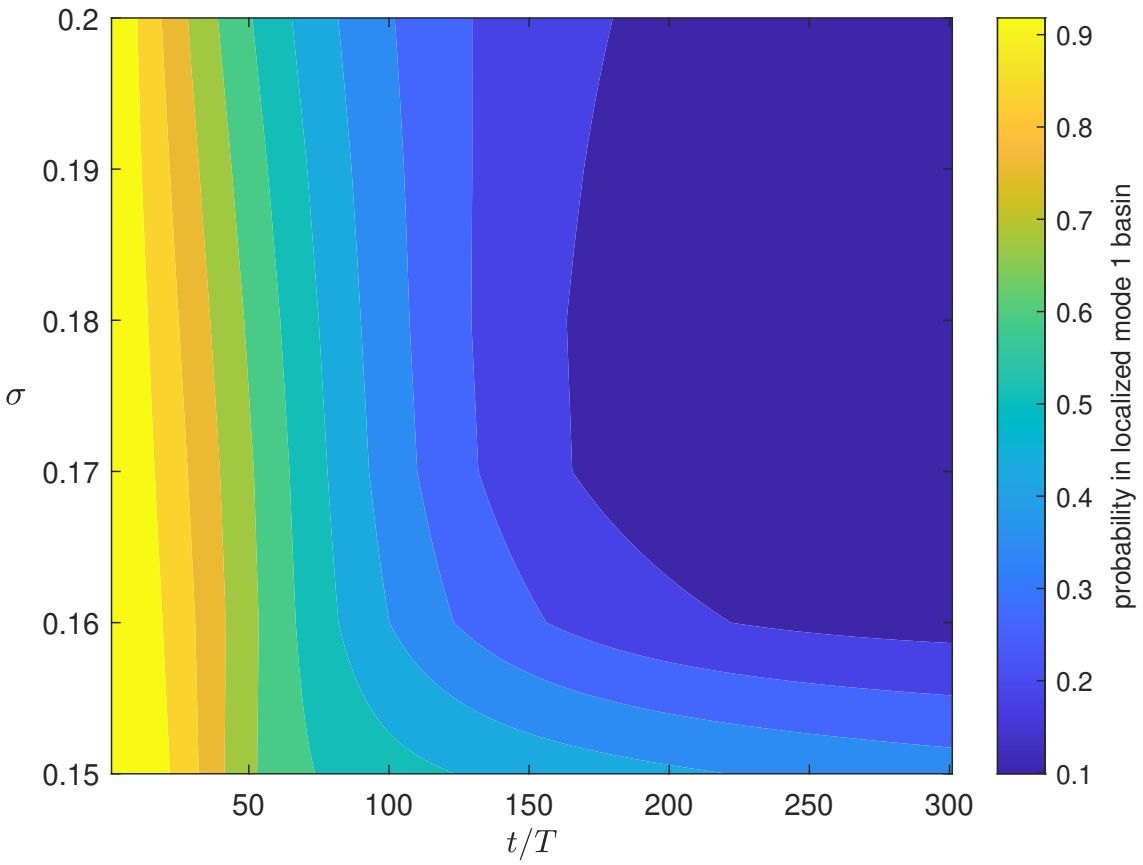


Figure 3.17: Probability in the initial localized mode's basin of attraction at each period for varying noise intensities. $k_c = 0.01$.

3.4 Conclusion

In this chapter, it has been shown how the Path Integral Method and an additional integration over the basins of attraction of the deterministic system can be used to quantify the probability that noise addition with a chosen intensity will result in a response jump for the harmonically forced Duffing oscillator and two coupled Duffing oscillators. The motivation here is to understand with what probability a short duration noise influence will either create or destroy high amplitude oscillations and energy localizations. This

is relevant to energy yield in harvesting systems and mechanical integrity of blade disk systems.

For hardening Duffing oscillator systems, the probability that noise will escape out of the high amplitude mode in the multistability region has been quantified. In the chosen parameter space it has been illustrated how noise intensities $\sigma \leq 0.12$ with 95% probability, fail to escape the high amplitude mode in the first 1000 periods. Likewise, with higher noise intensities, the system escapes the high amplitude mode with some probability greater than 5%in the first 1000 periods, and that associated probability was quantified.

For the arrays of two coupled Duffing oscillators, the probability that noise addition with a chosen intensity will escape a localized mode was quantified. In this analysis, it was shown that for noise intensity $\sigma = 0.2$, with a high probability, the system escapes the localized mode faster in the high coupling strength case than in the low coupling strength case. In addition to generating quantitative values for the probability in each basin, the shift in probability density at different energy levels was visualized, which is useful for understanding the effect of noise on the system.

A novel modification to the Path Integral Method originally presented by Yu *et al.* [6] was presented; this modification facilitates reduction in computational time and memory requirements. Specifically, through convergence analysis, it was demonstrated that the choice of N_μ points near the means of the next iteration map can generate a similar accuracy with a reduced number of computations in contrast to the previous method. This allowed for quantifications of probabilities in the 4D system.

In this study, PIM was found to be much faster than Monte Carlo approaches to

generating the PDF of the systems. However, PIM as formulated by Yu *et al.* [6] is unfortunately affected by the curse of dimensionality, and generating high dimensional grids of phase space for two oscillators becomes extremely taxing on system memory. The modification described in this work to an extent decreases computational cost with negligible loss in accuracy, but like the original method it is also limited by the curse of dimensionality. For low dimensional cases, the proposed faster approach yields adequate approximations. Through, the enhancement of speed, there is the opportunity to perform parameter space analysis as exemplified in this work with the effect of noise intensity and the effect of coupling constant on the probabilities. Furthermore, the analysis over the basins of attraction is applicable to alternative PDF generating methods, which while time-consuming are less limited by the curse of dimensionality. One of these alternatives is Monte Carlo Euler-Maruyama simulations, which has been included as an example in this work.

In future work, one could carry out a parameter space study by identifying optimum values of noise intensity in these systems in regard to the probability of transitions when starting in different attractors.

It is also mentioned that the integration over the basins of attraction as is, requires interpolation of the PDF to new integration points, and requires defining basin number to fixed geometry cells. This method can be enhanced as well, noting that as is, it is a simple approach that yields adequate approximations of the probability in each basin.

Chapter 4: Most Probable Escape paths in Periodically Driven Nonlinear Oscillators

A methodology for finding most probable escape paths and estimating the transition rates in the small noise limit is developed and applied to a collection of arrays of coupled monostable oscillators with cubic nonlinearity, small damping, and harmonic external forcing. The methodology is built upon the action plot method [7] and relies on the large deviation theory, optimal control theory, and the Floquet theory. The action plot method is promoted for use with non-autonomous high dimensional systems; the resulting optimization problem with a discontinuous objective function restricted to a certain manifold is solved using a novel algorithm. The most probable escape paths between stable vibrational modes in arrays of up to five oscillators and the corresponding quasipotential barriers are computed and visualized. The discussion focuses on dependence of the quasipotential barrier on the parameters of the system including the excitation frequency and the coupling coefficient. The original work in this chapter was peer reviewed and published [96] in *Chaos: An Interdisciplinary Journal of Nonlinear Science*.

4.1 Introduction

In this dissertation, the effect of random perturbations (noise) on physics-based models of mechanical systems are studied, as noise can induce transitions into and out of undesired stable modes. As discussed in Chapters 1 and 2, many of these systems can be modeled as coupled Duffing oscillator [46] arrays with external periodic forcing, $\boldsymbol{f}(t)$, and a weak white noise, $\sqrt{\epsilon}\boldsymbol{\eta(t)}$, accounting for random influences, as shown below:

$$\ddot{\boldsymbol{x}} + \delta_c\dot{\boldsymbol{x}} + \alpha\boldsymbol{x} + \beta\boldsymbol{x}^3 + \nu\boldsymbol{D}_N\boldsymbol{x} = \boldsymbol{f}(t) + \sqrt{\epsilon}\boldsymbol{\eta(t)}, \quad \boldsymbol{x} \in \mathbb{R}^N. \tag{4.1}$$

Here, N is the number of oscillators, $\boldsymbol{x}$ is the vector of beam tip displacements from their respective equilibrium positions, δ_c is a damping related coefficient, α and β are scalar constants that render each oscillator monostable, $\boldsymbol{x}^3$ denotes the elementwise cube of the vector, ν is the inter-oscillator coupling coefficient, and $\boldsymbol{D}_N$ is the coupling matrix that takes the following form:

$$\boldsymbol{D}_1 = 0, \quad \boldsymbol{D}_2 = \begin{bmatrix} 1 & -1 \\ -1 & 1 \end{bmatrix}, \tag{4.2}$$

$$\boldsymbol{D}_N = \begin{bmatrix} 2 & -1 & & -1 \\ -1 & 2 & -1 & \\ & \ddots & \ddots & \ddots \\ -1 & & -1 & 2 \end{bmatrix}, \quad N > 2.$$

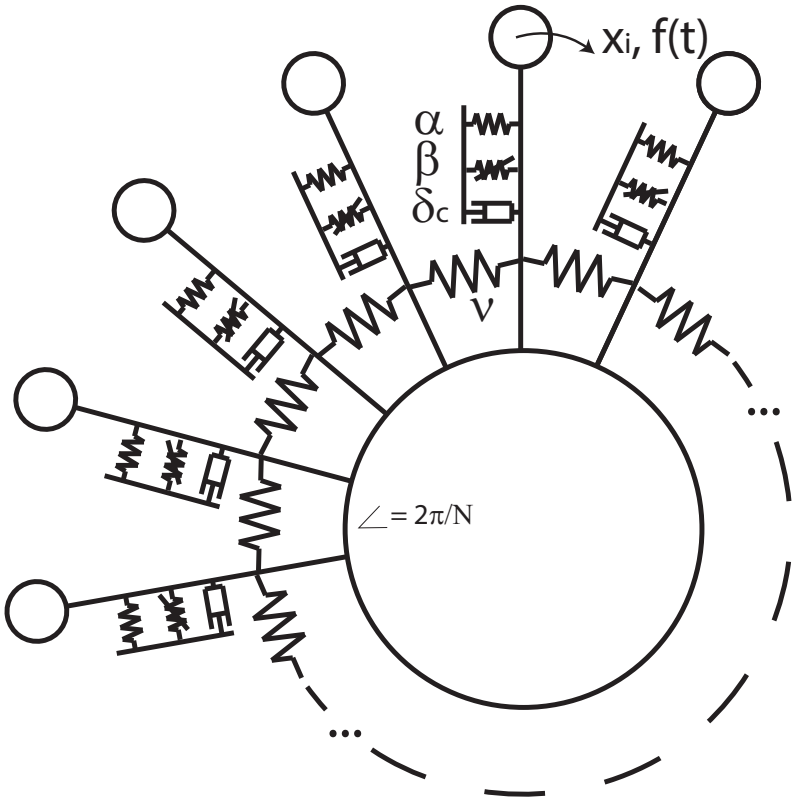


Figure 4.1: Schematic of linearly coupled nonlinear spring– mass-damper systems arranged in a cyclical array.

It is noted that if the number of oscillators is greater than two, they are coupled in a circular array configuration, as depicted in Fig. 4.1.

When $\epsilon = 0$, the corresponding deterministic ordinary differential equations (ODE) system:

$$\ddot{\boldsymbol{x}} + \delta_c \dot{\boldsymbol{x}} + \alpha \boldsymbol{x} + \beta \boldsymbol{x}^3 + \nu \boldsymbol{D}_N \boldsymbol{x} = \boldsymbol{f}(t), \quad \boldsymbol{x} \in \mathbb{R}^N. \tag{4.3}$$

It is known that the ODE system (4.3) may admit multiple attractors [1–3, 25, 27];

that is, stable periodic solutions that attract other solutions from appropriate open subsets of the initial condition space $(\boldsymbol{x}(0), \dot{\boldsymbol{x}}(0))$. The response of the system (4.3) to the forcing $\boldsymbol{f}$ with frequency ω for a circular array of $N = 5$ coupled Duffing oscillators is shown in Fig. 4.2. Each periodic solution $\boldsymbol{q}(t) \equiv (\boldsymbol{x}(t), \dot{\boldsymbol{x}}(t))$ to (4.3) is represented by a L_2-like norm

$$||\boldsymbol{q}(t)||_{L_2} = \sqrt{\int_0^1 \sum_i^{2N} \left(q_i \left(sT\right)\right)^2 ds}, \tag{4.4}$$

where $T = {}^{2\pi}/_{\omega}$ is the period.

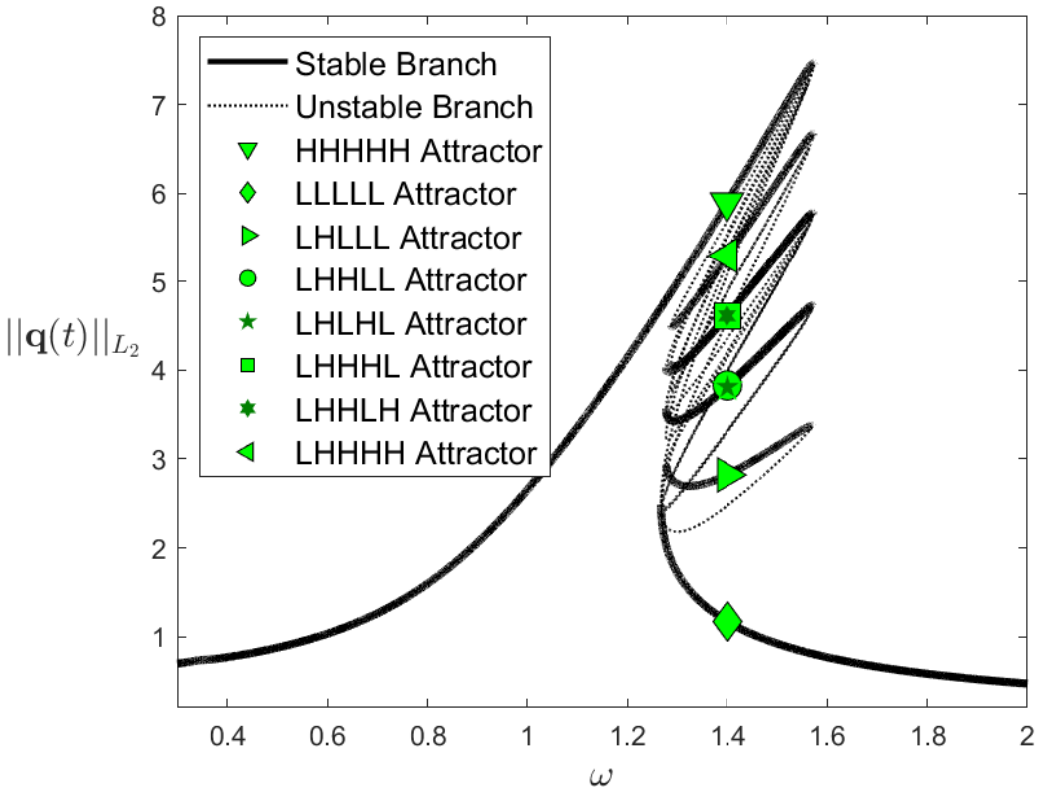


Figure 4.2: Frequency response of a circular array of $N = 5$ coupled forced Duffing oscillators as a function of excitation frequency, ω. At the frequency $\omega = 1.4$, unique attractors of the array are highlighted. This figure is generated by using the continuation package AUTO2007 [51]. The parameters in the ODE system (4.3) are set to $\alpha = 1$, $\beta = 0.3$, $\delta = 0.1$, $\nu = 0.01$, and the periodic excitation is of the form $f(t) = 0.4\cos(\omega t)$. Solid (dotted) lines in the figure correspond to stable (unstable) periodic solutions of the system (4.3). Here, it is of interest to examine how random perturbations influence the transition from one stable solution to another.

Each attractor is encoded by a sequence of symbols $X_1X_2X_3X_4X_5$, $X_j \in \{\mathrm{L}, \mathrm{H}\}$, $j = 1, \ldots, 5$, where L and H stand, respectively, for "low amplitude" and "high

amplitude". For example, LHLLL refers to the stable periodic solution where oscillator 2 has high amplitude while the rest of the oscillators have low amplitudes. From Fig. 4.2, it is discernible that if the frequency ω of the external forcing is far from the primary resonance, there exists at least one stable periodic solution. Furthermore, at a certain range of $\omega_1 < \omega < \omega_2$, there are a total of at least 32 periodic attractors corresponding to which each oscillator is in either a low or high amplitude state. This region with multiple stable solutions is referred to as the hysteresis region of the frequency response. In this region, the state (stable response) of the system is sensitive to initial (prior) conditions. Note that some solution branches in Fig. 4.2 coincide due to circular symmetry or closeness of their representations by $||\boldsymbol{q}(t)||_{L_2}$. This phenomenon wherein a smaller subset of the system (one or more oscillators but not all) consists of high amplitude responses is called *localization*. This chapter refers to *response localization* exclusively as the stable response mode in which only *one* oscillator oscillates with a high amplitude while all of other oscillators oscillate with low amplitudes.

Response localizations have been demonstrated in experiments of macro-cantilever beam arrays, wherein the beams represent the blades or components of turbomachinery and VEHs [4, 30–32, 34]. The localized high amplitude oscillations can, on one hand, be destructive in turbomachinery [3, 19, 20, 22, 28] and, on the other hand, be beneficial for energy harvesting systems [24, 29].

It is remarked that localization in the system governed by (4.3) is a nonlinear phenomenon: it would not occur if $\beta = 0$. However, localization may occur also in linear systems due to inhomogeneity [19, 21–24]; that is, if $\beta = 0$ and α is replaced with the vector $(\alpha_1, \ldots, \alpha_N)$. In the systems with $N = 3$ and $N = 5$, here, all stable response

localizations have symmetric, anti-phase, neighboring oscillators.

Adding a stochastic perturbation (noise) to an array of coupled Duffing oscillators; that is, replacing ODE (4.3) with (4.1) can facilitate transitions between various attractors (modes) of these systems [4]. Therefore, in an application, noise may be used to transition a system out of an undesirable localized mode in a bladed rotor or may help a VEH to get into the desirable high amplitude regime.

4.2 Objectives and Structure

The following two objectives are achieved in this chapter.

1. Conduct a case study on the noise-induced most probable escape paths out of undesired oscillations modes such as response localizations that exist only under the influence of deterministic periodic excitations in circular arrays of nonlinear oscillators.

2. Develop a computational tool for accomplishing Objective 1; that is, for finding the quasipotential barriers and most probable escape paths of nonlinear systems with multiple attractors subjected to both deterministic periodic excitations and weak random perturbations.

Objective 1 is relevant to a highly active area of research and motivates Objective 2, since there is no alternative methodology to compute these escape paths and quasipotential barriers for these high dimensional systems with low damping and deterministic time-dependent external excitations.

The focus of this chapter is on the weak white noise limit; that is the limit $\epsilon \to 0$. In a nonlinear system with multiple attractors, the probability of a transition between its attractors is non-zero no matter how small the white noise intensity is [75]. The asymptotic estimates for the weak noise limit often remain relevant for a broad range of noise intensities.

The current work relies on four building blocks:

1. The use of Freidlin's and Wentzell's large deviations theory (LDT) [75] to define the action functional (FW action) whose minimizers are the most probable escape paths from basins of attractors of (4.3). The corresponding minimal values of the action, which are the values of a certain function called the *quasipotential*, serve as a quantitative measure for the difficulty of escape from an attractor and the consequent transition.

2. The optimal control theory and Pontryagin's maximum principle [97] are used to identify the set of paths called *Hamiltonian paths*, which are the candidates for being the minimizers of the FW action. As a result, the problem of minimization of the FW action reduces to an optimization problem on the set of initial conditions for the Hamiltonian paths.

3. The action plot method [7] provides a nice recipe for cutting the dimensionality of this optimization problem by a factor of two through linearization of the system and approximation of the *Lagrangian manifold* containing the desired minimizing initial conditions.

4. Following Ref. [82], Floquet theory is used for linear ODEs with periodic

coefficients [98] to adapt this recipe for periodic attractors of non-autonomous stochastic differential equations (SDEs) (4.1).

The use of these building blocks is illustrated via the flow chart in Fig. 4.3

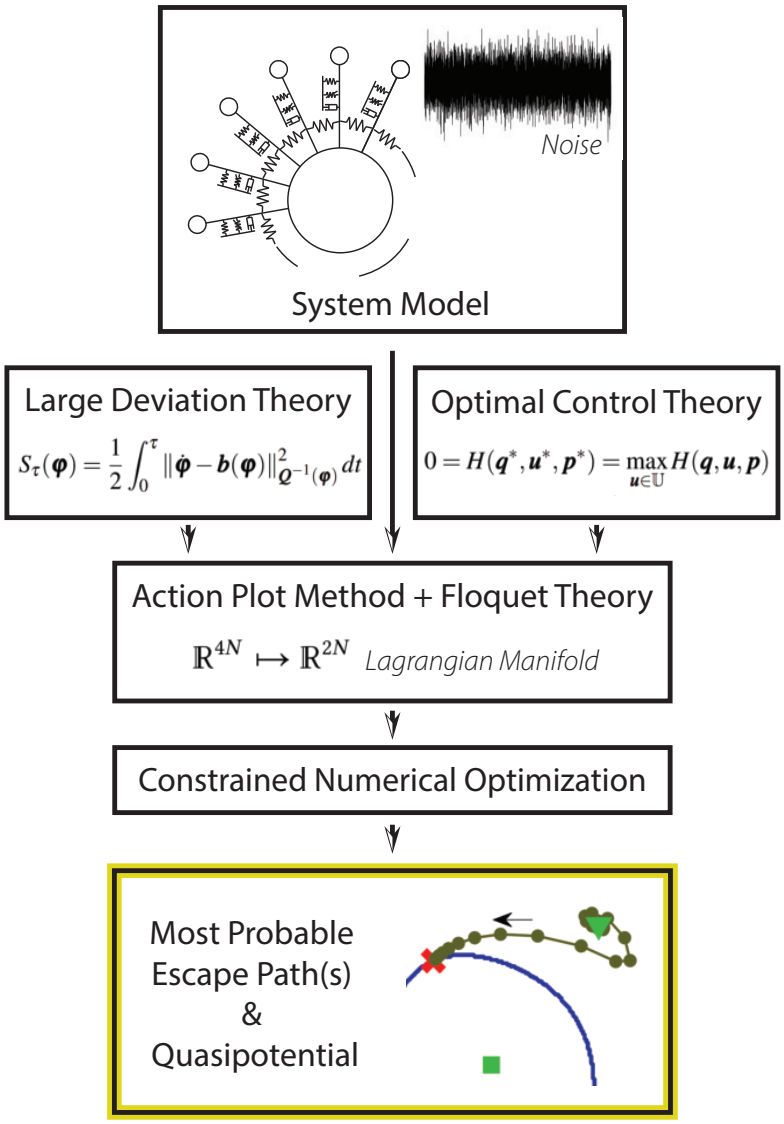


Figure 4.3: A flowchart overview of the main concepts in this chapter. Background is presented on a noise influenced system model, large deviation theory, and optimal control theory. A methodology built on the action plot method combined with the Floquet theory and numerical optimization is used to compute most probable escape paths and the quasipotential barriers of escapes from attractors of the system model.

The resulting optimization problem for the optimal set of initial conditions for the

Hamiltonian paths is still very challenging because the objective function is discontinuous and this function's minima lie next to its "cliffs". In the case of a 2-dimensional system, i.e., only one unforced oscillator, this problem can be solved graphically as it has been done in references [7, 90]. For the higher dimensional problems considered in this work, an optimization algorithm, *stochastic unit vector (SUV)*, is proposed for finding the minimizers of the FW action.

First, the developed methodology is applied to a single Duffing oscillator to quantify transitions between this system's low amplitude and high amplitude attractors. This example is highly instructive as it is visual and illuminates the technical difficulties for $N > 1$. Next, the most probable escape paths between attractors of arrays consisting of two, three, and five coupled Duffing oscillators are discussed. Finally, the dependencies of the quasipotential values characterizing the difficulty of escapes from the basins of attractors on the external forcing frequency ω and inter-oscillator coupling coefficient ν are visualized. These plots are helpful in validating the obtained results.

The rest of the chapter is organized as follows. In Section 4.3, fundamental background from large deviations theory and optimal control theory is discussed. The proposed methodology is detailed in 4.4. Results obtained for a single forced Duffing oscillator, two coupled forced Duffing oscillators, and two circular arrays of $N = 3$ and $N = 5$ Duffing oscillators are described in Sections 4.5, 4.6, and 4.7, respectively. The chapter is concluded with a discussion in Section 4.8. Details and parameter values for the computations conducted in this work chapter found in Section 4.9. Tables 4.3 and 4.4 in Section 4.9 are provided as a nomenclature reference for the reader.

4.3 Background

4.3.1 Large Deviations Theory

This section includes a brief background from Large Deviations Theory, which is used in this work to define the quasipotential.

The Freidlin-Wentzell large deviations theory [75] primarily deals with *autonomous* SDEs with *non-degenerate* noise

$$d\boldsymbol{q} = \boldsymbol{b}(\boldsymbol{q})dt + \sqrt{\varepsilon}\,\boldsymbol{G}(\boldsymbol{q})\,d\boldsymbol{W}(t), \tag{4.5}$$

where $d\mathbf{W}(t)$ is the standard Brownian motion. The drift field $\boldsymbol{b}$ and the diffusion matrix $\boldsymbol{Q}(\boldsymbol{q}) = \boldsymbol{G}\boldsymbol{G}^{\top}$ are assumed to be continuously differentiable.

The work performed by random perturbations can be quantified with the action functional $S_\tau(\boldsymbol{\varphi})$. When $\boldsymbol{Q}$ is invertible; that is, the noise in equation (4.5) is non-degenerate, the Freidlin-Wentzell action is defined on the set of absolutely continuous paths for $\boldsymbol{\varphi}$ by [75]

$$S_\tau(\boldsymbol{\varphi}) = \frac{1}{2}\int_0^\tau \|\dot{\boldsymbol{\varphi}} - \boldsymbol{b}(\boldsymbol{\varphi})\|^2_{\boldsymbol{Q}^{-1}(\boldsymbol{\varphi})}\,dt, \tag{4.6}$$

where $\|\cdot\|^2_{\boldsymbol{Q}^{-1}}$ denotes the inner product $\langle\cdot, \boldsymbol{Q}^{-1}\cdot\rangle$. One takeaway from (4.6) is that the action is zero if the path $\boldsymbol{\varphi}$ follows a deterministic trajectory of the corresponding ODE system

$$\dot{\boldsymbol{q}} = \boldsymbol{b}(\boldsymbol{q}). \tag{4.7}$$

The probability for a stochastic trajectory of SDEs (4.5) to follow a small δ-tube

surrounding a given absolutely continuous path $\boldsymbol{\varphi}$ scales with ϵ as $\exp\{-S_\tau(\boldsymbol{\varphi})/\epsilon\}$ (see Refs. [75, 99]).

The *quasipotential* $U_{\mathcal{A}}(\boldsymbol{q})$ *at a point* $\boldsymbol{q}$ *with respect to an attractor* $\mathcal{A}$ of (4.7) is defined as the infimum of the action taken over all possible absolutely continuous paths starting at $\mathcal{A}$ and ending at $\boldsymbol{q}$ and all travel times τ:

$$U_{\mathcal{A}}(\boldsymbol{q}) = \inf_{\boldsymbol{\varphi},\tau}\{S_\tau(\boldsymbol{\varphi}) \,|\, \boldsymbol{\varphi}(0) \in \mathcal{A},\ \boldsymbol{\varphi}(\tau) = \boldsymbol{q}\}. \tag{4.8}$$

Note that this infimum is achieved at $\tau = \infty$ as it takes infinitely long time to escape from the attractor in the weak noise limit. Furthermore, if the attractor is not a point attractor but a limit cycle or a more complex object, the infimum is achieved via an escape path of infinite length, as it makes infinitely many revolutions in neighborhood of the attractor while escaping from it. This minimizing path is called the *minimum action path* or *MAP*.

Let D be a domain with a smooth boundary ∂D lying in the basin of $\mathcal{A}$. The quasipotential allows one to estimate the expected exit time τ_{exit} from D up to the exponential order [75, 99]:

$$\lim_{\varepsilon\to 0} \varepsilon \log E\left[\tau_{exit}\right] = \inf_{\boldsymbol{q}\in\partial D} U_{\mathcal{A}}(\boldsymbol{q}) \tag{4.9}$$

Therefore, in the limit $\epsilon \to 0$, the system escapes the domain D after a waiting time logarithmically equivalent to $\exp\{-\inf_{\boldsymbol{q}\in\partial D} U_{\mathcal{A}}(\boldsymbol{q})/\epsilon\}$. Moreover, the escape path lies in a small tube surrounding the minimizer of the FW action (4.6), i.e. the MAP, with probability tending to one as $\epsilon \to 0$. Consequently, this MAP is often referred to as the

most probable escape path (MPEP). This chapter focuses on the escape from the basin of attraction of $\mathcal{A}$. Therefore, D is chosen to be the basin of attraction and ∂D is the basin boundary.

The generalization of these results of LDT for systems with inertia has been addressed only partially in the mathematical literature. This has been done for the dynamics governed by $\ddot{\boldsymbol{x}} + \delta_c \dot{\boldsymbol{x}} + \boldsymbol{b}(\boldsymbol{x}) = \sqrt{\varepsilon}\dot{\boldsymbol{W}}(t)$ for the case where $\boldsymbol{b}$ is either uniformly Lipschitz [100] or a gradient of a smooth potential function [101] $\boldsymbol{b} = -\nabla \boldsymbol{V}$. The conjecture that similar results for the MPEPs and the expected exit times hold for oscillators of the form (4.1) has been in physical literature since at least 1979 – see reference [102]. This conjecture is rooted in Feynman's path integral theory [103]. A rigorous proof of an estimate for the exit time similar to (4.9) for the dynamics governed by SDEs (4.1) is yet to be given.

Finally, it worth mentioning that there is strong numerical evidence suggesting that the MPEP for a nonlinear oscillator with external periodic forcing is the MAP obtained by matching the MAP with the plot of the prehistory probability distribution [90].

4.3.2 Definitions for periodically driven nonlinear oscillators

Now consider SDE (4.1) with periodic forcing $\boldsymbol{f}(t)$ of period T and the corresponding ODE (4.3). There is an important difference between a periodic solution of an autonomous ODE and a periodic solution of the time-dependent or non-autonomous ODE (4.3). Any time shift of a periodic solution of an autonomous ODE gives another periodic solution of the same ODE. In contrast, only time shifts of periodic solutions to

(4.3) that are multiples of the period result in other periodic solutions to (4.3). Therefore, every point $(\boldsymbol{x}, \boldsymbol{v})$ of a periodic solution to (4.3) is associated with a particular phase $\theta := t \bmod T$. Hence, it is natural to make ODE (4.3) autonomous by introducing the phase variable

$$\theta := t \bmod T \in \mathbb{S}^1_T \equiv \mathbb{S}^1(T/2\pi),$$

where $\mathbb{S}^1_T$ is a circle of radius $T/2\pi$. The resulting autonomous ODE on the manifold $\mathbb{R}^{2N} \times \mathbb{S}^1_T$ is:

$$\begin{aligned} \dot{\boldsymbol{x}} &= \boldsymbol{v}, \\ \dot{\boldsymbol{v}} &= -\delta_c \boldsymbol{v} - \boldsymbol{K}(\boldsymbol{x}) + \boldsymbol{f}(\theta), \\ \dot{\theta} &= 1, \\ \boldsymbol{x} &\in \mathbb{R}^N, \quad \boldsymbol{v} \in \mathbb{R}^N, \quad \theta \in \mathbb{S}^1_T. \end{aligned} \tag{4.10}$$

Here, the notation $\boldsymbol{K}(x) := \alpha \boldsymbol{x} + \beta \boldsymbol{x}^3 + \nu \boldsymbol{D}_N \boldsymbol{x}$ is introduced for brevity and convenience of generalization. The attracting periodic trajectories of the ODE (4.3) are the attractors of (4.10).

The corresponding SDE (4.1) is made autonomous in the same way:

$$\begin{aligned} d\boldsymbol{x} &= \boldsymbol{v}\, dt \\ d\boldsymbol{v} &= (-\delta_c \boldsymbol{v} - \boldsymbol{K}(\boldsymbol{x}) + \boldsymbol{f}(\theta))\, dt + \sqrt{\varepsilon}\, d\boldsymbol{W}(t) \\ d\theta &= dt \\ \boldsymbol{x} &\in \mathbb{R}^N, \quad \boldsymbol{v} \in \mathbb{R}^N, \quad \theta \in \mathbb{S}^1_T. \end{aligned} \tag{4.11}$$

The action functional for SDE (4.11) on the set of absolutely continuous paths $\{[\boldsymbol{\varphi}(t), \theta(t)] \mid t_0 \leq t \leq \tau\} \subset \mathbb{R}^N \times \mathbb{S}^1_T$ is defined as

$$S_{[t_0,\tau]}([\boldsymbol{\varphi}, \theta]) = \frac{1}{2} \int_{t_0}^{\tau} ||\ddot{\boldsymbol{\varphi}} + \delta_c \dot{\boldsymbol{\varphi}} + \boldsymbol{K}(\boldsymbol{\varphi}) - \boldsymbol{f}(\theta)||^2 dt \tag{4.12}$$

According to Dykman's and Krivoglaz's conjecture [102], which is consistent with Feyman's path integral theory [103], and supported by a strong numerical evidence [90], the minimizers of (4.12) have the following significance. Let $[\boldsymbol{\varphi}^*(t), \theta^*(t)]$, $t_0 \leq t \leq \tau$, be a minimizer of (4.12) amongst all paths satisfying $[\boldsymbol{\varphi}(t_0), \theta(t_0)] = [\boldsymbol{\varphi}^*(t_0), \theta^*(t_0)]$ and $[\boldsymbol{\varphi}(\tau), \theta(\tau)] = [\boldsymbol{\varphi}^*(\tau), \theta^*(\tau)]$. Then the probability for a trajectory of (4.11) starting at $[\boldsymbol{\varphi}^*(t_0), \theta^*(t_0)]$ and ending at $[\boldsymbol{\varphi}^*(\tau), \theta^*(\tau)]$ to follow a small tube around a path connecting these points is maximized if this path is a minimizer of (4.12). Moreover, this probability scales with the parameter ϵ in (4.11) as $\exp\{-S_{[t_0,\tau]}([\boldsymbol{\phi}^*, \theta^*])/\epsilon\}$. Therefore, in order to find the most probable escape path from a basin of attractor $\hat{\boldsymbol{A}}_0$ of (4.10), one should minimize (4.12) with respect to all paths and all times $t_0 \in [0, T)$ and $\tau \in [0, \infty]$ satisfying the boundary conditions $[\boldsymbol{\varphi}(t_0), \theta(t_0)] \in \hat{\boldsymbol{A}}_0$, $[\boldsymbol{\varphi}(\tau), \theta(\tau)] \in \partial B_0$ where B_0 denotes the basin of $\hat{\boldsymbol{A}}_0$.

4.3.3 Pontryagin's Maximum Principle

Once the action functional (the cost functional) is known, one can use optimal control theory [97, 104] to simplify the problem of minimizing it. The relevant ODE

with an $N-$dimensional control function $\boldsymbol{u}(t)$ is given by

$$\begin{aligned}
\dot{\boldsymbol{x}} &= \boldsymbol{v}, \\
\dot{\boldsymbol{v}} &= -\delta_c \boldsymbol{v} - \boldsymbol{K}(\boldsymbol{x}) + \boldsymbol{f}(\theta) + \boldsymbol{u}(t), \\
\dot{\theta} &= 1, \\
\boldsymbol{x} &\in \mathbb{R}^N, \quad \boldsymbol{v} \in \mathbb{R}^N, \quad \theta \in \mathbb{S}^1_T.
\end{aligned} \tag{4.13}$$

Expressing $\boldsymbol{u}$ from the equation for $\dot{\boldsymbol{v}}$ and comparing it to the action functional (4.12) we obtain the cost functional

$$S(\boldsymbol{u}) = \frac{1}{2} \int_{t_0}^{\tau} \|\boldsymbol{u}\|^2 \, dt. \tag{4.14}$$

The optimal control problem consists in finding a function $\boldsymbol{u}$ that minimizes the cost functional subject to some user-chosen constraints.

Suppose that ODEs (4.10) admit $n_a > 1$ attractors, $\hat{\boldsymbol{A}}_k$, $0 \leq k \leq n_a - 1$. Denote the basin of $\hat{\boldsymbol{A}}_k$ by B_k and the basin boundary by ∂B_k, $0 \leq k \leq n_a - 1$. Index 0 is reserved for the initial attractor, from which the most probable escape path emerges. Thus, the constraints are set as

$$(\boldsymbol{x}(t_0), \boldsymbol{v}(t_0), \theta(t_0)) \in \hat{\boldsymbol{A}}_0, \quad (\boldsymbol{x}(\tau), \boldsymbol{v}(\tau), \theta(\tau)) \in \partial B_0. \tag{4.15}$$

The optimal control problem

$$S(\boldsymbol{u}) = \frac{1}{2}\int_{t_0}^{\tau} \|\boldsymbol{u}\|^2\, dt \to \min \tag{4.16}$$

subject to (4.13) and (4.15)

will be solved with the aid of *Pontryagin's Maximum Principle* [97] whose basic form is the following. Suppose a controlled system is governed by a system of ODEs

$$\dot{\boldsymbol{q}} = \boldsymbol{b}(\boldsymbol{q}, \boldsymbol{u}). \tag{4.17}$$

Let the cost functional be

$$S(\boldsymbol{u}) = \int_{t_0}^{t_1} L(\boldsymbol{q}, \boldsymbol{u})\, dt. \tag{4.18}$$

Then, the *control theory Hamiltonian* is defined by

$$H(\boldsymbol{q}, \boldsymbol{u}, \boldsymbol{p}) := \boldsymbol{p}^\top \boldsymbol{b}(\boldsymbol{q}, \boldsymbol{u}) - L(\boldsymbol{q}, \boldsymbol{u}), \tag{4.19}$$

where $\boldsymbol{p}$ is a costate variable. *Pontryagin's maximum principle* states that if $\boldsymbol{u}^*(t)$ is the minimizer of (4.18) and $\boldsymbol{q}^*(t)$ is the corresponding optimal trajectory of (4.17) then there exists a function $\boldsymbol{p}^*(t)$, that, together with $\boldsymbol{q}^*(t)$ satisfies the Hamilton canonical equations [97]

$$\begin{pmatrix} \dot{\boldsymbol{q}} \\ \dot{\boldsymbol{p}} \end{pmatrix} = \begin{pmatrix} \nabla_{\boldsymbol{p}} H \\ -\nabla_{\boldsymbol{q}} H \end{pmatrix}. \tag{4.20}$$

The costate variables $\boldsymbol{p}$ are the momenta in the context of classical mechanics [105] but

they do not have that physical meaning in the current problem.

Furthermore, according to Pontryagin's maximum principle, the Hamiltonian is identically equal to zero and achieves its maximum along the optimal trajectory $(\boldsymbol{q}^*, \boldsymbol{p}^*)$ of (4.20):

$$0 = H(\boldsymbol{q}^*, \boldsymbol{u}^*, \boldsymbol{p}^*) = \max_{\boldsymbol{u} \in \mathbb{U}} H(\boldsymbol{q}, \boldsymbol{u}, \boldsymbol{p}), \tag{4.21}$$

where $\mathbb{U}$ is the set of admissible controls.

For the control problem (4.16), the state and costate variables are

$$\hat{\boldsymbol{q}} \equiv \begin{pmatrix} \boldsymbol{q} \\ \theta \end{pmatrix} = \begin{pmatrix} \boldsymbol{x} \\ \boldsymbol{v} \\ \theta \end{pmatrix} \quad \text{and} \quad \hat{\boldsymbol{p}} \equiv \begin{pmatrix} \boldsymbol{p} \\ p_\theta \end{pmatrix} = \begin{pmatrix} \boldsymbol{p}_{\boldsymbol{x}} \\ \boldsymbol{p}_{\boldsymbol{v}} \\ p_\theta \end{pmatrix}.$$

The optimal control $\boldsymbol{u}^*$ can be found using the fact that the Hamiltonian achieves its maximum at the optimal control $\boldsymbol{u}^*$. Therefore

$$\begin{aligned} 0 =& \nabla_{\boldsymbol{u}} H(\hat{\boldsymbol{q}}, \boldsymbol{u}^*, \hat{\boldsymbol{p}}) \\ =& \nabla_{\boldsymbol{u}} \left(\boldsymbol{p}_{\boldsymbol{x}}^\top \boldsymbol{v} + \boldsymbol{p}_{\boldsymbol{v}}^\top \left[-\delta_c \boldsymbol{v} - \boldsymbol{K}(\boldsymbol{x}) + \boldsymbol{f}(\theta) + \boldsymbol{u}^* \right] \right. \\ & \left. + p_\theta - \frac{1}{2} \|\boldsymbol{u}^*\|^2 \right) \\ =& \boldsymbol{p}_{\boldsymbol{v}} - \boldsymbol{u}^*. \end{aligned} \tag{4.22}$$

Hence $\boldsymbol{u}^* = \boldsymbol{p}_{\boldsymbol{v}}^*$ and the optimal path satisfies the Hamiltonian dynamical system

$$\begin{pmatrix} \dot{\boldsymbol{x}} \\ \dot{\boldsymbol{v}} \\ \dot{\theta} \\ \dot{\boldsymbol{p}}_{\boldsymbol{x}} \\ \dot{\boldsymbol{p}}_{\boldsymbol{v}} \\ \dot{p}_\theta \end{pmatrix} = \begin{pmatrix} \boldsymbol{v} \\ -\delta_c \boldsymbol{v} - \boldsymbol{K}(\boldsymbol{x}) + \boldsymbol{f}(\theta) + \boldsymbol{p}_{\boldsymbol{v}} \\ 1 \\ \nabla_{\boldsymbol{x}} \left(\boldsymbol{p}_{\boldsymbol{v}}^\top \boldsymbol{K}(\boldsymbol{x}) \right) \\ -\boldsymbol{p}_{\boldsymbol{x}} + \delta_c \boldsymbol{p}_{\boldsymbol{v}} \\ -\boldsymbol{p}_{\boldsymbol{v}}^\top \boldsymbol{f}'(\theta) \end{pmatrix}. \tag{4.23}$$

Any attractor $\hat{\boldsymbol{A}}_k$ of the ODEs (4.10) can be mapped onto a saddle-type invariant set $\bar{\boldsymbol{A}}_k$ of the corresponding Hamiltonian ODEs (4.23) by including the costate variables $\hat{\boldsymbol{p}}$ and setting them to zero. Since the first boundary condition in (4.15) is set at the attractor $\hat{\boldsymbol{A}}_0$, the corresponding trajectory of (4.23) passing through $(\hat{\boldsymbol{q}}(t_0), \boldsymbol{0})$ will stay forever at the corresponding saddle-type invariant set $\bar{\boldsymbol{A}}_0$. On the other hand, a whole family of trajectories called the *Hamiltonian paths* emanates from $\bar{\boldsymbol{A}}_0$ at time $t_0 = -\infty$ and constitutes the $(2N+1)$-dimensional unstable manifold of $\bar{\boldsymbol{A}}_0$ called the *Lagrangian manifold*. This will be clear from the structure of the Jacobian matrix obtained in Section 4.4.1.

Therefore, the optimal control problem (4.16) is reduced to finding the initial condition for the optimal Hamiltonian path at some finite moment in time. This is done by surrounding the attractor $\hat{\boldsymbol{A}}_0$ with a small neighborhood and searching for the initial conditions for the optimal Hamiltonian path in the intersection of the boundary of this neighborhood and the Largangian manifold. This construction is elaborated in Section

4.4.1.

4.4 Methodology

The methodology is developed for SDEs of the form (4.11) where the external forcing $\boldsymbol{f}(t)$ is periodic. It is assumed that the corresponding ODEs (4.10) admit $n_a \geq 2$ attractors $\hat{\boldsymbol{A}}_0$, ..., $\hat{\boldsymbol{A}}_{n_a-1}$ with basins B_0, ..., B_{n_a-1}, and these *attractors are periodic orbits*. The intersections of basin boundaries ∂B_k and ∂B_l are denoted by ∂B_{kl}, $0 \leq k, l \leq n_a - 1$.

Let the system governed by SDEs (4.11) be initially located near attractor $\hat{\boldsymbol{A}}_0$. The implication of Pontryagin's maximum principle is that the minimizer of the action functional (4.12) is a Hamiltonian path given by (4.23). As soon as the Hamiltonian path reaches the basin boundary ∂B_0, the costates $\boldsymbol{p_x}$ and $\boldsymbol{p_v}$ reset and are fixed to zero. From that point, the path continues a trajectory of (4.10) restricted to basin boundary ∂B_0. This trajectory approaches an attractor S for the dynamics restricted to ∂B_0. For the systems studied in this work, S is always a saddle cycle. Let $S \equiv S_{0k}$ belongs to ∂B_{0k} separating basins of $\hat{\boldsymbol{A}}_0$ and $\hat{\boldsymbol{A}}_k$, $k \neq 0$. Then, one can complete the transition path from $\hat{\boldsymbol{A}}_0$ to $\hat{\boldsymbol{A}}_k$ by adding a trajectory going from S_{0k} to $\hat{\boldsymbol{A}}_k$. Since the contribution to action (13) along any trajectory is zero, the total action along the transition path from $\hat{\boldsymbol{A}}_0$ to $\hat{\boldsymbol{A}}_k$ is equal to the action along the Hamiltonian path. Numerical experiments suggest (see Figs. 4.15, 4.16, 4.20, 4.22, 4.24, 4.27) that the maximum likelihood transition path from $\hat{\boldsymbol{A}}_0$ to $\hat{\boldsymbol{A}}_k$ is a concatenation of (i) a Hamiltonian path that approaches S_{0k} that is infinitely long, (ii) the saddle periodic orbit S_{0k}, and (iii) a trajectory of (4.10) starting infinitely close

to S_{0k} and approaching $\hat{\boldsymbol{A}}_k$. The key challenge is that the initial condition for the optimal Hamiltonian path is unknown.

4.4.1 The Lagrangian Manifold

The action plot method [7] utilizes Pontryagin's maximum principle to reduce the problem of finding the most probable escape path (MPEP) to the problem of finding the initial condition for the Hamiltonian path and offers an elegant way to simplify this problem. This is done by linearizing the Hamiltonian system near an invariant set corresponding to an attractor of the original ODE and approximating the unstable Lagrangian manifold by a linear relationship between $\hat{\boldsymbol{q}}(0)$ and $\hat{\boldsymbol{p}}(0)$. The construction of the Lagrangian manifold adapted for the case of periodic forcing is detailed below. The Floquet theory [98] for linear ODEs with periodic coefficients is used to facilitate finding the unstable manifold. The latter is inspired by Ref. [82].

The equations for θ and p_θ in the Hamiltonian ODE (4.23) can be omitted, as they do not affect the other equations. The resulting non-autonomous Hamiltonian ODE system is given by

$$\begin{pmatrix} \dot{\boldsymbol{x}} \\ \dot{\boldsymbol{v}} \\ \dot{\boldsymbol{p}}_{\boldsymbol{x}} \\ \dot{\boldsymbol{p}}_{\boldsymbol{v}} \end{pmatrix} = \begin{pmatrix} \boldsymbol{v} \\ -\delta_c \boldsymbol{v} - \boldsymbol{K}(\boldsymbol{x}) + \boldsymbol{f}(t) + \boldsymbol{p}_{\boldsymbol{v}} \\ \nabla_{\boldsymbol{x}} \left(\boldsymbol{p}_{\boldsymbol{v}}^\top \boldsymbol{K}(\boldsymbol{x}) \right) \\ -\boldsymbol{p}_{\boldsymbol{x}} + \delta_c \boldsymbol{p}_{\boldsymbol{v}} \end{pmatrix}. \tag{4.24}$$

The periodic trajectories of (4.23) are naturally mapped onto periodic trajectories of (4.24) by dropping of the components θ and p_θ. Let $\hat{\boldsymbol{A}}_0 =: (\boldsymbol{x}(t), \boldsymbol{v}(t), \theta(t))$ be an attractor of the ODE system (4.10). It corresponds to a saddle-type periodic trajectory $\bar{\boldsymbol{A}}_0$ of the

Hamiltonian dynamical system (4.23). In turn, $\bar{\boldsymbol{A}}_0$ corresponds to a periodic solution $\tilde{\boldsymbol{A}}_0 := (\boldsymbol{x}(t), \boldsymbol{v}(t), \mathbf{0}, \mathbf{0}))$ of the non-autonomous Hamiltonian dynamical system (4.24). The goal is to find the set of the initial conditions for the Hamiltonian paths forming the Lagrangian manifold. To do so, one needs to linearize ODEs (4.24) near the periodic solution $\tilde{\boldsymbol{A}}_0$. The Jacobian of the right-hand side of (4.24) is

$$
\begin{aligned}
&J(\boldsymbol{x}, \boldsymbol{v}, \boldsymbol{p}_{\boldsymbol{x}}, \boldsymbol{p}_{\boldsymbol{v}}, t_0) \\
&= \begin{pmatrix}
\mathbf{0} & \boldsymbol{I} & 0 & 0 \\
-\boldsymbol{J}_{\boldsymbol{K}}(\boldsymbol{x}) & -\delta_c \boldsymbol{I} & 0 & \boldsymbol{I} \\
\nabla_{\boldsymbol{x}} \nabla_{\boldsymbol{x}} \left[\boldsymbol{p}_{\boldsymbol{v}}^{\top} \boldsymbol{K}(\boldsymbol{x})\right] & 0 & 0 & \boldsymbol{J}_{\boldsymbol{K}}(\boldsymbol{x})^{\top} \\
\mathbf{0} & 0 & -\boldsymbol{I} & \delta_c \boldsymbol{I}
\end{pmatrix},
\end{aligned}
\tag{4.25}
$$

and its value at $(\hat{\boldsymbol{x}}(t), \hat{\boldsymbol{v}}(t), \mathbf{0}, \mathbf{0}))$ is

$$
\begin{aligned}
&J(\hat{\boldsymbol{x}}, \hat{\boldsymbol{v}}, \mathbf{0}, \mathbf{0}, t_0) \\
&= \begin{pmatrix}
\mathbf{0} & \boldsymbol{I} & 0 & 0 \\
-\boldsymbol{J}_{\boldsymbol{K}}(\hat{\boldsymbol{x}}) & -\delta_c \boldsymbol{I} & 0 & \boldsymbol{I} \\
\mathbf{0} & 0 & 0 & \boldsymbol{J}_{\boldsymbol{K}}(\hat{\boldsymbol{x}})^{\top} \\
\mathbf{0} & 0 & -\boldsymbol{I} & \delta_c \boldsymbol{I}
\end{pmatrix} \equiv J_{\tilde{\boldsymbol{A}}_0}(t_0).
\end{aligned}
\tag{4.26}
$$

In equations (4.25) and (4.26), $\boldsymbol{J}_{\boldsymbol{K}}$ denotes the Jacobian matrix of the vector field $\boldsymbol{K}$. The linear ODE with periodic coefficients of period T approximating (4.24) near $\tilde{\boldsymbol{A}}_0$ is of the form

$$
\dot{\boldsymbol{z}} = J_{\tilde{\boldsymbol{A}}_0}(t_0) \boldsymbol{z}. \tag{4.27}
$$

Equation (4.27) has a fundamental solution matrix $\mathbf{\Psi}(t)$. According to Floquet's theorem [98], the monodromy matrix

$$\mathbf{\Psi}(t_0 + T)\mathbf{\Psi}(t_0)^{-1} \tag{4.28}$$

provides a coordinate change that results in the Poincaré mapping for the corresponding linearized autonomous system with $\theta_0 = t_0 \bmod T \in \mathbb{S}^1_T$. The eigenvalues of the monodromy matrix, called *characteristic multipliers*, are intrinsic to the ODE, as they remain invariant for all $t_0 \in \mathbb{R}$. The corresponding matrix of eigenvectors is a periodic function of t_0. The structure of the matrix $J_{\tilde{\boldsymbol{A}}_0}(t_0)$ implies that the monodromy matrix has $2N$ eigenvalues less than 1 (stable) and $2N$ eigenvalues greater than 1 (unstable). The $4N \times 2N$ matrix functions $\mathbf{\Phi}^s_{\theta_0}$ and $\mathbf{\Phi}^u_{\theta_0}$ are formed, respectively, by the stable and unstable eigenvectors. At each fixed $\theta_0 \in [0, T]$, the span of $\mathbf{\Phi}^u_{\theta_0}$ is the linear unstable manifold. Since ODE (4.27) describes the time evolution of the first-order perturbation to the periodic solution $\tilde{\boldsymbol{A}}_0$, the Lagrangian manifold near $\tilde{\boldsymbol{A}}_0$ is approximated by the sum of trajectories of the Hamiltonian ODE (4.24) passing through the set of initial conditions

$$\left\{ \tilde{\boldsymbol{A}}_0(\theta_0) + \hat{\gamma}\mathbf{\Phi}^u_{\theta_0}\boldsymbol{c} \;\middle|\; \boldsymbol{c} \in \mathbb{R}^{2N}, \theta_0 \in \mathbb{S}^1_T \right\}, \tag{4.29}$$

where $\hat{\gamma} > 0$ is a scaling parameter. It is worth noting that the choice of $\hat{\gamma}$ would be arbitrary if equation (4.24) were linear, and θ_0 could be set to zero if equation (4.24) were autonomous. However, since (4.24) is nonlinear and non-autonomous, $\hat{\gamma}|\boldsymbol{c}|$ needs to be small and all $\theta_0 \in [0, T)$ should be considered.

Any escape path in $\mathbb{R}^{2N} \times \mathbb{S}^1$ leaving $\hat{\boldsymbol{A}}_0$ must cross through a torus that surrounds $\hat{\boldsymbol{A}}_0$. For each fixed $\theta_0 \in \mathbb{S}^1_T$, the point $\hat{\boldsymbol{A}}_0(\theta_0)$ can be completely surrounded by a $2N-1$-

dimensional sphere embedded in $\mathbb{R}^{2N}$. This allows one to further reduce the optimization space as follows. Consider the sphere of radius γ:

$$\mathbb{S}_{\gamma}^{2N-1} = \{\boldsymbol{q}_{\gamma} \in \mathbb{R}^{2N} \text{ such that } |\boldsymbol{q}_{\gamma}| = \gamma\}. \tag{4.30}$$

The values of $\boldsymbol{q}_{\gamma}$ that are in the Lagrangian manifold must satisfy

$$\boldsymbol{A}_0(\theta_0) + \hat{\gamma}\boldsymbol{Z}_{\boldsymbol{q},\theta_0}\boldsymbol{c} = \boldsymbol{A}_0(\theta_0) + \boldsymbol{q}_{\gamma}, \tag{4.31}$$

where $\boldsymbol{A}_0(\theta_0)$ consists of $\boldsymbol{x}$- and $\boldsymbol{v}$-components of $\tilde{\boldsymbol{A}}_0(\theta_0)$ and the matrix, $\boldsymbol{Z}_{\boldsymbol{q},\theta_0}$ is a sub-matrix of dimension $2N \times 2N$ extracted from $\boldsymbol{\Phi}_{\theta_0}^{u}$ such that

$$\begin{bmatrix} \boldsymbol{Z}_{\boldsymbol{q},\theta_0} \\ \boldsymbol{Z}_{\boldsymbol{p},\theta_0} \end{bmatrix} \equiv \boldsymbol{\Phi}_{\theta_0}^{u}. \tag{4.32}$$

It follows from (4.31) that

$$\hat{\gamma}\boldsymbol{c} = \boldsymbol{Z}_{\boldsymbol{q},\theta_0}^{-1}\boldsymbol{q}_{\gamma}, \tag{4.33}$$

which can be used to solve for the initial costate perturbations:

$$\begin{aligned} \boldsymbol{p}_{\gamma,\theta_0} &= \boldsymbol{Z}_{\boldsymbol{p},\theta_0}\hat{\gamma}\boldsymbol{c} \\ &= \boldsymbol{Z}_{\boldsymbol{p},\theta_0}\boldsymbol{Z}_{\boldsymbol{q},\theta_0}^{-1}\boldsymbol{q}_{\gamma}. \end{aligned} \tag{4.34}$$

With the aid of (4.30) and (4.34), one can define the space of initial conditions as

$$W \equiv \left\{ \tilde{\boldsymbol{A}}_0(\theta_0) + \begin{bmatrix} \boldsymbol{q}_\gamma \\ \\ \boldsymbol{p}_{\gamma,\theta_0} \end{bmatrix} \;\middle|\; \boldsymbol{q}_\gamma \in \mathbb{S}^{2N-1}_\gamma, \theta_0 \in \mathbb{S}^1_T \right\}, \tag{4.35}$$

which is now a $2N$-dimensional manifold.

In this chapter, $\gamma = 10^{-20}$ for $N = 1$, a single oscillator, and $\gamma = 10^{-15}$ for the $N > 1$ oscillators. Note that it is not worth it to pick γ too small as there is a trade-off between the error in the approximation of the Lagrangian manifold and the error accumulating due to numerical integration of Hamiltonian paths.

4.4.2 The Escape Time

The escape cost from the basin of $\hat{\boldsymbol{A}}_0$ for a Hamiltonian path $(\boldsymbol{q}, \boldsymbol{p})$ defined by (4.24) and the initial condition $(\boldsymbol{q}_0, \boldsymbol{p}_0)$ of the form (4.35) is found by numerical integration of the action (4.12) until the moment of time $\tau(\boldsymbol{q}_\gamma, \theta_0)$ when the path reaches the basin boundary ∂B_0:

$$\tau(\boldsymbol{q}_\gamma, \theta_0) = \inf_{t \in \mathbf{R}} \{ \boldsymbol{q}(t) \in \partial B_0, \; \|\boldsymbol{q}(\theta_0)\| = \gamma \}. \tag{4.36}$$

The escape time for most Hamiltonian paths is finite when radius γ in (4.35) is positive, except for when the path is a heteroclinic orbit. In fact, the results presented in this chapter suggest that it is exactly the case that the most probable escape paths approach attractors as $t \to -\infty$ and approach saddle cycles on basin boundaries as $t \to +\infty$.

4.4.3 Optimization and Implementation

Based on the argument presented in Sections 4.4.1 and 4.4.2 the optimization problem (4.16) for the most probable escape path (MPEP) is reduced to

$$C(\boldsymbol{q}_\gamma, \theta_0) = \frac{1}{2} \int_{\theta_0}^{\tau(\boldsymbol{q}_\gamma, \theta_0)} ||\boldsymbol{p}_{\boldsymbol{v}}(t)||^2 dt \to \min \tag{4.37}$$

where $\boldsymbol{p}_{\boldsymbol{v}} \equiv \boldsymbol{u}$ follows the dynamics of (4.24) with initial conditions defined by (4.35). The integral time bounds are defined by (4.35) and (4.36). Equation (4.37) is minimized with respect to both $\boldsymbol{q}_\gamma$ and θ_0 in the manifold $\mathcal{M} := \mathbb{S}^{2N-1}_\gamma \times \mathbb{S}^1_T$. The contribution of θ_0 to the minimizers is discussed in Section 4.5.

A set of n_{init} initial points $\boldsymbol{q}_\gamma$ and θ_0 is sampled uniformly on the manifold $\mathcal{M} := \mathbb{S}^{2N-1}_\gamma \times \mathbb{S}^1_T$. The corresponding initial conditions for the Hamiltonian paths are defined according to (4.35). Next, each Hamiltonian path (4.24) together with its cost functional (4.12) is integrated until a crossing of the basin boundary is detected. The corresponding moment of time is $\tau(\boldsymbol{q}_\gamma, \theta_0)$. The found values of the cost functional are first sorted in the ascending order, and then $n_s < n_{\text{init}}$ initial points $\boldsymbol{q}_\gamma$ and θ_0 corresponding to n_s smallest values of the cost functional are selected as the candidates for local minimizers. The values of n_{init} and n_s are found in Table 4.2 in Section 4.9.

The cost function (4.37) is discontinuous and its minima lie at the bottoms of its "cliffs" – see Figure 4.10 ahead depicting the escape cost for a single oscillator. Such behavior of the cost function can be understood as follows. Consider a sequence of Hamiltonian paths with initial conditions $(\boldsymbol{q}^j_\gamma, \theta^j_0)$ escaping from the basin of the attractor

$\hat{\boldsymbol{A}}_0$ whose escape points approach a saddle cycle lying at the boundary of B_0 and whose escape costs $C(\boldsymbol{q}_\gamma^j, \theta_0^j)$ decrease. The goal of numerical minimization of (4.37) is to generate a sequence of Hamiltonian paths converging to a limiting path that has minimal escape cost and approaches the saddle cycle infinitely long. Suppose the optimizer "overshoots". Then the path will fail to exit the basin of $\hat{\boldsymbol{A}}_0$ near the saddle and proceed to an extra loop causing a jump in the escape cost. This phenomenon is illustrated on a simple example of a bistable Duffing oscillator $\ddot{x} + \dot{x} - x + x^3 = \sqrt{\epsilon}\eta(t)$ in Figure 4.4.

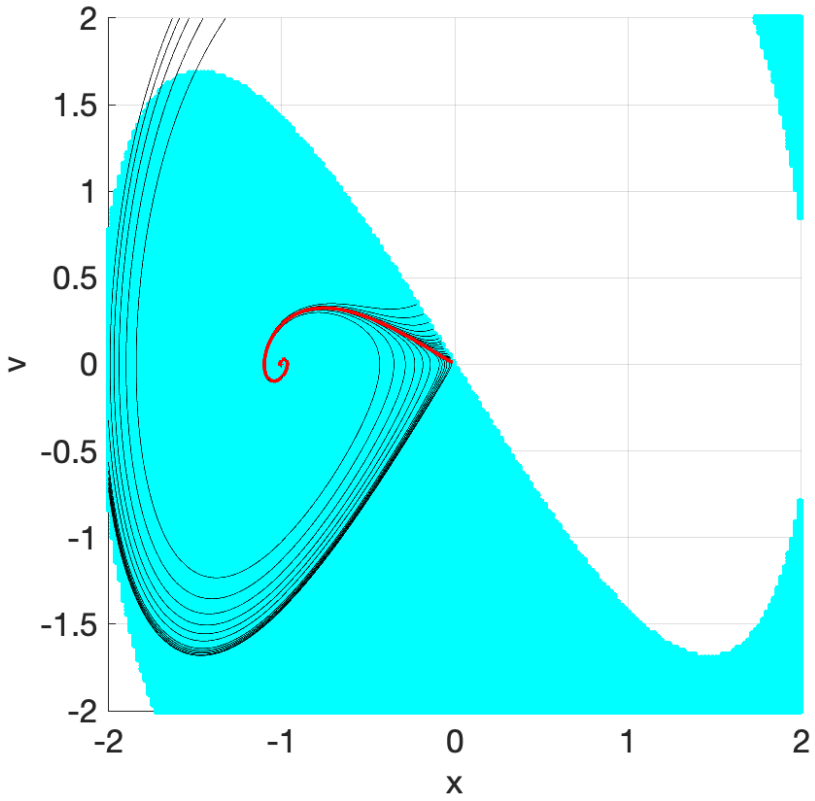


Figure 4.4: An illustration for the origin of discontinuities in the cost function (4.37) on the example of a single bistable Duffing oscillator $\ddot{x}+\dot{x}-x+x^3 = \sqrt{\epsilon}\eta(t)$. This oscillator has stable equilibria at $(\pm 1, 0)$ and a saddle at the origin. The basin of $(-1, 0)$ is shaded cyan. The optimal Hamiltonian escape path and a collection of other Hamiltonian paths with close initial conditions are shown in red and black, respectively. It is apparent that overshooting initial conditions results in a much longer escape route and a sharp increase of escape cost.

A variety of gradient-based and gradient-free methods and their combinations have been explored as optimizers for (4.37). The gradient of the cost function has been approximated by finite differences.

The gradient-based methods include the gradient descent and the Fletcher-Reeves nonlinear conjugate gradient methods projected on the manifold $\mathcal{M} = \mathbb{S}^{2N-1}_{\gamma} \times \mathbb{S}^{1}_{T}$. The gradient-free techniques that are used are the Nelder-Mead simplex method and an originally developed *stochastic unit vectors* method (SUV) summarized in the pseudocode in Algorithm 2. While gradient-based methods are more efficient while stepping within smooth regions of the cost function than Nelder-Mead or SUV, they are unable to crawl along the edges of the bottoms of the cliffs. Hence, as a proximity of a cliff is detected, a gradient-free method continues the search. It is found that there is no significant advantage in starting minimization with a gradient-based technique. Furthermore, the brute-force SUV algorithm turned out to work the most robustly and reliably on the problems addressed in this work.

As with all gradient free methods that cannot guarantee convergence to a global minimum, it is best to validate the minimizer with a secondary approach. The probability of finding a global minimum is increased by first sampling the cost function space with a large number of initial points prior to beginning the optimization as mentioned earlier in this section. The minimizers are validated by checking that they approach saddle cycles, and that the resulting quasipotential values follow a trend with respect to parameters such as frequency and coupling. Since the optimization and the initial sampling are stochastic, the minimizers are also validated by running the optimization multiple times with different randomly picked initial conditions.

Algorithm 2: Stochastic Unit Vectors

Initialization *Select an initial point* $\boldsymbol{x}_0$ *on a* d*-dimensional manifold* $\mathcal{M}$ *and an initial step size* σ*. Set* $i = 0$*. Select the minimal step size* $\sigma_{\min}$*.*

Main Body

while $\sigma \geq \sigma_{\min}$ **do**

1: Sample a random unit vector $\boldsymbol{e}_1 \in T_{\boldsymbol{x}_i}\mathcal{M}$ (the tangent space of $\mathcal{M}$ at $\boldsymbol{x}_i$) from a uniform distribution.

2: Complete $\boldsymbol{e}_1$ to an orthonormal basis $[\boldsymbol{e}_1, \boldsymbol{e}_2, ..., \boldsymbol{e}_d]$ in the tangent space $T_{\boldsymbol{x}_i}\mathcal{M}$.

3: Consider a collection of points $Y = \{\, \boldsymbol{y}_j = \boldsymbol{x}_i + \sigma\, \boldsymbol{e}_j,\ j = [1, 2, ..., d],$
$\boldsymbol{y}_j = \boldsymbol{x}_i - \sigma\, \boldsymbol{e}_j, \quad j = [d+1, d+2, ..., 2d]\}$.

4: Calculate the cost $C(\boldsymbol{y}_j)$ at each $\boldsymbol{y}_j$, $1 \leq j \leq 2d$.

5: if $\min_{1\leq j\leq 2d} C(\boldsymbol{y}_j) \geq C(\boldsymbol{x}_i)$ **then**

Remain at $\boldsymbol{x}_i$ and reduce the step size: $\boldsymbol{x}_{i+1} = \boldsymbol{x}_i,\ \sigma = \sigma/2$.

else

Set $\tilde{\boldsymbol{x}} = \arg\min_{1\leq j\leq 2d} C(\boldsymbol{y}_j)$ and project $\tilde{\boldsymbol{x}}$ onto the manifold $\mathcal{M}$: $\boldsymbol{x}_{i+1} = \mathsf{Proj}_{\mathcal{M}}(\tilde{\boldsymbol{x}})$.

end

6: $i = i + 1$.

end

The other challenge of numerical minimization of the cost function (4.37) for two or more oscillators, i.e., when the dimension d of the manifold $\mathcal{M}$ is four or higher, is that the basins of attraction must be sampled online during optimization as it is impossible to store high resolution data of the basins of attraction or the basin boundaries for $d \geq 4$. Only the attractors are determined offline and stored. Therefore, Step 4 of Algorithm 2; that is, the calculation of the exit cost that involves the integration of Hamiltonian paths and the detection of crossing basin boundary requires elaboration. Each Hamiltonian path $(\boldsymbol{q}(t), \boldsymbol{p}(t))$ traced by the minimization algorithm is checked at equispaced moments of time t_i, $i = 1, 2, \ldots$ for having left or not the basin of the initial attractor. This is done by integrating the original unperturbed ODE (4.3) starting from the point $\boldsymbol{q}(t_i) = (\boldsymbol{x}(t_i), \dot{\boldsymbol{x}}(t_i))$ at time t_i forward in time. If it is found that that $(\boldsymbol{q}(t_i), t_i \bmod T)$ does not belong to the basin of the initial attractor, tracing of the Hamiltonian path is stopped and

a refinement procedure is implemented to determine the escape time $\tau(\boldsymbol{q}_\gamma, \theta_0) \in (t_{i-1}, t_i)$ more precisely. The evaluation of exit cost is detailed in Algorithm 3 and illustrated in Fig. 4.5. An important parameter in this Algorithm is dT, the time interval between any two consecutive check times t_i and t_{i+1}. If dT is too small, the cost function can take a long time to evaluate. If dT is too large, the unstable dynamics of the Hamiltonian system blow up during the time span, which increases the integration time and can cause the algorithm to miss the initial escape from the basin. It is found that a good default value for dT is half-period, $T/2$. However, when the basins are shallow or small, a smaller value of dT should be used. The code is set up to decrease dT and restart automatically if a blow-up of a Hamiltonian path is detected. The code is written in MATLAB. The ODE solver `ode45` with absolute and relative error tolerances of 10^{-8} is used for numerical integration.

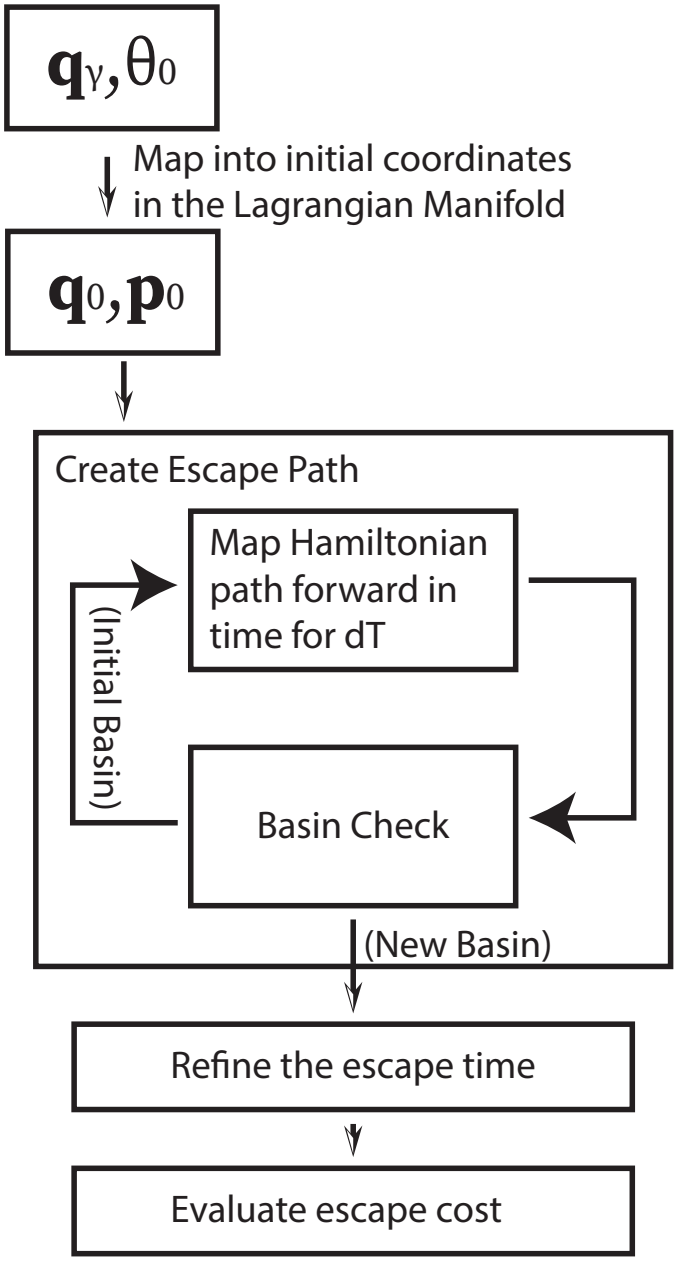


Figure 4.5: A flow chart of the process of evaluating the cost function given an input $\boldsymbol{q}_\gamma$ and θ_0. A detailed version of the process shown here is described in the pseudocode of Algorithm 2.

Algorithm 3: The Cost Function: Step 4 in Algorithm 2

Input: Initial conditions $\mathbf{q}_\gamma, \theta_\mathbf{0}$

Initialization

i: Define $t_i \leftarrow \theta_0$, $i \leftarrow 0$

ii: Define initial condition $(\boldsymbol{q}(t_i), \boldsymbol{p}(t_i)) \in W$ using $\mathbf{q}_\gamma, \theta_\mathbf{0}$

iii: Let `index0` be the index of the initial attractor.

iv: Define a function, `Aindex`$(\boldsymbol{q}(t))$, that returns m if $\|\boldsymbol{q}(t) - \boldsymbol{A}_m(t)\| \leq R \quad \forall m = [0, 1, ..., n_a - 1]$ or `noindex` otherwise. Here, R is a small radius and $\boldsymbol{A}_m(t)$ is the position of attractor m at time t.

v: Define the system's differential equations as ODE_S

vi: Define the system's corresponding Hamiltonian differential equations as ODE_H

Escape via Integration

while index $== 0$ **do**

1: $i \leftarrow i + 1$, $t_i \leftarrow t_{i-1} + dT$

2: Evaluate $(\boldsymbol{q}(t_i), \boldsymbol{p}(t_i))$ by integrating ODE_H forward in time from t_{i-1} to t_i with initial condition $(\boldsymbol{q}(t_{i-1}), \boldsymbol{p}(t_{i-1}))$.

3: $j \leftarrow 0$, $\check{t}_j \leftarrow t_i$, $\check{\boldsymbol{q}}(\check{t}_j) \leftarrow \boldsymbol{q}(t_i)$

4: **while** `Aindex`$(\check{\boldsymbol{q}}(\check{t}_j)) ==$ `noindex` **do**

a: $j \leftarrow j + 1$, $\check{t}_j \leftarrow \check{t}_{j-1} + dT$

b: Evaluate $\check{\boldsymbol{q}}(\check{t}_j)$ by integrating ODE_S forward in time from $\check{t}_{j-1}$ to $\check{t}_j$ with initial condition $\check{\boldsymbol{q}}(\check{t}_{j-1})$.

end

5: `index` $\leftarrow$ `Aindex`$(\check{\boldsymbol{q}}(\check{t}_j))$

end

Continued on next page

Algorithm 3 continued

Refine the Escape Time

i: Define upper and lower time bounds for the escape time: $\tau_H = t_i, \tau_L = t_{i-1}$

ii: $d\tau \leftarrow \tau_H - \tau_L$

while $d\tau > \epsilon$ **do**

1: $\tau \leftarrow (\tau_L + \tau_H)/2$

2: $j \leftarrow 0$, $\check{t}_j \leftarrow \tau$, $\check{\boldsymbol{q}}(\check{t}_j) \leftarrow \boldsymbol{q}(\tau)$

3: while $\texttt{Aindex}(\check{\boldsymbol{q}}(\check{t}_j)) == \texttt{noindex}$ **do**

a: $j \leftarrow j + 1$, $\check{t}_j \leftarrow \check{t}_{j-1} + dT$

b: Evaluate $\check{\boldsymbol{q}}(\check{t}_j)$ by integrating ODE_S forward in time from $\check{t}_{j-1}$ to $\check{t}_j$ with initial condition $\check{\boldsymbol{q}}(\check{t}_{j-1})$.

end

4: if $\texttt{Aindex}(\check{\boldsymbol{q}}(\check{t}_j)) == \texttt{index0}$ **then**

$\tau_L \leftarrow \tau$

else

$\tau_H \leftarrow \tau$

end

5: $d\tau \leftarrow \tau_H - \tau_L$

end

Evaluate the Cost

Evaluate the cost by integrating (4.37) along the path $(\boldsymbol{q}(t), \boldsymbol{p}(t))$ on the time interval $\theta_0 \leq t \leq \tau$.

The location of the attractors and the frequency response diagrams in sections 4.5,4.6, and 4.7 are computed by using a combination of the shooting method and a continuation package. The shooting method is used to generate a stable solution of the system at one excitation frequency. The continuation package AUTO2007 [51] is used to continue the solution branch for different frequency values. The use of the continuation procedure allows for determining the stable solutions branches, the unstable solution branches, the Floquet multipliers of each solution, and the bifurcation points with respect to the excitation frequency. This additional information is useful for visualization and understanding of the behavior of the system, but not necessary to solve the optimization problem for the most probable escape path.

4.5 Forced Duffing Oscillator

This section is devoted to a detailed analysis of noise-driven transitions between the high amplitude and low amplitude attractors of a single monostable Duffing oscillator with external harmonic forcing. The methodology introduced in the previous section is applied to find the MPEPs. The case of a single oscillator is instructive and visual, as its study illuminates the difficulties of the problem and explains the technical decisions that are made.

The dynamics of the Duffing oscillator studied in this section is governed by SDE (4.1) with $N = 1$. The values of the parameters chosen are $\alpha = 1$, $\beta = 0.3$, $\delta = 0.1$, and $F(t) = 0.4\cos(\omega t)$. These are nondimensional parameters that exhibit the characteristics of a hardening oscillator. The frequency response of this oscillator is shown in Fig. 4.6.

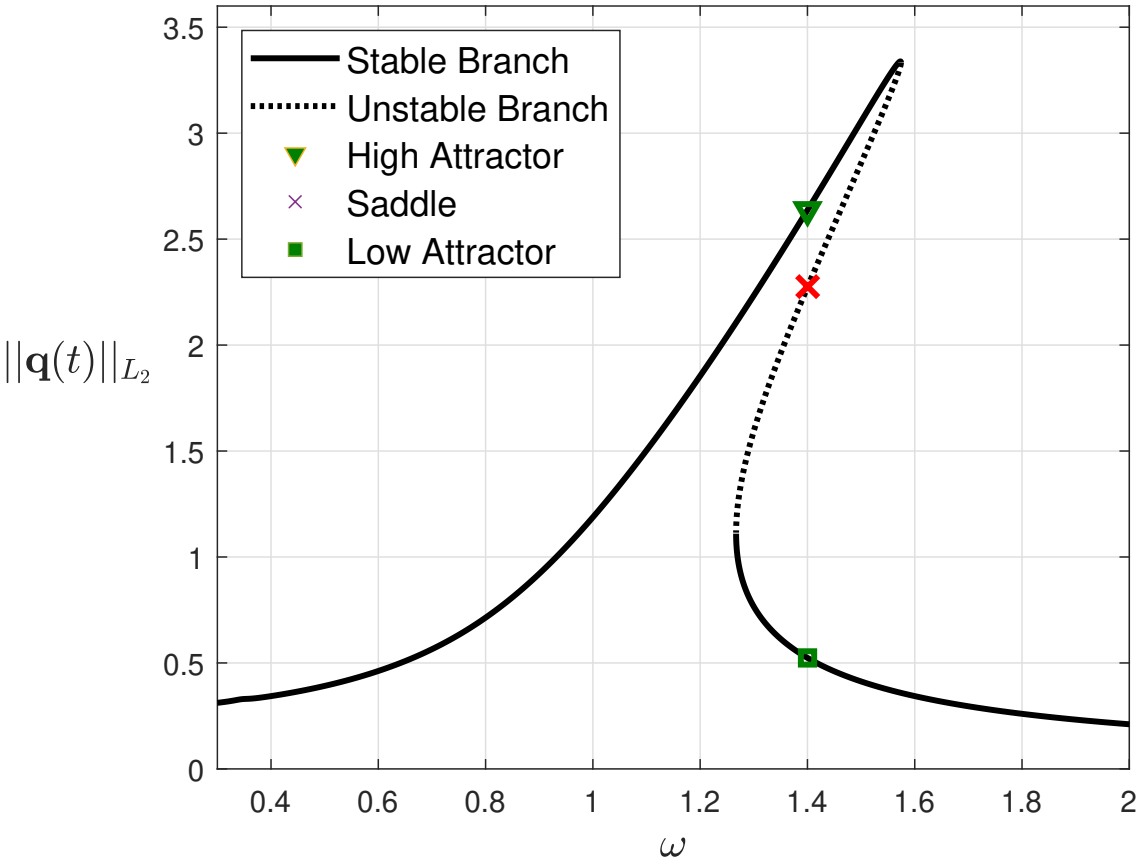


Figure 4.6: Frequency response of a forced Duffing oscillator as a function of excitation frequency, ω. Attractor and saddle locations are highlighted at the frequency of $\omega = 1.4$. This figure is generated by using the continuation package AUTO2007 [51].

As the frequency ω of the external force increases, the dynamics of the Duffing oscillator undergoes bifurcations at $\omega_1 \approx 1.27$ and at $\omega_2 \approx 1.57$. At $0 < \omega < \omega_1$, at least one periodic solution exists and its L_2-norm is an increasing function of ω. At $\omega = \omega_1$, a pair of a stable and unstable periodic solutions are born. As a result, there exist two stable periodic solutions for $\omega_1 < \omega < \omega_2$, one of which with the smaller L_2-norm is born at $\omega = \omega_1$, while the other with higher L_2-norm one continues to exist from lower values of ω. They will be referred to as the low amplitude attractor and the high amplitude

attractor, respectively. At $\omega = \omega_2$, the high amplitude periodic solution annihilates with the unstable periodic solution born at $\omega = \omega_1$. Only the low amplitude attractor exists for $\omega > \omega_2$, and its L_2-norm decreases as ω increases.

For the frequency of $\omega = 1.4$, the Poincaré map of the periodic solutions and the basins of attractions of each attracting solution at $\theta = 0$ is shown in Fig. 4.7.

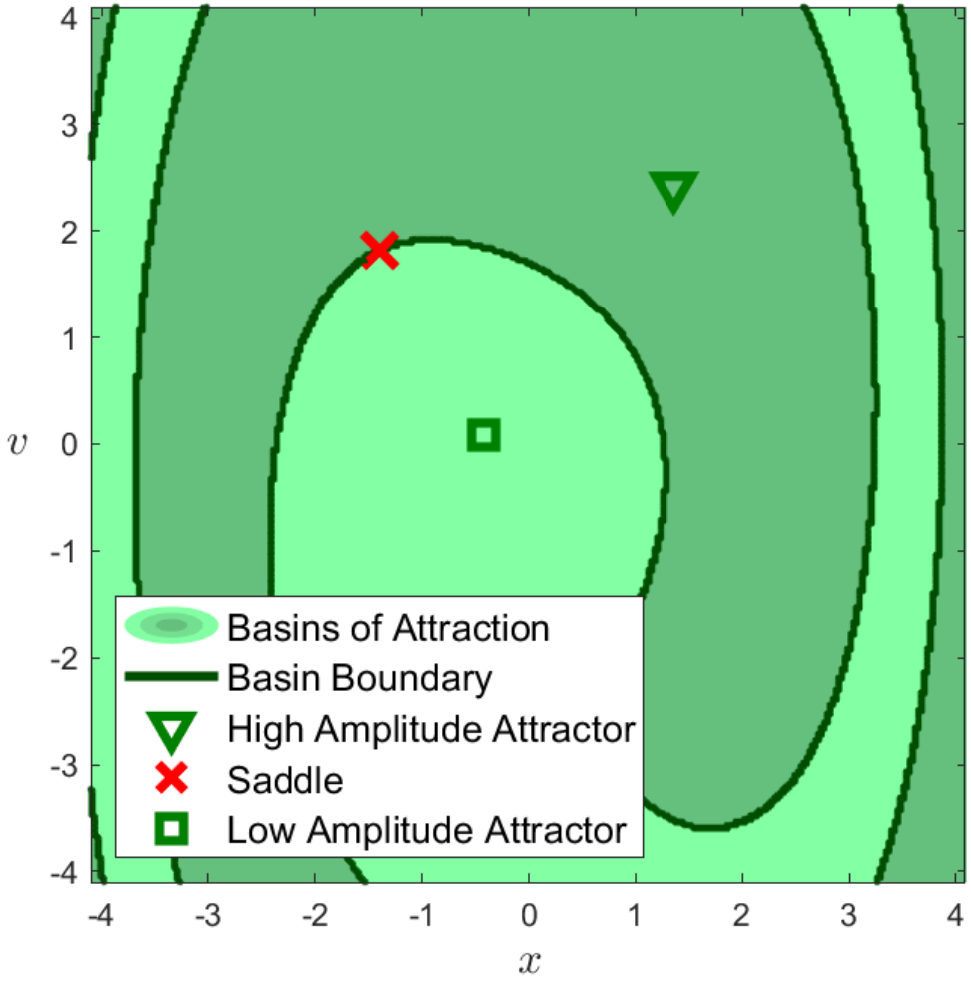


Figure 4.7: Poincaré Map of the Basins of Attraction at the frequency of $\omega = 1.4$.

The autonomous Hamiltonian system corresponding to this oscillator is given by

$$\begin{pmatrix} \dot{q}_1 \\ \dot{q}_2 \\ \dot{p}_1 \\ \dot{p}_2 \\ \dot{\theta} \end{pmatrix} = \begin{pmatrix} q_2 \\ -\beta\, {q_1}^3 - \alpha\, q_1 + p_2 - \delta_c\, q_2 + F\cos(\omega\theta) \\ p_2\ (3\,\beta\, {q_1}^2 + \alpha) \\ \delta_c\, p_2 - p_1 \\ 1 \end{pmatrix}, \tag{4.38}$$

where $(q_1, q_2, p_1, p_2, \theta) \in \mathbb{R}^4 \times \mathbb{S}^1_T$. The action functional for this system is:

$$\begin{aligned} S(\varphi, \theta) &= \frac{1}{2}\int_{\theta_0}^{\tau} p_2^2\, dt \\ &= \frac{1}{2}\int_{\theta_0}^{\tau} \left(\beta\,\varphi^3 + \alpha\,\varphi + \ddot{\varphi} + \delta_c\,\dot{\varphi} - F\cos(\omega\theta)\right)^2 dt. \end{aligned} \tag{4.39}$$

The Lagrangian manifold for this system is three dimensional, and the set W of initial conditions for the Hamiltonian paths is, respectively, two dimensional: $(\boldsymbol{q}_\gamma, \theta_0) \in \mathbb{S}^1_\gamma \times \mathbb{S}^1_T$.

The escape cost from the high amplitude attractor to the low amplitude attractor is displayed in Fig. 4.8 as a function of $(\zeta, \theta_0) \in \mathbb{S}^1_\gamma \times \mathbb{S}^1_T$. The variable ζ is the angle around the circle $\mathbb{S}^1_\gamma$. Fig. 4.8 is used to elucidate the complexity of the optimization problem. Discontinuities of the cost function form "cliffs". The cost function has multiple local minima located at the bottom of the cliffs. Furthermore, the cost function along the curves delineating the bottom of the cliffs is nearly constant, as one can see in Figs. 4.8, 4.9, and 4.10 – its variation along these curves is comparable to the numerical errors. Therefore, there are whole families of escape paths with values of cost functional matching up to numerical errors. Hence, MPEPs are non-unique at least up to the available numerical

accuracy.

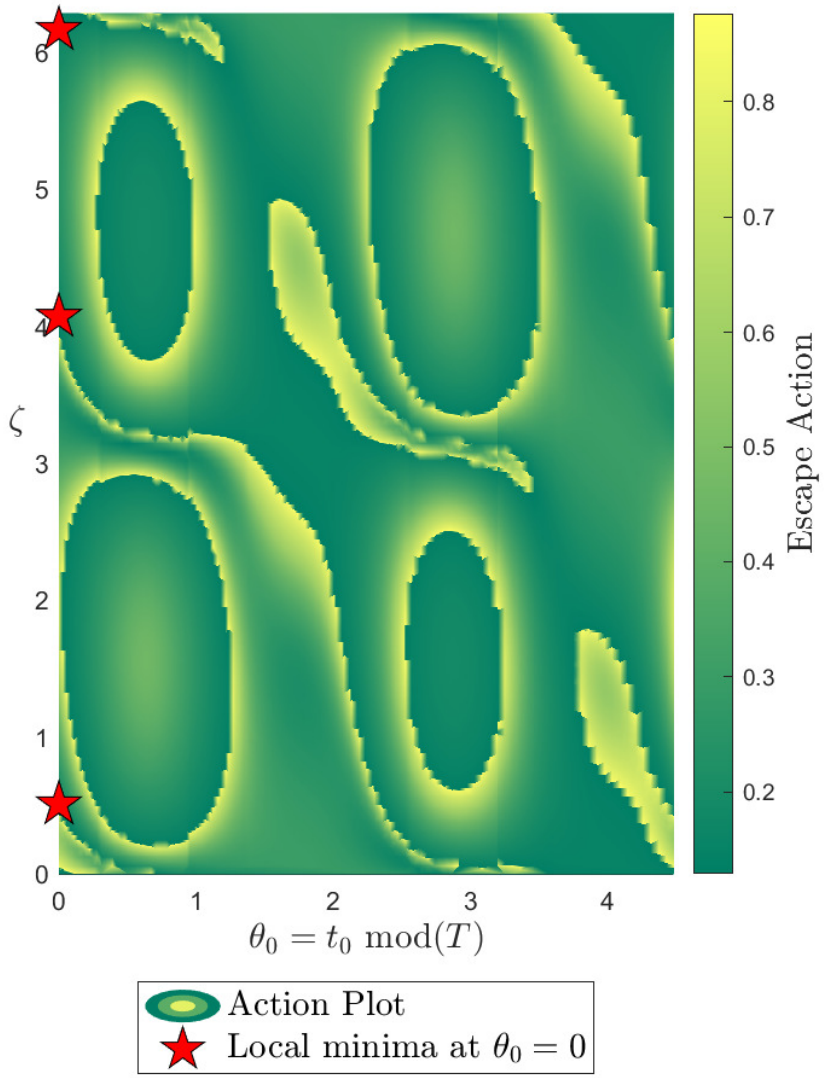


Figure 4.8: The cost (4.39) to escape from the high amplitude attractor as a function of ζ and the initial time $\theta_0 = t_0 \bmod T$. The variable ζ is the angle around a circle that completely surrounds the initial attractor at time θ_0. Three lowest local minima at $\theta_0 = 0$ are marked with red stars. They correspond to the minimum escape cost up to numerical errors.

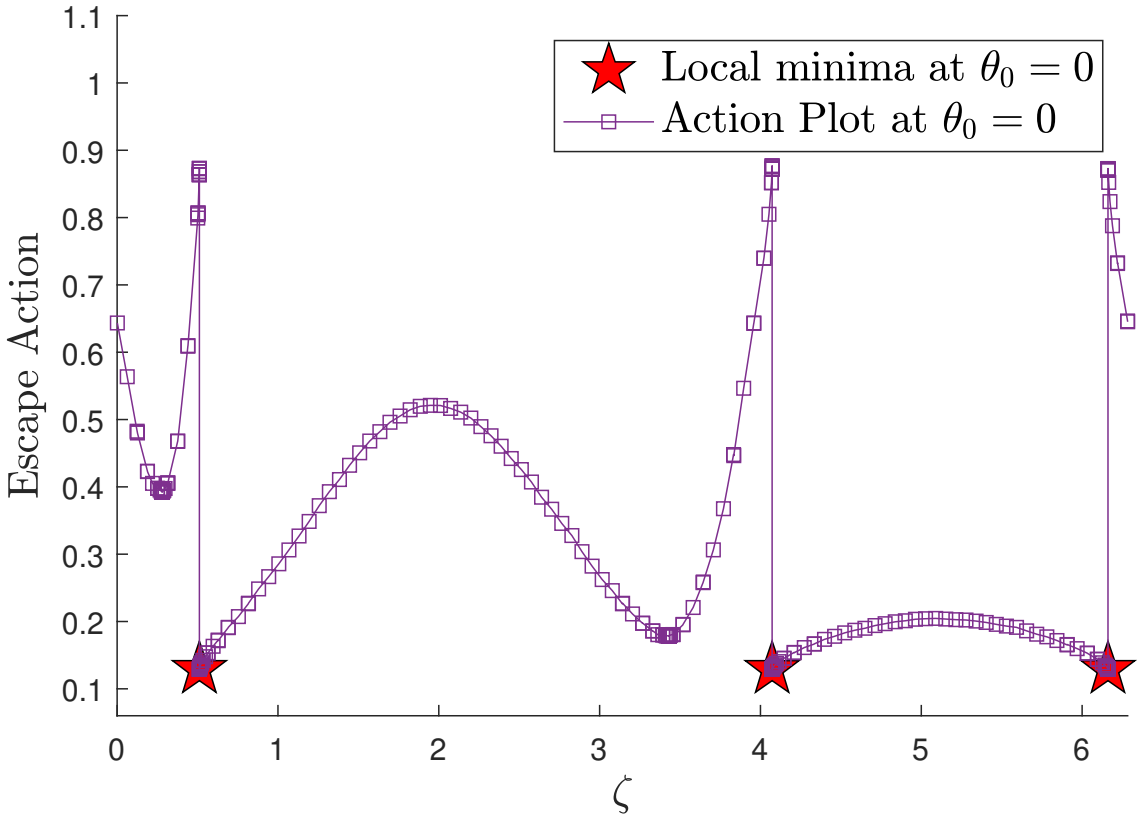


Figure 4.9: The cost to escape from the high amplitude attractor as a function of ζ for fixed phase $\theta_0 = 0$. The variable ζ is the angle around a circle that completely surrounds the initial attractor at θ_0. Note that the minimizers of the cost function arise immediately next to discontinuities.

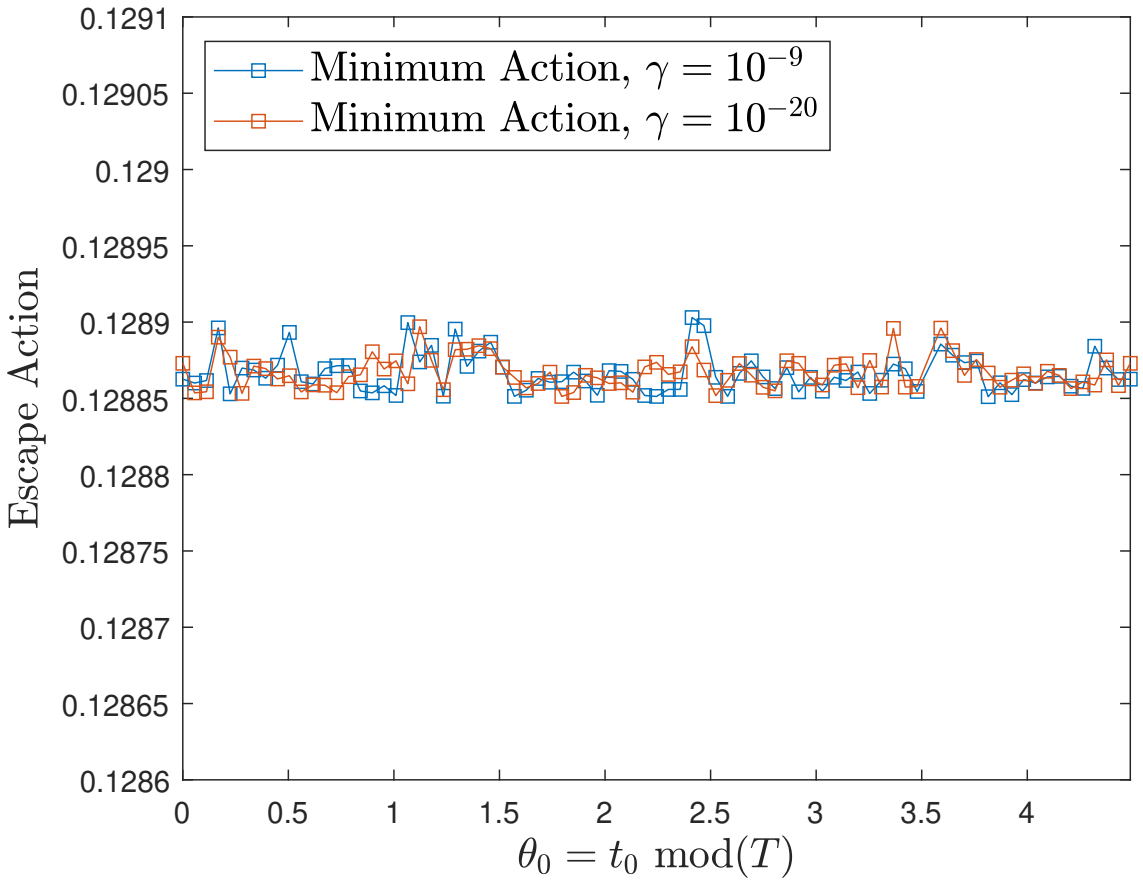


Figure 4.10: The escape action from the high amplitude attractor is minimized with respect to ζ at each initial phase θ_0. Notice that with some small error tolerance, the minimum action does not change with θ_0.

The Poincaré section of one of the MPEPs corresponding to the global minimum of the cost functional (4.39), specifically, the one corresponding to the initial condition marked with the bottom red star in Fig. 4.8, is shown in Fig. 4.11. Here and throughout the rest of the chapter, the Poincaré sections all correspond to the phase angle $\theta = 0$. The solid marks are the intersections of the MPEP with the plane $\theta = 0$. The MPEP goes through one revolution between each pair of consecutive points of its Poincaré section. The line segments connecting the marks are added only to indicate the ordering of these

intersections – they are *not* the projections of the MPEP segments onto the plane $\theta = 0$.

The Poincaré section of the MPEPs defined by the initial conditions corresponding to the three red stars in Fig. 4.8 are shown in Fig. 4.12. These MPEPs escape from the high amplitude attractor and approach the saddle cycle lying in the basin boundary of the high and low amplitude attractors. The Poincaré section of a MPEP going from the low amplitude attractor to the saddle cycle is shown in Fig. 4.13. Figures 4.12 and 4.13 suggest that *all MPEPs* have infinitely long escape from the attractors and an infinitely long approach to the saddle cycles lying in the basin boundaries.

For comparison, the Poincaré section of a trajectory of (4.3) going from the saddle cycle to the high amplitude attractor is visualized in Fig. 4.14. Note that both Poincaré sections of the MPEPs from the high amplitude attractor to the saddle cycle and of the trajectory going the other way around are clockwise.

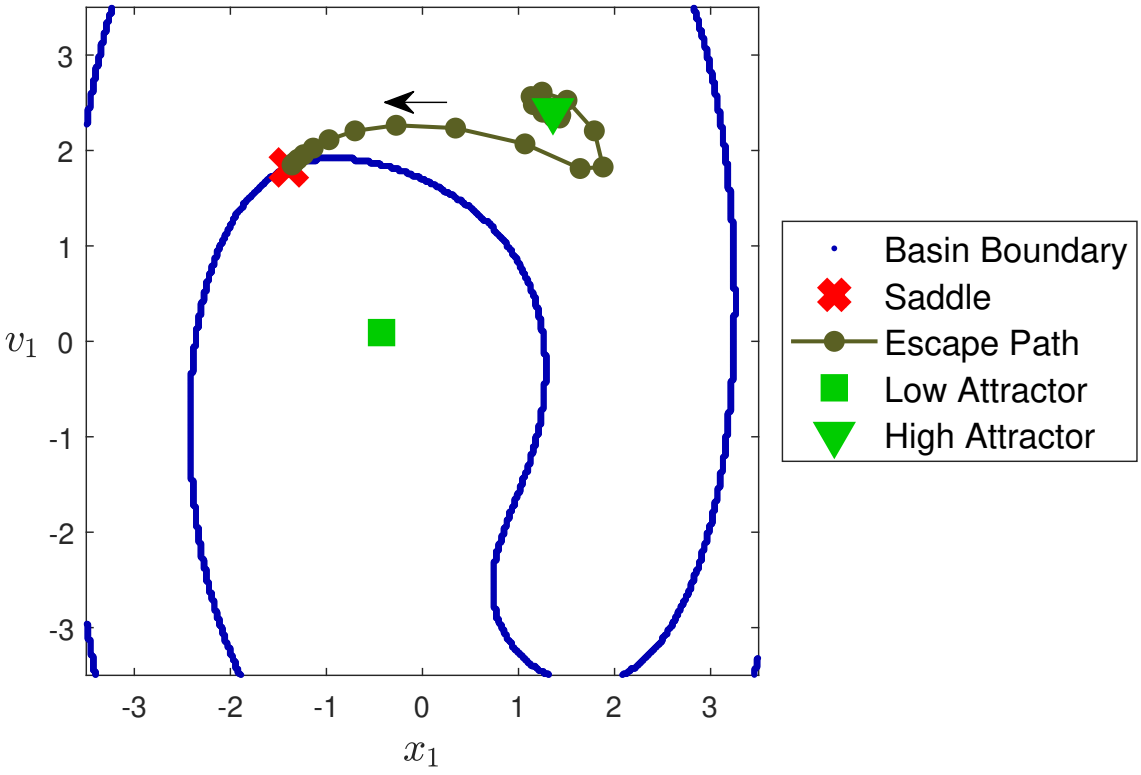


Figure 4.11: The Poincaré section of one MPEP that escapes the high amplitude attractor. This escape path begins at the attractor, rotates clockwise in the Poincaré section, and ends at the saddle.

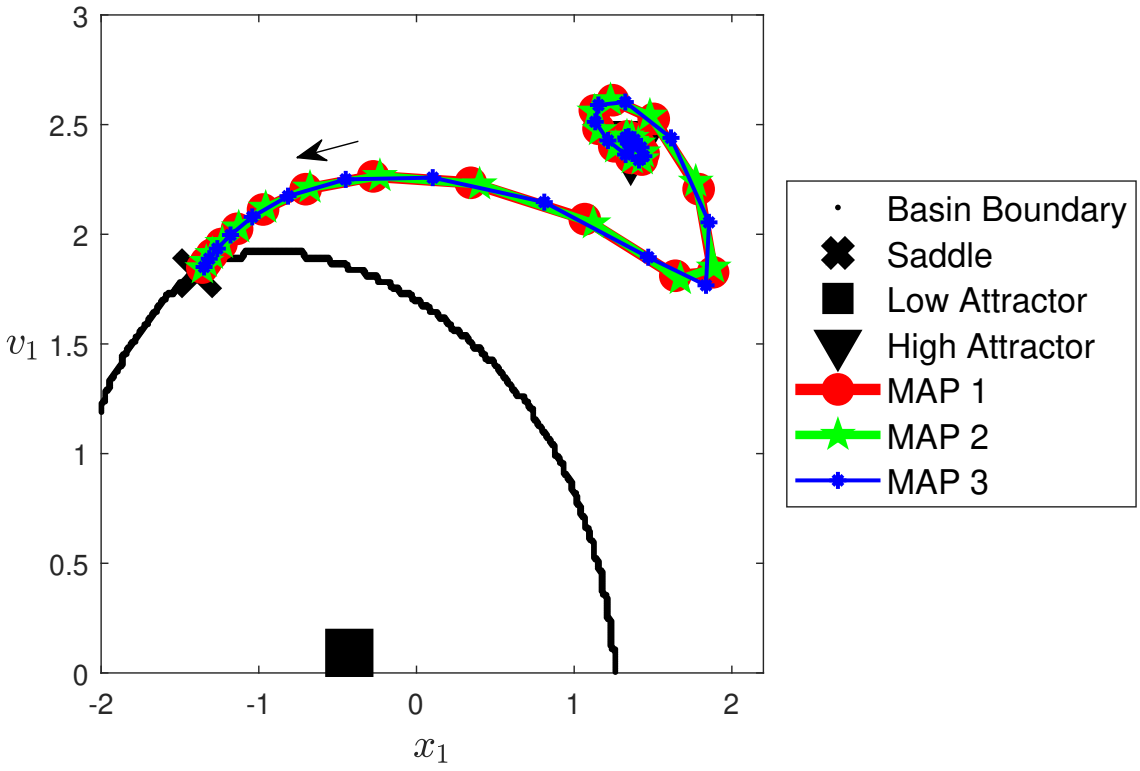


Figure 4.12: The Poincaré sections of three MPEPs, which escape the high amplitude attractor with $\theta_0 = 0$, are plotted on top of each other. Notice that these escape paths all overlap in phase space, but cross the Poincaré section at different times. These MPEPs and all other MPEPs of this system share the same quasipotential, share this same characteristic in phase space, and have the same probability of occurrence.

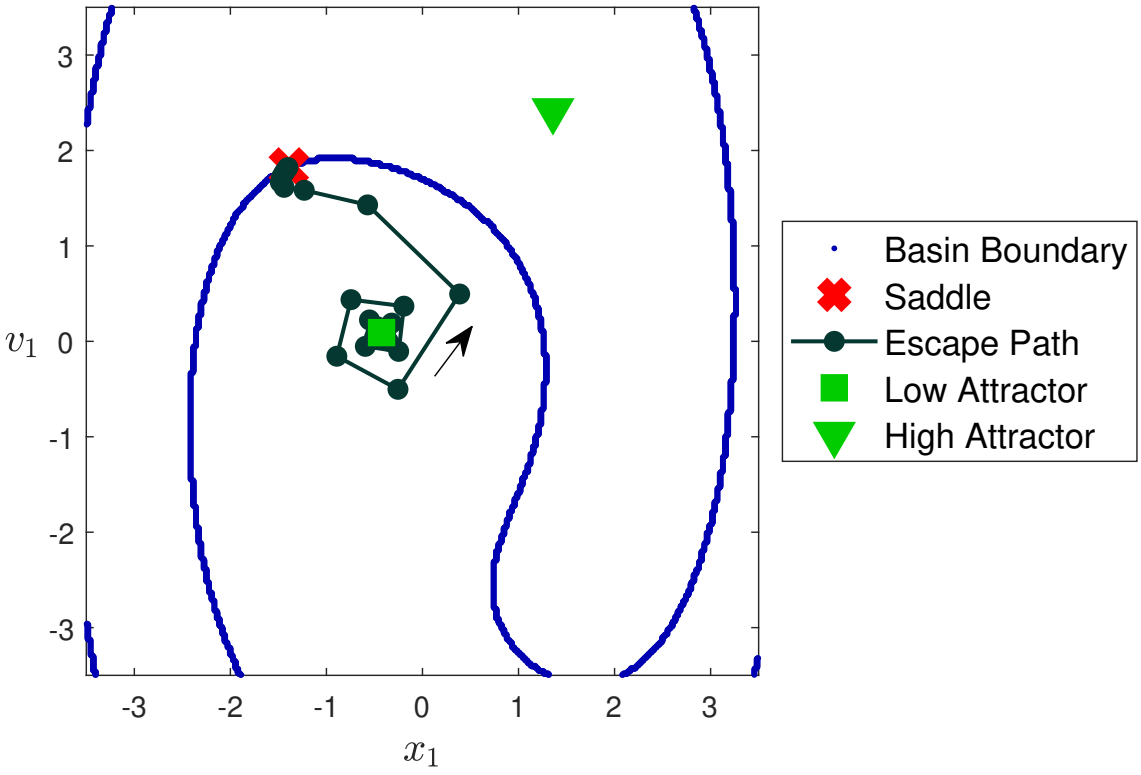


Figure 4.13: The Poincaré section of a MPEP that escapes the low amplitude attractor. This escape path begins at the attractor, rotates counter-clockwise in the Poincaré section, and ends at the saddle.

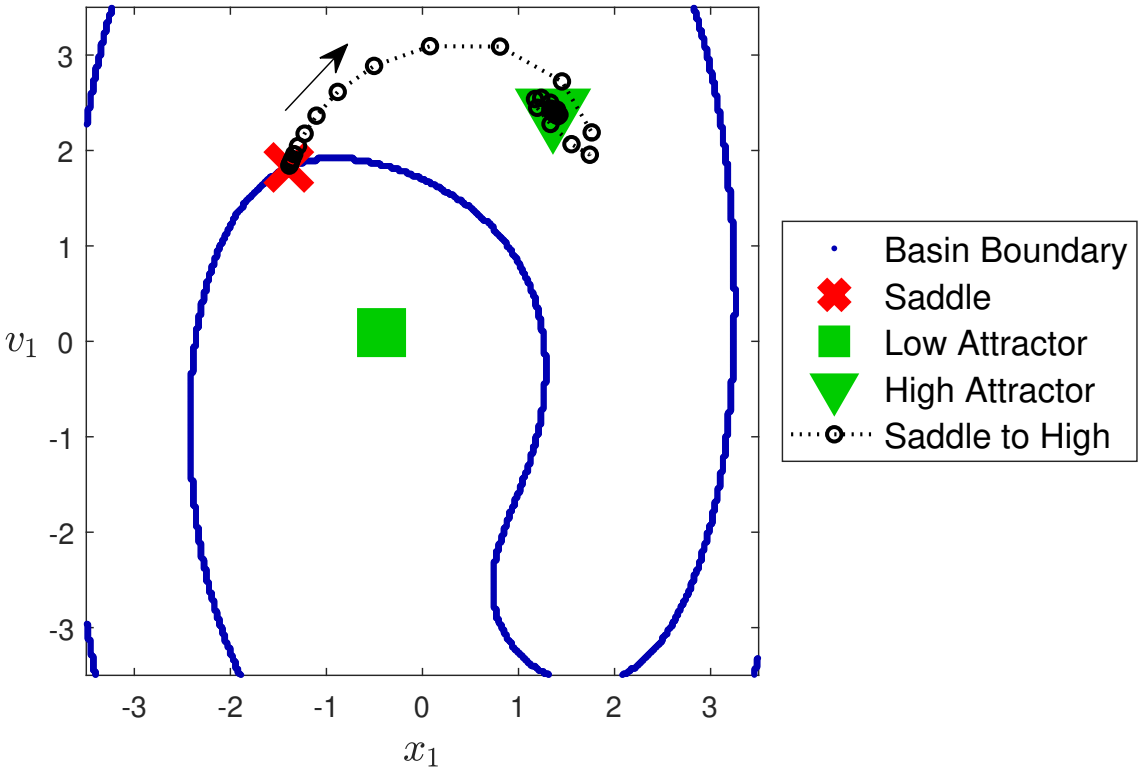


Figure 4.14: The Poincaré section of a trajectory of equation (3) for $N = 1$ that is drawn to the saddle cycle as $t \to -\infty$, is rotated clockwise in the Poincaré section, and is drawn to the high amplitude attractor as $t \to \infty$. The rotation of the trajectory in phase space matches the rotation of the escape path of that same basin; this is common in lower dimensional systems such as the bistable unforced Duffing oscillator shown in Fig. 4.4, and is noteworthy because one could naively expect the most probable escape paths to move along the space of a trajectory but in the opposite direction, and this is not the case.

Another way to visualize a MPEP is to plot the Euclidean norm of its $\mathbf{q}$-components versus time. The advantage of this technique is that it allows for visualization of escape paths in a system consisting of an arbitrary number of oscillators. The Euclidean norm of the MPEP (the solid line) corresponding to the bottom star in Fig. 4.8 is displayed in Fig.

4.15. This MPEP is concatenated with a heteroclinic trajectory (the dotted line) going from the saddle cycle to the low amplitude attractor. A similar visualization of a MPEP going from the low to the high amplitude attractor is presented in Fig. 4.16.

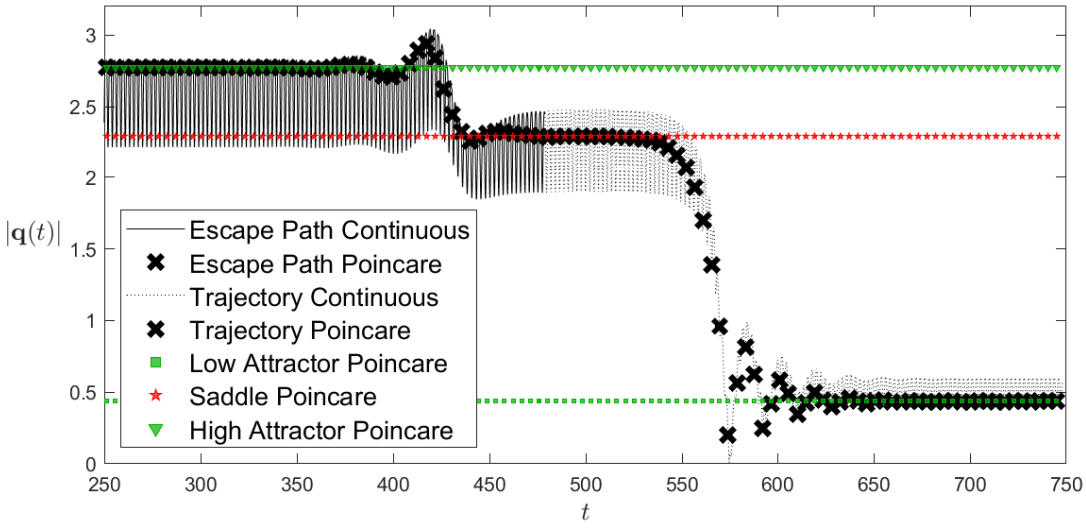


Figure 4.15: Euclidean norm, $|\boldsymbol{q}(t)| = \sqrt{\sum_i^{2N} q_i\left(t\right)^2}$, at all time steps of a MPEP that escapes the high amplitude attractor (solid) and of an unperturbed trajectory that descends from the saddle to the low amplitude attractor (dotted).

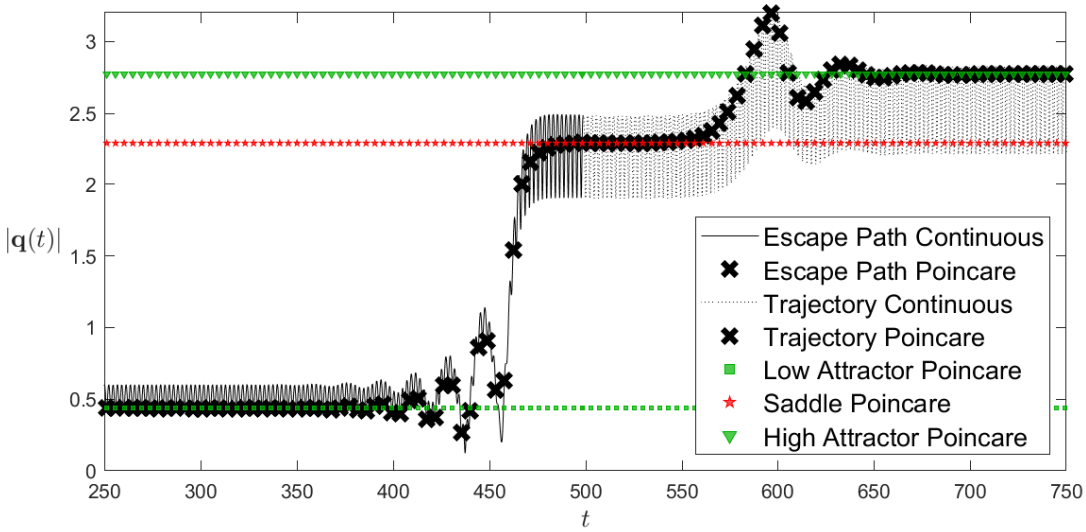


Figure 4.16: Euclidean norm of a MPEP that escapes the low amplitude attractor (solid) and of an unperturbed trajectory that ascends from the saddle to the high amplitude attractor (dotted).

The escape costs from the low to high amplitude attractor and vice versa; that is, the *quasipotential barriers*, are plotted as functions of the excitation frequency ω in Fig. 4.17. The quasipotential barrier to escape the low amplitude attractor approaches zero near the bifurcation point of the deterministic dynamics at $\omega \approx 1.27$. This agrees with experimental and numerical observations in literature [4, 5], wherein noise is more likely to induce a change in stable mode from the low to the high amplitude attractor near the jump up point of the hysteresis region. Similarly, the quasipotential barrier for the escape from the high to low amplitude attractor decays to zero as the frequency approaches the second bifurcation point $\omega = \omega_2 \approx 1.57$ at which the high amplitude attractor annihilates. Therefore, the quasipotential barrier serves as a quantifier of the escape difficulty from the basin of the corresponding attractor. At $\omega \approx 1.38$, the quasipotential barriers for both escapes are the same.

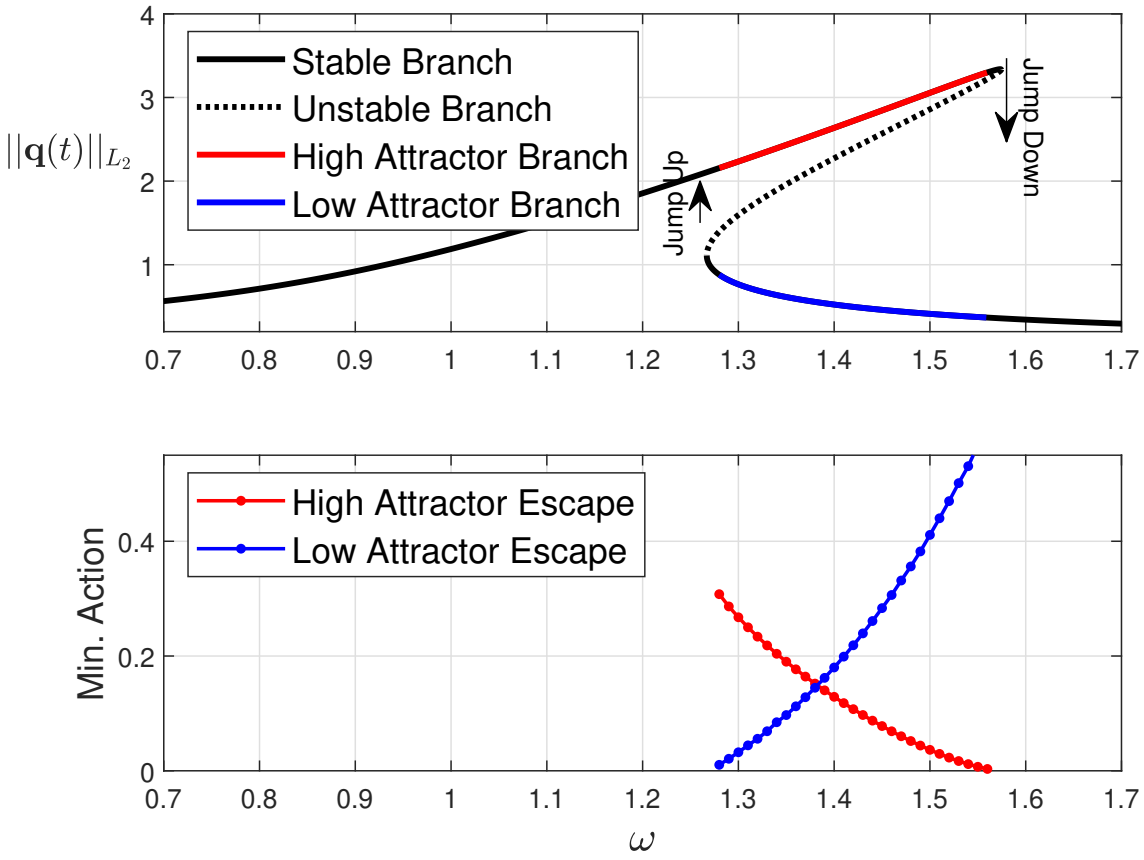


Figure 4.17: (top) L_2 norm of the frequency response of the forced Duffing oscillator with attractor branches highlighted in color in the hysteresis region. (bottom) The quasipotential as a function of excitation frequency; action values corresponding to escapes from the low and high amplitude attractors are shown in blue and red, respectively.

4.6 Two Coupled Oscillators

The case of two coupled Duffing oscillators is interesting because this is the simplest example that illuminates the effect of coupling and sheds the light on transition mechanisms in larger oscillator arrays. Its dimensionality is high enough to require online

detection of basin crossing by Hamiltonian paths, as outlined in Algorithm 3. The values of the parameters $\alpha = 1$, $\beta = 0.3$, $\delta = 0.1$, and $F(t) = 0.4\cos(\omega t)$ are the same as for the single oscillator in the previous section. The coupling coefficient is set to be $\nu = 0.01$.

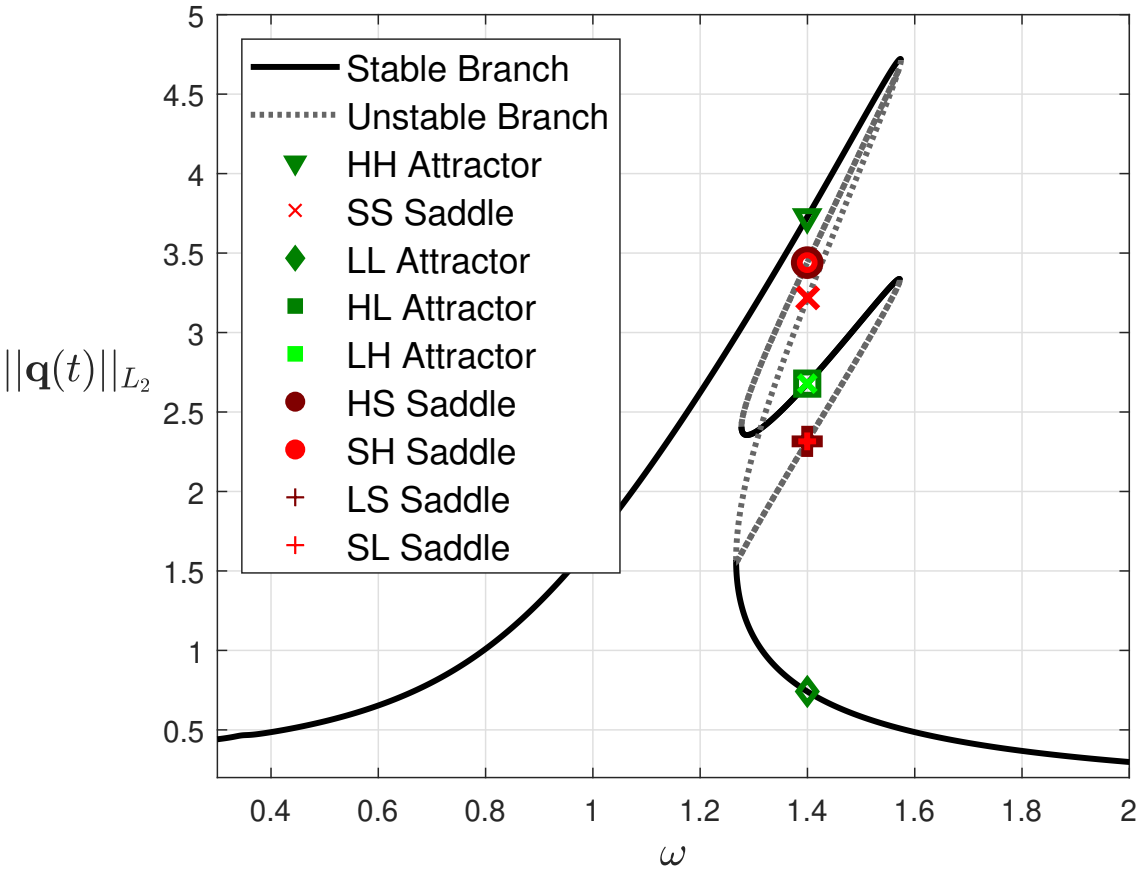


Figure 4.18: Frequency response of two coupled forced Duffing oscillators as a function of excitation frequency, ω. Attractor and saddle locations are shown at the frequency $\omega = 1.4$. This figure is generated by using the continuation package AUTO2007 [51].

With these parameter values, the deterministic system exhibits the frequency response depicted in Fig. 4.18. In the hysteresis region $\omega_1 < \omega < \omega_2$, where, $\omega_1 \approx 1.27$ and $\omega_2 \approx 1.57$, there are 9 solution branches. Solid and dashed curves represent stable and unstable periodic solutions, respectively. As described in Section 4.1, letters H

and L denote states of individual oscillators moving along a high amplitude orbit and a low amplitude orbit, respectively. The letter S encodes an intermediate state in which an oscillator is close to the saddle orbit of the single oscillator studied in Section 4.5. The highest (lowest) branch corresponds to the stable periodic solution in which both oscillators vibrate at high (low) amplitudes, the HH and LL attractors, respectively. Two overlapping stable branches (the HL and LH attractors) in the middle represent two symmetric stable periodic solutions where the first oscillator (oscillator 1) has high amplitude while the second oscillator (oscillator 2) has low amplitude and vice versa. The remaining branches correspond to unstable periodic solutions of the saddle type.

For $N = 2$ coupled oscillators, the optimization problem for the initial condition for the optimal Hamiltonian path is four-dimensional. That is, the optimal initial condition $(\boldsymbol{q}_\gamma^*, \theta_0^*)$ is sought on $\mathbb{S}^3_\gamma \times \mathbb{S}^1_T$, the direct product of the three dimensional sphere of radius γ embedded into $\mathbb{R}^4$ and the circle of circumference T. This optimization problem has been solved to find optimal escape paths from the attractors HH, LL, and HL. Due to symmetry, the solution for the escape from the LH attractor is found for the one for the HL attractor by switching the oscillators. A collection of optimal paths visualized in Figs. 4.19–4.24 corresponds to the excitation frequency $\omega = 1.4$.

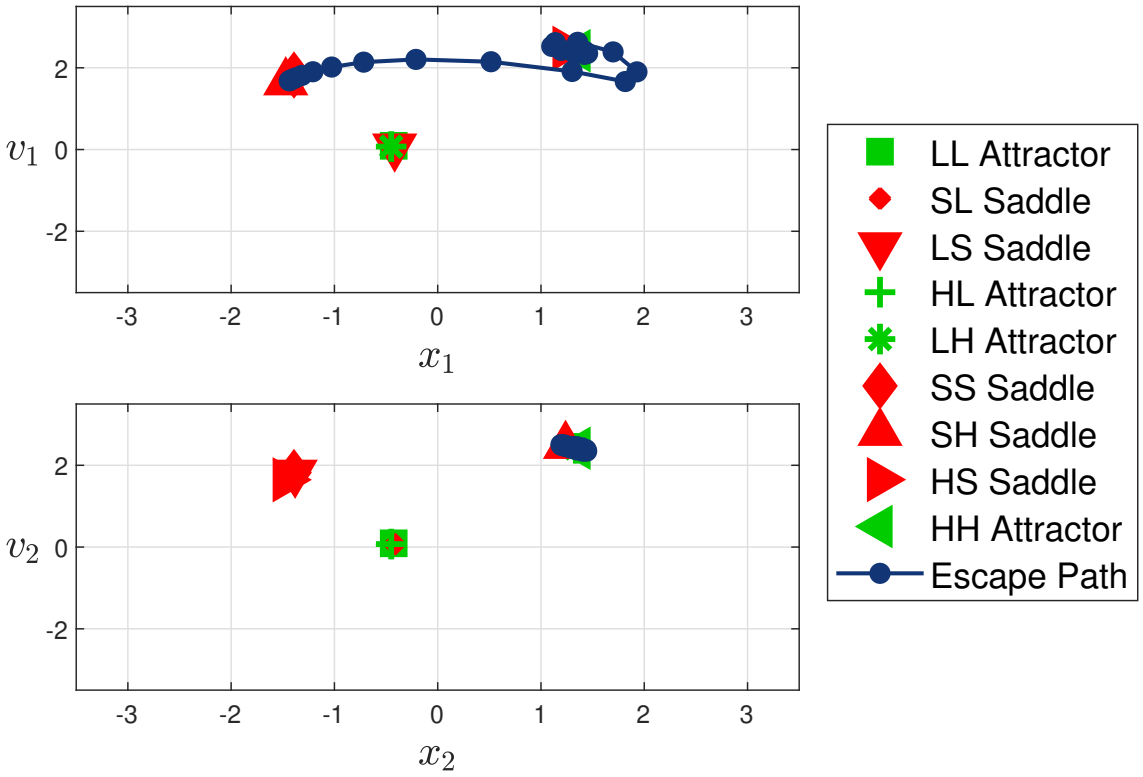


Figure 4.19: Hyperplanes of a Poincaré map of a MAP that escapes the HH attractor.

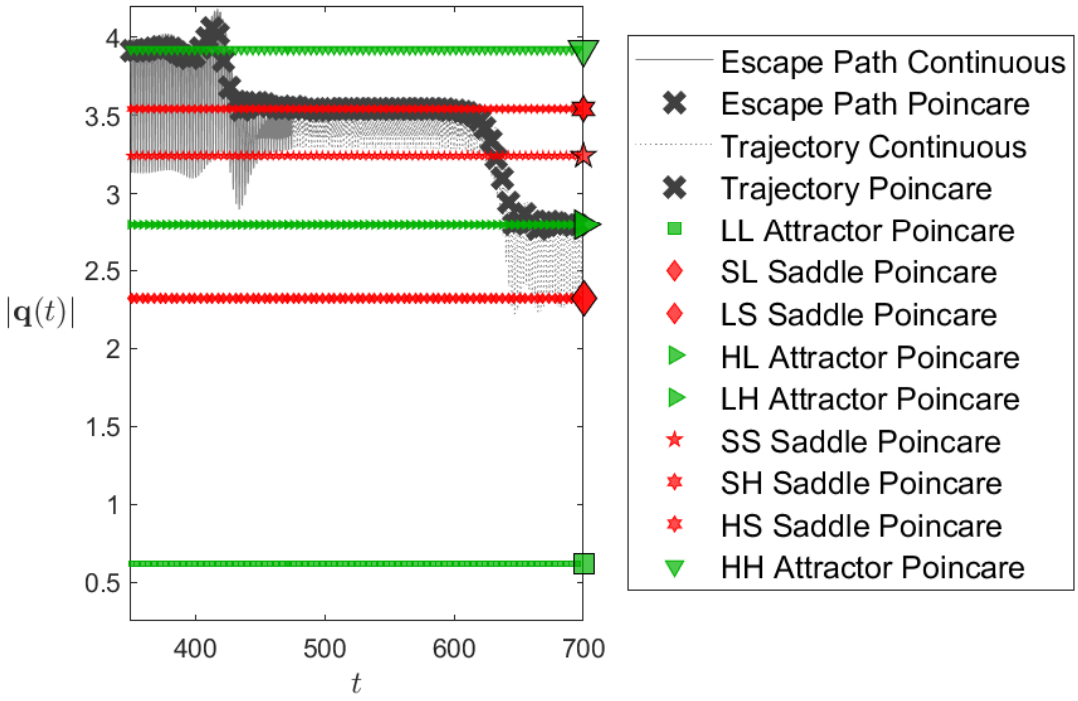


Figure 4.20: Euclidean norm of a MAP that escapes the HH attractor (solid) and of an unperturbed trajectory that from the SH saddle to the LH attractor (dotted).

The escape path from the HH attractor is displayed in Fig. 4.19 by plotting the Poincaré sections of its projections onto (x_1, v_1)- and (x_2, v_2)-planes. After escaping from the basin of the HH attractor along this path, the system arrives at the SH saddle. From there, it can descend either to the LH attractor or back to the HH attractor. Fig. 4.19 shows that the first oscillator follows a path similar to the escape path from the high to low amplitude attractor of a single oscillator in Fig. 4.12, while the motion of the second oscillator experiences a relatively small change throughout this transition. Note the closeness of the projections of the HH and LH attractors onto the (x_2, v_2)-plane. The L_2-norm of the $\boldsymbol{q}(t)$-component of the transition path from the HH to the LH attractor

via the SH saddle is plotted in Fig. 4.20.

The escape path from the LL attractor to the LS saddle lying on the boundary separating the LL and LH basins is shown in Figs. 4.21 and 4.22. The path from LL to SL can be found using symmetry.

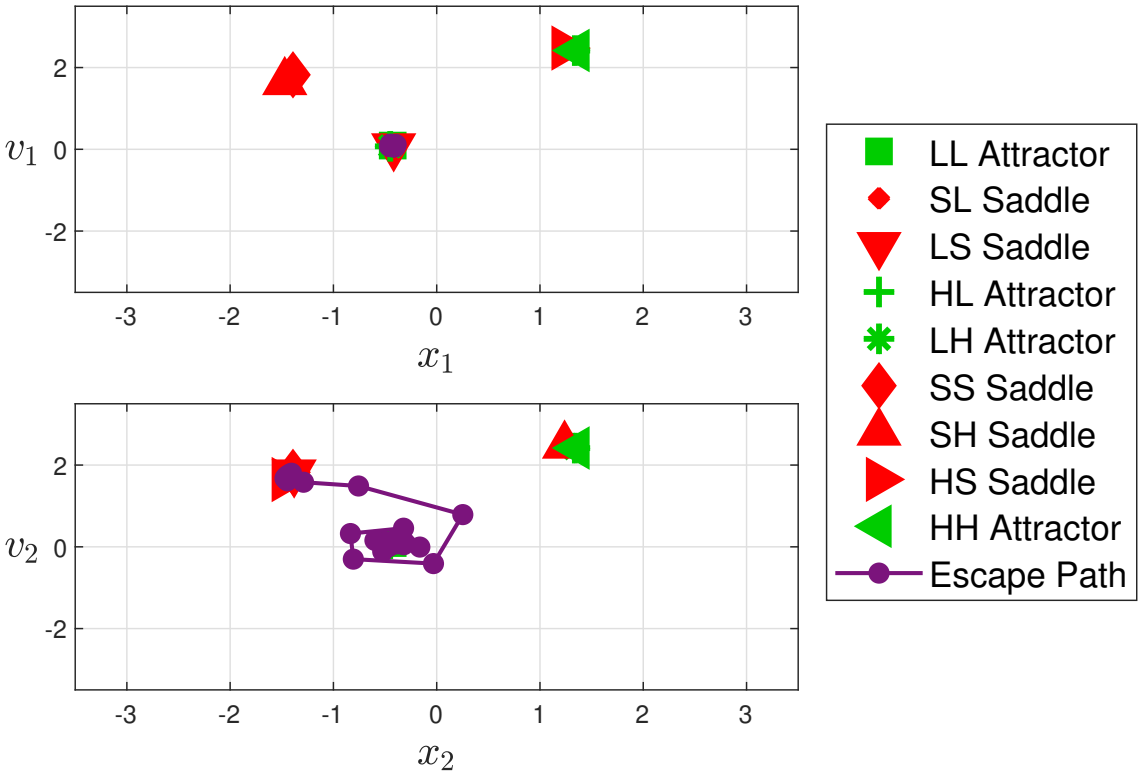


Figure 4.21: Hyperplanes of a Poincaré map of a MPEP that escapes the LL attractor.

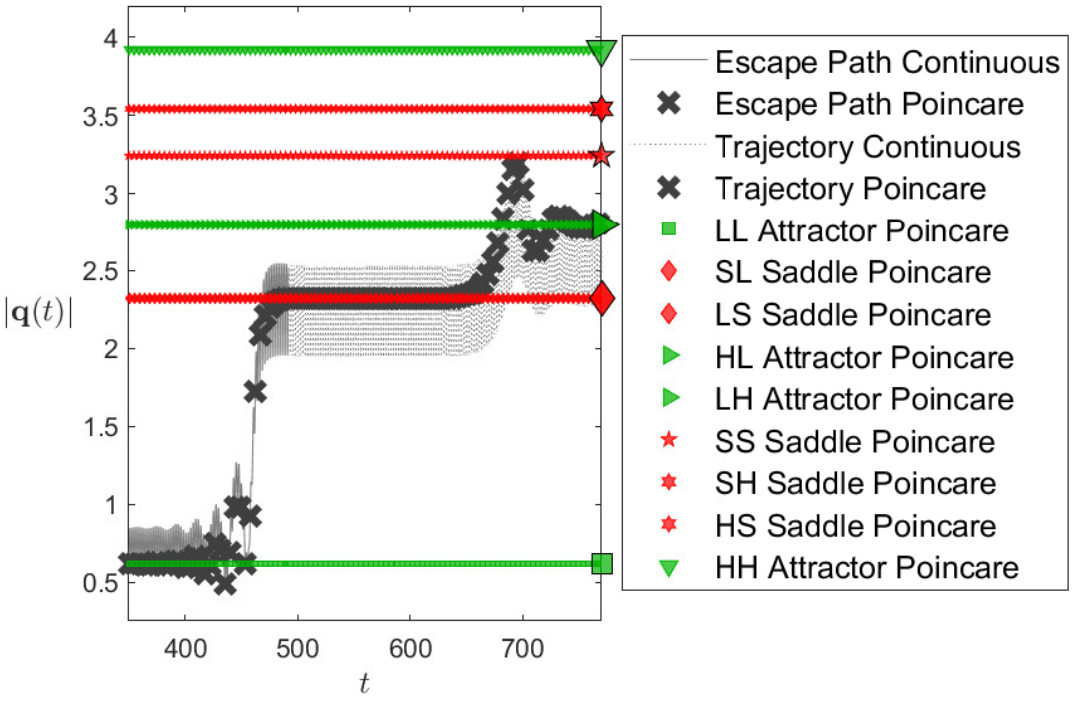


Figure 4.22: Euclidean norm of a MPEP that escapes the LL attractor (solid) and of an unperturbed trajectory that ascends from the LS saddle to the LH attractor (dotted).

The escape path from the HL attractor shown in Figs. 4.23 and 4.24 leads to the SL saddle. It has been found that the quasipotential of the SL saddle with respect to the HL attractor is lower than that of the HS saddle. This means that the escape from HL via HS is exponentially less likely than the escape via SL. Furthermore, no direct transition between the localized modes HL and LH has been found. This suggests that a transition between HL and LH can only be accomplished in the weak noise limit by visiting the LL or the HH mode in-between.

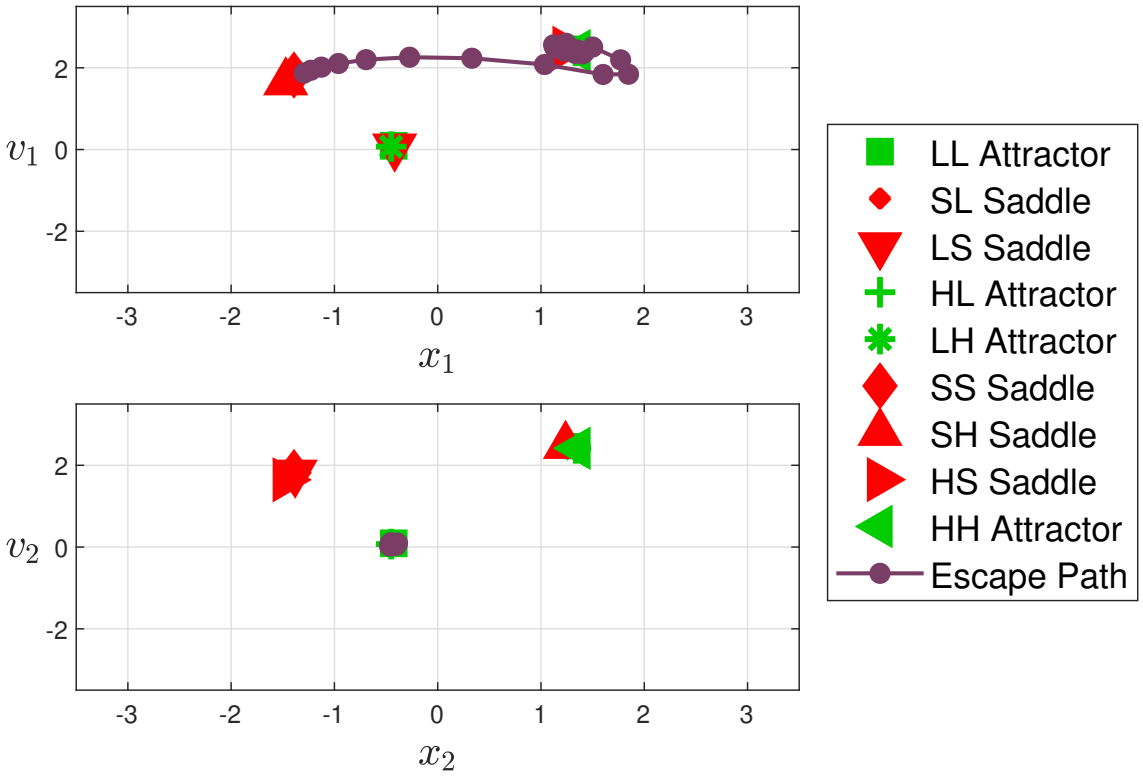


Figure 4.23: Hyperplanes of a Poincaré map of a MPEP that escapes the HL attractor.

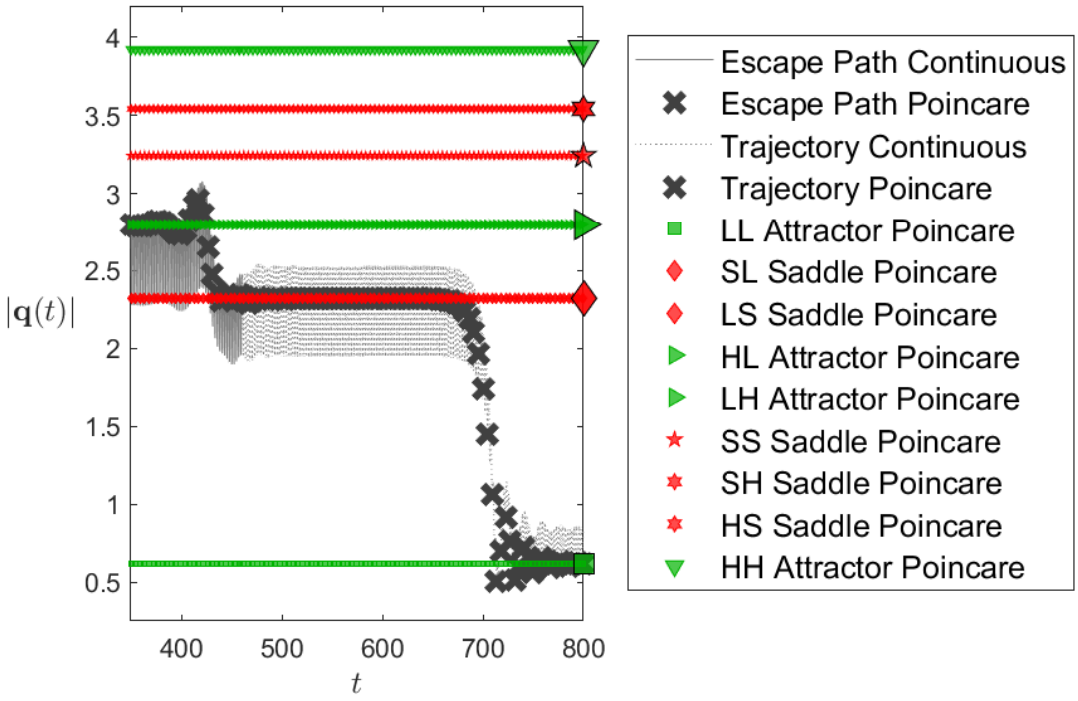


Figure 4.24: Euclidean norm of a MPEP that escapes the HL attractor (solid) and of an unperturbed trajectory that descends from the SL saddle to the LL attractor (dotted).

The MPEPs and the corresponding quasipotential barriers have been computed for a set of values of the excitation frequency ω spanning the hysteresis region $[\omega_1, \omega_2]$. The quasipotential barriers between each attractor and the corresponding lowest saddle are plotted as functions of ω in Fig. 4.25. It is instructive to compare this figure with the similar figure for the single oscillator (Fig. 4.17). It is evident that in the case of weak coupling considered here, the transitions to and from the localized modes in the two oscillator system are well approximated by the transitions in the single oscillator. The values of the quasipotential barriers for the escapes from the LL , HL , and HH attractors for $\omega = 1.4$ and the coupling coefficient $\nu = 0.01$ are given in Table 4.1.

Furthermore, the following observation can be made:

- Escape from the LL mode requires smaller minimum action near the jump up frequency and larger minimum action near the jump down frequency.

- Escape from the HH mode requires larger minimum action near the jump up frequency and goes to zero near the jump down frequency.

- The Λ-shape of the orange curve in Fig. 4.25 is caused by the fact that there are two possible escapes from each localized mode: to HH and to LL. For $\omega < 1.3825$, the required minimum action for the escape from HL is close but slightly less than the quasipotential barrier for the escape from LL. For $\omega > 1.3825$, the required minimum action for the escape from HL is close but slightly less than the quasipotential barrier for the escape from HH. This reduction in quasipotential is due to the coupling: the optimal escape paths for $N = 2$ are sought in a larger space than for $N = 1$. Hence the quasipotential barriers for $N = 2$ can only decrease in comparison to those for the single oscillator.

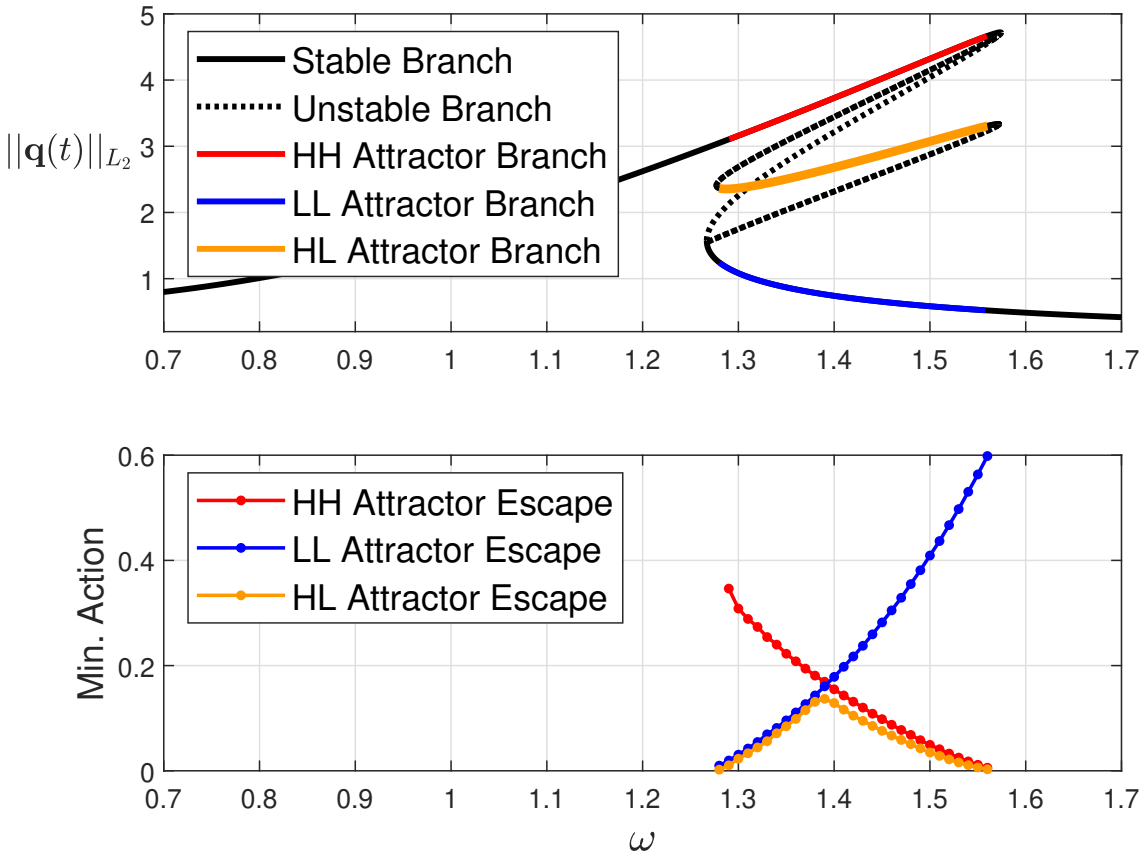


Figure 4.25: (top) L_2 norm of the frequency response of the $N = 2$ system with attractor branches highlighted in color in the hysteresis region. (bottom) The quasipotential as a function of excitation frequency; action values corresponding to escapes from the LL, HL, HH attractors are shown in blue, yellow, and red respectively.

4.7 Circular Oscillator Arrays

The application to circular three and five oscillator arrays presented in this section demonstrates the viability of the proposed methodology for high dimensional systems and sheds light of noise-induced transitions in larger circular arrays.

The systems under consideration are governed by SDE (4.1) with $N = 3$ and $N =$

5, i.e., with three and five oscillators, respectively. They are models of vibrations of blades of turbomachinery or cyclically arranged VEHs. The parameter values are the same as for $N = 2$. The frequency responses of $N = 3$ and $N = 5$ systems are shown, respectively, in Figs. 4.26 and 4.2. Provided that the coupling is weak, the number of stable vibrating modes grows dramatically with N. For $N = 3$, this number is at least 8, while for $N = 5$, it is at least 32, as mentioned in the introduction. Two of the stable modes correspond to all oscillators vibrating at low or high amplitudes, while the rest are localized modes in which some oscillators have high amplitudes while others have low amplitudes. Each localized mode has a number of equivalent localized modes obtained by circular shift and/or changing direction of rotation of oscillator indexing. Moreover, non-equivalent localized modes with equal numbers of high amplitude oscillators have very close time-averaged L_2-norms of their $\boldsymbol{q}$-components (4.4) resulting in indistinguishable points in the frequency-response diagram. The focus here is on escapes from localized modes for $N = 3$ and $N = 5$ in which one oscillator has high amplitude while the other $N - 1$ oscillators have low amplitudes. The escapes from these modes are the most relevant to noise influenced turbomachinery.

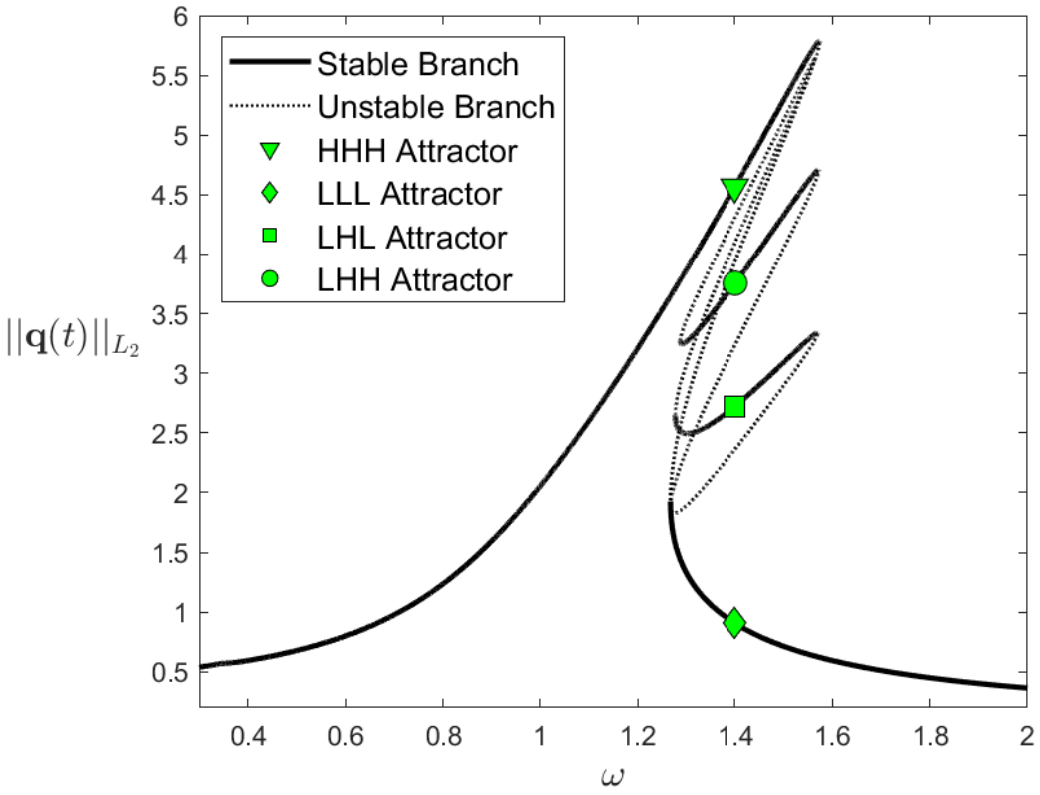


Figure 4.26: Frequency response of a circular array of $N = 3$ coupled forced Duffing oscillators as a function of excitation frequency, ω. Unique attractors are shown at the frequency $\omega = 1.4$. This figure is generated by using the continuation package AUTO2007 [51].

The most probable escape paths from the basins of the LHL and $LHLLL$ attractors of the $N = 3$ and $N = 5$ systems at frequency $\omega = 1.4$ and coupling coefficient $\nu = 0.01$ are shown in Figs. 4.27 and 4.28, respectively. After these escapes, the systems land onto the attractors in which all oscillators have low amplitudes. These escape paths are similar to the MPEP leaving the localized mode of the $N = 2$ system: the path of the oscillator originally at high amplitude resembles the escape path of the single oscillator, $(N = 1)$,

from its high attractor, while the motions of the other oscillators are only slightly affected. The quasipotential barriers for these escapes, U_{LHL} and U_{LHLLL} are slightly smaller than the quasipotential barrier U_H for the escape of the single oscillator from its H attractor basin. Furthermore, as expected, the following trend is observed:

$$U_H > U_{HL} > U_{LHL} \approx U_{LHLLL}.$$

The values of these barriers are given in Table 4.1.

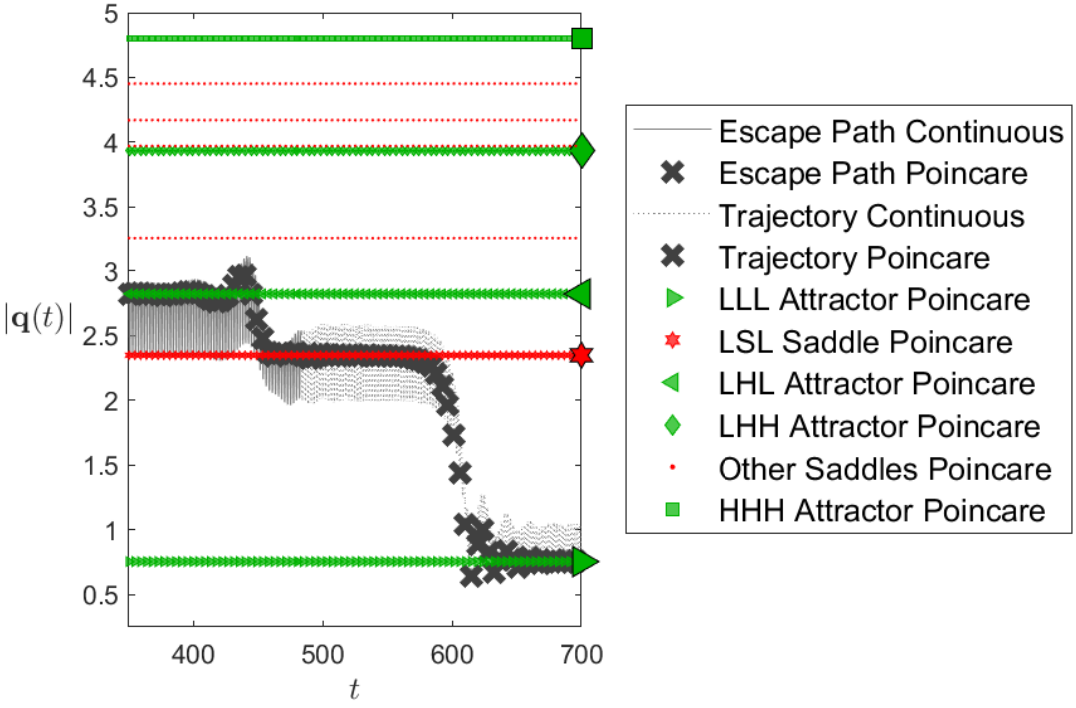


Figure 4.27: Euclidean norm of a MPEP that escapes the LHL attractor (solid) and of an unperturbed trajectory that descends from the LSL saddle to the LLL attractor (dotted).

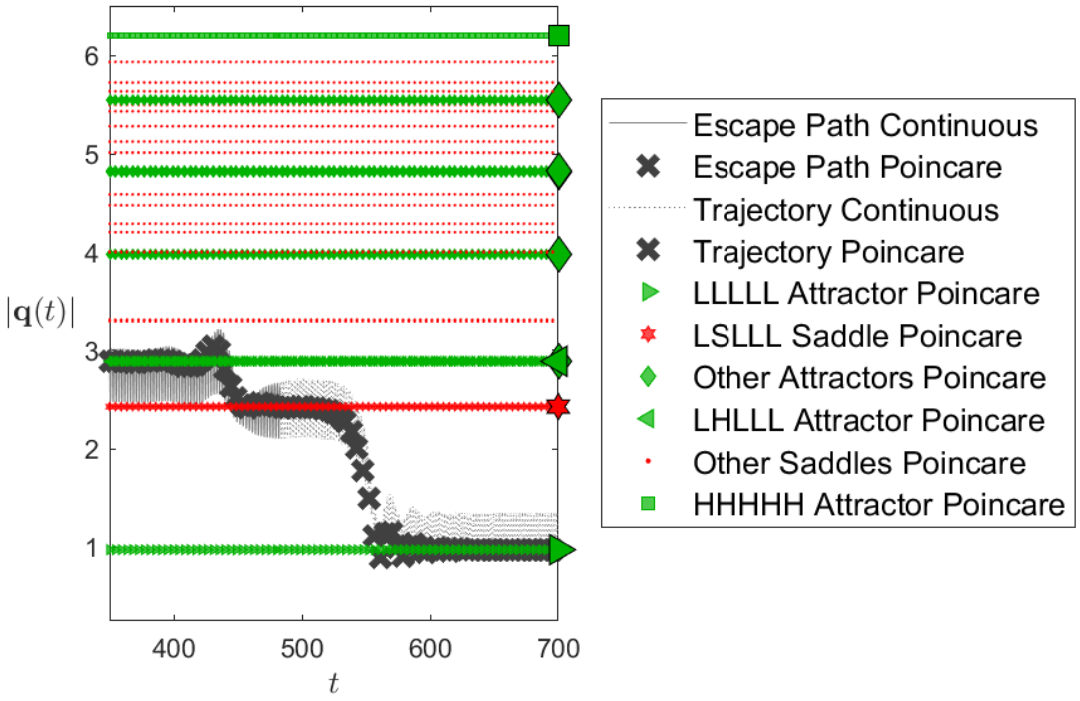


Figure 4.28: Euclidean norm of a MPEP that escapes the $LHLLL$ attractor (solid) and of an unperturbed trajectory that descends from the $LSLLL$ saddle to the $LLLLL$ attractor (dotted).

The dependence of the quasipotential barrier for the escape from the LHL attractor on the excitation frequency ω in the hysteresis region for three oscillators is very similar to the one for the escape from the HL attractor for $N = 2$ – compare Figs. 4.29 and 4.25.

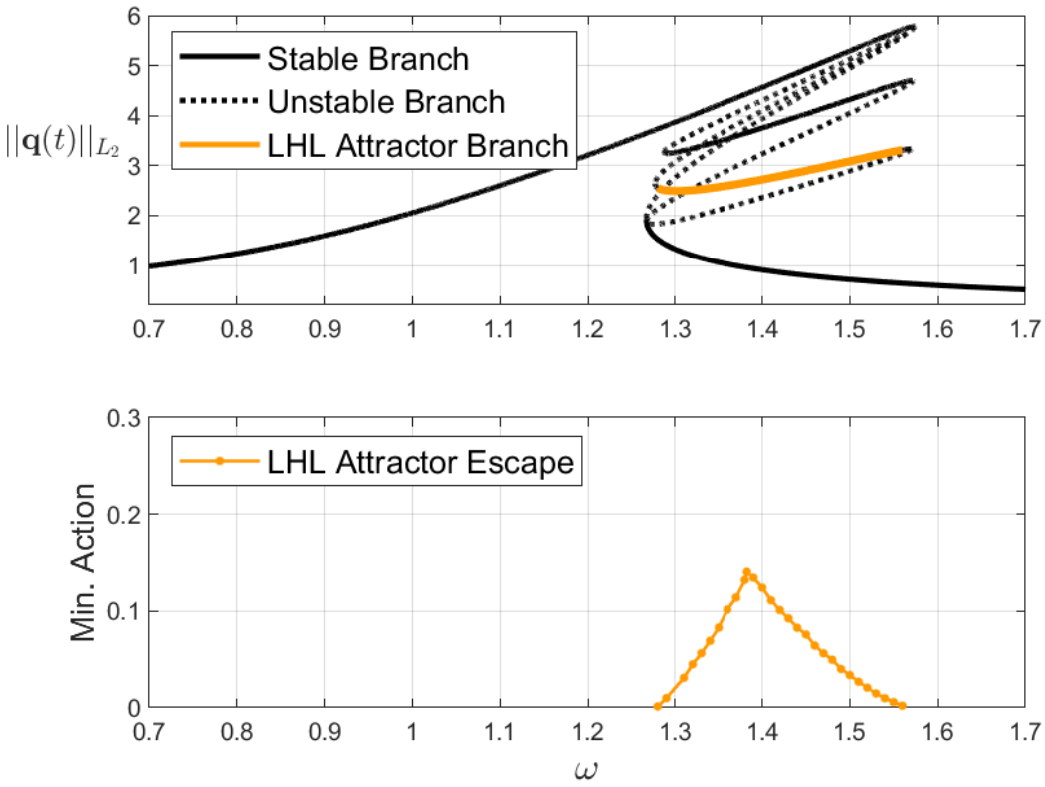


Figure 4.29: (top) The L_2-norm (4.4) of the frequency response of the $N = 3$ system with attractor branches highlighted in color in the hysteresis region. (bottom) The quasipotential corresponding to escapes from the LHL attractor as a function of excitation frequency.

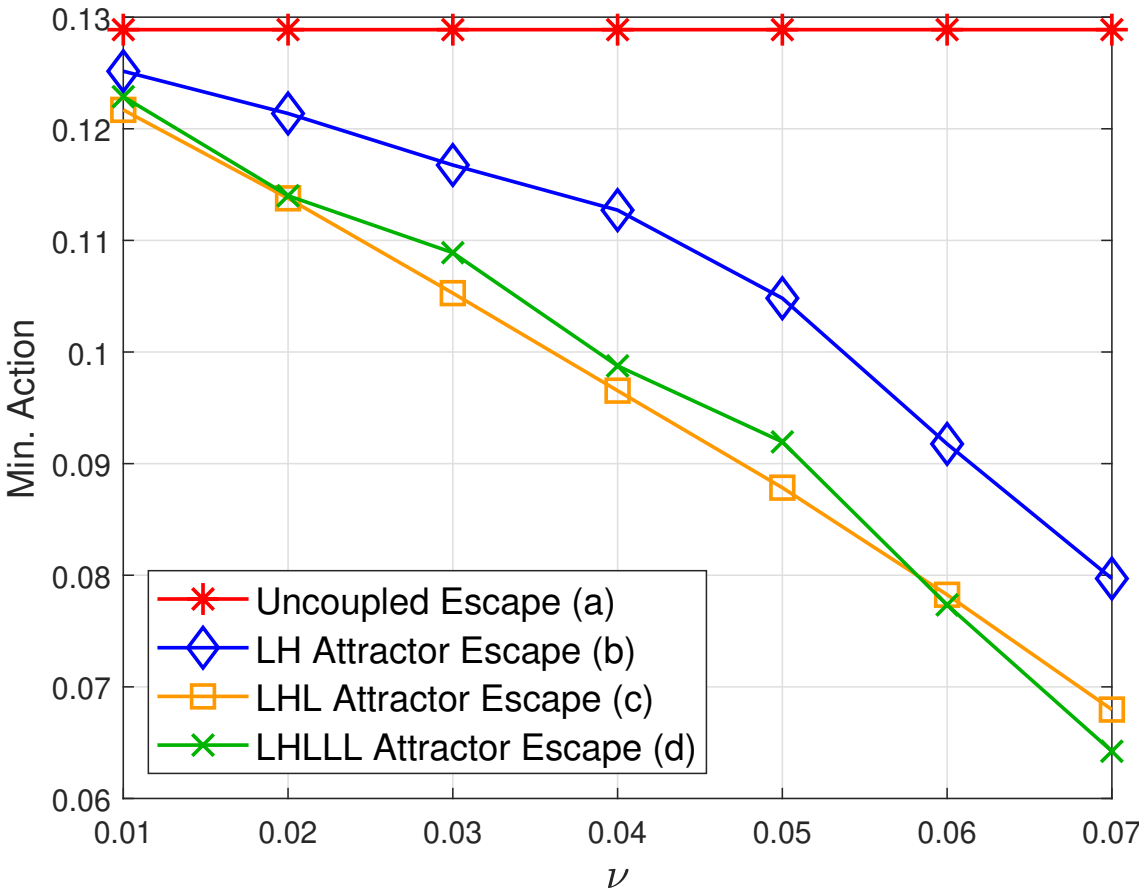


Figure 4.30: The quasipotential barriers as a function of coupling coefficient ν that correspond to the following: (a) escapes from the H attractor of the single Duffing oscillator, (b) escapes from the localized mode of the single side coupling ($N = 2$) system, and (c) and (d) escapes from the localized mode with a single oscillator being at high amplitude in circular arrays ($N = 3$) and ($N = 5$), respectively.

The dependencies of the quasipotential barriers U_H, U_{HL}, U_{LHL}, and U_{LHLLL} on the coupling coefficient ν at $\omega = 1.4$ are plotted in Fig. 4.30. The barriers for the circular array are lower than those for the single oscillator. In turn, the barriers for $N = 3$ and $N = 5$ are smaller than for $N = 2$. Moreover, the difference between these barriers grows with the increase in the inter-oscillator coupling coefficient ν. Note that the basins

Table 4.1: The quasipotential barriers for the escapes from localized modes at which only one oscillator has high amplitude for $N = 1, 2, 3, 5$ and from all modes for $N = 2$ at the frequency of $\omega = 1.4$ with $\nu = 0.01$.

N	Initial Attractor	Final Attractor	$S(\varphi)$
1	H	L	0.129
2	HL	LL	0.125
3	LHL	LLL	0.122
5	$LHLLL$	$LLLLL$	0.122
1	L	H	0.180
2	LL	HL	0.179
2	HH	HL	0.155

of localized modes get shallower as ν increases, and as a consequence, it is difficult to find most probable escape paths for $\nu > 0.07$. Furthermore, the localized modes become unstable as ν reaches 0.08; hence, localizations do not exist for strong inter-oscillator couplings, which is also noted in prior studies [8].

Fig. 4.30 indicates a very important fact that one can predict the qualitative behavior of most probable escape paths and the values of the quasipotential barriers for the escapes from the localized mode where only one oscillator has high amplitude by comparing the results obtained for $N = 3$ and $N = 5$. It is evident that the differences between the quasipotential barriers U_{LHL} and U_{LHLLL} at the feasible range of ν are small and comparable with numerical errors. Therefore, for weak inter-oscillator coupling facilitating the existence of response localizations, one can consider the barrier U_{LHL} as an adequate approximation for U_{LHLLL}. This suggests that the circular nature of coupling effectively limits the influence of the array on a given oscillator to the influence of its nearest neighbors. As a consequence, the quasipotential barriers for the escapes from the localized modes $LHL \ldots L$ for $N > 5$ are close to those for $N = 3$ and $N = 5$.

Meanwhile, the numerical solution is cheaper and more accurate for $N = 3$ than for larger N.

4.8 Discussion

The contribution of this work is two-fold.

1. A methodology for computing most probable escape paths and quasipotential barriers from periodic attractors of arrays of nonlinear oscillators with external periodic forcing and small white noise has been developed.

2. This methodology has been applied for a case study of a single monostable harmonically driven Duffing oscillator and circular arrays of $N = 2$, 3, and 5 oscillators.

The methodology relies on the large deviations theory [75] and Feynman's path integral theory [103], exploits Pontryagin's maximum principle for the optimal control problems [97] and the Floquet theory for linear ODEs with periodic coefficients [98], and uses the Action Plot Method [7] as a building block. This is the first work in which the Action Plot Method was promoted to high dimensions. The main challenges in this promotion are:

1. the arising optimization problem for the initial condition for the optimal Hamiltonian path has a discontinuous objective function with multiple local minima located at the bottoms of the "cliffs";

2. the final time for a Hamiltonian path is the time when it reaches the appropriate basin boundary, and basin boundaries need to be identified during the optimizations

for higher dimensional systems.

The first challenge has been tackled by the introduction of the Stochastic Unit Vectors (SUV) method, while the second one has been overcome via routine checks in which basin the state of the system is in and refinement of the escape time and location once a basin switch is detected. These techniques have shown themselves to be very robust and suitable for high dimensions.

The maximal number of coupled oscillators $N = 5$ considered in this work is not the limit for the proposed methodology. However, as the number of oscillators N increases, the runtime of the optimization routine grows as $O(N^2)$ (see Section 4.9). Furthermore, the behavior of the green curve in Fig. 4.30 corresponding to $N = 5$ suggests that the found MPEP and the corresponding quasipotential barrier become less accurate. Therefore, in order to apply the proposed methodology to larger oscillator arrays it is desirable to make the optimization method more efficient.

The case study of circular oscillator arrays has shown an important trend: the predictions for the most probable escape paths and quasipotential barriers for response localizations in large arrays can be made based on the results for small arrays. In particular, it has been shown that the results for $N = 5$ are well-approximated by those for $N = 3$. This is consistent with the results obtained by means of reduced-order modeling in Ref. [8].

The methodology described here has been generalized for different stiffness models. In this case study, $K(\boldsymbol{x}) = \alpha\boldsymbol{x} + \beta\boldsymbol{x}^3 + \nu D_N\boldsymbol{x}$, but $K(\boldsymbol{x})$ could contain higher order nonlinear stiffness terms, higher order coupling terms, or inhomogeneous

stiffness models, for example. In particular, quantifying quasipotentials for escapes from response localizations subjected to noise in systems that have both cubic stiffness and cubic coupling could be a direction of future work. It is known that such systems exhibit two types of response localizations known as s-t mode and p-mode, and that the two types of localized modes change stability depending on the cubic stiffness coefficient and the cubic coupling coefficient. Quantifying the quasipotential for those systems would reveal how robust the two types of localized modes are to noise.

The methodology developed in this work has an important limitation: the noise term in SDE (4.1) is the standard Brownian motion. On each fixed interval Δt, the increment of the Brownian motion is N-dimensional Gaussian random variable with mean 0 and the covariance matrix $I_{N\times N}$, which is unbounded. In physical experiments, only bounded amplitude and bounded bandwidth noise can be realized. Bounded amplitude can be modeled by truncating and renormalizing increments of Brownian motion. This will result in rendering all Hamiltonian paths for which $\|\boldsymbol{p_v}\|$ exceeds the maximum allowed noise magnitude infeasible, i.e., the corresponding action functional value is $+\infty$. Modifying the action functional for noise of limited bandwidth is less straightforward. The extension for more realistic noise models is left for the future.

4.9 Notes on Computational Cost and Nomenclature

This section includes an estimate of the computational cost of the optimization algorithm for finding MPEPs and three examples of parameter choices. The purpose of this section is to facilitate the reproduction of the results of this work by a third party

with reasonable expectations of computational cost.

To save computational cost, a $2N-1$-dimensional sphere of radius r_{A_0} embedded in $\mathbb{R}^{2N}$ that surrounds the initial attractor $\boldsymbol{A}_0(\theta)$ at a fixed moment of time, θ, is introduced. Here, $\boldsymbol{A}_0(\theta)$ describes the $(\boldsymbol{x}, \boldsymbol{v})$ coordinates of the attractor at time θ. The radius r_{A_0} is chosen so that if the path is still within the sphere, the path has not left the current basin yet. Similarly, r_{A_k}, is the radius of a $2N-1$-dimensional sphere that surrounds attractor A_k. When computing the domains of attraction online, it is assumed that if a trajectory enters the sphere surrounding attractor, A_k than the trajectory is in the basin of attractor k.

Table 4.2 is a list of the definitions of many of the parameters relevant to the oscillator arrays studied in this work and to the proposed numerical algorithms. Omitted parameters are of lesser influence on the computational cost. t_i is the cost of the initial sample set of the cost function space and t_o is time cost of the parallel optimizations using the SUV algorithm. The order of t_o is loosely bounded by an inequality that depends on the number of optimizations running because the algorithm is allowed to throw out high cost, poor improvement descents while preserving useful descents. This is a gradient free optimization scheme on a cost function with many local minima and discontinuities; finding a global minima is not guaranteed.

One could estimate the influence of the parameters on the computational costs as

$$
\begin{aligned}
O(t_i) &\approx O\left(\frac{d \times n_{init}}{c \times e \times dT}\right) \\
O\left(\frac{2d^2 \times n_m}{c \times e \times dT}\right) \leq O(t_o) &\leq O\left(\frac{2d^2 \times n_s \times i_m}{c \times e \times dT}\right) \\
t &\approx t_i + t_o
\end{aligned}
\tag{4.40}
$$

The principle idea of (4.40) is that the computational cost of evaluating the cost function scales with $d \times n/dT$ and that the cost of optimization using SUV scales the number of cost function evaluations by a multiple of $2d$. With efficient implementations at the excitation frequency of $\omega = 1.4$, finding a solution to the $N = 5$ system was a 10 dimensional optimization problem that took 80 minutes to solve with 24 processors in MATLAB. Additional examples are shown in Table 4.2. These results are produced on the Maryland Advanced Research and Computing Center's (MARCC) Intel Haswell dual socket, 12-core processors, 2.5GHz, 30MB cache, 128GB RAM node.

The important nomenclature in this work is summarized in Tables 4.3 and 4.4. This nomenclature is also described in the work as it is used.

Table 4.2: Parameters and computational cost

Description	Symbol	Example 1	Example 2	Example 3
Number of oscillators	N	1	2	5
Excitation Frequency	ω	1.4	1.4	1.4
Coupling Coefficient	ν	-	0.01	0.01
Dimension of cost function	d	2	4	10
Sphere Magnitude	γ	10^{-20}	10^{-15}	10^{-15}
Basin check interval	dT	π/ω	π/ω	π/ω
Min. Escape Radius	r_{A_0}	0.1	0.2	0.5
Min. Attracted Radius	r_{A_k}	0.1	0.2	0.5
Number of initial samples of cost space	n_{init}	300	1000	1000
Number of parallel optimizations	n_s	10	15	15
Initial SUV step size	σ	0.25	0.25	0.25
Maximum optimization iterations	i_m	35	35	35
Min. number of optimizations to keep	n_m	5	5	5
Number of available processors	c	24	24	24
Average Processor Efficiency (%)	e	54%	69%	81%
Real time cost (seconds)	t	160	365	4942

Table 4.3: Chapter 4 nomenclature

Symbol	Type	Description
N	$\mathbb{W}$	Number of oscillators
t	$\mathbb{R}$	Time
$\boldsymbol{x}$	$\mathbb{R}^N$	Beam tip displacements
$\boldsymbol{v}$	$\mathbb{R}^N$	Beam tip velocities
$\boldsymbol{f}(t)$	$\mathbb{R}^N$	Deterministic periodic external excitation
$\boldsymbol{\eta}(t)$	$\mathbb{R}^N$	Stochastic external excitation
δ_s	$\mathbb{R}$	Damping coefficient
α	$\mathbb{R}$	Linear stiffness coefficient
β	$\mathbb{R}$	Cubic stiffness coefficient
ν	$\mathbb{R}$	Linear coupling coefficient
ϵ	$\mathbb{R}$	Noise intensity/multiplier
ω	$\mathbb{R}$	Periodic excitation frequency
T	$\mathbb{R}$	Periodic excitation period
$\boldsymbol{D}_N$	$\mathbb{R}^{N\times N}$	Linear Coupling Matrix
$\boldsymbol{q}$	$\mathbb{R}^{2N}$	Vector of displacement states and velocity states $(\boldsymbol{x}, \boldsymbol{v})$
$\boldsymbol{p}$	$\mathbb{R}^{2N}$	Vector of costates $(\boldsymbol{p}_{\boldsymbol{x}}, \boldsymbol{p}_{\boldsymbol{v}})$
$\boldsymbol{u}$	$\mathbb{R}^N$	Vector of deterministic control inputs
$\|\|\boldsymbol{q}\|\|_{L_2}$	$\mathbb{R}$	L_2-like norm
$\boldsymbol{b}(\boldsymbol{q})$	$\mathbb{R}^{2N}$	Drift vector
$\boldsymbol{Q}(\boldsymbol{q})$	$\mathbb{R}^{2N\times 2N}$	Diffusion matrix
$S_\tau(\boldsymbol{\varphi})$	$\mathbb{R}$	Action functional
$\boldsymbol{\varphi}$	$\mathbb{R}^{2N}$	Candidate escape path
τ	$\mathbb{R}$	Travel time, final time boundary of φ, escape time

Table 4.4: Chapter 4 nomenclature (continued)

$\mathcal{A}$	char	Attractor
B	char	Basin of attraction
∂B	char	Basin boundary
D	char	Domain
∂D	char	Domain boundary
$\mathbb{S}_T$	$\mathbb{S}^1$	A circle with circumference T
$\boldsymbol{K}(\boldsymbol{x})$	$\mathbb{R}^N$	Generalized restoring force function of $\boldsymbol{x}$
θ	$\mathbb{S}_T$	A periodic time coordinate
$\hat{\boldsymbol{q}}$	$\mathbb{R}^{2N} \times \mathbb{S}_T$	Augmented state vector for autonomous system, $(\boldsymbol{x}, \boldsymbol{v}, \theta)$
$\hat{\boldsymbol{p}}$	$\mathbb{R}^{2N+1}$	Augmented costate vector for autonomous system, $(\boldsymbol{p_x}, \boldsymbol{p_v}, p_\theta)$
n_a	$\mathbb{W}$	Number of attractors
k	$\{0, 1, ..., n_a\}$	Index of n_a attractors
$k = 0$		Index of the initial attractor
A_k	char	The attractor with index k
B_k	char	Basin of attraction of A_k
∂B_k	char	Basin boundary of A_k
∂B_{kl}	char	Intersection of Basin boundary of A_k and A_l
$\boldsymbol{A}_k(\theta)$	$\mathbb{R}^{2N}$	The location in coordinates $(\boldsymbol{x}(\theta), \boldsymbol{v}(\theta))$ of attractor with index k at time θ
$\boldsymbol{A}_0$	$\mathbb{R}^{2N}$	The location of the initial attractor
$\hat{\boldsymbol{A}}_k$	$\mathbb{R}^{2N} \times \mathbb{S}_T$	The location in coordinates $(\boldsymbol{x}, \boldsymbol{v}, \theta)$ of attractor with index k
$\bar{\boldsymbol{A}}_k$	$\mathbb{R}^{4N+1} \times \mathbb{S}_T$	Augmented $\bar{\boldsymbol{A}}_k$ in Hamiltonian coordinates, $(\boldsymbol{x}, \boldsymbol{v}, \theta, \boldsymbol{0}, \boldsymbol{0}, 0)$
$\tilde{\boldsymbol{A}}_k(\theta)$	$\mathbb{R}^{4N}$	Augmented $\boldsymbol{A}_k(\theta)$ in Hamiltonian coords. w/o explicit θ and p_θ, $(\boldsymbol{x}(\theta), \boldsymbol{v}(\theta), \boldsymbol{0}, \boldsymbol{0})$
J	$\mathbb{R}^{4N \times 4N}$	Jacobian of Hamiltonian system
$\boldsymbol{J_K}$	$\mathbb{R}^{N \times N}$	Jacobian of vector field $\boldsymbol{K}(\boldsymbol{x})$
$\boldsymbol{z}$	$\mathbb{R}^{4N}$	Coordinates of linearized system
$\boldsymbol{\Psi}(t)$	$\mathbb{R}^{4N \times 4N}$	Fundamental solution matrix
$\boldsymbol{\Phi}(t)^s_{\theta_0}$	$\mathbb{R}^{4N \times 2N}$	Stable eigenvectors of Monodromy matrix
$\boldsymbol{\Phi}(t)^u_{\theta_0}$	$\mathbb{R}^{4N \times 2N}$	Untable eigenvectors of Monodromy matrix
γ	$\mathbb{R}$	Small radius of a sphere that surrounds the initial attractor at fixed time
$\mathbb{S}^{2N-1}_\gamma$	$\mathbb{S}^{2N-1}$	A 2N sphere with radius γ
$\boldsymbol{q}_\gamma$	$\mathbb{S}^{2N-1}_\gamma$	A value of $\boldsymbol{q}$ with euclidean norm equal to γ
dT	$\mathbb{R}$	The amount of time to numerically map the path forward in time prior to checking if the path has entered a new basin of attraction
L	char	"Low amplitude"
H	char	"High amplitude"

Chapter 5: Influence of Noise on a Rotating Cantilever Beam

5.1 Introduction

An experimental arrangement and a set of experiments is developed to generate empirical evidence for the effect of noise on a rotating macro-scale cantilever beam. The experiment is a controlled representation of a blade of rotating machinery. Due to nonlinear restoring forces on the cantilever beam, the response demonstrates characteristic nonlinear phenomena, including multiple stability and hysteresis. In this chapter, it is shown that random perturbations can be used to create a transition between a high amplitude response and a low amplitude response of the cantilever beam. Moreover, techniques are explored for quantifying the expected escape time, quantifying the probability of escape, and modeling the stochastic behavior of the mechanical system. The contents of this chapter were presented at the 2022 European Solid Mechanics Conference in Galway, Ireland [106].

A thorough literature review of the problem of interest and related work is available in Chapter 1. The methodology presented in Chapter 4 is used to provide some simulation results in part of this chapter. The rest of this chapter is organized as follows. The experiment is presented in Section 5.2. The nonlinear phenomena of interest in the frequency response is discussed in Section 5.3. In Section 5.4, a system model and

system identification approach are proposed. Results obtained via experiment trials and simulations are presented in Sections 5.5 and 5.6, respectively. The chapter is concluded with a discussion in Section 5.7.

5.2 Experimental Arrangement and Experiments

The experiment is designed to operate autonomously to reduce human error and allow for the generation of a high quantity of long duration noise trials with limited supervision. The setup consists of an excitation system, a data acquisition system, a test piece, and mechanical supports that interact as shown in Fig. 5.1.

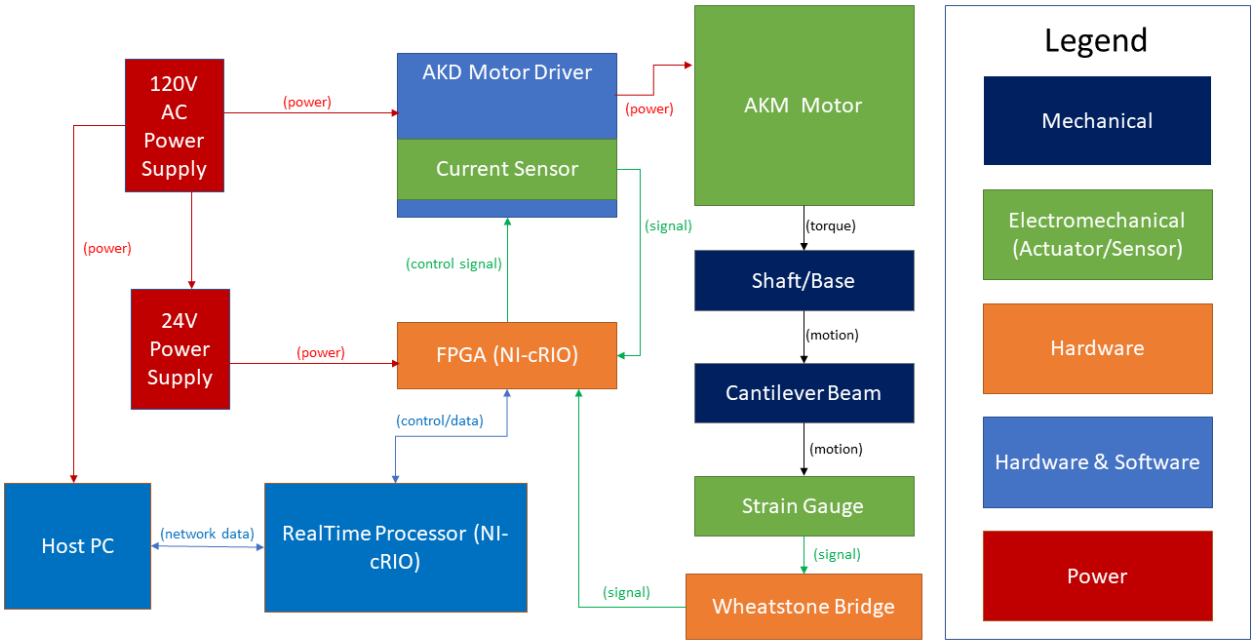


Figure 5.1: Schematic of the data and energy flow in the experiment.

An image of the prototype is shown in Fig. 5.2. The excitation system consists of a feedback controller, a motor driver, and a motor. The control is provided via the

combined efforts of a real-time controller and a FPGA module in an NI-cRIO9074 and a host computer running Windows 10. The FPGA module is used to update a voltage output at 80 kHz in order to generate harmonic excitations and additive random perturbations.

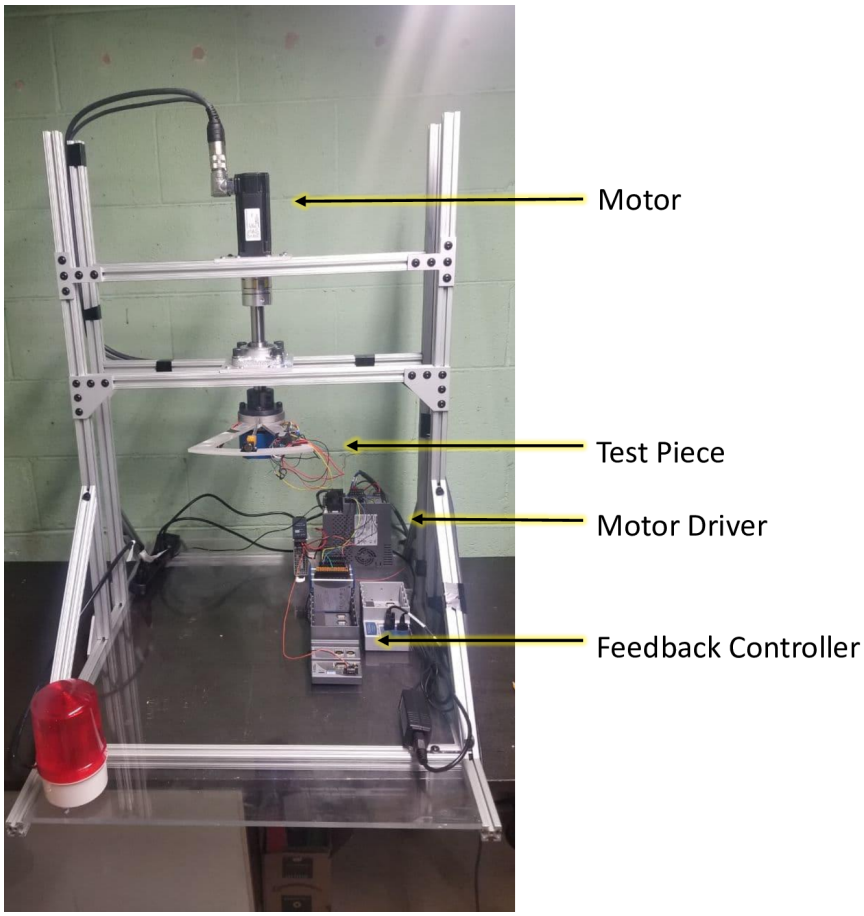


Figure 5.2: Experimental prototype with one cantilever beam.

It is also used to collect data at 5kHz from a strain gauge and store it locally. The real time control module is used to down sample the collected data to 500 Hz and to send the data via a network. This module is also used to make mid-level control decisions such as adjusting the excitation frequency at the appropriate phase and verifying safe conditions prior to enabling the motor. The host computer is used to log data sent via the network and make high level decisions such as selecting the desired excitation amplitude

and frequency, and controlling noise duration. A Kollmorgen AKD motor drive receives an analog signal as a reference signal from the controller and is used to perform high speed proportional control on the motor current. A Kollmorgen AKM motor delivers torque via a shaft; this generates accelerations of the base that vibrate the test piece. By nature and design, the motor is not a high frequency excitation system. The motor will cutoff high frequency components of the reference signal and act as a low pass filter. In comparison to a shaker designed for high frequency excitation, this cutoff frequency is lower for the motor. The low pass filtering effect of the rotating motor is more similar to the real applied use cases of the considered rotating cantilever arrays, but can be more difficult to model.

The test piece is the cantilever steel structure shown in Fig. 5.3. The cantilever is 15.24 cm (6 inches) in length. A permanent magnet is attached to the tip of the cantilever beam and held in place by a 3D printed component. A strain gauge, which is located at 3.81 cm (1.5 inches) from the base, is used to estimate the displacement of the cantilever tip. A larger, more rigid structure under the cantilever beam holds a second permanent magnet. This structure moves as a rigid body with the shaft. The interaction between the magnets creates a nonlinear restoring force, primarily affecting the position of the tip of the cantilever beam.

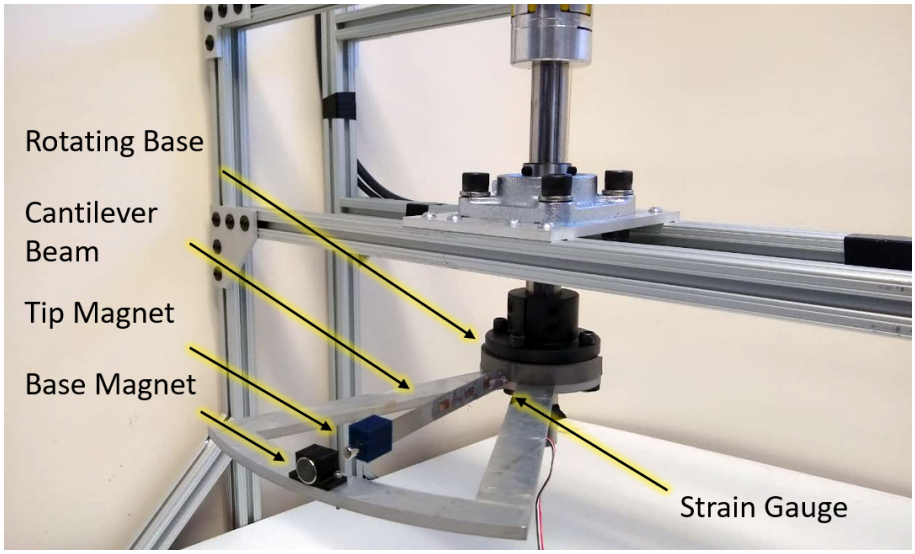


Figure 5.3: Test piece prototype with one cantilever beam.

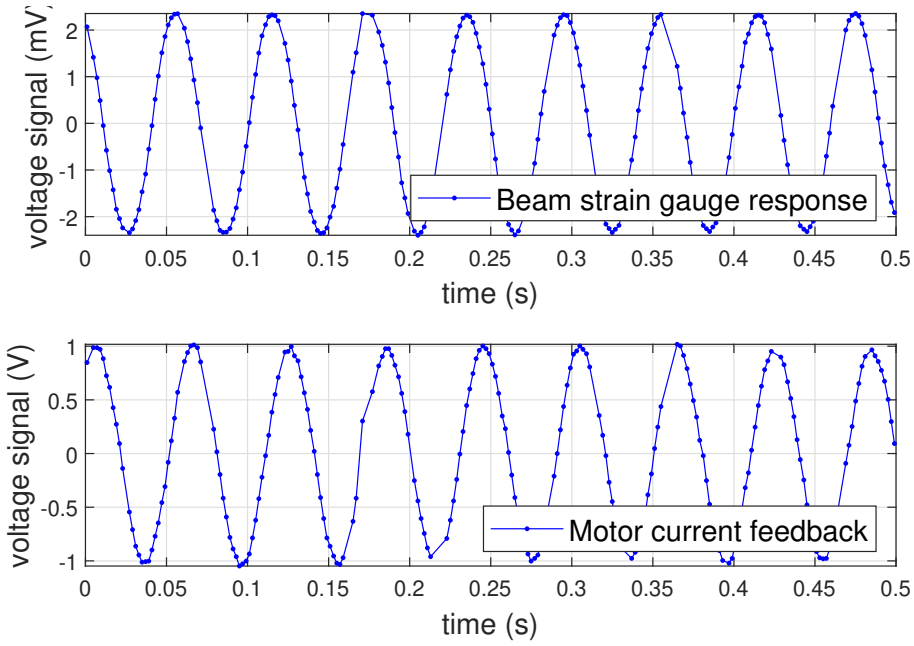


Figure 5.4: Time series response example with (top) the voltage signal read from the strain gauge and (bottom) a voltage signal proportional to the motor current read from a current sensor in the Kollmorgen AKD motor drive.

Data collected while running the experiment takes the form shown in Fig. 5.4. This

includes a voltage signal proportional to the output of the strain gauge and another voltage signal proportional to the current in the motor.

5.3 Frequency Response

One way to capture the nonlinear behavior of the system is by performing a frequency sweep. The frequency sweep consists of quasi-statically changing the excitation frequency; that is, sustaining each excitation frequency for a sufficient duration that the steady state oscillations of the system can be recorded. The time series responses of the beam obtained when slowly changing the frequency are shown in Figs. 5.5 and 5.6. One can observe that in the up sweep (Fig. 5.5) the response is of low amplitude for a long period of time until it jumps to a high amplitude response with amplitude close to 1mV at a time of approximately 6500 seconds. The frequency at which this jump occurs is the *jump up* frequency. On the other hand, in the down sweep (Fig. 5.6), the response increases in amplitude with decreasing frequency to an amplitude of approximately 2mV at around 4000 seconds. As the excitation frequency continues to decrease, the system transitions to a low amplitude response. The frequency at which this transition occurs is the *jump down* frequency. The behavior illustrated in these two figures is evidence of the nonlinear phenomenon known as hysteresis; in this case, there is a sensitivity of the system to the initial condition of the system when the excitation frequency is changed. Furthermore, there is a large bandwidth of frequencies at which the first mode of the system can vibrate at a high amplitude.

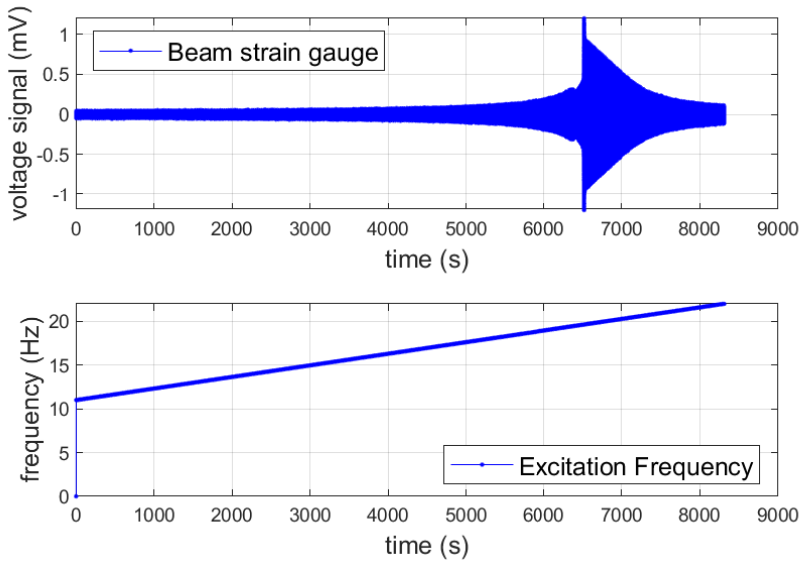


Figure 5.5: Time series response of the beam near resonance when slowly increasing the excitation frequency.

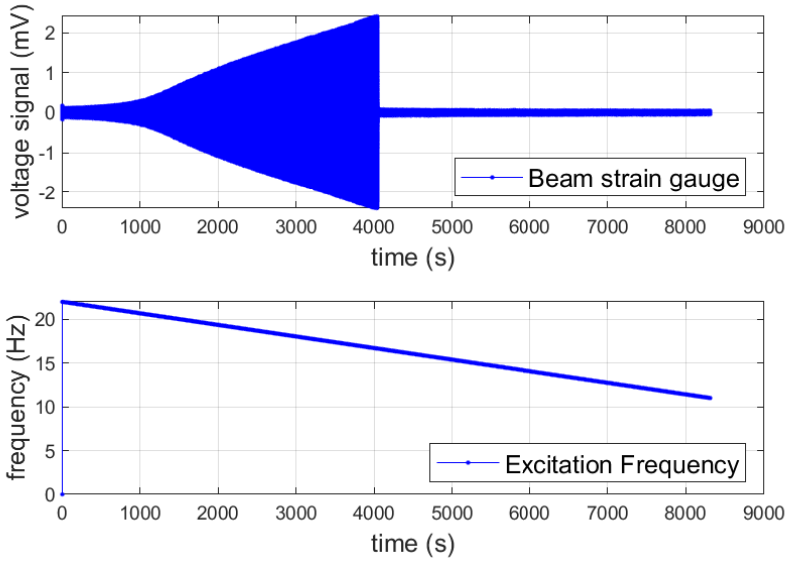


Figure 5.6: Time series response of the beam near resonance when slowly decreasing the excitation frequency.

The first harmonic amplitude of the response at each excitation frequency can be calculated as follows:

$$\begin{aligned} a_c(f_i) &= \int_{\frac{\tau_1+\tau_2}{2}}^{\tau_2} x(t)\cos(2\pi f_i t)dt \\ a_s(f_i) &= \int_{\frac{\tau_1+\tau_2}{2}}^{\tau_2} x(t)\sin(2\pi f_i t)dt \\ a(f_i) &= \sqrt{a_c(f_i)^2 + a_s(f_i)^2} \end{aligned} \tag{5.1}$$

Here $x(t)$ is the strain measurement, $f(t)$ is the excitation frequency at time t, and

$$\begin{aligned} \tau_1 &= \inf_t\{f(t) = f_i\} \\ \tau_2 &= \sup_t\{f(t) = f_i\} \end{aligned} \tag{5.2}$$

are the time bounds at which the excitation frequency is at a constant value f_i. The first harmonic amplitude of the response is evaluated starting at $\frac{\tau_1+\tau_2}{2}$ to allow the response to reach steady state after a change in frequency. By using (5.1) and the data from Figs. 5.5 and 5.6, the frequency response of the system can be visualized as shown in 5.7.

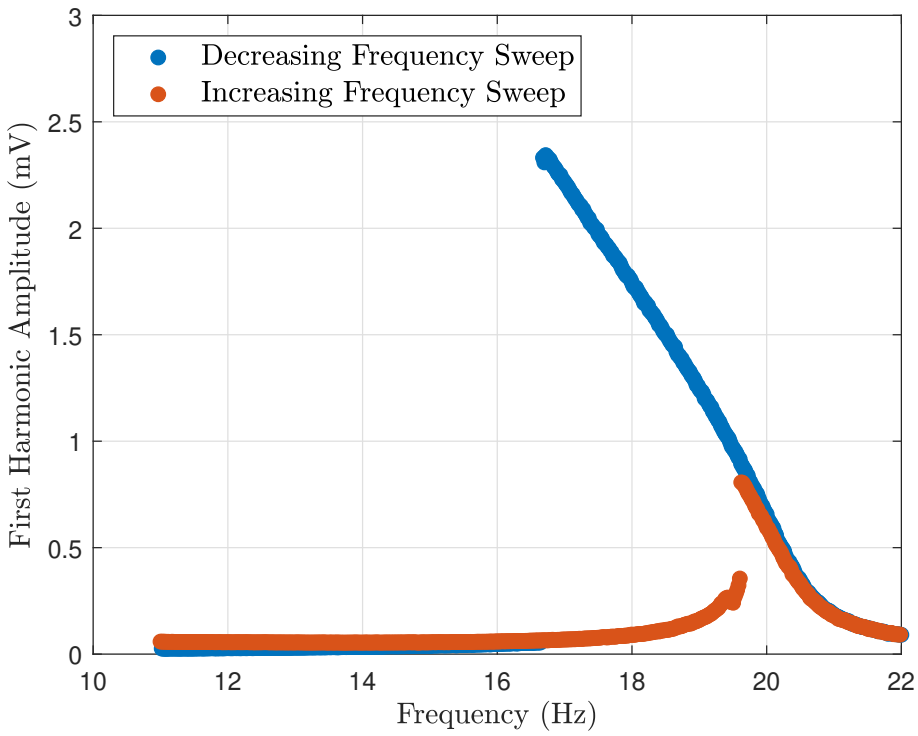


Figure 5.7: First harmonic amplitude of the response, a, as a function of frequency, f.

Notice from Fig. 5.7 that between $f \approx 16.6$ Hz and $f \approx 19.6$ Hz there exists two stable steady state responses of the system at each excitation frequency. The high amplitude response is shown in blue and the low amplitude response is shown in red. A noise induced transition between high amplitude vibrations and low amplitude vibrations is simply the system switching from the red to the blue or vice versa due to random external perturbations. The maximum amplitude of all responses at all frequencies is a_p. This value is important for system identification to nondimensionalize the data.

5.4 System Identification

In this section, a system identification approach to curve fit experimental data to the stable frequency response of Duffing oscillators is presented. This approach expands on the system identification method described by Agarwal *et al.* [41].

5.4.1 System Model

Consider the cantilever beam shown in Fig. 5.8. This cantilever has area moment of inertia, I, modulus of elasticity E, length r, mass density ρ, and a mass concentrated at the tip m_t. Using linear assumptions, as shown in the work by Irvine [44], the effective mass of this system at the tip is $m \approx (.2234\rho r + m_t)$ and the stiffness is $k = \frac{3EI}{r^3}$.

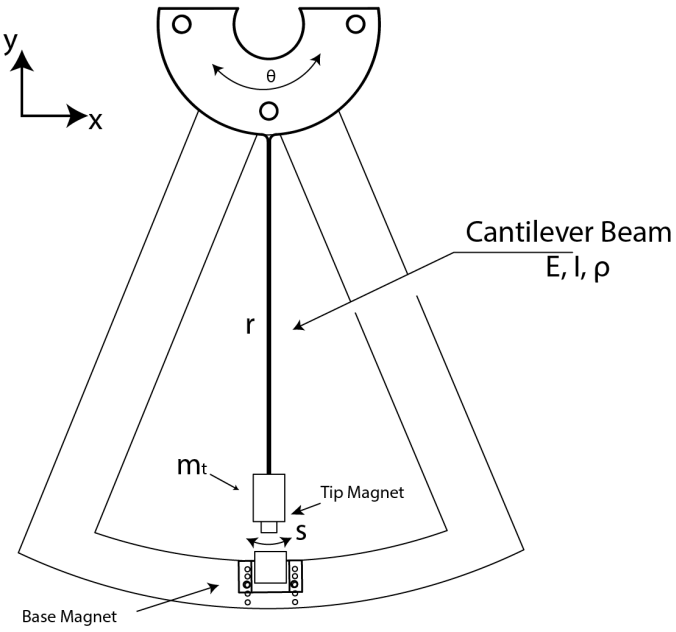


Figure 5.8: Top side visualization of the test piece, including the cantilever beam with a tip mass and a tip magnet, and a rigid base with a secondary magnet. The structure rotates following the angle θ with axis centered at the shaft mount. The beam tip displaces with coordinate s. This coordinate would be an arc length if the system was a rigid structure, and is a more complicated lateral displacement in the flexible structure.

A linear differential equation governing the displacement, s, of the tip of the beam is

$$m\ddot{s} + ks = F. \tag{5.3}$$

Here F is an external excitation delivered via the base in the tangential direction. Using θ as the angular position of the shaft, $\ddot{\theta}$ is the angular acceleration of the base of the beam. If this system were a rigid body, then s would be the arc-displacement of the tip mass and $\ddot{s} = \ddot{\theta}r$ would be the acceleration of the tip mass. Considering that this system is not a

rigid body, then $\ddot{s} = r\ddot{\theta} - \frac{k}{m}s$, and as a result

$$F(t) = mr\ddot{\theta}(t) = \frac{mr}{I_z}\mathbb{T}(t) \tag{5.4}$$

where $\mathbb{T}(t)$ is the torque delivered by the motor to the base of the beam, and I_z is the inertia of the rotating structure in the direction orthogonal to the plane created by θ.

The system in Fig. 5.8 includes a magnet at the tip that interacts with a second magnet rigidly attached to the base. Assuming that the magnets can be modeled as point charges and that the attraction between the two magnetic poles with pole strength p_1 and p_2 follow Coulomb's law, then an attraction force between the magnets is

$$F_m = \frac{\mu_0}{4\pi}\frac{p_1 p_2}{d^2} \tag{5.5}$$

where μ_0 is Coulomb's constant and d is the distance between the magnetic poles when the cantilever beam is at rest. After using the geometry shown in Fig. 5.9, the restoring force due to the magnets can be modeled as

$$\begin{aligned} F_r(s) &= \frac{\mu_0}{4\pi}\frac{p_1 p_2}{(d^2+s^2)}\cos(\varphi) \\ &= C\frac{\cos(\tan^{-1}(d/s))}{(d^2+s^2)} \\ &= C\frac{1}{\sqrt{\frac{d^2}{s^2}+1}\,(d^2+s^2)} \\ &\approx C_1 s - C_2 s^3 + O(s^5), \quad C_1 > 0,\, C_2 > 0. \end{aligned} \tag{5.6}$$

Here, the expression is simplified by assuming small displacements and taking a Taylor series expansion centered at $s = 0$.

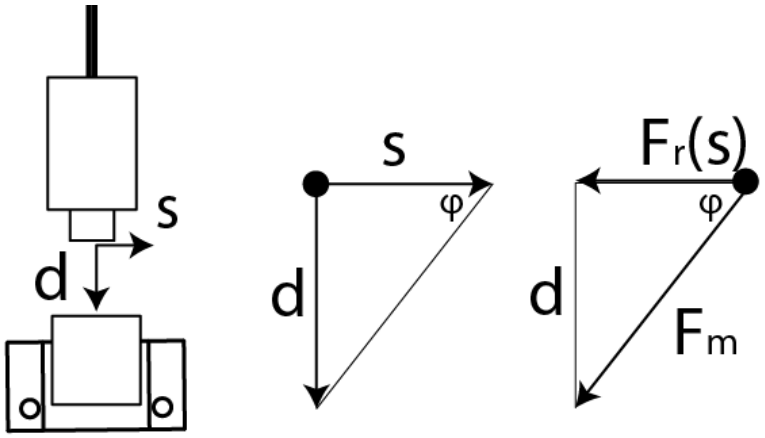


Figure 5.9: Geometry of the beam tip displacement relative to the base magnet, assuming small displacements.

The updated model containing the magnetic restoring force takes the form:

$$m\ddot{s} + c\dot{s} + (k + C_1)s - C_2 s^3 = \frac{mr}{I_z}\mathbb{T}(t). \tag{5.7}$$

Here there is also a linear damping term included with some unknown coefficient, c. Note that a linear assumption is made in deriving the stiffness of the beam, and that magnetic restoring force is approximated to the third order. Higher order terms are neglected. In this experiment, strong neodymium magnets are used, and it is a reasonable assumption that the nonlinear restoring forces from the magnet are more significant than the much weaker nonlinear restoring forces from the cantilever beam.

5.4.2 Parametric System Identification

In order to fit the system model to the frequency response data from Section 5.3, first, a nondimensional analytical approximation to the frequency response is defined. With $k_1 = k + C_1$, $k_3 = -C_2$, $F_0\cos(\omega t) = \frac{mr}{I_z}\mathbb{T}(t)$ and $y = s$, equation (5.7) takes the form

$$m\ddot{y} + c\dot{y} + k_1 y + k_3 y^3 = F_0 \cos(\omega t). \tag{5.8}$$

This system is nondimensionalized with respect to time using the change of variables $\omega_n = \sqrt{k_1/m}$, $\tau = \omega_n t$, and $\frac{d}{d\tau} = \{.\}'$:

$$y'' + \eta y' + \alpha y + \hat{k}_3 y^3 = \tilde{F}_0 \cos(\Omega\tau) \tag{5.9}$$

Here $\Omega = \frac{\omega}{\omega_n}$, $\eta = \frac{c}{m\omega_n}$, $\alpha = \frac{k_1}{m\omega_n^2}$, $\hat{k}_3 = \frac{k_3}{m\omega_n}^2$, $\tilde{F}_0 = \frac{F_0}{m\omega_n^2}$. This is further nondimensionalized with respect to the strain signal units by using $x = y/a_p$. Here a_p is just a constant chosen for convenience to be the maximum amplitude of the response considering all frequencies. Applying the change of variables, the system takes the form

$$x'' + \eta x' + \alpha x + \beta x^3 = \hat{F}_0 \cos(\Omega\tau) \tag{5.10}$$

with $\beta = \hat{k}_3 a_p^2$ and $\hat{F} = \frac{\tilde{F}_0}{a_p}$. Assuming weak nonlinearities, weak damping, and weak forcing, it can be shown that the analytical approximation to the frequency response for this system is

$$\left[\frac{\eta^2}{4} + \left(\Omega - 1 - \frac{3}{8}\beta A^2\right)^2\right] = \frac{\hat{F}_0^2}{4A^2} \tag{5.11}$$

by taking the analytical approximation for the frequency response near primary resonance of a Duffing oscillator as derived in [47], and applying a change of variables. In (5.11), $A = \frac{a}{a_p}$.

Parametric system identification can be performed by fitting the experimental data in Fig. 5.7 to (5.11). Equation (5.11), is simplified as the function of A:

$$\Omega = 1 + \frac{3}{8}\beta A^2 \pm \sqrt{\frac{\hat{F}_0^2}{4A^2} - \frac{\eta^2}{4}} \tag{5.12}$$

The maximum amplitude of all frequencies, a_p, occurs at the jump down frequency. As a result, at the jump down frequency, $A = 1$. For $A > 1$ solutions of the analytical curve are complex numbers. The transition to complex numbers occur when $\sqrt{\frac{\hat{F}_0^2}{4A^2} - \frac{\eta^2}{4}} = 0$, which for $A = 1$ occurs when $\hat{F}_0 = \eta$. With the constraint, $\hat{F}_0 = \eta$, solving for the best fit of the experimental frequency response to the analytical frequency response is a two-dimensional optimization problem with the cost function

$$\begin{aligned} C(\beta, \hat{F}_0) &= \sqrt{\sum_{i=1}^{N} \left(1 + \frac{3}{8}\beta A_i^2 + (-1)^{p(i)} \sqrt{\frac{\hat{F}_0^2}{4A_i^2} - \frac{\hat{F}_0^2}{4}} - \Omega_i \right)^2} \\ p(i) &= \begin{cases} 0, & \text{sample } i \text{ to fit high amplitude branch} \\ 1, & \text{sample } i \text{ to fit low amplitude branch} \end{cases} \end{aligned} \tag{5.13}$$

Here A_i and Ω_i are the nondimensionalized, experimental, first harmonic amplitudes and frequencies from Section 5.3, respectively. The nonlinear regression problem is to minimize (5.13) with respect to β and $\hat{F}_0$. This is a low dimensional problem that is

convenient to solve with common nonlinear optimization packages.

The frequency response from Fig. 5.7 is shown in nondimensionalized form in Fig. 5.10. The analytical curve that corresponds to $\beta = -0.48$ and $\hat{F}_0 = \eta = 0.0104$ which is the minimizer of (5.13) is also shown for comparison to the experimental data.

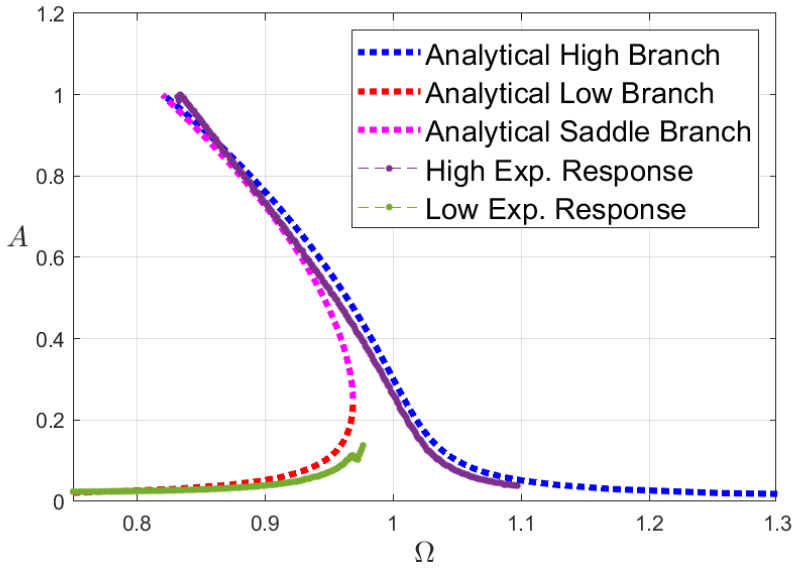


Figure 5.10: The experimental frequency response in nondimensionalized form, compared to the analytical approximation to the frequency response of the Duffing oscillator with parameters that minimize (5.13). Here, $\beta = -0.48$, $\hat{F}_0 = \eta = 0.0104$.

Note that the analytical curve includes a saddle branch that corresponds to unstable solutions that are not observed in the experimental data.

The analytical approximation for the frequency response derived in [47] uses assumptions of weak nonlinearities, but the nonlinear system (5.10) that arises with cubic coefficient $\beta = -0.48$ is not weakly nonlinear. An additional correction step is applied to the model parameters; the shooting method and numerical continuation of periodic

solutions is used to generate the frequency response of the system without the weakly nonlinear assumptions, and the parameters are adjusted to refit the numerical response. The numerical continuation package COCO [52] is used for this step. Numerical continuation is much more computationally expensive, so it is only used as a minor parameter correction step and not as the sole system identification approach.

The frequency response using numerical continuation is shown alongside the experimental data in Fig. 5.11. The corrected parameters are $\beta = -0.48$, $\hat{F}_0 = 0.007$, and $\eta = 0.009$.

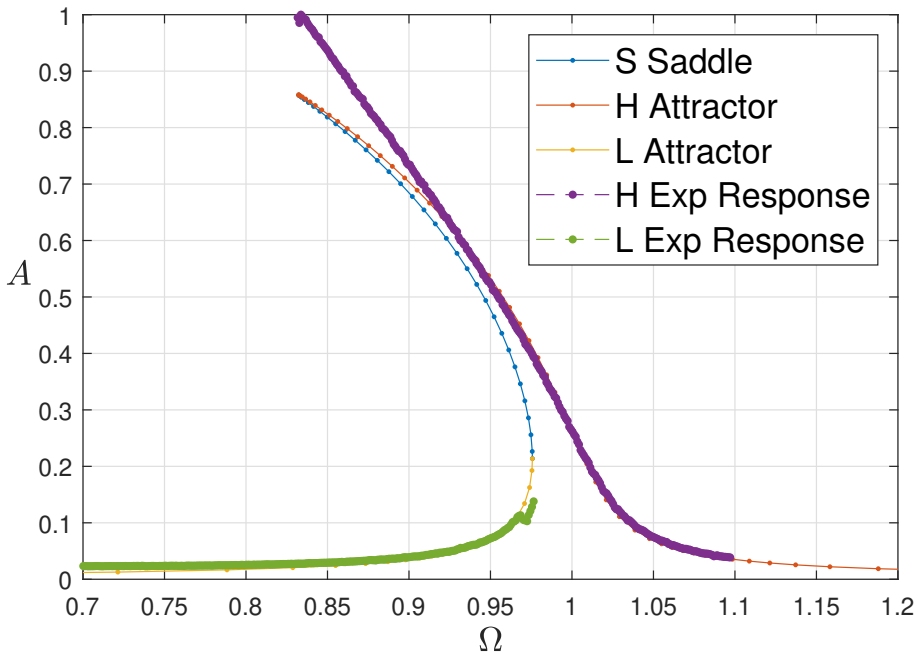


Figure 5.11: The experimental frequency response in nondimensionalized form compared to the frequency response of the Duffing oscillator computed via numerical continuation. Here, $\beta = -0.48$, $\hat{F}_0 = 0.007$, and $\eta = 0.009$.

In the more accurate numerical continuation response, the experimental data diverges from the best fit model response at high amplitudes. Additional nonlinear terms

such as the omitted $O(x^5)$ term from (5.6) or modeling the cantilever beam with more degrees of freedom could explain the higher amplitude behavior. That said, this model is chosen because it is a simple nonlinear system model that is appropriate for this data, and this model can still provide useful insight into the stochastic nonlinear behavior of the mechanical system.

5.5 Experimental Results

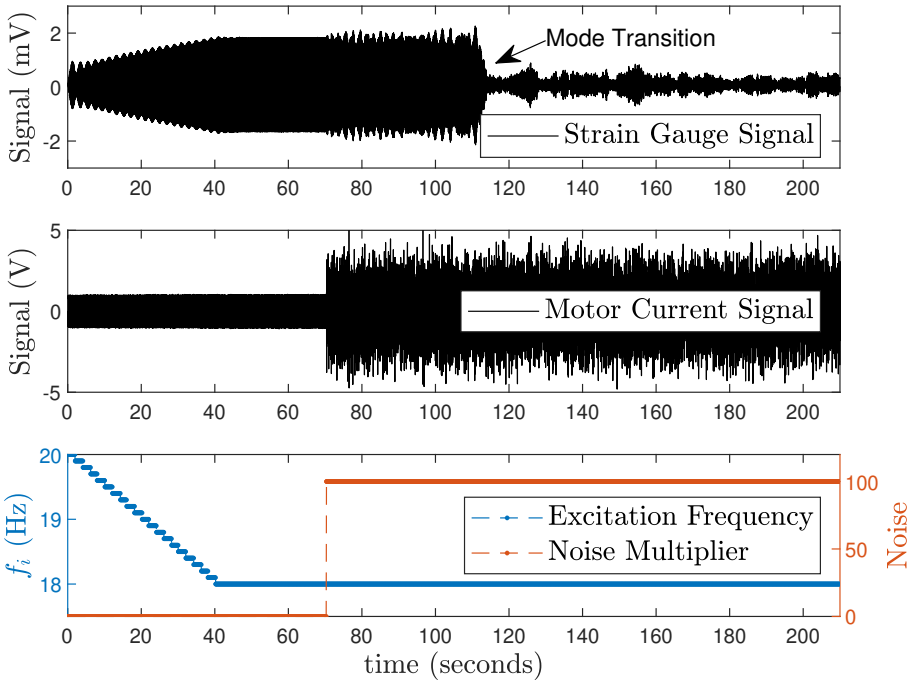


Figure 5.12: An example noise trial of the experiment. Each trial began with a gradual decrease of the frequency of excitation, f_i, which leads the strain response to a high amplitude stable mode. At $t \approx 70$, noise is added to the control signal. After some time, the random perturbations induced a transition from the high amplitude strain response to a low amplitude strain response.

The experiment is used to create empirical evidence of transitions occurring from the high amplitude mode to the low amplitude mode due to the effect of noise. A noise trial of the experiment takes the form shown in Fig. 5.12, which consists of plots of the strain, the motor current, the excitation frequency parameter f_i, and the noise multiplier parameter, σ_E. First, note that in the first 70 seconds of a trial, $\sigma_E = 0$, meaning there is no additive noise being intentionally added to the system. In the first 40 seconds, the excitation frequency f_i is slowly decreased from 20Hz to 18Hz. Notice that as the excitation frequency decreases, the strain increases; the system follows the blue curve of Fig. 5.7 to higher amplitude responses. At the 40-second mark, the frequency of excitation is fixed to the constant value of 18 Hz. Between $40 \leq t \leq 70$, no parameters are changed, and the strain reaches a steady state oscillation. At $t > 70$, σ_E is set to 100. The magnitude of σ_E has no direct physical meaning because the control signal is scaled by multiple controllers and actuators prior to reaching the cantilever beam. Notice that the motor current at σ_E transitions from smooth sinusoidal oscillations to noisy oscillations at $t = 70$. The average power spectrum of the noisy control signal is shown in Fig. 5.13. There is a peak of the control signal at 18Hz corresponding to the cosine deterministic excitation. There is also a low pass filter effect on the noise.

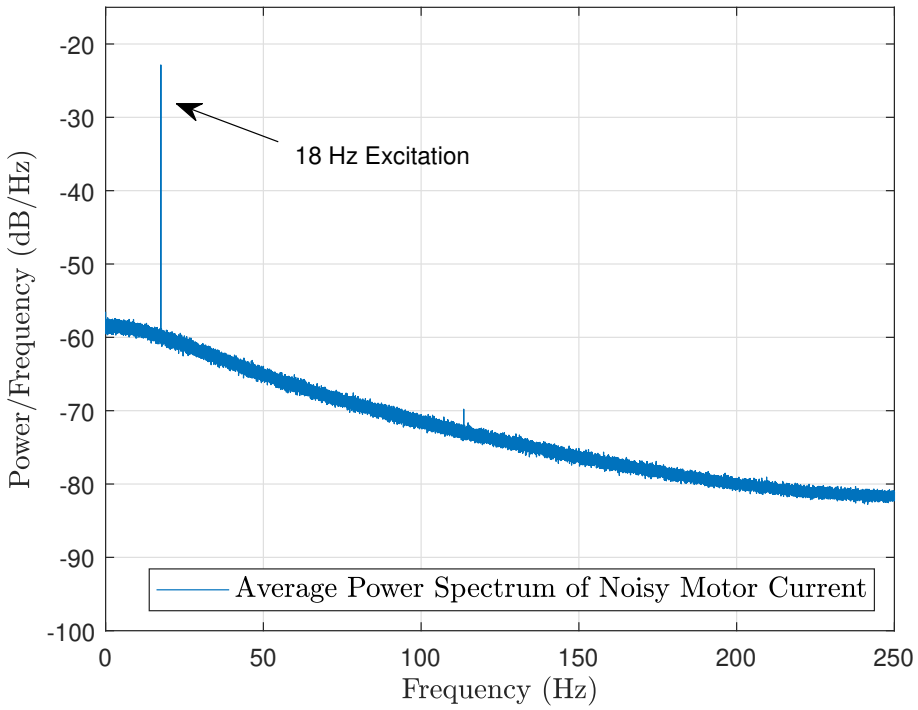


Figure 5.13: The power spectrum of the noisy control signal averaged over 500 trials for $\sigma_E = 100$. Notice a sharp peak at 18Hz corresponding to the deterministic cosine excitation and attenuation of the signal at higher frequencies that occurs due to the low pass behavior of the motor.

Despite the seemingly high amount of noise, the strain response does not immediately transition from the high amplitude mode to the low amplitude mode. A transition is depicted in Fig. 5.12 at $t \approx 110$ which is after approximately 720 periods of excitation since the noise begins. The trial always ends at $t \approx 225$, regardless of whether a transition has been observed. The full duration of each trial is run to capture the possibility for the system to transition back to the high amplitude mode; a transition from the low amplitude response to the high amplitude response is never observed in any of the trials. Only a single trial is depicted in Fig. 5.12. The controller is programmed to

repeat these trials autonomously 500 times for one set of excitation frequency and noise multiplier parameters. A set of 500 trials takes between 35 to 40 hours to complete. Due to the nature of the random perturbations in the control signal, the transition between the high amplitude mode and the low amplitude mode occur at different times in each trial.

Box plots of the transition time of 500 trials of different noise intensities are shown in Fig. 5.14. One can observe roughly an exponential relationship between the median transition time and a linear change in the noise intensity.

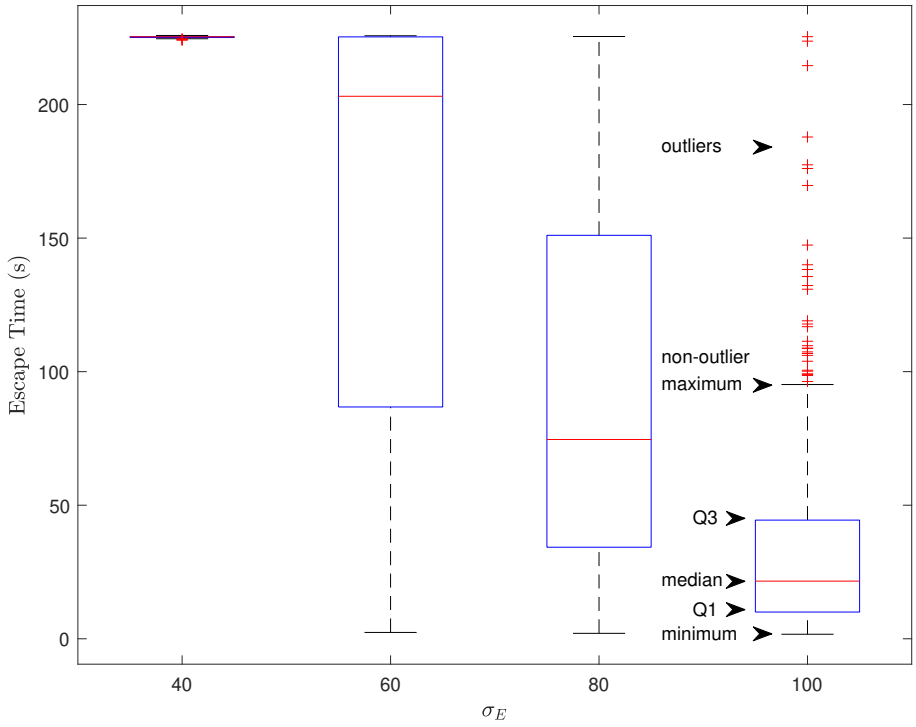


Figure 5.14: Box plots of the noise trials. Each box plot consists of 500 experimental trials for a different value of the noise multiplier. Here the excitation frequency is 18 Hz.

The median is used in place of the mean because the mean can be significantly skewed by the maximum time limit of the trial. For example, for the noise intensity $\sigma_E = 100$, the noise trials have the escape time histogram shown in Fig. 5.15. A common

Kolmogorov-Smirnov [107] statistical test performed on this data fails to reject the null hypothesis with 95% confidence that this data comes from a normal distribution. That is, this data may be normally distributed, and the median could approach the expected escape time value as long as that value is within the trial time limits.

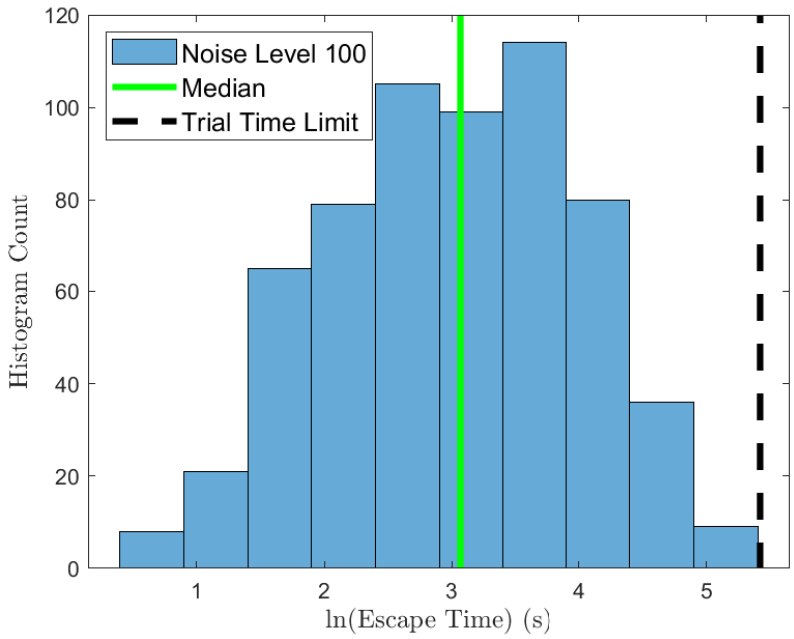


Figure 5.15: Histogram of the natural log of experimental escape times for $\sigma_E = 100$.

This is further illustrated in Fig. 5.16 with a histogram of the set of escape times for $\sigma_E = 80$. In Fig. 5.16, all escape times that reached the trial limit of 225 seconds are omitted. One could assume from visual inspection of the figure that this data set could come from a normal distribution truncated at $t = 225$. The medians between the truncated data set, and the entire data set do not vary much, and should converge to the same value as the number of trials goes to infinity. The means, however, would not necessarily converge as they would be skewed by the trial limit. In this data set, only 15% of the data set fails

to escape with 225 seconds. For the lower noise intensities of $\sigma_E = 40$ and $\sigma_E = 60$, 90% and 40% of the trials do not escape in less than 225 seconds, respectively. It is assumed the median is approximately accurate for $\sigma_E = 60$. For $\sigma_E = 40$, the expected escape time is likely larger than 225 seconds. In collecting this data, there is a tradeoff at play between the number of trials that can be collected and the size of the trial time limit.

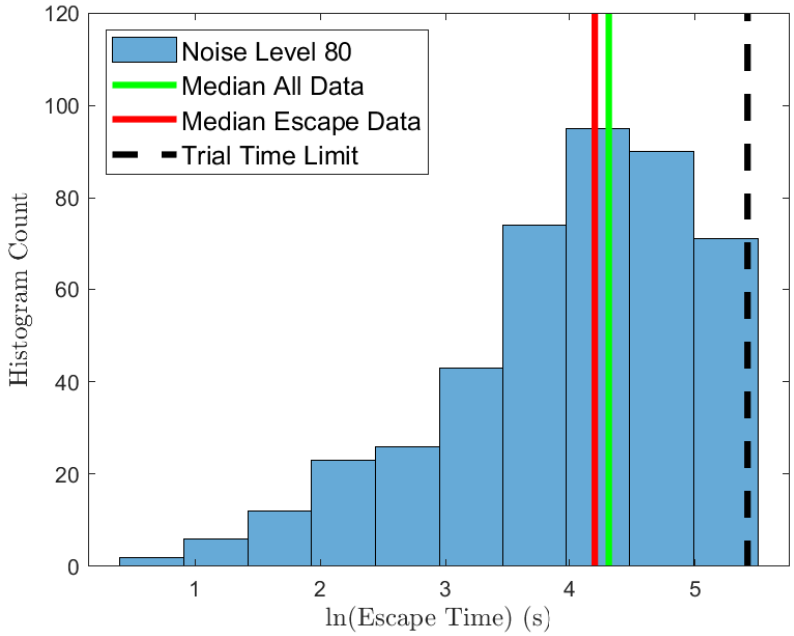


Figure 5.16: Histogram of the natural log of experimental escape times for $\sigma_E = 80$.

An alternative interpretation of this data can be expressed as the probability of the system remaining in the high amplitude response for different noise intensities and

durations. Using the escape times, this probability can be estimated as follows:

$$P_H(t) = \frac{\sum_{i=1}^{n} \delta_e(\tau_i)}{n}$$
$$\delta_e(t, \tau_i) = \begin{cases} 1, & t < \tau_i \\ 0, & t \geq \tau_i \end{cases} \tag{5.14}$$

Here τ_i is the escape time of trial i, and δ_e is a function that gives a trial a value of 1 at times before the response has transitioned out of the high amplitude response, and zero otherwise. The variable n is the bin size of trials in the estimate. The probability estimates for different noise intensities at the excitation frequency of 18 Hz are shown in Fig. 5.17. In Fig. 5.17, $n = 50$, and trials are randomly selected from the set 500 trials for the calculation. A total of 10 estimates are determined for each noise intensity, and the resulting 10 estimates are averaged and graphed alongside with the standard deviation as an indicator of the error of the estimate. In Fig. 5.17, on the solid green curve corresponding to $\sigma_E = 40$, the system has a high probability of remaining in the high amplitude response. On the black curve corresponding to $\sigma_E = 100$, the system has the lowest probability of remaining in the high amplitude response after a short amount of time. The other curves follow the same trend with varying noise intensity.

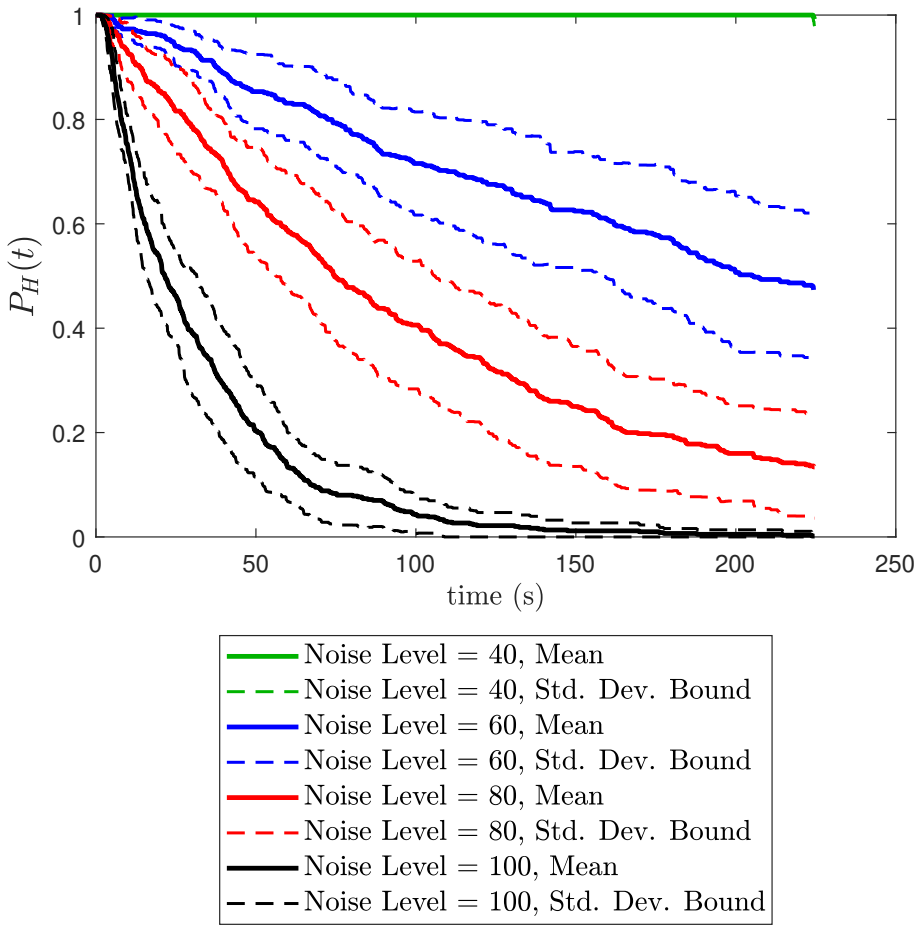


Figure 5.17: Estimate of the probability of remaining in the high amplitude attractor as a function of time and noise intensity, σ_E. Here, the excitation frequency is fixed to $f_i = 18$ Hz. These curves are created by using (5.14) on the experimental escape times.

Additionally, the dependence of the escape times and the probability estimates on the excitation frequency is studied. 500 trials are performed for each of four excitation frequencies in the multi-stability region of the frequency response. The noise intensity is kept constant at $\sigma_E = 100$. Box plots of the escape times from the high amplitude response as a function of noise intensity are shown in Fig. 5.18. One can observe in Fig. 5.18 an exponential relationship between the median escape time with linear changes in

excitation frequency. In particular, for excitation frequencies of 17.5, 18.0, and 18.5 Hz the majority of trials escape the high amplitude response within the 5000 period maximum time limit. On the other hand, for the excitation frequency of 19.0 Hz, the majority of trials do not escape within the first 5000 periods. These results support observations in related work [9], which indicate that transitions from the high amplitude response to the low amplitude response are more probable near the jump down point of the frequency response, and less probable near the jump up point of the frequency response.

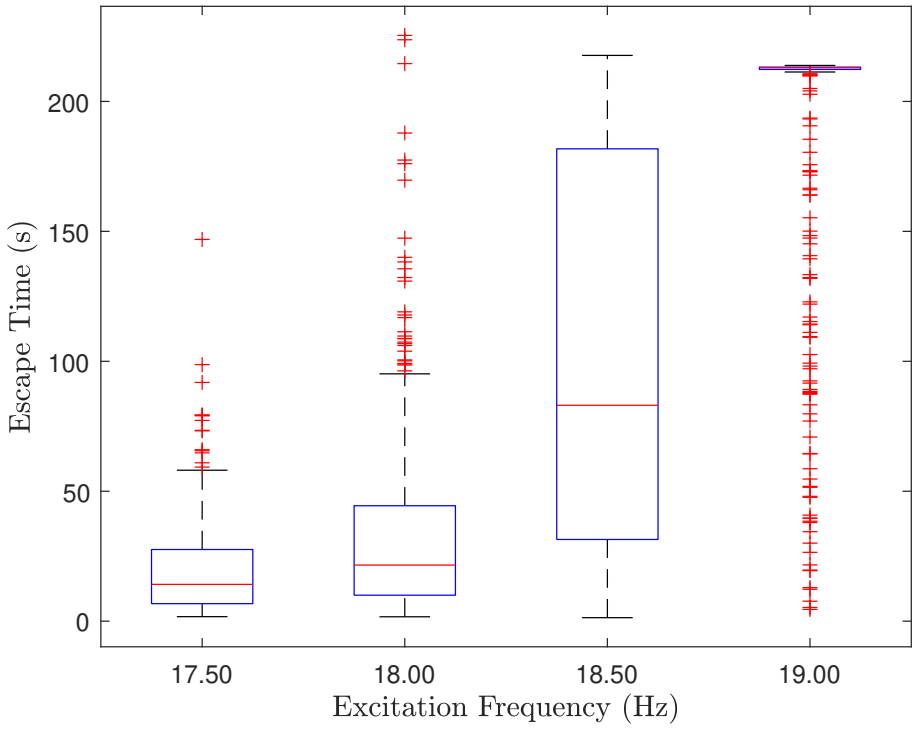


Figure 5.18: Box plots of the noise trials. Each box plot consists of 500 experimental trials for a different value of the excitation frequency, f_i. Here $\sigma_E = 100$.

The probability estimates are also calculated for this varying frequency data. The probability estimates are shown in Fig. 5.19. One can observe a significant relationship between the probability estimates and the excitation frequency.

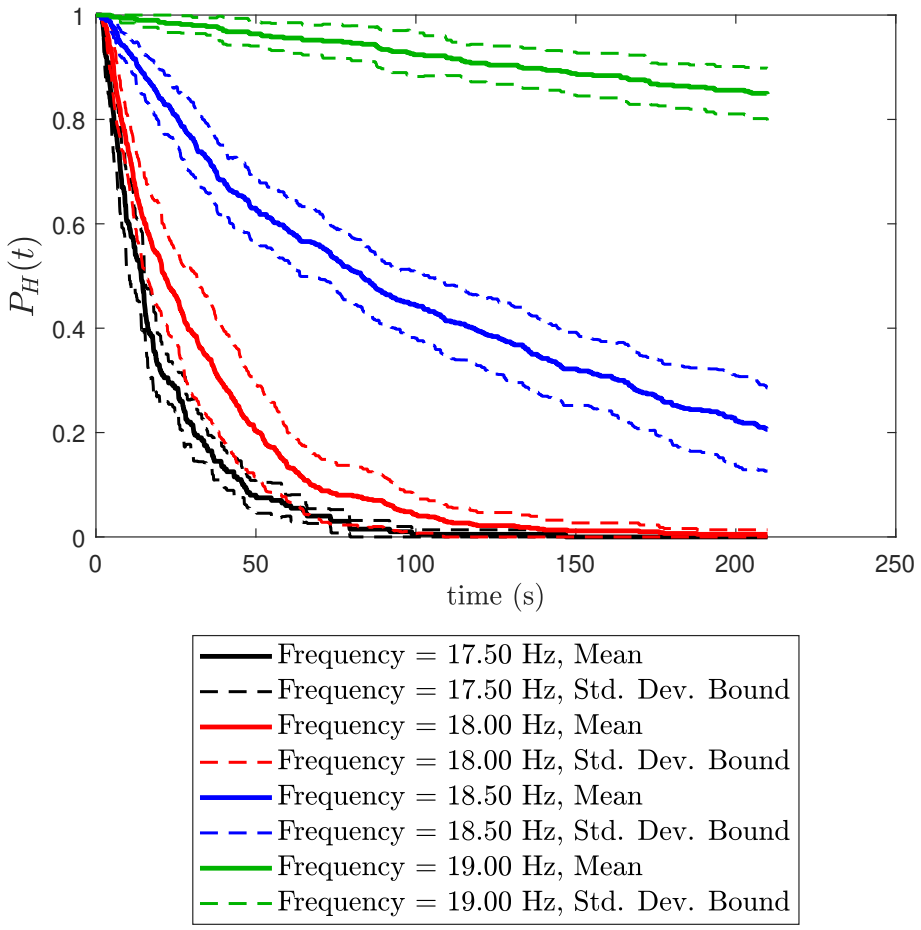


Figure 5.19: Estimate of the probability of remaining in the high amplitude attractor as a function of time and excitation frequency. Here, the noise intensity is fixed to $\sigma_E = 100$. These curves are created by using (5.14) on the experimental escape times.

A transition between the high amplitude response and the low amplitude response is a change in the periodic displacement and velocity states of the system. One way to visualize these transitions is to plot stroboscopic measurements sampled once a period of the response. This is similar to plotting the Poincaré section of the nonlinear system. Two example transitions are plotted in Fig. 5.20.

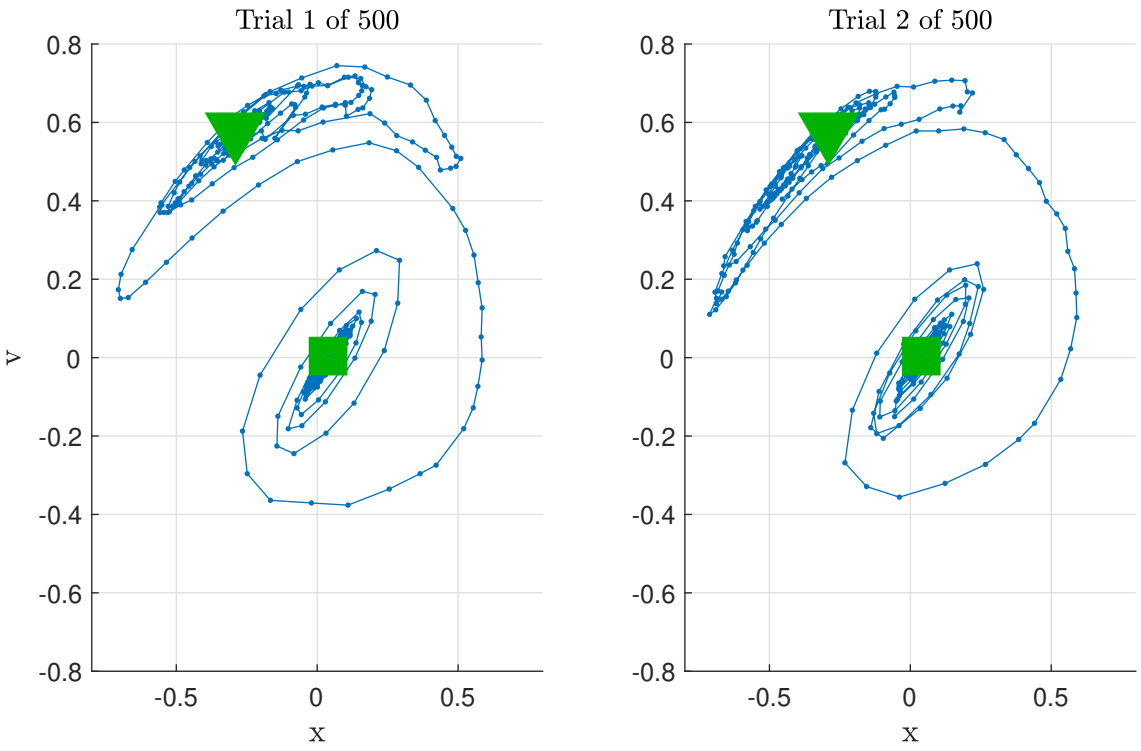


Figure 5.20: Experimental escape paths of trial 1 and 2 of 500 for $\sigma_E = 60$ and $f_i = 18Hz$. The paths are visualized via a stroboscopic map sampled once a period of displacement and velocity. The velocities are calculated by using a first order central difference scheme on the displacement. The path includes the state of the system 200 periods before and after the transition.

Notice from both transition plots that the system begins at the high amplitude response depicted by the triangle, rotates counterclockwise away from the triangle, and then takes a detour in which the system changes from a counterclockwise rotation to a clockwise rotation down into the low amplitude response depicted by the square. These plots show 200 periods before the transition and 200 periods after the transition. The path taken by the system in the transition is similar for all trials in which a transition occurs, however, even between these two plots there are some differences. The most notable

difference is that the location of the stable responses are not exactly the same in both plots, and this is because it is difficult to determine the exact phase of the experimental response relative to the excitation since the excitation is intentionally very noisy during the trial.

5.6 Simulation Results

The system identification approach in Section 5.4 produced the nondimensional ODE

$$x'' + 0.009x' + x - 0.48x^3 = 0.007\cos(\Omega\tau). \tag{5.15}$$

Including an additive white noise excitation, the corresponding stochastic differential equation (SDE) is

$$x'' + 0.009x' + x - 0.48x^3 = 0.007\cos(\Omega\tau) + \sigma dW(\tau). \tag{5.16}$$

Here σ is the noise intensity multiplier and $dW(\tau)$ is additive white noise. The excitation frequency $f_i = 18$ Hz is equivalent to $\Omega = 0.9$ in nondimensional form. The basins of attraction of (5.15) for $\Omega = 0.9$ are shown in Fig. 5.21. The high amplitude and low amplitude attractors have the basin of attractions shown in red and green, respectively. The blue region corresponds to initial conditions that are unstable and grow to infinity. Unstable vibrations that grow to infinity do not occur in the experiment, so it is assumed the model is valid and to be used within the domain of the green and red region. For low σ and initial conditions of ODE (5.15) near one of the two attractors, the system with high

probability remains in the red or green regions and does not enter the unrealistic unstable domain.

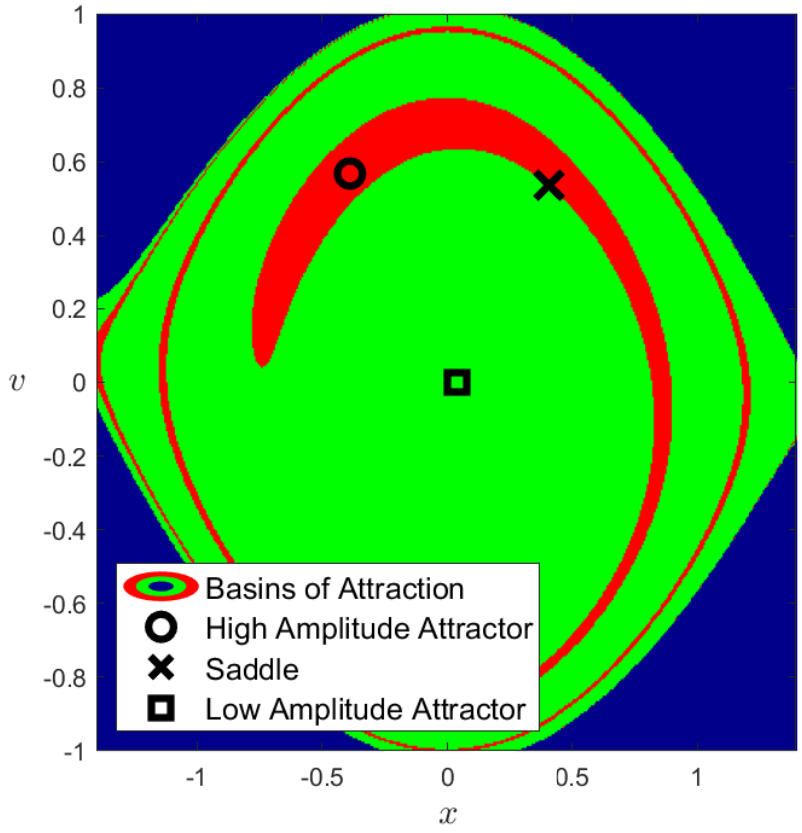


Figure 5.21: Basins of attraction of the system model at $\Omega = 0.9$ or equivalently $f_i = 18$Hz. The basin of the high amplitude attractor and the low amplitude attractor are shown in red and green, respectively. An unstable basin in which the response blows up to infinity is shown in blue.

Transitions in the system model from the high amplitude attractor to the low amplitude attractor are responses of the system in which the system starts near the high amplitude attractor (the circle of Fig. 5.21), moves towards the green basin of attraction via the work performed by random perturbations, and then moves along trajectories of

(5.15) to the square of Fig. 5.21. Note that the high amplitude basin is much smaller than the low amplitude basin in size.

The escape time out of the high amplitude basin of attraction of (5.15) is estimated using numerical experiments. The Euler-Maruyama method [69] is used to integrate the SDE forward in time with the high amplitude attractor as the initial condition. A small timestep of 0.0001 is used for the simulation. At these small timesteps, the stochastic simulations converge with respect to the timestep. The Euclidean norm of the Poincaré section of a single simulation starting at the high amplitude attractor and transitioning to the low amplitude attractor due to the influence of noise with multiplier, $\sigma = 0.0045$ is shown in Fig. 5.22.

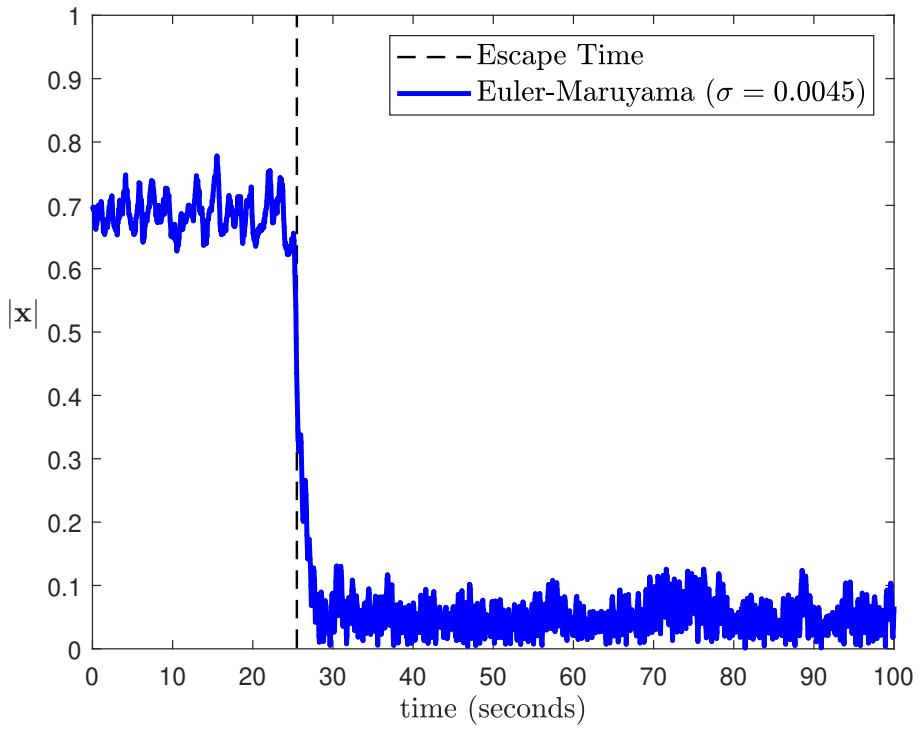


Figure 5.22: The Euclidean norm of the Poincaré section of the stochastic response of the system model simulated using the Euler-Maruyama scheme. The transition time between a high amplitude response and the low amplitude response is highlighted with the dashed line.

For each σ, 200 trials of the numerical experiment are computed. Each trial had a fixed end time of 5000 periods of excitation. These are long duration trials; each numerical trial has $3.5 * 10^8$ timesteps, and takes on average about 50 minutes to compute. High performance parallelization of the numerical trials is performed on the Maryland Advanced Research Computing Center.

The median escape times of the numerical experiments are shown in Fig. 5.23.

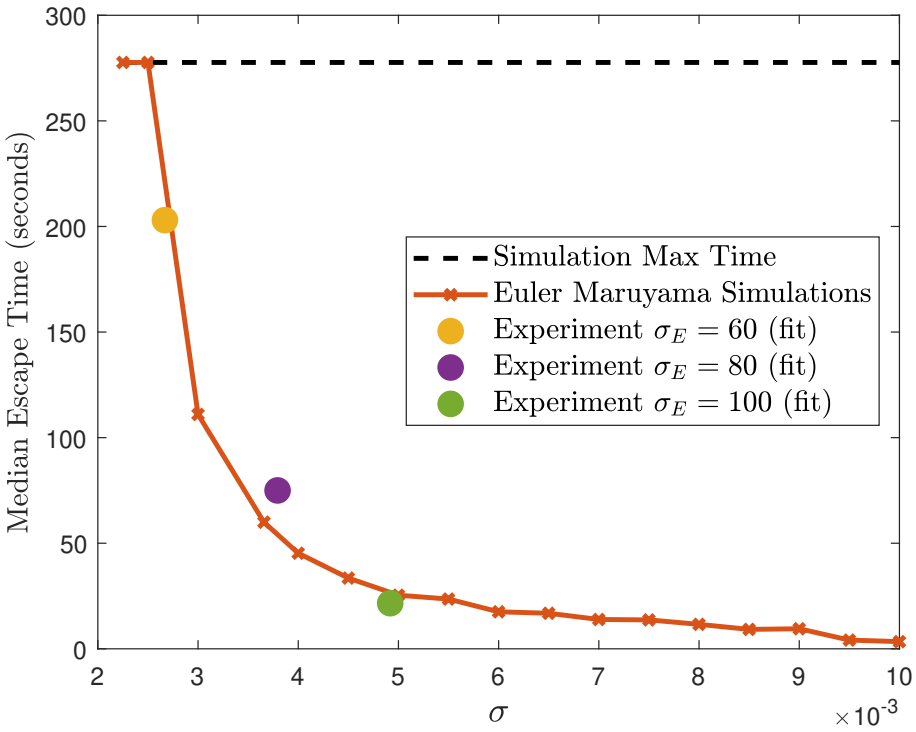


Figure 5.23: The median escape time for sets of Euler-Maruyama simulations that begin at the high amplitude attractor as a function of the noise intensity σ. Each data point is calculated using 200 Euler-Maruyama simulations. Each simulation used $\Omega = 0.9$ that is equivalent to $f_i = 18$Hz. The experimental escape times are fit to the natural log simulated escape times for comparison.

For $\sigma < 3 * 10^{-3}$, the median escape time exceeds the maximum time of the numerical trials. For larger noise intensities, the simulations follow an exponential decay of median escape times. In Fig. 5.23, the experimental escape times are graphed with the numerical escape times. Note that σ, the noise multiplier from (5.16), is not directly comparable to σ_E, the experimental noise intensity. To create Fig. 5.23, least squares optimization is performed to minimize the error between the escape times in the natural log scale. Resulting from the optimization, σ_E is rescaled to fit the numerical

experiment. There is high sensitivity of the escape times to noise intensity, and these fitted comparisons are performed to show only qualitative similarities between the experimental and numerical results. The experimental noise intensities of $60, 80,$ and 100 are fitted to $\sigma = 0.0027, 0.0038,$ and 0.0049, respectively.

The probability estimate for (5.16) to remain in the basin of the high amplitude attractor at these noise intensities are shown in Fig. 5.24. These estimates are simulated and computed for the deterministic excitation frequency of $18Hz$. The resulting trend of decreasing probability with higher noise intensities is similar to that of the experimental system.

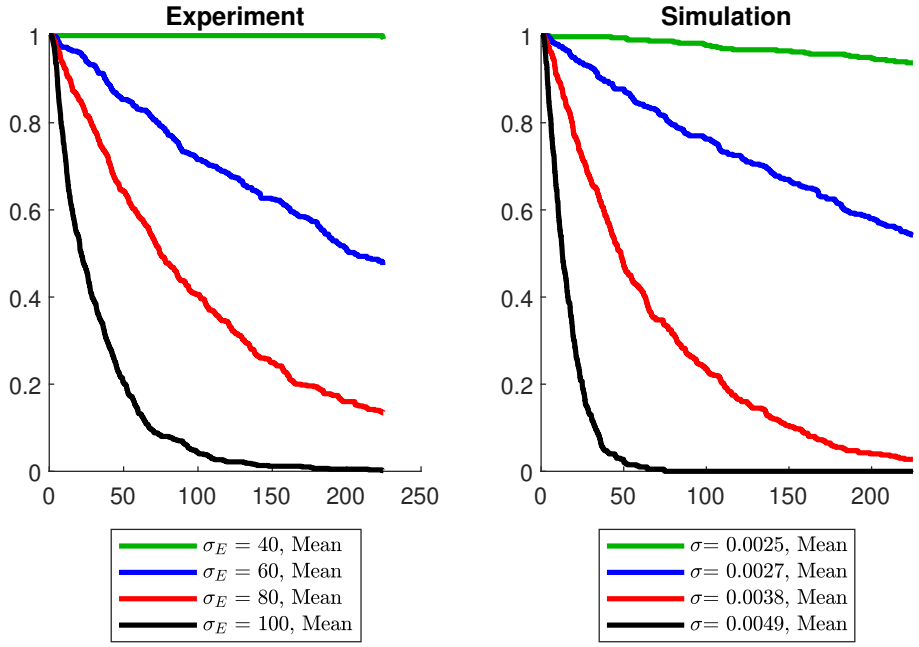


Figure 5.24: Estimates of the probability of remaining in the high amplitude attractor of the experiment (left) and simulation (right) data as a function of time and noise intensity. Here, $f_i = 18$Hz.

The probability curves in Fig. 5.24 can be used to estimate the quasipotential.

The quasipotential, U is a quantitative measure of the difficulty of escape such that the expected escape time is proportional to $\exp\{-U/\epsilon\}$; here $\epsilon = \sigma^2$. Formal definitions for U from the Friendlin and Wentzell are available in [75] and also in Chapter 4 of this dissertation. Assume that the probability of remaining in the high amplitude basin has the model,

$$\begin{aligned} P(\tau_{escape} > t) &= \exp\{-\lambda(\epsilon)t\} \\ \lambda(\epsilon) &= C\exp\{-U/\epsilon\} \end{aligned} \tag{5.17}$$

Then $\lambda(\epsilon) = -(1/t)logP(\tau_{escape} > t)$ and $U = \log(\lambda(\sigma)) = -U/\epsilon + \log C$. After using these equations, assuming $P(\tau_{escape} > t) \approx P_H(t)$, and $\epsilon = \sigma^2$, the quasipotential, U can be extracted from a slope of the best fit line between $\log(\lambda(\sigma))$ and $1/\sigma^2$ as shown in Fig. 5.25

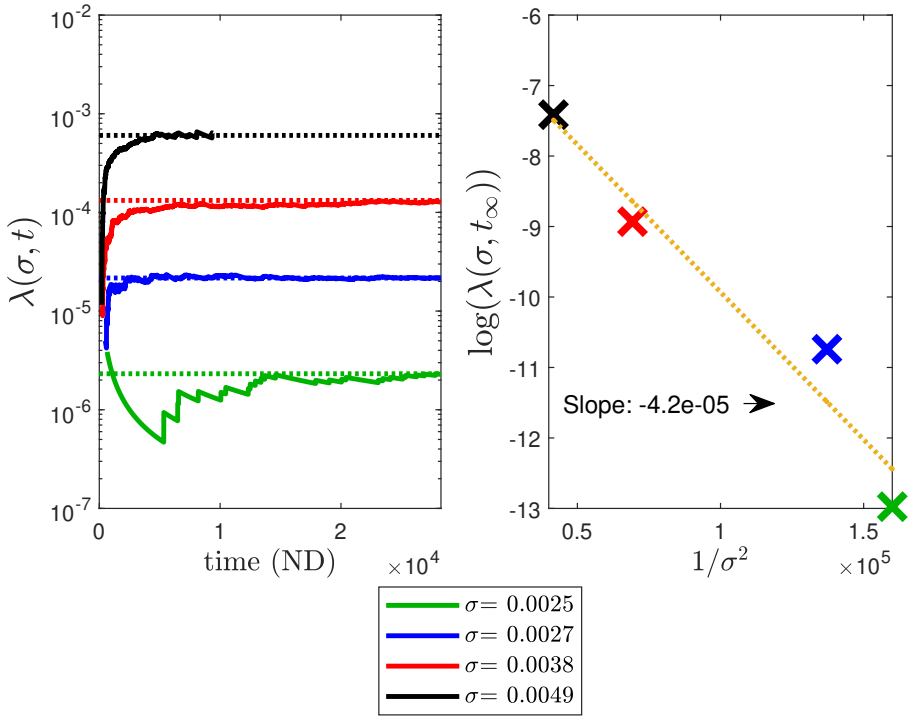


Figure 5.25: Estimates of the quasipotential U extracted from the slope of $\log(\lambda(\sigma))$ and $1/\sigma^2$.

Note that in Fig. 5.25, $\lambda(\sigma)$ is calculated at all values of t and approaches a constant after an initial transient. The negative of the slope of the best fit line to $\log(\lambda(\sigma))$ and $1/\sigma^2$ yields $U \approx 4.2E-5$. This is a stochastic estimate of the quasipotential extracted from stochastic numerical simulations at $f_i = 18Hz$ which is equivalent to $\Omega = 0.9$ in nondimensionalized form.

An exponential relationship between the excitation frequency and the escape time is observed in the experimental system. To explore, the origin of this behavior of the stochastic behavior of the system model as a function of frequency is also studied. The basins of attraction of the system model at the frequencies $f_i = [17.5, 18, 18.5, 19]$ Hz are shown in Fig. 5.26.

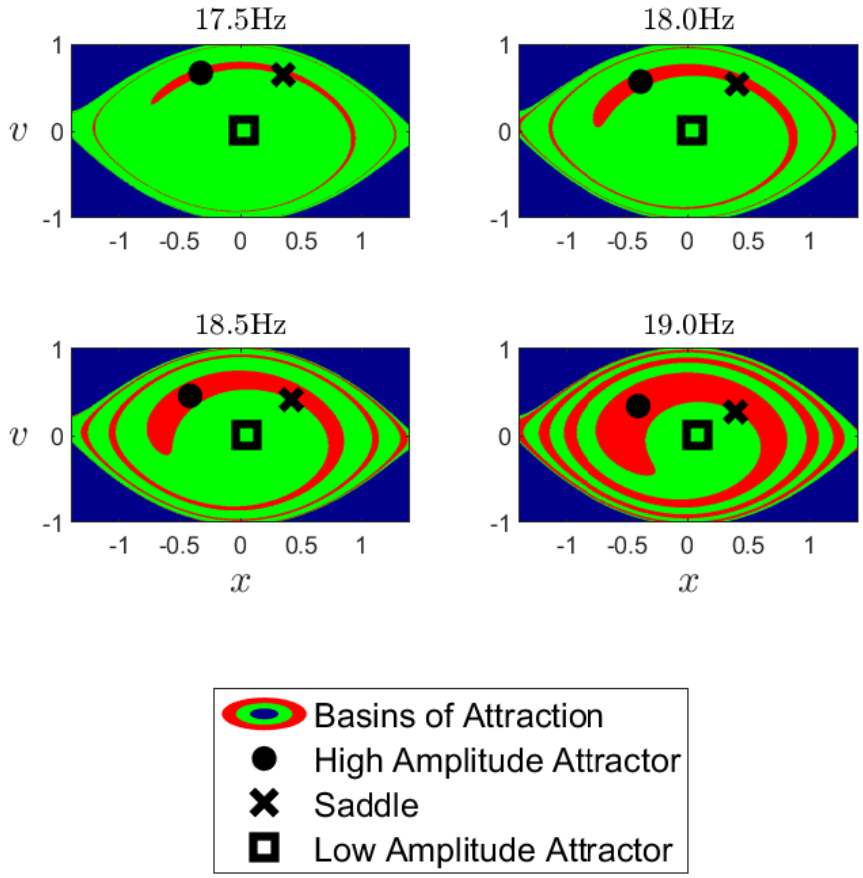


Figure 5.26: Basins of attraction of the system model for different excitation frequencies, f_i. Notice that the domain of the high amplitude basin of attraction increases in area with excitation frequency.

Notice that the high amplitude basin of attraction shown in red increases in size with increasing excitation frequency. These frequencies are all within the region of multiple stability of the system model. Box plots of the escape times as a function of excitation frequency are shown in Fig. 5.27. Similar to the experimental trials, the simulations results indicate an exponential relationship between the excitation frequency and the

median escape time.

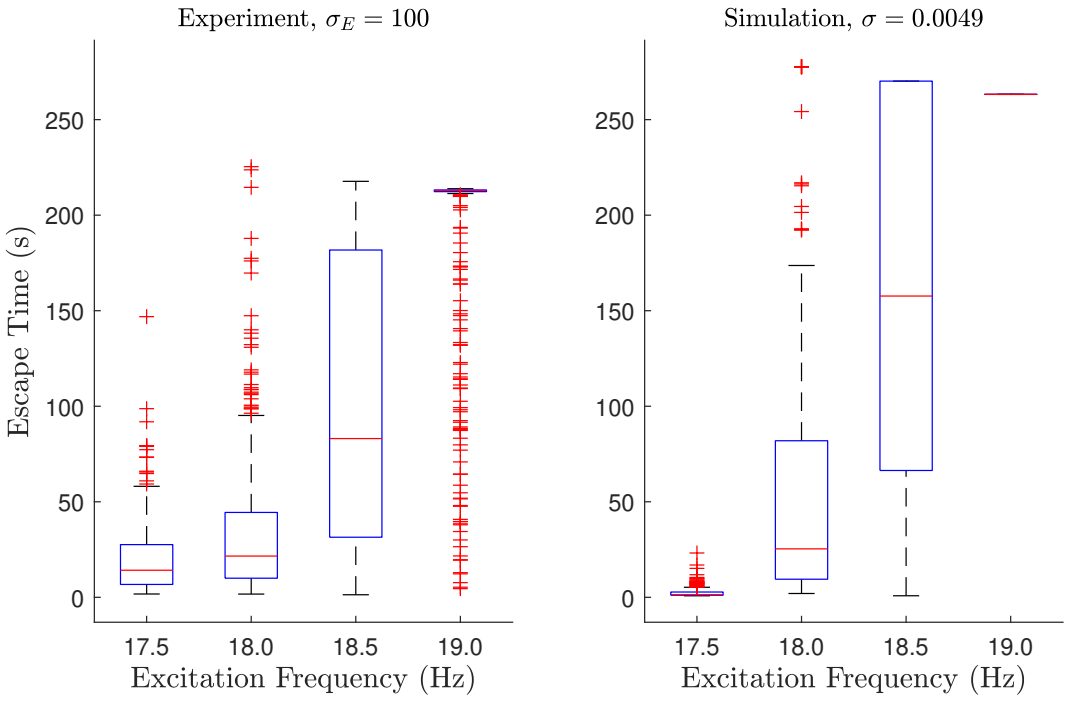


Figure 5.27: Box plots of the escape times of the experiment (left) and the Euler-Maruyama simulations (right) as a function of excitation frequency.

The probabilities of remaining in the high amplitude basin as a function of time and excitation frequency are shown in Fig. 5.28. This figure is qualitatively comparable to the experimental results in Fig. 5.19.

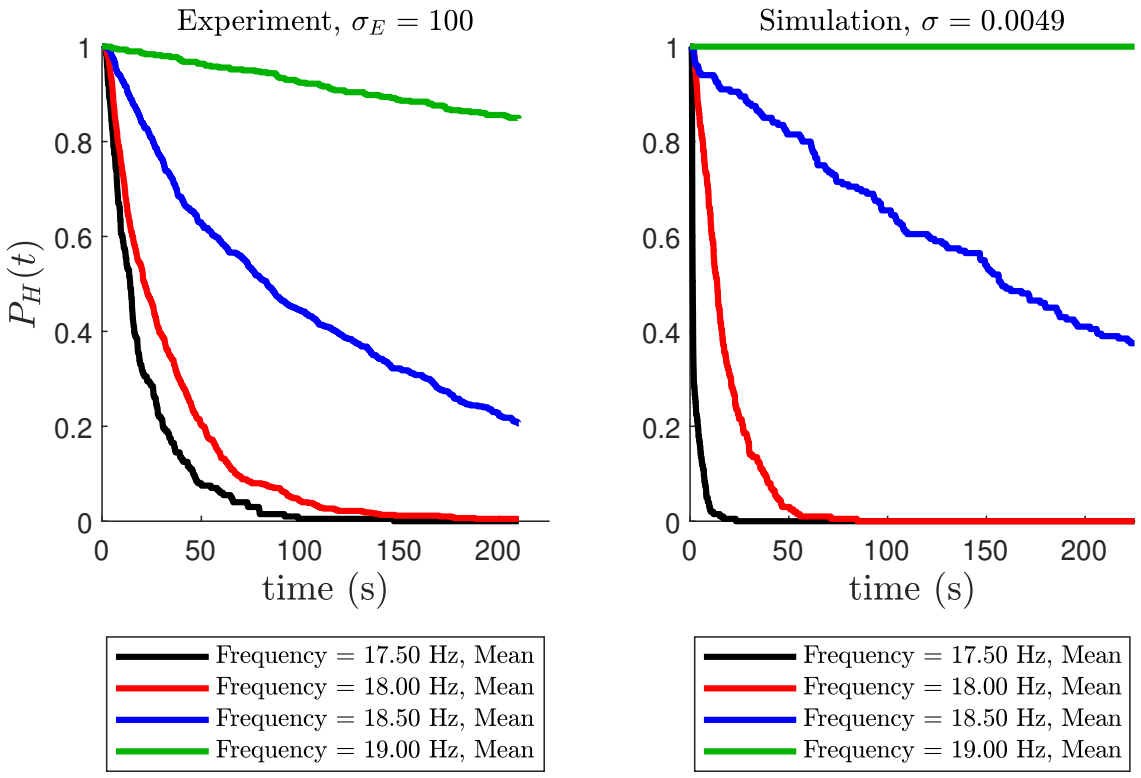


Figure 5.28: Estimates of the probability of remaining in the high amplitude attractor of the experiment (left) and simulation (right) data as a function of time and frequency.

By using the methodology discussed in Chapter 4, the optimal transition paths are computed for the parameters in the model of the cantilever beam. The Poincaré section of the resulting transitions are shown in Fig. 5.29 for the 4 excitation frequencies. The corresponding basins boundaries at each frequency are also shown in gray. The transition paths have obvious similarities, they all begin near the high amplitude attractor, rotate counterclockwise and then deviate towards the saddle. Via the saddle they escape the basin boundary and then descend following the deterministic dynamics of (5.15) to the low amplitude attractor. Noticeable differences include the number of loops in the descent to the low amplitude attractor, which is sensitive to the excitation frequency,

and that the area covered by the escape path in the high amplitude basin changes with the size of the basin of attraction. The numerical transition paths at the weak noise limit are comparable to the transition paths observed in the experiment, but they have some significant differences. Most importantly, the optimal escape paths cross the basin boundary at the saddle point, but the transition paths in the experiment have unknown basin boundaries and unknown location of saddle cycle. They can in practice move near the possible location of a saddle via either basin. That is, the optimal escape path is formulated with the assumption that $\sigma^2 \to 0$, but in the presence of finite σ, escape paths can take the form of crossing the basin boundary at any point of the basin boundary, and after crossing the paths can follow the stable manifold of the saddle to the saddle prior to continuing to the low amplitude attractor. There are no determined basins of attractions or saddle solutions for the experimental system that could be used for comparison.

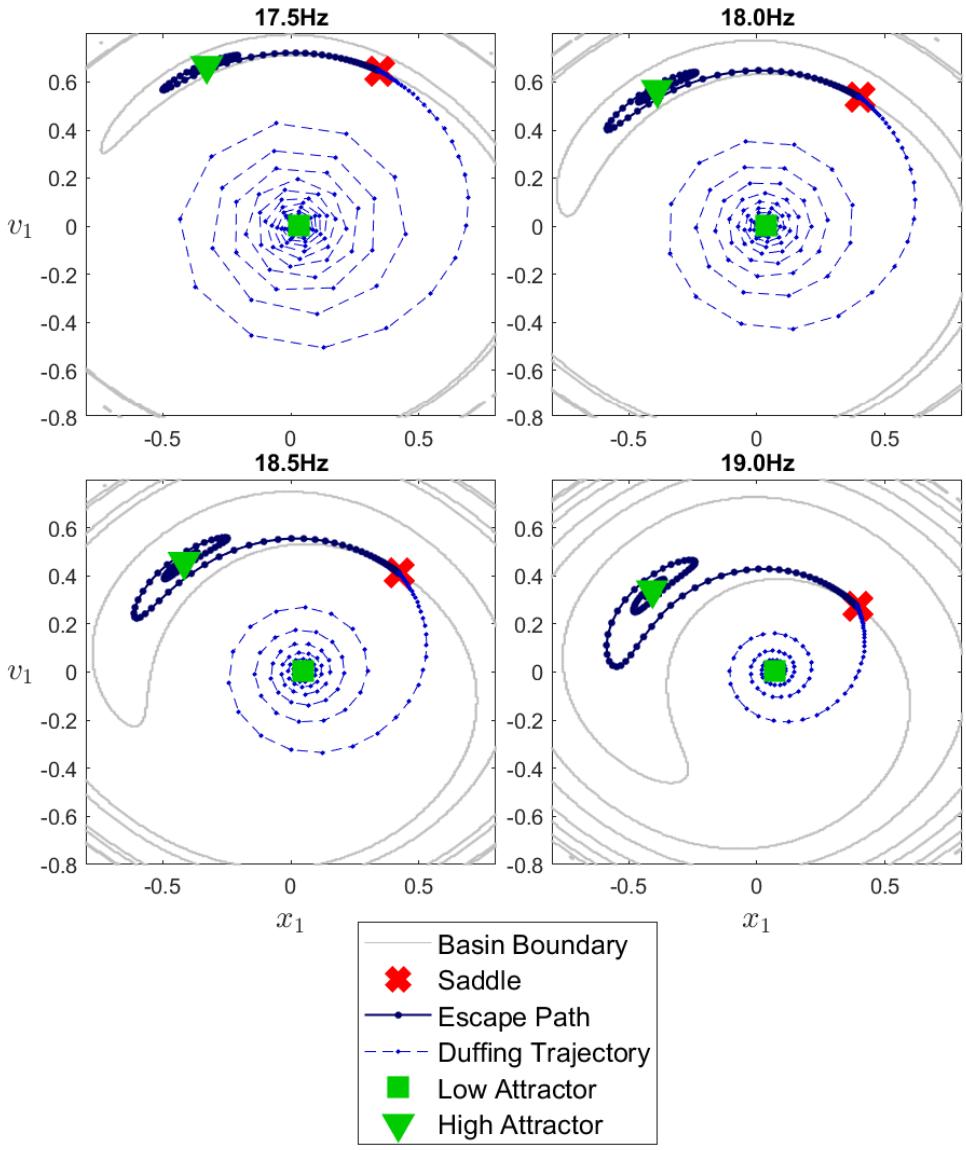


Figure 5.29: The most probable escape paths out of the high amplitude attractor of the system model for different excitation frequencies.

The optimal transition paths of the system model are interesting because these paths can be used to compute the quasipotential. The quasipotential is a function that quantifies

the minimum action, a type of work, required for a system to transition from one state to another state. In the context of escapes from basins of attraction, the quasipotential can quantify the action required to escape the basin, and it is the action required to create the optimal escape path. In this manner, the quasipotential is a quantifier of the size and depth of a basin of attraction. The quasipotential for different excitation frequencies of (5.16) are shown in Fig. 5.30

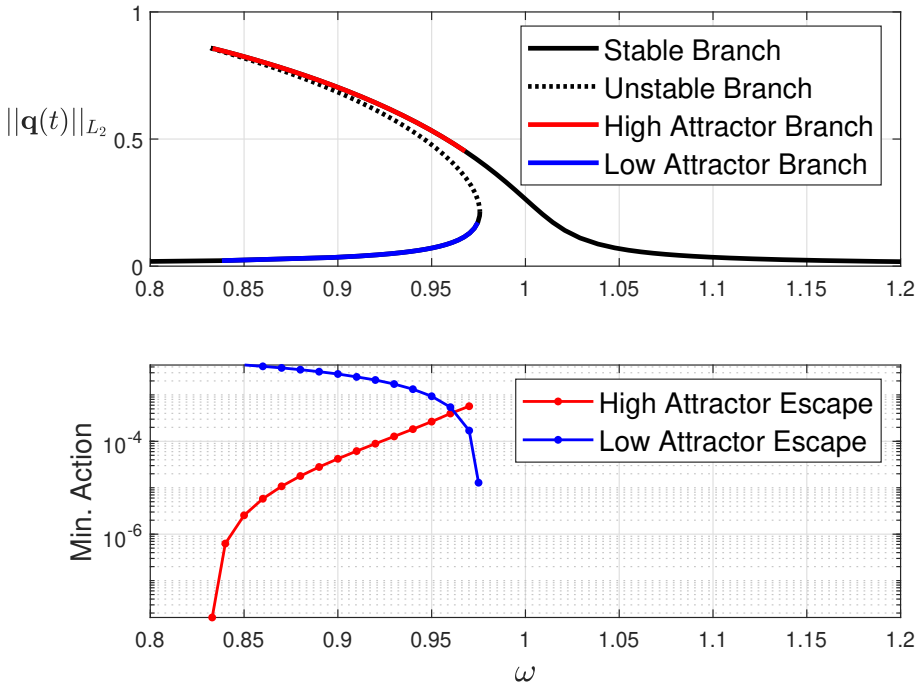


Figure 5.30: The quasipotential as a function of frequency for escapes out of the high amplitude and low amplitude attractors, shown in red and blue, respectively. Notice that the quasipotential to escape the high amplitude attractor is lower in magnitude than the quasipotential to escape the low amplitude attractor for the majorities, except for those very close to the jump up frequency. This suggests the probability of transitioning from high amplitude response to low amplitude response far exceeds the probability of transitioning from low amplitude response to high amplitude response for the majority of frequencies of excitation.

Notice that the minimum action to escape the high amplitude attractor is much smaller than the minimum action to escape the low amplitude attractor, except near the jump up frequencies.

5.7 Discussion

In this chapter, the effect of noise on a rotating cantilever structure and on a softening Duffing oscillator were examined. The experimental system was shown to demonstrate characteristic nonlinear phenomena, including multiple stable responses under the influence of an external periodic excitation. The experiment was designed to produce large quantity of long duration noise trials. Through these noise trials, evidence was created that shows noise could create transitions between the high amplitude response and the low amplitude response, with probabilities that depend on the intensity of the noise and the frequency of the external excitation.

In addition, hundreds of long duration noise trials were run that started at the low amplitude response. These trials were performed with a variety of noise intensities and excitation frequencies. The system did not transition from the low amplitude response to the high amplitude response in any of these trials. That is, it is so much less probable for this transition to occur that it was never observed experimentally at the considered range of frequencies. There was an exception to this observation: transitions did occur to a higher amplitude response at the jump up frequencies, however, these transitions when they were observed occurred with or without noise being added to the control signal.

By itself, the experimental results can provide interesting new insights. The cantilever beam structure in this chapter could, for example, represent a blade of turbomachinery. It was demonstrated that if this beam experiences nonlinear restoring forces, it can experience potentially undesired high amplitude responses. Furthermore, it was demonstrated that for certain designs influenced by noise, with much higher

probability, the system will transition out of the high amplitude response than into the high amplitude response. This nearly one directional behavior supports the idea that noise from the environment or an open loop control strategy can be useful to keeping a design in desirable operating conditions.

In order to explain the source of the stochastic nonlinear behavior in the experiment, a nonlinear, 1-DOF, lumped mass, spring-mass-damper system model for the cantilever structure was proposed. This model is a significant simplification of the experiment, yet it still provides useful insight into system behavior. In particular, it was demonstrated that the Euler-Maruyama simulations of the system model qualitatively reproduce the relationship between escape times and probability of escape with noise intensity and frequency of excitation parameters. Furthermore, it was demonstrated that similar transition paths can be observed in the experiment than in the system model. Additionally, it was shown how the quasipotential varies with frequency of excitation in this system; it was observed that the quasipotential of the escape from the high amplitude response are much smaller than the quasipotential of escapes from the low amplitude response. It stands to reason that the observed nearly one directional transition behavior in the experiments occur because the amount of action (work) required to escape the low amplitude response is much greater than the amount of action (work) to escape the high amplitude response. The nonlinear system model with numerical tools such as the one used in this chapter to quantify the probability of transitions and the action required for transitions could be used by designers to develop physical nonlinear systems that exhibit desirable responses to noise.

The system model has limitations. It was shown that at high amplitude

responses, the experimental frequency response diverges from the response of the model. Furthermore, the noise multiplier in the experiment cannot be compared via derivation to the noise multiplier in the system model. This is in part because the system model assumes white noise while the actuator in the experiment delivers filtered noise. Furthermore, the behavior of the experiment and the system model is highly sensitive to noise intensity, and small errors from assumptions in a derivation could lead to significantly different expected results.

Comparisons were created between the simulations and the experiment by using a best fit data driven approach between the measured escape times and the noise intensities. The resulting comparisons have errors that are adequate for qualitative observations of how the systems respond to parameter changes, but may be inadequate for prediction of the stochastic response. Note that the latter is not an objective of this work. Considerations of additional nonlinear terms, a model with more degrees of freedom, filtered noise models, or noise models with noise intensities calculated from the power spectrum could improve on the comparisons as a subject of future work.

Chapter 6: Influence of Noise on Response Localizations of a Circular Cantilever Beam Array

6.1 Introduction

An experiment is designed and prototyped to generate experimental evidence of the effect of noise on a circular oscillator array of macro scale cantilever beams. Each beam of the array could represent a blade of a bladed disk, for example. There are similarities between the experiments discussed in Chapter 5 and those discussed in this chapter, including that both experiments use the same excitation system, and similar experimental methodologies to add noise to the system and collect data. The system in this chapter is significantly more complex and achieves the following objectives:

1. The circular array reproduces nonlinear behavior in the frequency response including multi-stability and hysteresis.

2. The circular array can be used to study transitions between stable vibration modes.

3. The circular array can be tuned so that the observed multi-stability is primarily due to nonlinearity in the system and not due to inhomogeneity in the system.

4. The circular array can be manipulated such that expected nonlinear vibration modes

can be observed in the frequency response.

5. The stable vibration modes of the array are robust to small noise from the environment such that a dataset where no noise is intentionally added to the system serves as the control.

6. The experiment can be operated autonomously to produce a high quantity of long duration noise trials.

A full literature review of the problem of interest and prior experimental work is available in Chapter 2. The majority of prior work has focused on inline arrangements of oscillators arrays that are easier to design and implement. In this work, the beams are arranged with periodic boundary conditions, which are more realistic to application in turbomachinery. As discussed in Chapter 2, Niedergesäß *et al.* [34] also developed a circular oscillator array with three beams to provide evidence for nonlinear modes. Niedergesäß *et al.* used a shaker to vibrate the beams and used contact between the beams and a rigid surface to produce discontinuous hardening nonlinear behavior. In contrast, here, the array uses magnets to produce softening nonlinear behavior, has up to eight beams arranged in a symmetric cyclical manner, uses a stiffness tuning system to autonomously produce desired nonlinear modes including response localizations, and is primarily used to study the influence of noise on nonlinear vibration modes. Note that though experiments are performed on the array with up to eight beams, response localizations are observed only in arrays of up to four beams because as will be discussed in this chapter, high coupling interactions between the beams for the eight beam arrangement may have made response localizations unstable in the eight beam system.

6.2 Experimental Arrangement and Experiments

An introduction to the design of the excitation system and data acquisition system is available in Chapter 5. These same systems are used for the circular array as well, with minor modifications. An image of the entire experimental arrangement is shown in Fig. 6.1.

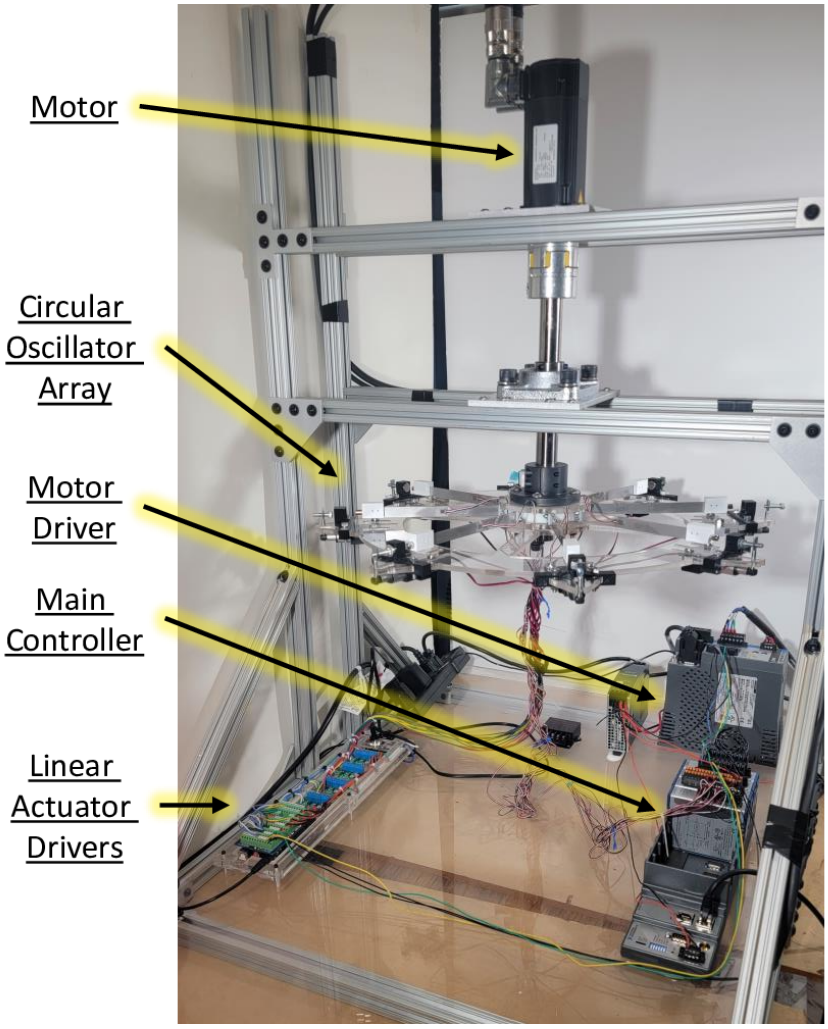


Figure 6.1: Picture of the experimental system with the excitation system consisting of motors, drivers, controllers, and the circular oscillator array.

The test piece in the experiment is entirely redesigned into the circular array of eight cantilevers beams shown in Fig. 6.2. As in Chapter 5, each cantilever contains a magnet at the tip, and the base of the test piece contains a set of magnets that rotate with the rigid base.

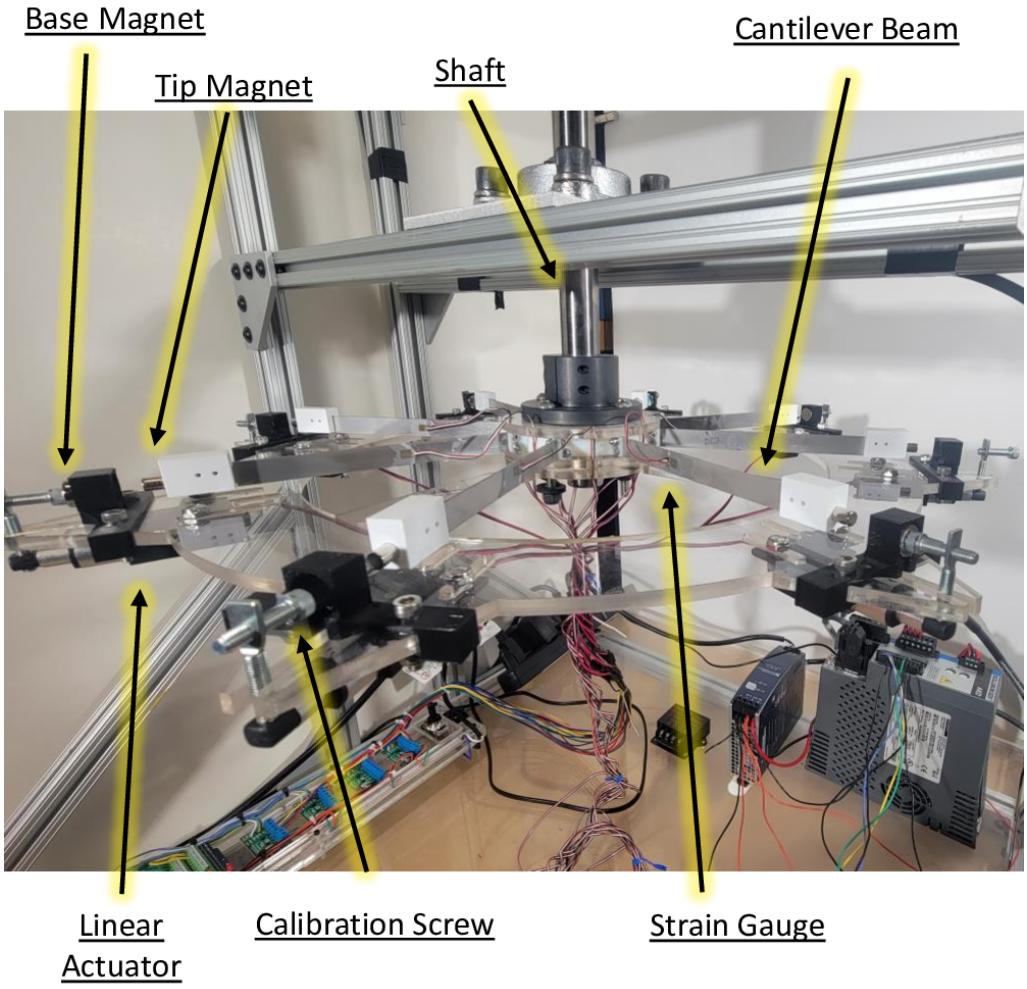


Figure 6.2: Picture of the circular oscillator array consisting of eight cantilever beams. The depicted 120Ω strain gauges are used for data acquisitions. The linear actuators are used for nonlinear mode manipulation. The permanent magnets and the calibration screws are used to calibrate the linear stiffness and nonlinear stiffness of the beams.

Special considerations went into the design and manufacturing of the system to ensure homogeneity between the cantilever structures. All beams are cut to a length of 16.5 cm with a water jet from 0.06 ± 0.005 cm thick multipurpose 304 steel sheet metal. The center mount is 3D printed using a Stratasys Objet500 Connex3 printer with *VeroWhitePlus RGD8350* connex as the material. The base is laser cut from 1/4" acrylic. Magnet holders are mounted into the acrylic base that allow the magnets to move and rotate on a single axis. A magnetic calibration screw mounted on a linear actuator is used to set the position of the magnet. The default position of the magnet can be adjusted by rotating the calibration screw. Without the magnets, each of the beams had a first resonance at $f_n \approx 10$Hz. With the magnets the beams could exhibit a range of natural frequencies that depended on the position of the magnet and the strength of each magnet.

A calibration procedure is developed to tune the beams to approximately the same natural frequency by adjusting the position of the magnets. The tuning (calibration) procedure had the following steps: (i) A heavy cloth is placed on all beams except the beam to be tuned to minimize forces from the vibration of other beams during tuning. (ii) The beam to be tuned is displaced using a finger about 1 cm from the at rest position. (iii) The transverse oscillations of the beam after removing the finger are acquired by using a strain gauge and recorded for 15 seconds at a sampling frequency of 500 Hz. (iv) The first 5 seconds of the recorded strain signal are thrown out to remove any undesired contributions from the finger and to allow transient high amplitude oscillations of the beam to die out. (v) An FFT of the remaining 10 seconds of recorded oscillations is used to identify the first linear natural frequency of the beam. (vi) If this linear natural frequency of the beam is higher than desired, the calibration screw is rotated bringing

the base magnet farther from the tip magnet and thereby reducing stiffness. Likewise, in the opposite scenario, the base magnet is moved in closer to the tip magnet to increase stiffness.

The data collection procedure is performed by using Labview with the strain gauge data coming from the cantilever beam acquired by using the National Instruments compactRIO9074 module. The procedure is not sensitive to the initial displacement of the beam since it is used to measure frequency of oscillation at low amplitudes and not the amplitudes themselves. The methodology has 0.1 Hz precision on the natural frequency of the beam. Tuning of all 8 beams within 0.1 Hz of a desired frequency usually takes about 30 minutes.

6.2.1 Real-time Stiffness Detuning System

This experiment is designed to study transitions due to noise out of or into response localizations of circular oscillator arrays. That said, creating response localizations to begin with is not a trivial task. Perkins *et al.* [4] and Alofi [9] used manual perturbations to create response localizations. This approach is time-consuming and not simple to reproduce. Niedergesäß *et al.* [34] used unspecified external forces to create response localizations. Kimura *et al.* [32] used electromagnets to manipulate response localizations in their linearly arranged macro-scale oscillator array. Electromagnets are either too weak or too heavy to use on a rotating circular cantilever array. Nevertheless, inspired by the work of Kimura *et al.* , a stiffness detuning system is developed that uses linear actuators to move permanent magnets and manipulate the initial conditions

of nonlinear modes of the system. The linear actuators are shown in Fig. 6.2. These actuators move permanent magnets towards the beams and then back to the default position on the command of the main controller.

The basic idea of the detuning system is as follows: By using excitation frequency control, the cantilever beams of interest are brought into a high amplitude oscillation mode wherein all desired cantilever beams vibrated in a high amplitude steady state. Then, the detuning system increases the stiffness of certain beams by moving the base permanent magnets closer to the respective beams. As a result of the increase in stiffness, the beams cease to resonate at the excitation frequency. When the permanent magnet return to the default position, these beams remain in a low amplitude vibration steady state because they did not have the initial condition to move towards the high amplitude steady state. When all but one beam changes from the high amplitude state to the low amplitude state, the resulting mode is a response localization. This procedure relies on sufficiently small interaction between the beams that response localizations are stable. For high coupling forces, the procedure results with all beams changing state to low amplitude modes or all beams remaining in the high amplitude mode after the permanent magnets return to the default positions.

6.3 Influence of Noise on Two Coupled Cantilever Beams

To study the response of the cantilever beam array with a focus on two beams, two of the eight beams on opposing sides of the array are tuned to a frequency of $f_n \approx 19.0 \pm 0.01$Hz. The beams are numbered in counterclockwise manner from 0 to 7 as shown in Fig. 6.20. In this case, Beam 3 and Beam 7 are the tuned beams of interest. The base magnet of the remaining cantilever beams are removed so that the other six beams vibrated freely with a first natural frequency of $f_n \approx 10$ Hz. The excitation system is used for excitation frequencies in the range $15 \leq f_i \leq 21$ Hz, and over these frequencies, the response of each of the other six beams is negligible.

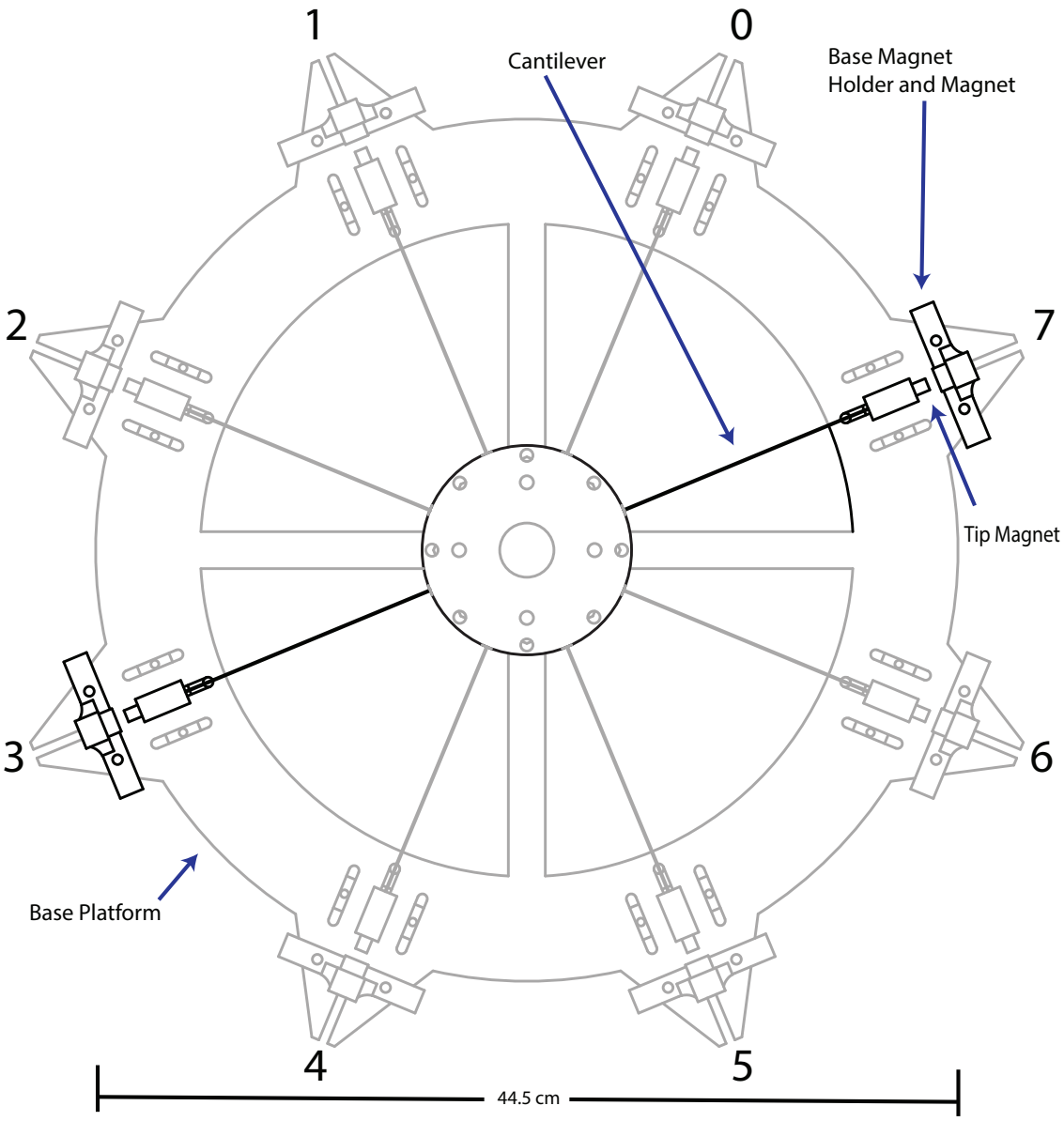


Figure 6.3: Top view schematic of the circular cantilever beam array with tuned beams of interest 3 and 7 highlighted in black.

6.3.1 Frequency Response

The frequency response of the system is acquired by using frequency sweeps similar to ones described in Section 5.3. In the down sweep shown in Fig. 6.4, both beams

gradually increase in amplitude with decreasing excitation frequency. At the excitation frequency, $f_i = 17.25$ Hz, due to the change in excitation frequency both beams transition from high amplitude oscillations to low amplitude oscillations; this is hereby referred to as the *jump down* frequency.

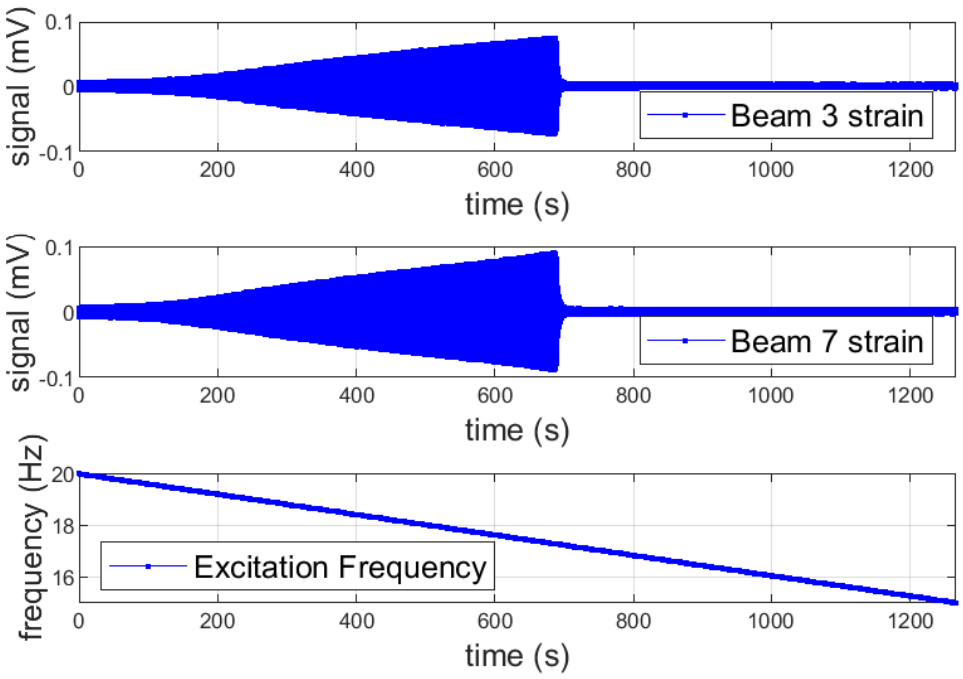


Figure 6.4: Response time histories for Beams 3 and 7 near resonance when slowly decreasing the excitation frequency.

On the other hand, in the up sweep shown in Fig. 6.5, both beams gradually increase in amplitude with increasing frequency until the beams suddenly transition to a much higher amplitude oscillation at $f_i = 18.6$ Hz; this is hereby referred to as the *jump up* frequency.

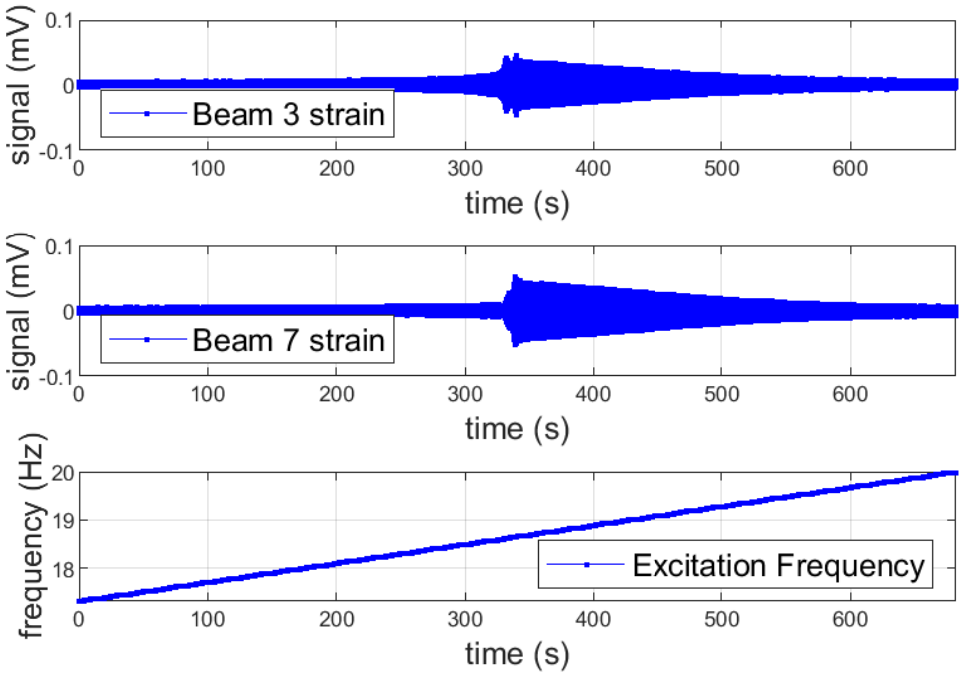


Figure 6.5: Response time histories for Beams 3 and 7 near resonance when slowly increasing the excitation frequency.

The region between the *jump down* and *jump up* frequency of this system, 17.25 Hz $\leq f_i \leq 18.6$ Hz is hereby referred to as the hysteresis region because the response of the system due to changes in excitation frequency depends on the state of the system at the time that the excitation frequency is changed. In this region, multiple stable responses exist for this system including the HH and LL modes, wherein both beams vibrate at high (H) amplitudes or both at low (L) amplitudes, respectively.

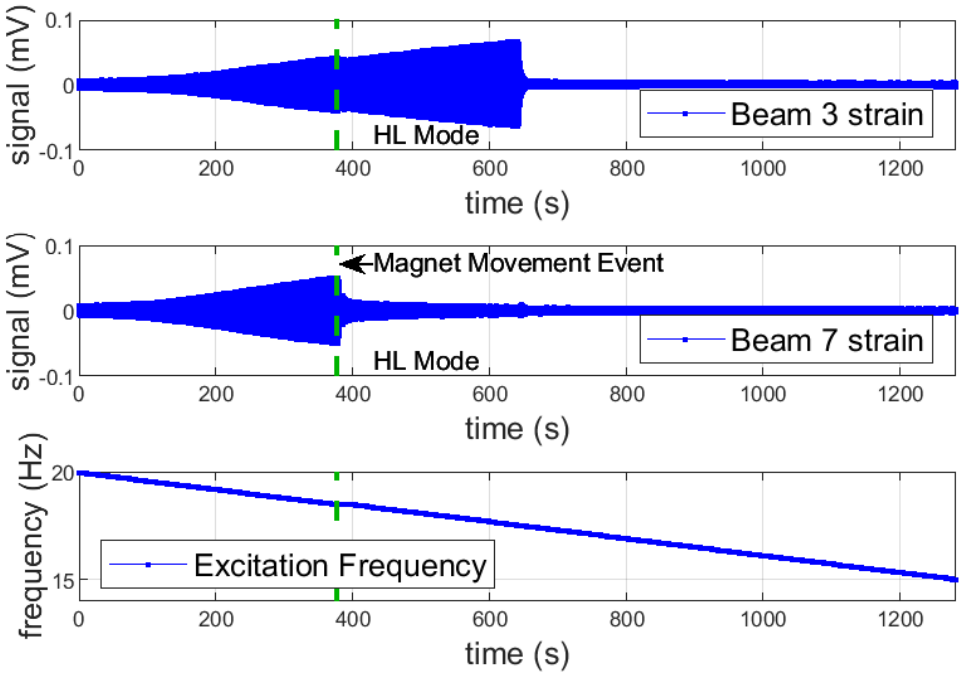


Figure 6.6: Response time histories for Beams 3 and 7 near resonance when slowly decreasing the excitation frequency. At a time of approximately 390 seconds, the linear actuator corresponding to Beam 7 is powered to displace the base magnet temporarily; this is labeled as the *Magnet Movement Event*. After the magnet movement event, the linear actuator returned the magnet to the original position and the frequency sweep continued in the HL mode.

A response localization in this circular array of two beams takes the form of one beam vibrating at a high amplitude while the other beam vibrates at a low amplitude. This is known as the HL mode. The HL mode is generated in the frequency sweep by first decreasing the frequency of excitation from 20 Hz to 18 Hz to get the beams in the HH mode. Second, the position of the base magnet of Beam 7 is moved creating a temporary

change in stiffness that changed the initial state of Beam 7. Thereafter, the frequency sweep is continued in both directions to observe the response of the HL mode to changes in the excitation frequency. The creation of the HL mode can be observed in Fig. 6.6 at the time of the magnet movement event. Furthermore, a transition from the HL mode to the LL mode can be observed at the jump down frequency due to changes in frequency. The first harmonic amplitude of the response of each beam at each frequency is calculated using (5.1) as in Section 5.3. The sum of the first harmonic amplitudes of Beam 3 and Beam 7 are shown in Fig. 6.7 as a function of excitation frequency for the HH, LL, and HL modes.

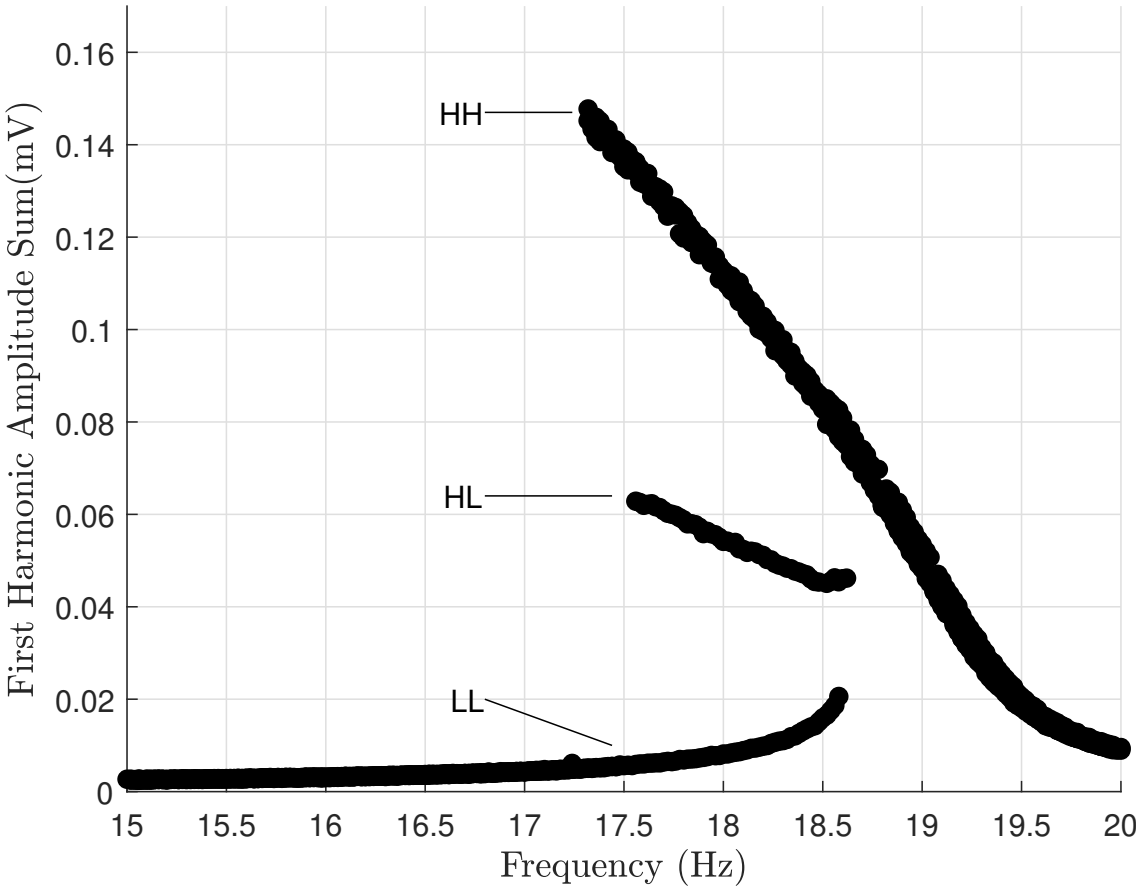


Figure 6.7: The sum of the first harmonic amplitudes of Beam 3 and Beam 7 for different excitation frequencies. A total of four frequency sweeps with different initial conditions are performed to acquire the data in this figure. The sweeps are conducted in a manner to record the steady-state response at each frequency.

6.3.2 System Identification

The system model for the circular array can be thought of as a set of coupled individual cantilever beams with dynamics that follow a similar model to (5.10) derived in Section 5.4.1. This model for an array of N oscillators with nondimensionalized

displacement vector, $\boldsymbol{x} \in \mathbb{R}^N$ can take the form

$$\boldsymbol{x}'' + \eta\boldsymbol{x}' + \alpha\boldsymbol{x} + \beta\boldsymbol{x}^3 = \hat{F}_0 \cos(\Omega\tau)\mathbf{1} + \boldsymbol{G}(\boldsymbol{x}) \tag{6.1}$$

Here η, α, β, $\hat{F}_0$, Ω, and τ are the damping coefficient, the linear stiffness coefficient, the cubic nonlinearity coefficient, the excitation force amplitude, the frequency of excitation, and time, respectively; all in nondimensionalized form. An N dimensional vector of ones is shown as $\mathbf{1}$. Furthermore, $\boldsymbol{x}'$ and $\boldsymbol{x}''$ are $d\boldsymbol{x}/d\tau$ and $d^2\boldsymbol{x}/d\tau^2$, respectively. In (6.1), $\boldsymbol{G}(\boldsymbol{x})$ is an unknown function that describes the forces that the vibration of one beam exerts on the other beams. System identification is performed first assuming $\boldsymbol{G}(\boldsymbol{x}) = \mathbf{0}$, and then a correction step is added with a non-trivial candidate for $\boldsymbol{G}(\boldsymbol{x})$. With $\boldsymbol{G}(\boldsymbol{x}) = \mathbf{0}$, an initial system identification can be performed similarly as in Section 5.4. That is, each tuned beam can be assumed to be independent and to have a frequency response that can be approximated by (5.11). The amplitude of each beam is nondimensionalized and then fitted to the cost function:

$$\begin{aligned} C(\beta, \hat{F}_0) &= \sqrt{\sum_{j=1}^{N}\sum_{i=1}^{n}\left(1 + \frac{3}{8}\beta A_{ij}^2 + (-1)^{p(i,j)}\sqrt{\frac{\hat{F}_0^2}{4A_{ij}^2} - \frac{\hat{F}_0^2}{4}} - \Omega_i\right)^2} \\ p(i,j) &= \begin{cases} 0, & \text{sample } i,j \text{ to fit } H^N \text{ branch} \\ 1, & \text{sample } i,j \text{ to fit } L^N \text{ branch} \end{cases} \end{aligned} \tag{6.2}$$

Here, A_{ij} is the nondimensionalized experimental amplitude of beam with index j at nondimensionalized excitation frequency Ω_i, $H^N \equiv HH...H$ for a total of N H

symbols for an N beam system, and similarly, for the notation L^N. The minimizer of (6.2) for the frequency response in Fig. 6.7 is the set of parameters $\beta_L = -0.2605, \hat{F}_{0L} = 0.0059$, and $\eta_L = 0.0059$. Here the subscript L is used to indicate the minimizers of the analytical curve. The minimizer is shown graphically in Fig. 6.8 with $A_\Sigma = \sum_{j=1}^{N} A_{ij}$ at all Ω_i. Typically, this procedure underestimates η. As in Chapter 5, the resulting analytical fit for the two beam system is checked by using the numerical continuation package COCO [52] and the best fit parameters are corrected. The corrected parameters using numerical continuation for the best fit of the HH and LL branch are $\beta = -0.2605, \hat{F}_0 = 0.0059, \eta = 0.0069$; the subscript L is removed for the final corrected, parameters.

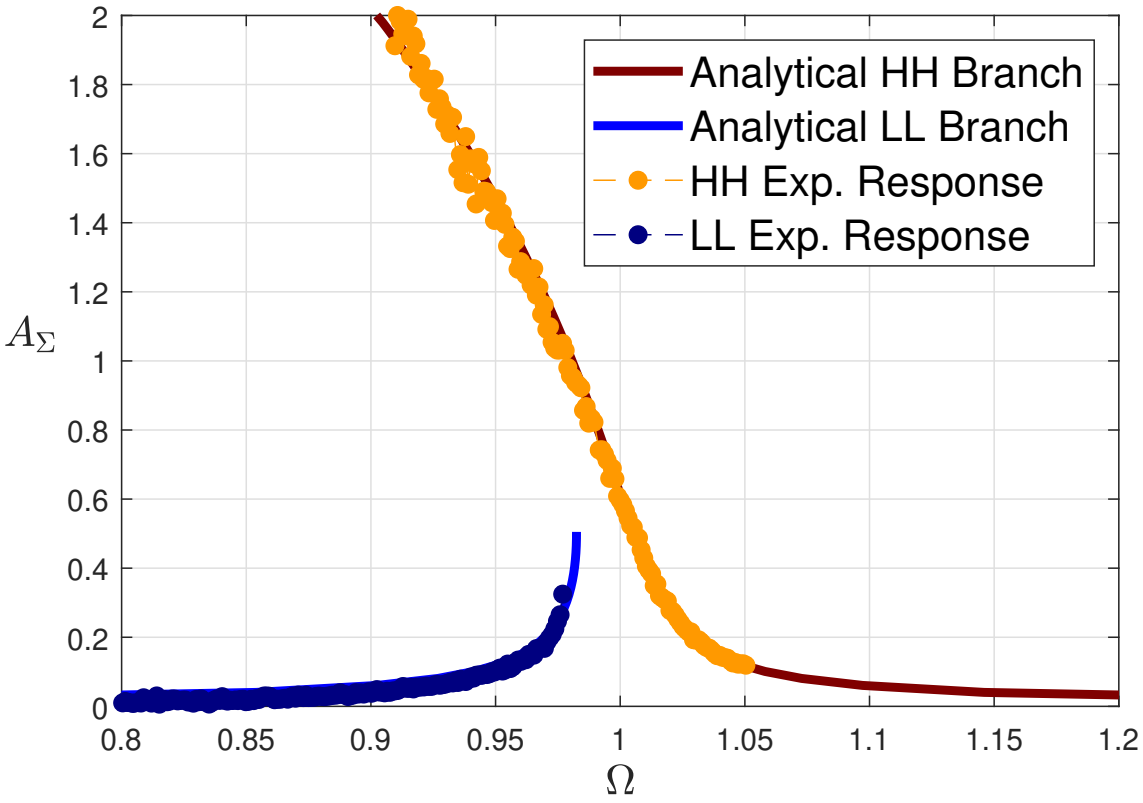


Figure 6.8: Best fit of the analytical approximation of the sum of the frequency response of four Duffing oscillators to the experimental data. The minimizing parameters are $\beta_L = -0.2605$, $\hat{F}_{0L} = 0.0059$, $\eta_L = 0.0059$.

The simplest non-trivial candidate for $\boldsymbol{G}(\boldsymbol{x})$ is the linear function $\boldsymbol{V}\boldsymbol{x}$. Here, $\boldsymbol{V}$ is a matrix of constant coefficients. Assuming that due to symmetry all beams affect each other equally through the base, a candidate for $\boldsymbol{V}$ is:

$$V_{kl} = \begin{cases} 0, & k = l \\ h, & k \neq l \end{cases} \tag{6.3}$$

Here, $h \in \mathbb{R}$. Applying the candidate $\boldsymbol{G}(\boldsymbol{x})$, the new model takes the form

$$x_k'' + \eta x_k' + (\alpha + \epsilon_\alpha)x_k + (\beta + \epsilon_\beta)x_k^3 = \hat{F}_0 \cos(\Omega\tau) + \sum_{l \neq k} h x_l \quad k \in [1, 2, ..., N] \quad (6.4)$$

where ϵ_α and ϵ_β are included as error corrections to the prior fit by the inclusion of non-trivial $\boldsymbol{G}(\boldsymbol{x})$ in the model. It can be shown that in the model for $\boldsymbol{G}(\boldsymbol{x}) = 0$, and in the experiment, the oscillators vibrate synchronously (in phase) in the H^N branch and the L^N branch. As a result, $x_k = x_l \forall \quad k, j \in [1, 2, ..., N]$ in the H^N and L^N branches, and applying this to (6.4), $\epsilon_\beta = 0$ and $\epsilon_\alpha = (N-1)h$. Therefore, the model takes the form

$$x_k'' + \eta x_k' + (\alpha + (N-1)h)x_k + \beta x_k^3 = \hat{F}_0 \cos(\Omega\tau) + \sum_{l \neq k} h x_l \quad k \in [1, 2, ..., N] \quad (6.5)$$

with h as the only remaining unknown. Since h from (6.5) is only relevant in asynchronous oscillations, and response localizations are asynchronous modes, h is solved for by minimizing the error between the experimental response localizations and the numerical response localization. In particular, it is observed that small changes to h had minor effect on the amplitude of the response localizations, but had large effect on the phase of the response localizations. As a result, the following cost function is developed to minimize the phase error between the experimental data and simulation data:

$$C_\phi(h) = \sqrt{\sum_{j=1}^{N} \sum_{i=1}^{n} \left(\phi_j(\Omega_i, h) - \phi_{Ej}(\Omega_i)\right)^2} \quad (6.6)$$

Here, $\phi_{Ej}(\Omega_i)$ is the experimental phase of beam with index j at excitation frequency Ω_i

and $\phi_j(\Omega_i, h)$ is the simulated phase of beam with index j at excitation frequency Ω_i using a given value of h. The cost function is evaluated for phase of the response localization HL and $LHLL$ for the two beam and four beam systems, respectively. The phase angles are calculated from the Fourier series coefficients a_c, a_s from (5.1):

$$\phi = \tan_2^{-1}(a_s, a_c) \tag{6.7}$$

Here $\tan_2^{-1}()$ is the four quadrant tangent inverse. The phase of the experimental strain signals are all relative to the control signal. The phase of three modes are shown for Beam 3 and Beam 7 for the two tuned oscillator (N=2) frequency sweeps in Fig. 6.9. Notice that both beams have nearly the same phase angle for the HH and LL mode. On the other hand, notice a significant difference in the phase angle between Beam 3 and Beam 7 in the HL mode.

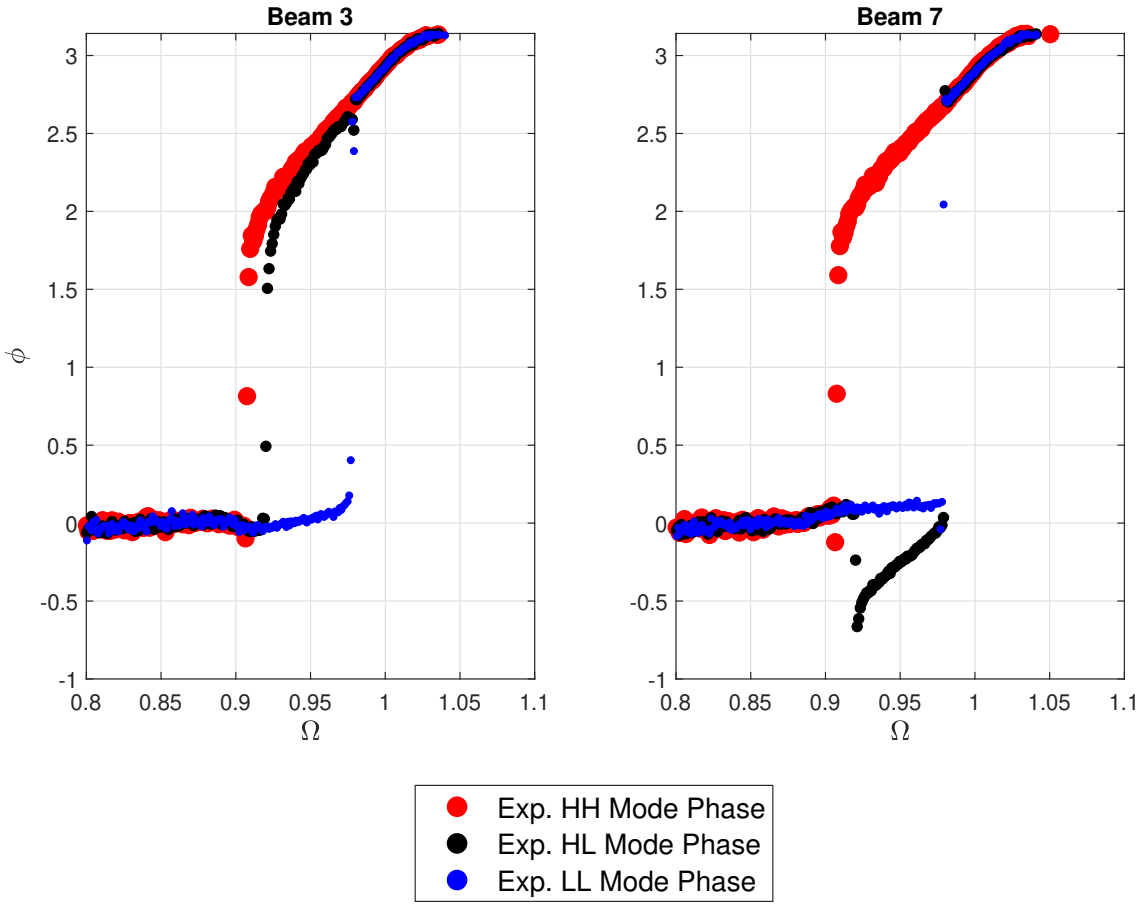


Figure 6.9: The experimental phase response of the LL, HL, and HH modes for each beam as a function of nondimensionalized excitation frequency. The phase angle, ϕ, is in radians.

The cost function (6.6) is shown as a function of h in Fig. 6.10. Notice a minimum at $h = -0.0045$.

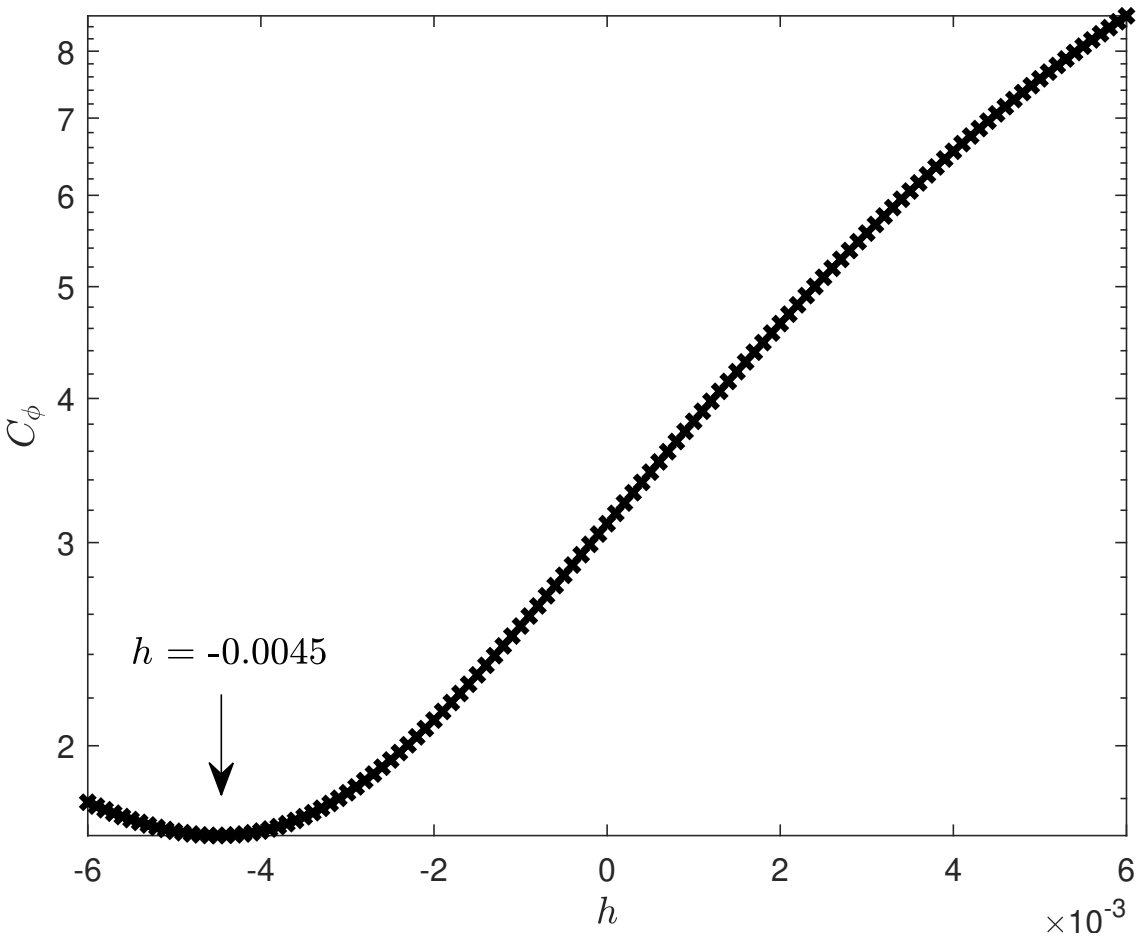


Figure 6.10: The phase cost (6.6) as a function of coupling force coefficient h.

Plots of the experimental and numerical HL mode phases are shown in Fig. 6.11 for $h = [-0.006, -0.0045, 0, 0.001]$. At a certain point for $h < -0.006$ the HL mode becomes unstable and then ceases to exist. The response $h = 0$ reflects the behavior of the system if the oscillators were to be independent (i.e., uncoupled) and not influence each other. It can be observed at $h = 0$ that the high oscillator in the HL mode has the phase of the HH mode and the low oscillator in the HL mode has the phase of the LL mode as would be expected if the oscillators were independent of each other.

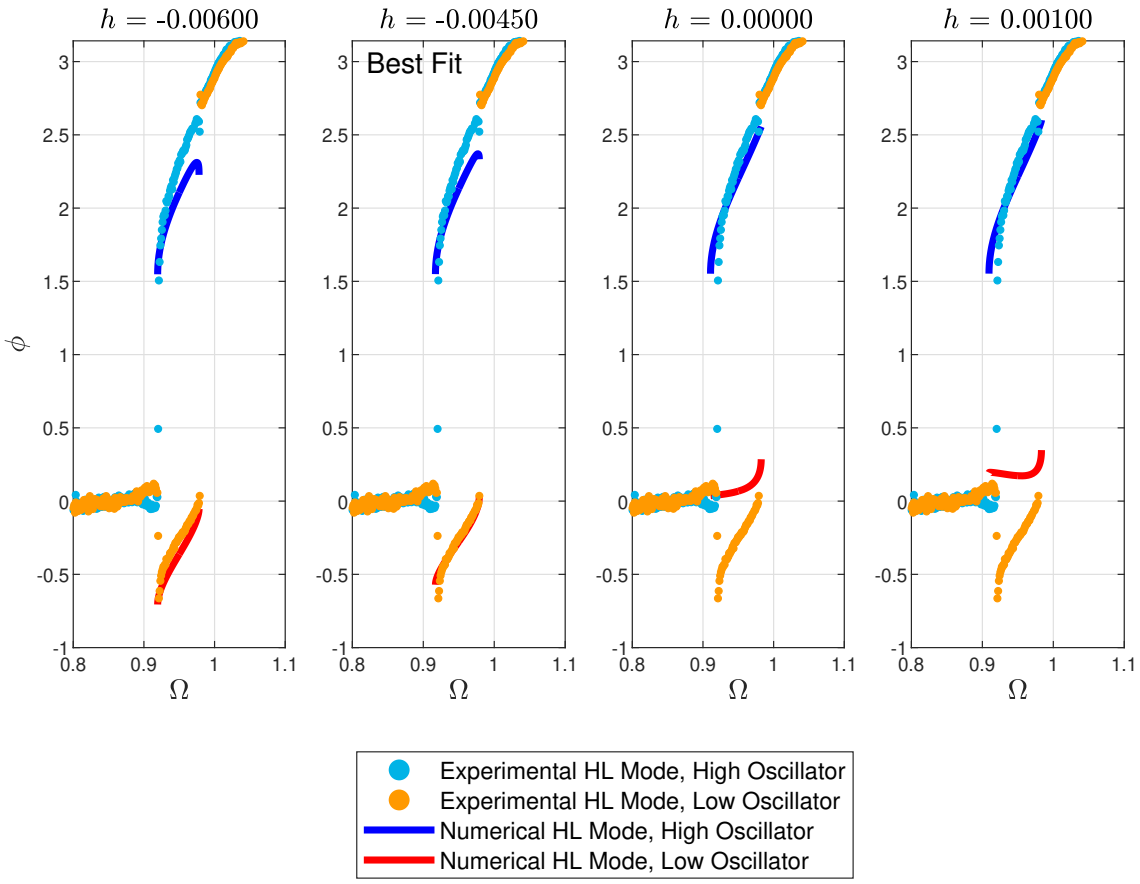


Figure 6.11: The phase response of the HL mode from experimental data and from the $N = 2$ system model of (6.5) for four different h values. In the legend, a high amplitude oscillator is denoted as "High oscillator", and a low amplitude oscillator is denoted as "Low oscillator". The phase angle, ϕ, is in radians.

The stable amplitude responses of the resulting system model with $\beta = -0.2605, \hat{F}_0 = 0.0059, \eta = 0.0069$, and $h = -0.0045$ are shown in Fig. 6.12 alongside the experimental data.

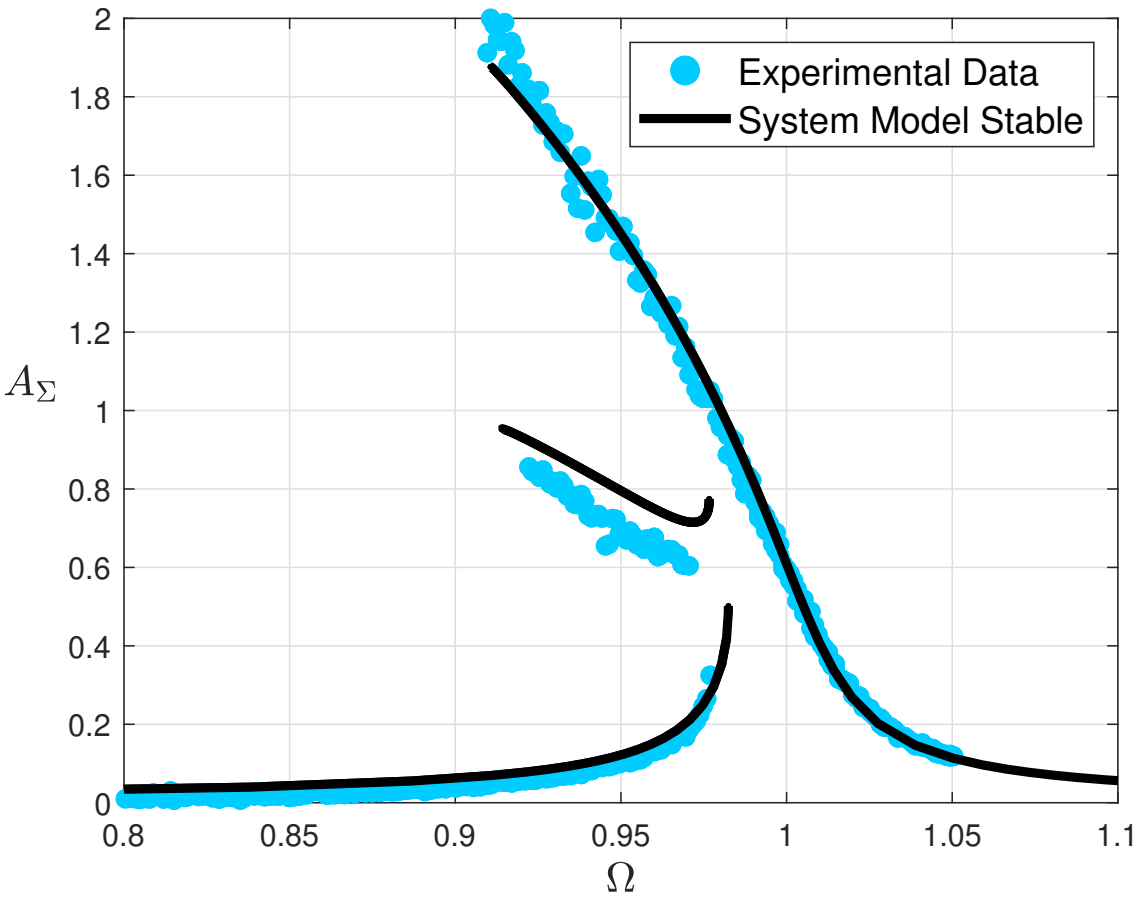


Figure 6.12: Numerical continuation frequency amplitude response of the stable modes of (6.5) with parameters $\alpha = 1, \beta = -0.2605, \eta = 0.0069, h = -0.0045, F = 0.0059$ shown with the experimental data.

6.3.3 Experimental Results

The experiment is used to create empirical evidence of transitions occurring from the HL mode to other modes due to the effect of noise. A noise trial of the experiment takes the form shown in Fig. 6.13. The responses of Beam 3 and Beam 7 are shown alongside changes to the excitation frequency, the position of the Beam 7 magnet, and the noise multiplier σ_E. For the first 40 seconds of the trial, the excitation frequency

is gradually decreased from 20 Hz to 18 Hz. For $40 \leq t \leq 70$ no changes are made to the excitation and the beams approached a steady state oscillation. At $t \approx 70$, an actuator displaced the base magnet of Beam 7 about 1 cm closer to Beam 7. In response to the change of stiffness, Beam 7 transitioned from a high amplitude oscillation to a low amplitude oscillation. At $t \approx 78$ seconds, the actuator brought the base magnet of Beam 7 back to the default position. Despite returning to the original configuration, Beam 7 remained in a low amplitude oscillation and the system as a whole approached a steady state HL mode oscillation. At $t \approx 115$ seconds, the noise multiplier is changed from 0 to 175. Despite the added noise, the system remained in the HL mode for some time until $t \approx 170$ seconds, when a transition occurred in Beam 3 from a high amplitude oscillation to a low amplitude oscillation, and the system as a whole transitioned to the LL mode due to the influence of noise.

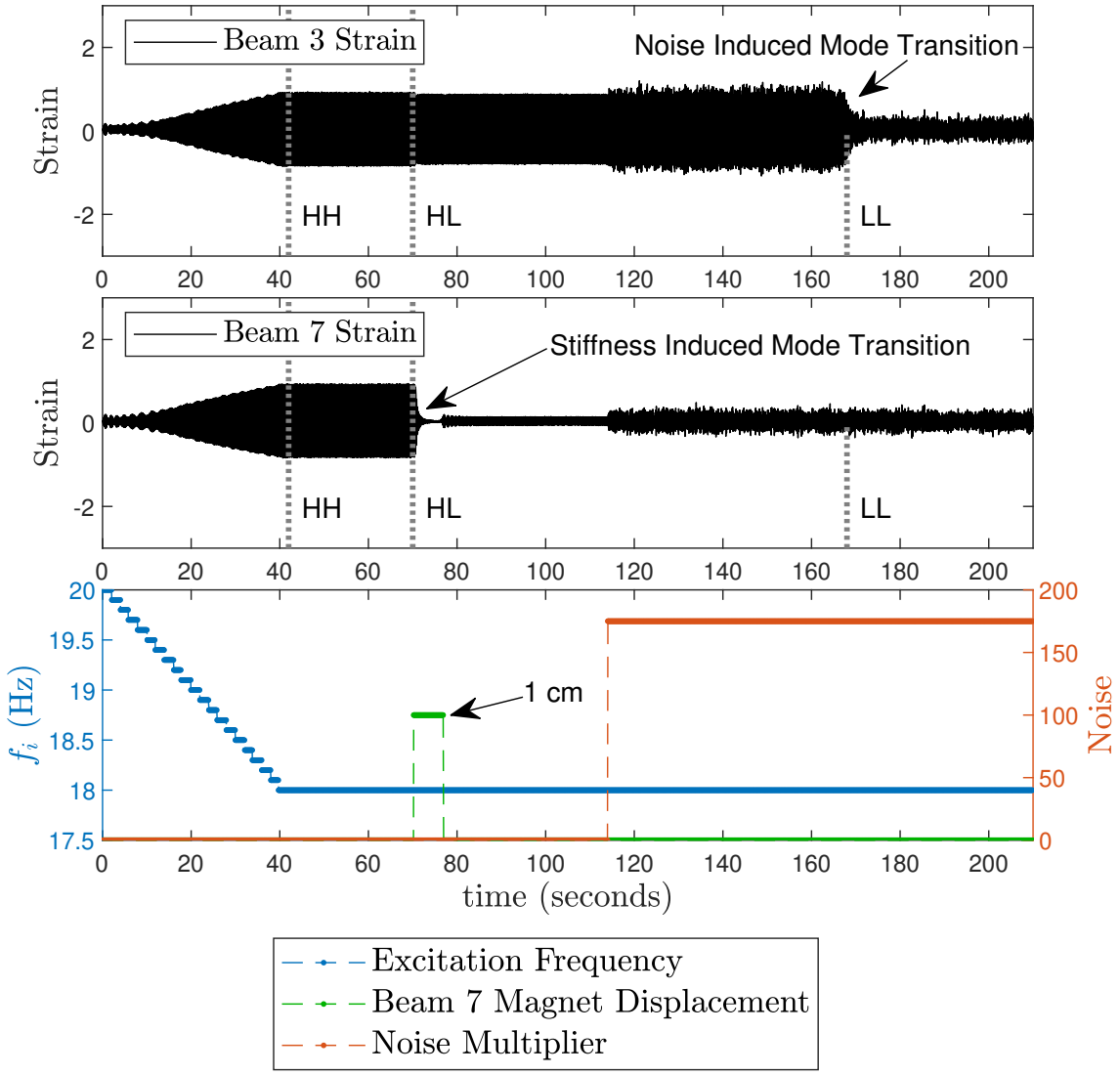


Figure 6.13: Time series representation of a single noise trial. (1-2) strain response of cantilevers 3 and 7. (3) Runtime experimental parameters including the excitation frequency, the displacement of the Beam 7 base magnet, and the noise multiplier. Notice that the strain response increases in both cantilevers into the HH mode with decreases in the excitation frequency, the cantilevers transition in the HL mode with the magnet movement event, and then the cantilevers transition to the LL mode due to the influence of noise.

Sets of 500 trials for different noise multipliers and different excitation frequency are run to estimate the expected escape time out of the response localization and the probability of remaining in the response localization. It is theoretically possible for the system to transition from the HL mode to the HH mode or the LH mode due to noise; nevertheless, in all trials, the system either transitioned from the HL mode to the LL mode or remained in the HL mode for the duration of the trial. The escape (transition) times out of the HL mode are shown in Fig. 6.14 for different noise multipliers at the excitation frequency of 18 Hz.

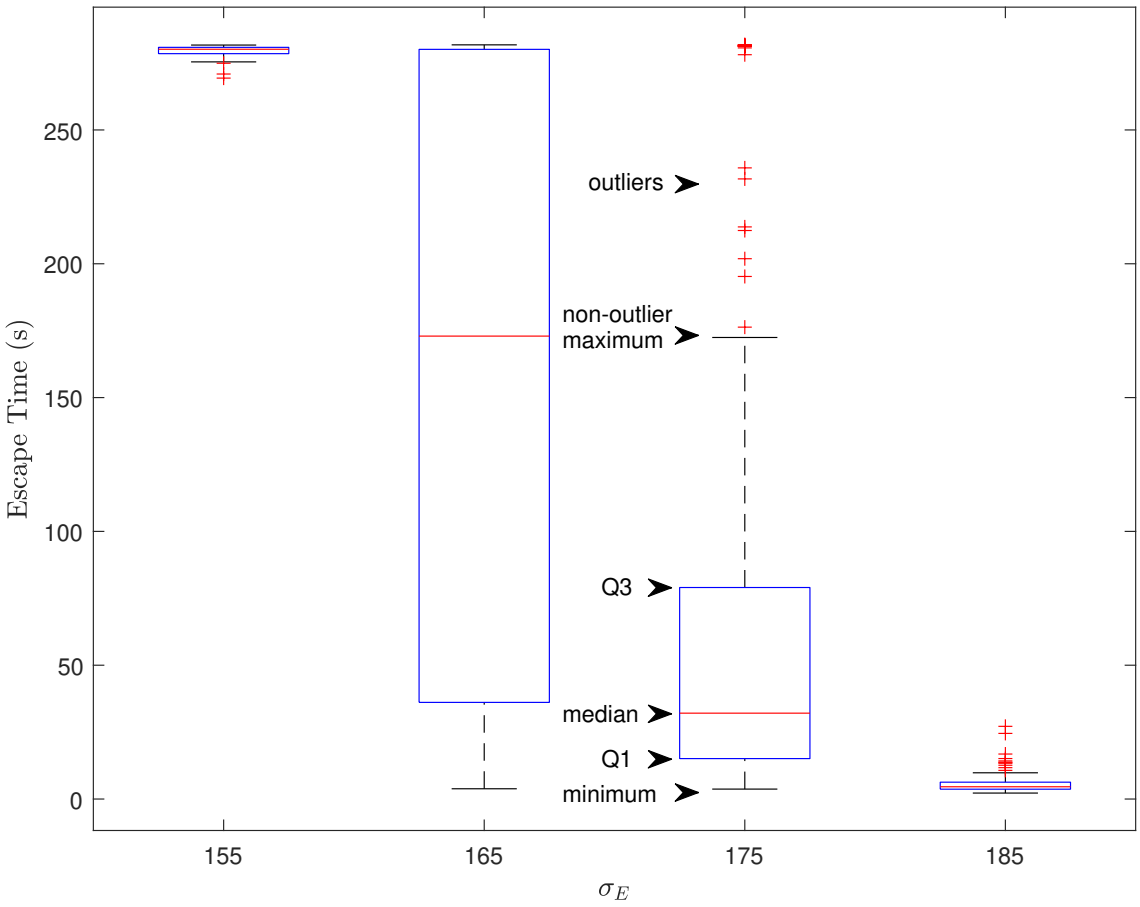


Figure 6.14: Box plots of transitions times out of the HL mode for varying noise intensity and constant excitation frequency, $f_i = 18$Hz.

The probability of remaining in the HL mode is calculated using the experimental escape times τ_i for trial i as follows:

$$P_{HL}(t) = \frac{\sum_{i=1}^{n} \delta_e(t, \tau_i)}{n}$$
$$\delta_e(t, \tau_i) = \begin{cases} 1, & t < \tau_i \\ 0, & t \geq \tau_i \end{cases} \tag{6.8}$$

P_{HL} is shown as a function of time in Fig. 6.15. Bins of 50 trials are used to create multiple estimates of P_{HL} and the standard deviation of the different P_{HL} estimates is used to provide an estimate of the error bound in Fig. 6.15.

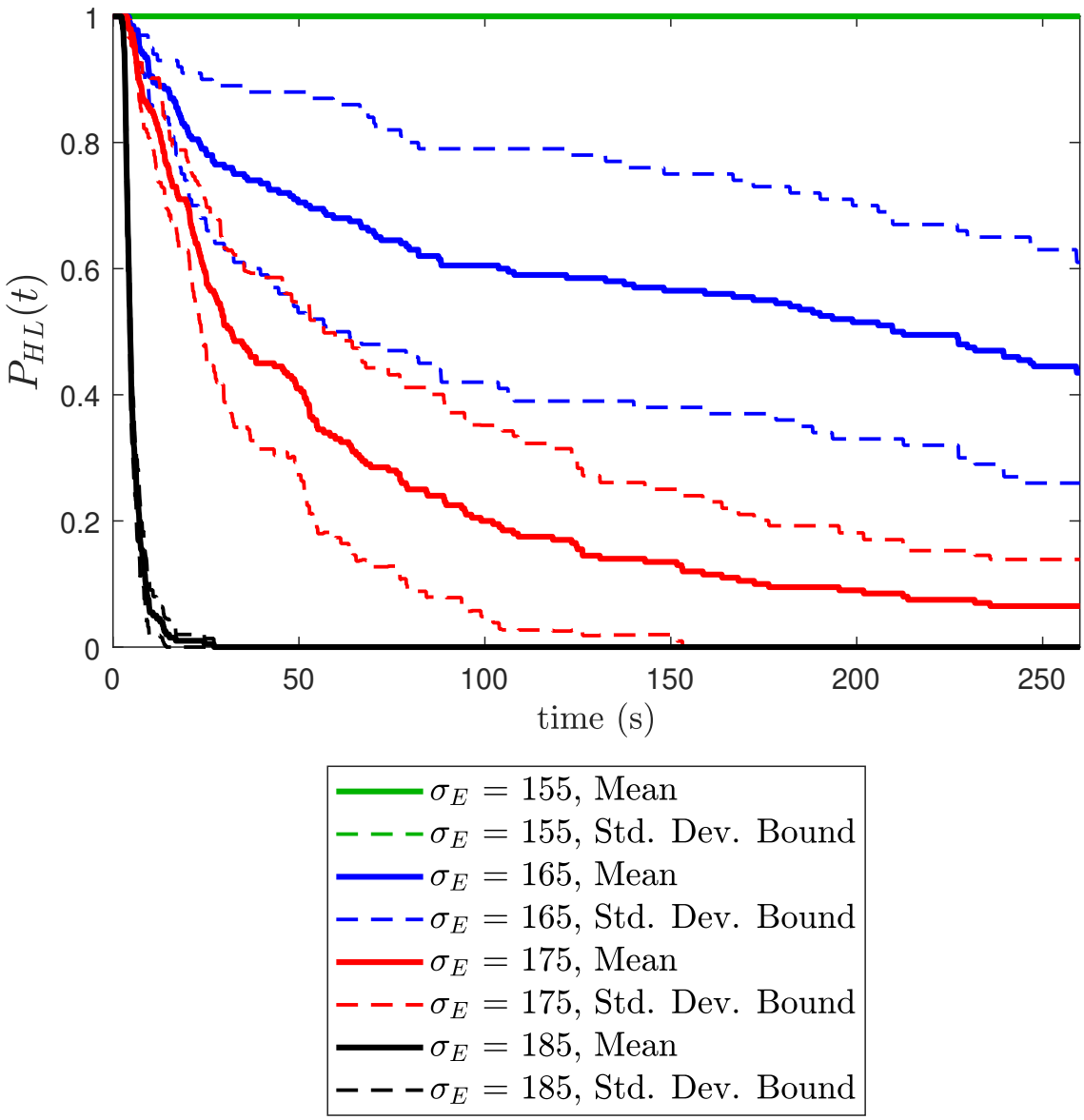


Figure 6.15: Average probability of remaining in the HL mode. Each curve corresponds to a different noise intensity and is made up of 10 bins of 50 trials each. The dashed lines indicate $\pm$ one standard deviation bound as an estimate of the error. All curves correspond to the excitation frequency of 18Hz.

The transition times out of the HL mode are shown for different excitation frequencies in Fig. 6.16. Here $\sigma_E = 175$. Since the hysteresis region of the HL mode

in the two beam system is much smaller than the hysteresis region of the one cantilever experiment in Chapter 5, small changes in frequency made a huge difference in the escape times of this system for fixed σ_E.

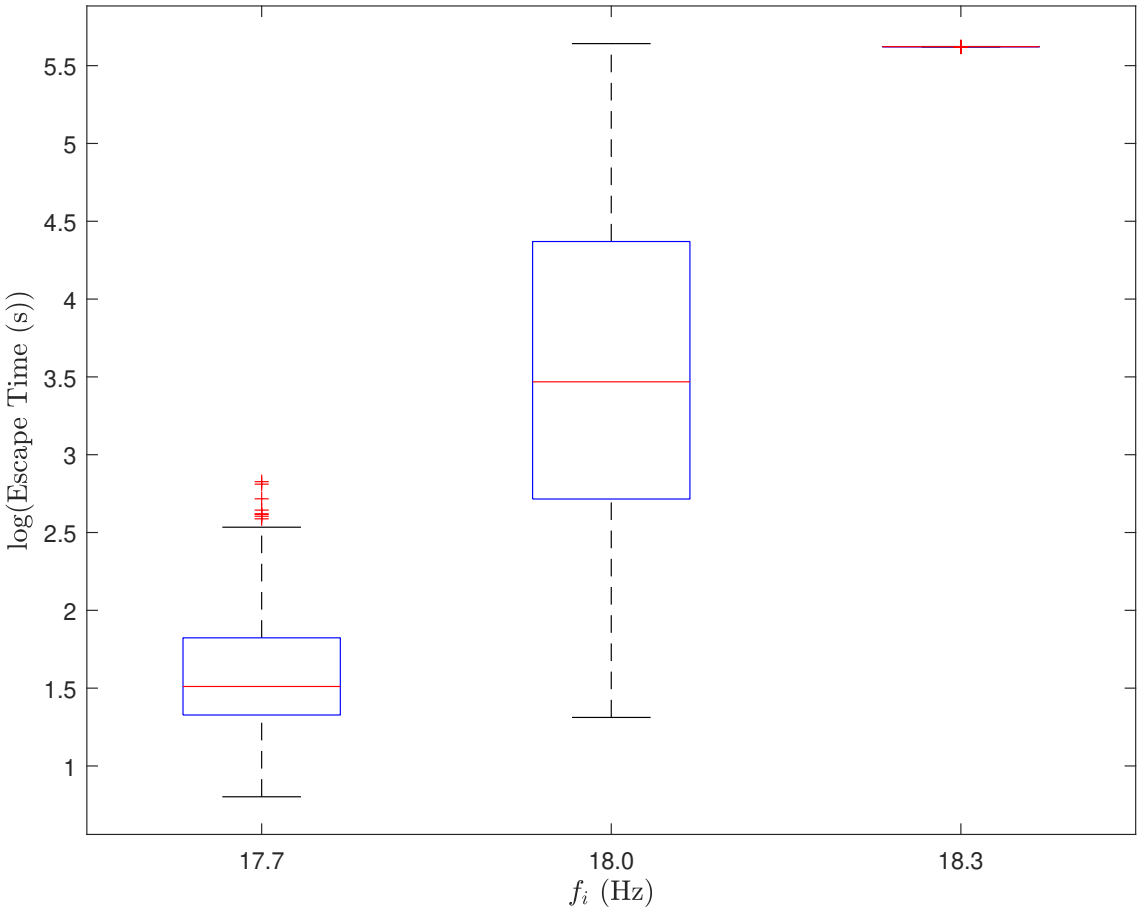


Figure 6.16: Box plots of transitions times out of the HL mode for varying excitation frequency and constant noise intensity, $\sigma_E = 175$.

6.3.4 Simulation Results

The system model, (6.5), has the analogous SDE

$$x_k''+\eta x_k'+(\alpha+(N-1)h)x_k+\beta x_k^3 = \hat{F}_0\cos(\Omega\tau)+\sum_{l\neq k} hx_l+\sigma dW(\tau), \quad k\in[1,2,...,N] \tag{6.9}$$

with σ as the noise multiplier and $dW(\tau)$ as a scalar additive white noise that affects all oscillators equally. Stochastic trajectories of (6.9) are simulated using the Euler-Maruyama scheme. The initial condition for each simulation is the stable HL mode. Two hundred trajectories of 5000 periods of excitations are simulated for each parameter set. The median escape times from the HL mode of the simulation are shown in Fig. 6.17 for the excitation frequency of 18 Hz and values of σ.

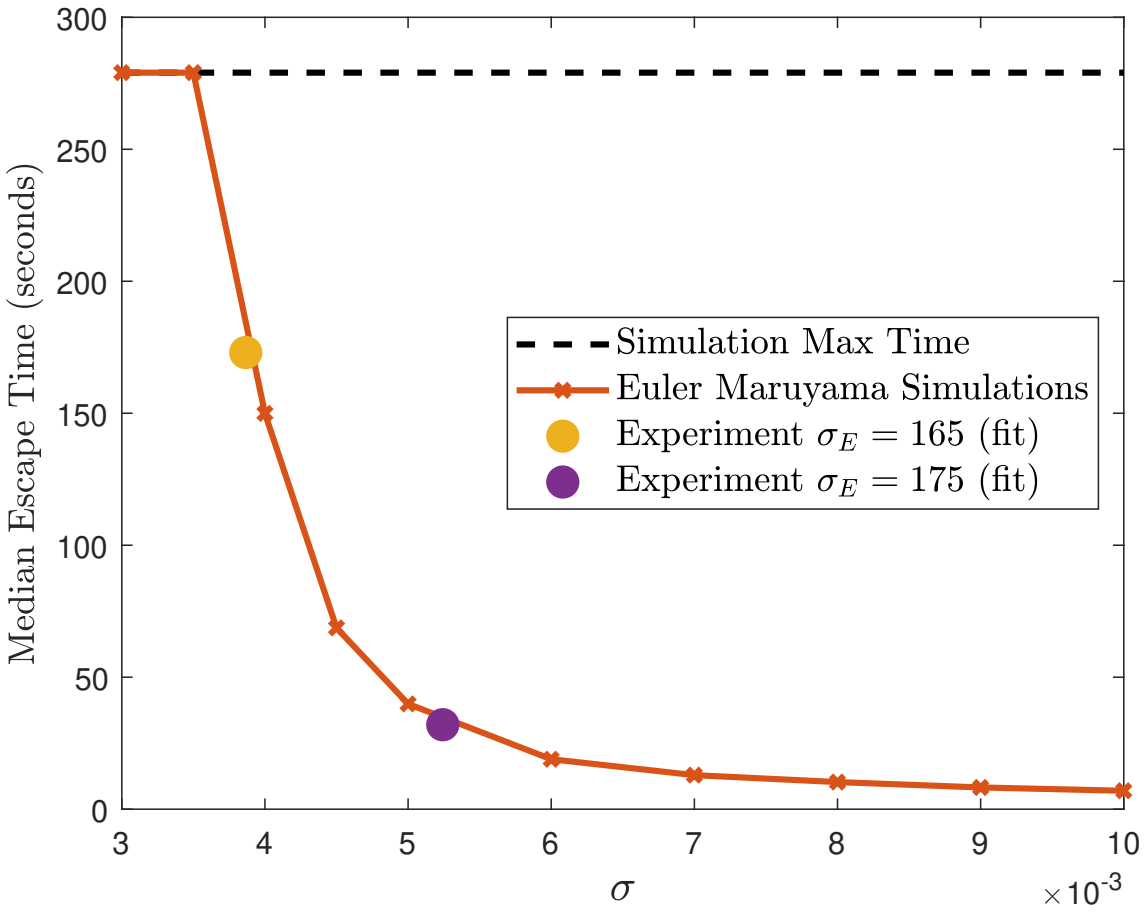


Figure 6.17: The median transition times of transitions out of the HL mode for different noise intensities, σ. Each point of the red curve is the median from 200 numerical trials. The experimental points are shown alongside the numerical data. The location of the experimental data with respect to σ is determined by finding a scalar multiplier for σ_E and an offset that best fits the numerical data.

Notice that for $\sigma \leq 0.35$ the median escape time is greater than the simulation maximum time limit. The experimental median escape times are fitted to the numerical escape times to approximate the values of σ that corresponds to values of σ_E. Probability estimates of remaining in the HL mode are calculated by using (6.8) and graphed alongside the experimental probability estimates in Fig. 6.18. Notice qualitative

similarities in the probability estimates between remaining in the HL mode for the experiment and simulations with approximate σ values.

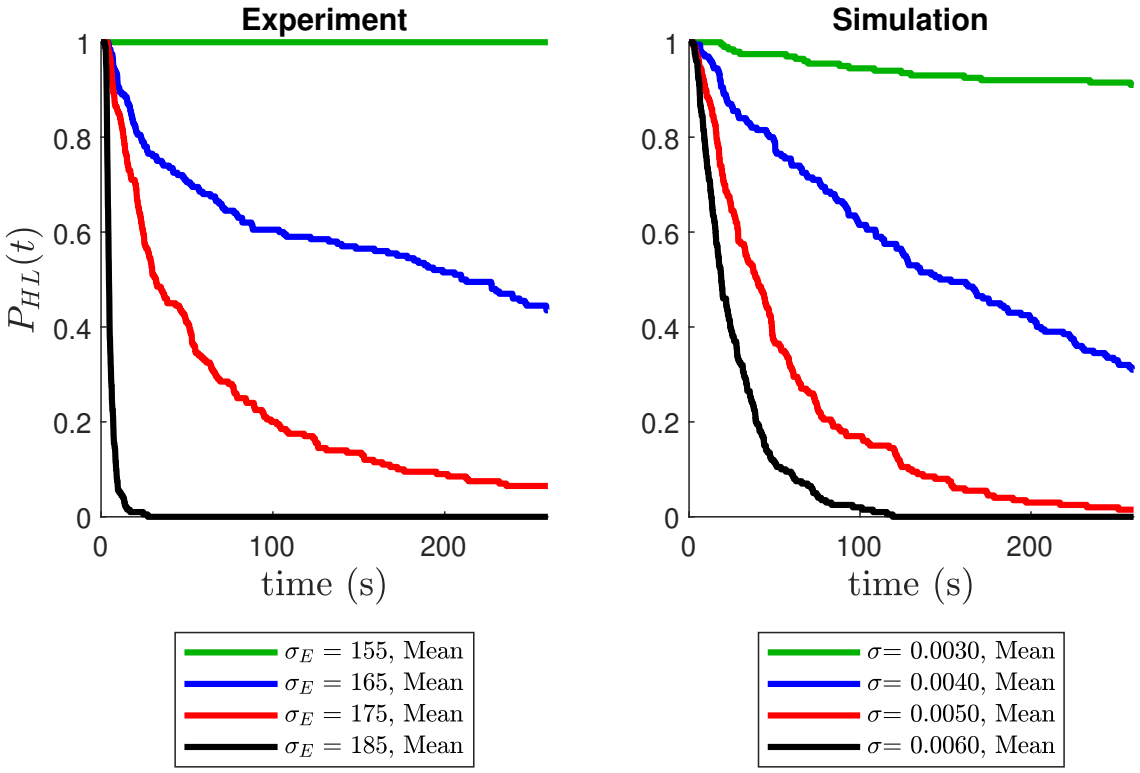


Figure 6.18: The probability of remaining in the HL mode for both the experiments and the simulations for different noise intensities. Here the excitation frequency is 18Hz.

The simulations are also performed for constant σ and varying f_i to compare with the experimental results. The median escape time for both the experimental and numerical results are shown in Fig. 6.19. This escape time increases with increasing f_i in the hysteresis region.

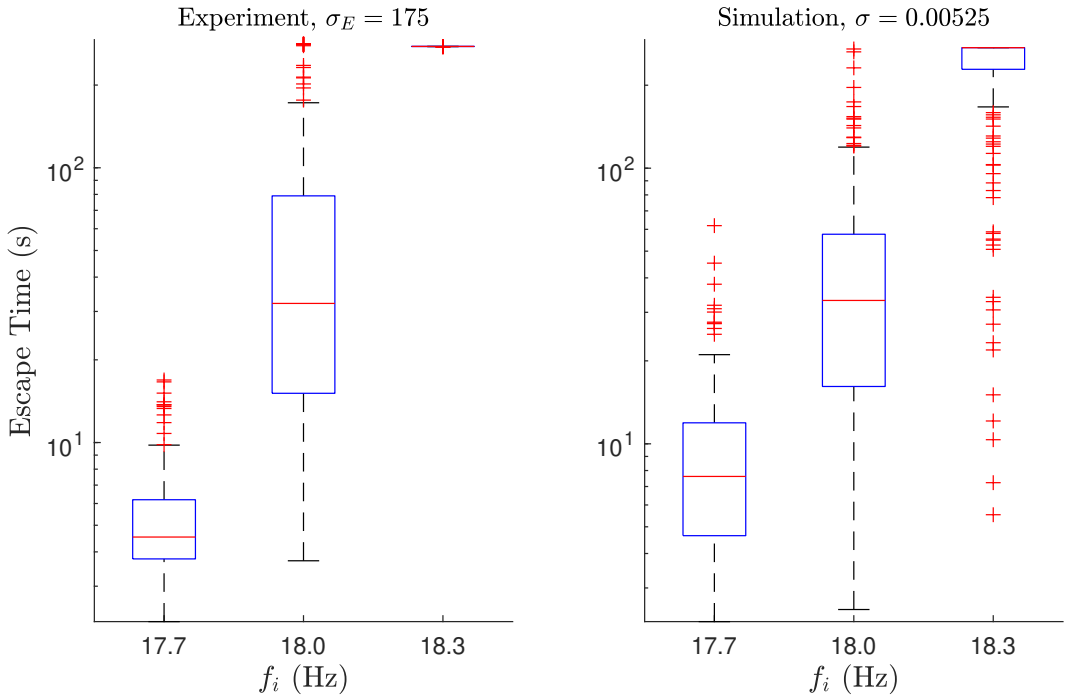


Figure 6.19: Box plots of the transition times from the HL mode to the LL mode for both the experimental and simulation results for different excitation frequencies, f_i and constant noise intensity.

6.4 Influence of Noise on Four Coupled Cantilever Beams

Response localizations of a four beam cantilever array are studied by tuning 4 of the 8 beams to a first natural frequency of $f_n = 24$ Hz while the remaining beams are left detuned to approximately 10 Hz; Beams 1,3,5,and 7 labeled as shown in Fig. 6.20 are the tuned beams of interest. It is assumed here that due to the significant difference in natural frequency, for the excitation frequencies in the range $20 \leq f_i \leq 26$, the coupling forces from beams 0,2,4, and 6 are negligible. Indeed, it can be observed that these beams have very small amplitude oscillations.

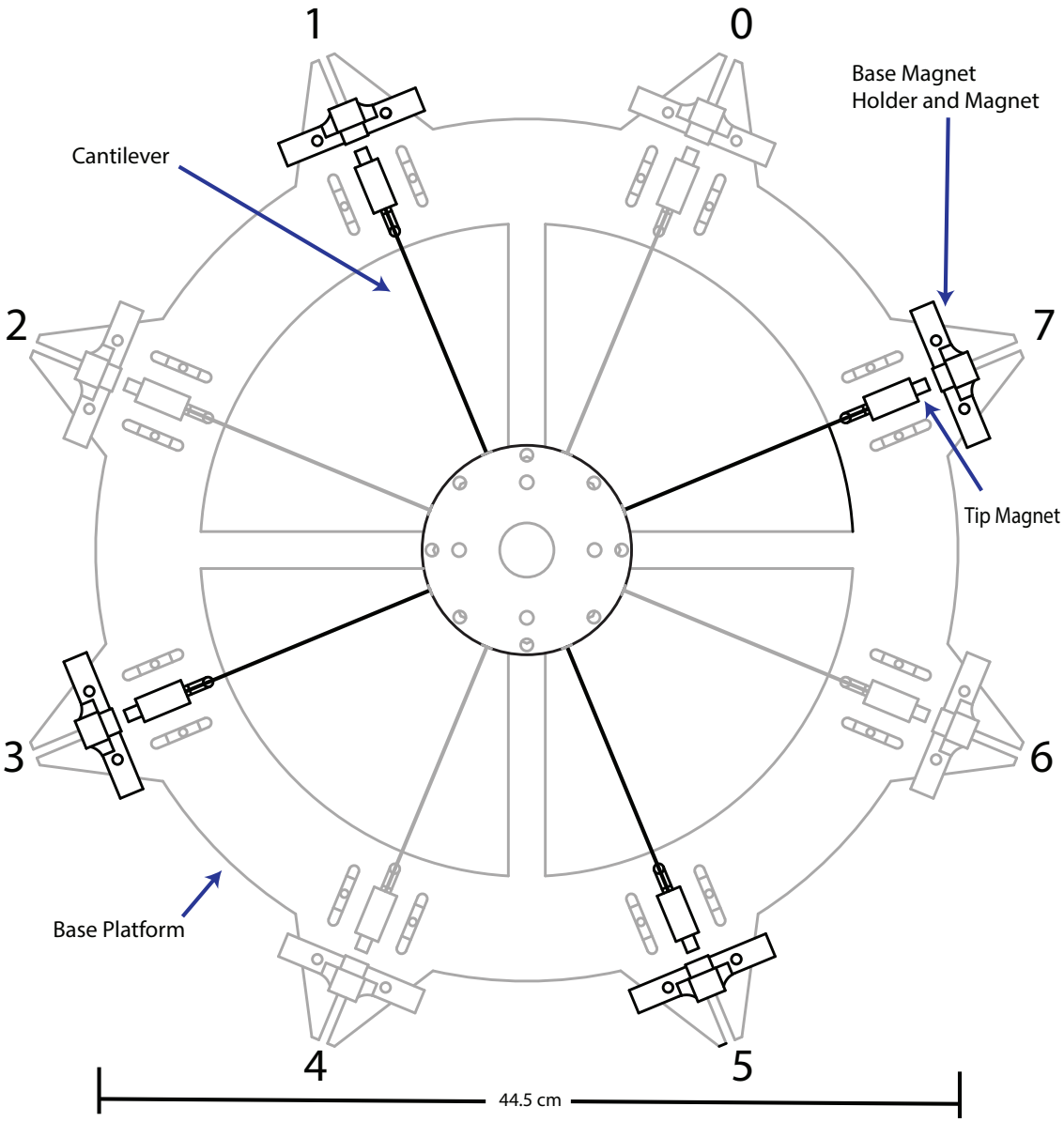


Figure 6.20: Top view schematic of the circular cantilever beam array with tuned beams of interest 1, 3, 5, and 7 highlighted in black.

6.4.1 Frequency Response

A set of frequencies sweeps is performed for the four beam system as for the two beam system in Section 6.3.1. The sum of the first harmonic amplitudes of the response

of the beams are shown as a function of excitation frequency in Fig. 6.21.

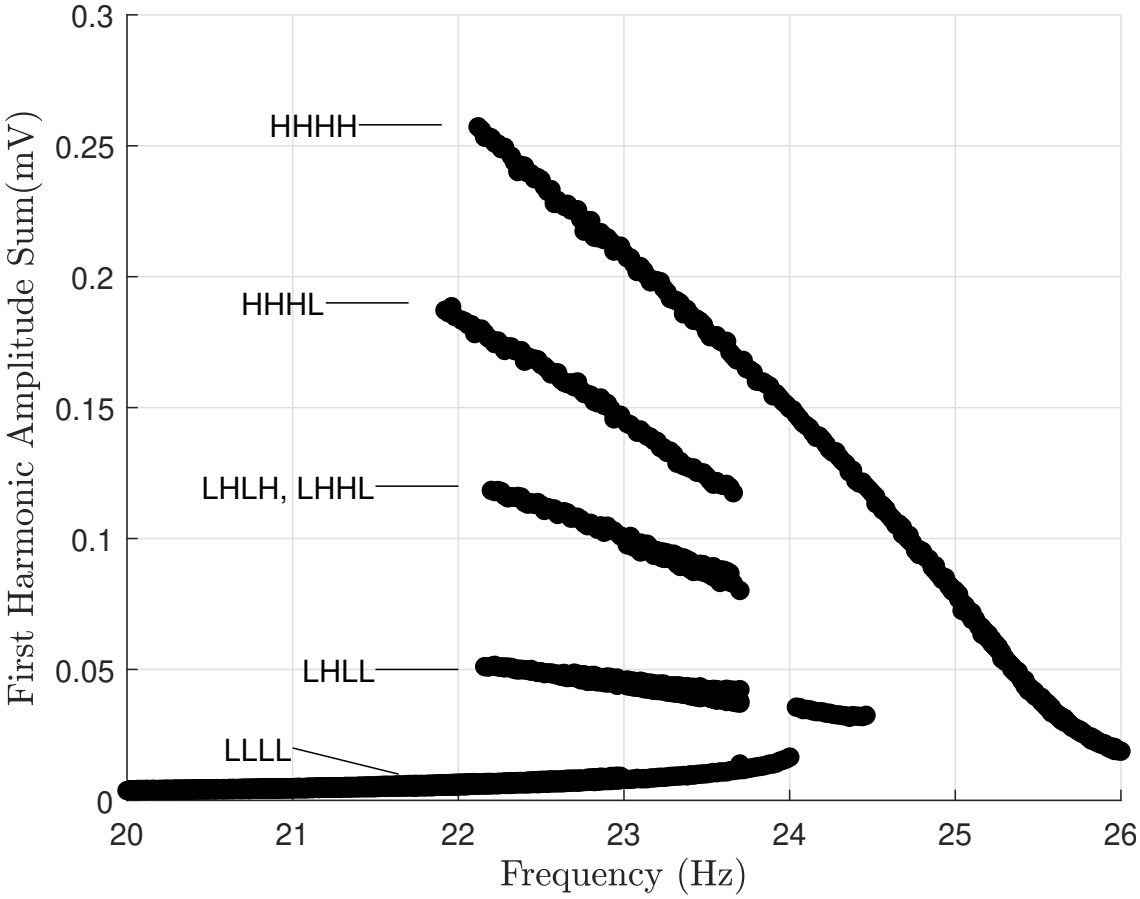


Figure 6.21: The sum of the first harmonic amplitude responses of the four beam system as a function of excitation frequency. Notice 6 unique nonlinear modes labeled in this figure. Additional symmetric modes are also observed but not shown here.

Between the excitation frequencies of $f_i \approx 22$ Hz and $f_i \approx 23.7$ Hz six different nonlinear modes are present, as shown in Fig. 6.21. Since this is a circular array, there are also symmetric configurations of these modes that are not shown in Fig. 6.21. The nonlinear mode of interest is the $LHLL$ mode in which only one beam is oscillating at a high amplitude.

6.4.2 System Identification

The same system identification approach used in Section 6.3.2 is used for the four beam system. Note that in Section 6.3.2, the system identification approach is described generalized for N beams. The nondimensionalized frequency response data of the synchronous $HHHH$ and $LLLL$ modes from Fig. 6.21 are used with cost function (6.2) to find the best fit parameters of (6.1) to the experimental data. The resulting minimizing parameter values are $\beta = -0.2989$, $F = 0.0068$, $\eta = 0.0068$, and the best fit curve is shown alongside the experimental data in Fig. 6.22.

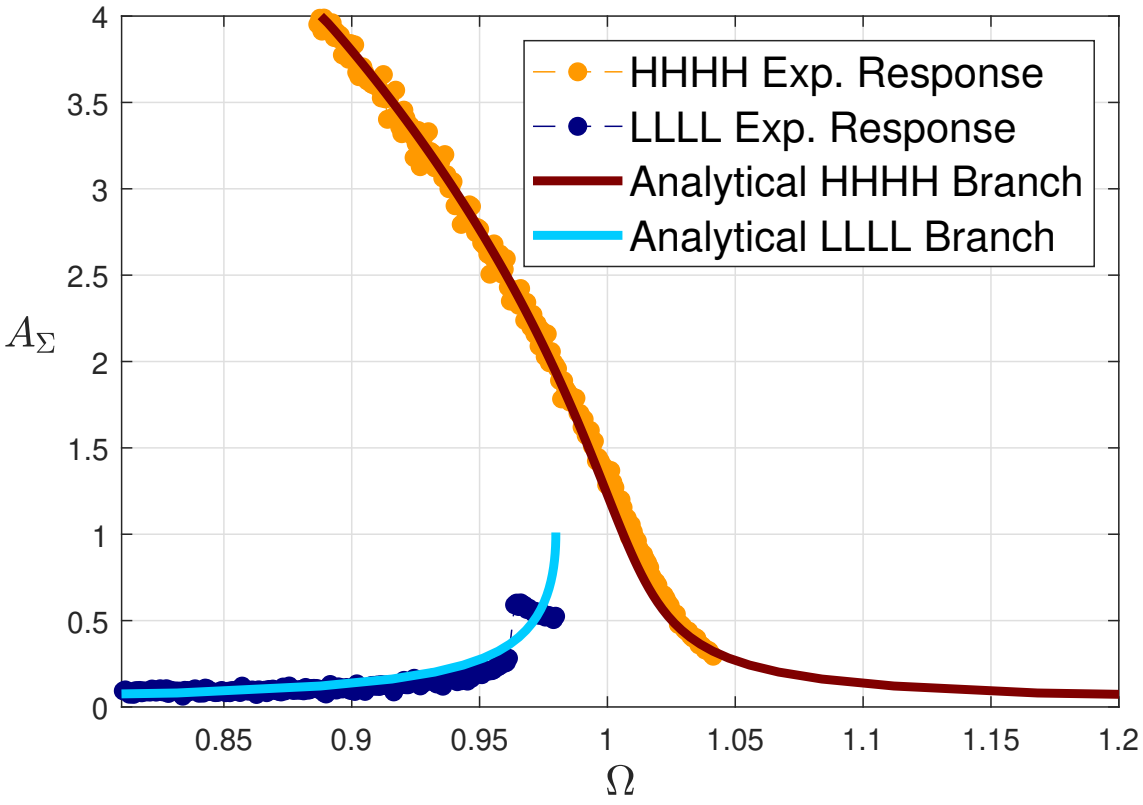


Figure 6.22: Best fit of the analytical approximation of the sum of the frequency response of four Duffing oscillators to the experimental data. The minimizing parameters are $\beta = -0.2989$, $F = 0.0068$, and $\eta = 0.0068$.

The fit to the analytical approximation underestimates the damping term, so the damping parameter is corrected by using an additional fit with numerical continuation carried out with the continuation package COCO [52]. The corrected parameters of (6.1) are $\beta = -0.2989$, $F = 0.0068$, and $\eta = 0.0078$. The obtained $HHHH$ mode and the $LLLL$ mode with these parameters are shown in Fig. 6.26

The experimental phase responses of the $LLLL$, $LHLL$, and $HHHH$ modes are shown for each beam as a function of nondimensionalized excitation frequency in Fig. 6.23. Notice that each beam has approximately the same phase for the $LLLL$ mode and the $HHHH$ mode, but that there is a significant difference in the phase angle for the high amplitude oscillator of $LHLL$ mode than the low amplitude oscillators of the $LHLL$ mode.

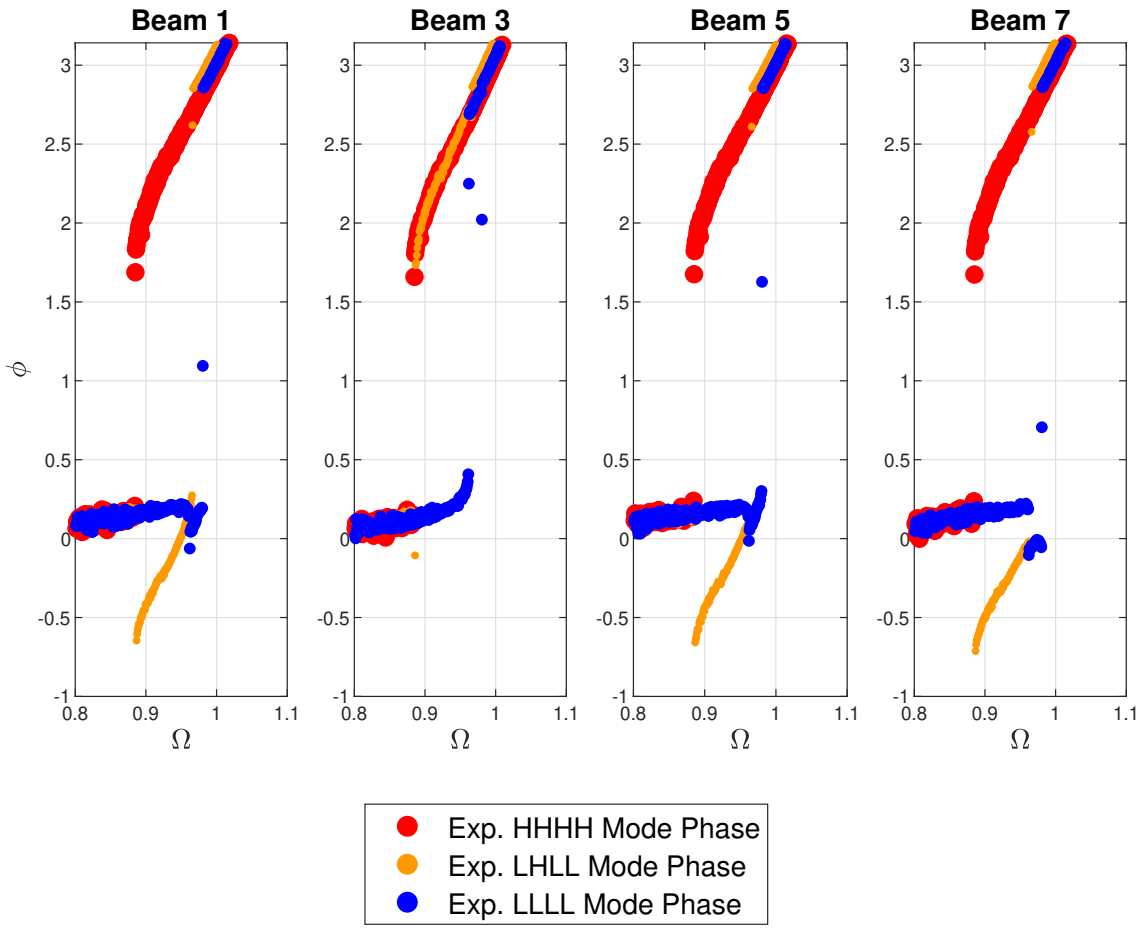


Figure 6.23: The experimental phase response of the $LLLL$, $LHLL$, and $HHHH$ modes for each beam as a function of nondimensionalized excitation frequency. The phase angle, ϕ, is in radians.

The phase angles of the experimental $LHLL$ mode are fitted to the phase of the numerically computed $LHLL$ mode of equation (6.5) as a function of the coupling force coefficient h by using the cost function (6.6). The phase cost function is shown in Fig. 6.24. Notice a minimum at $h = -0.0023$.

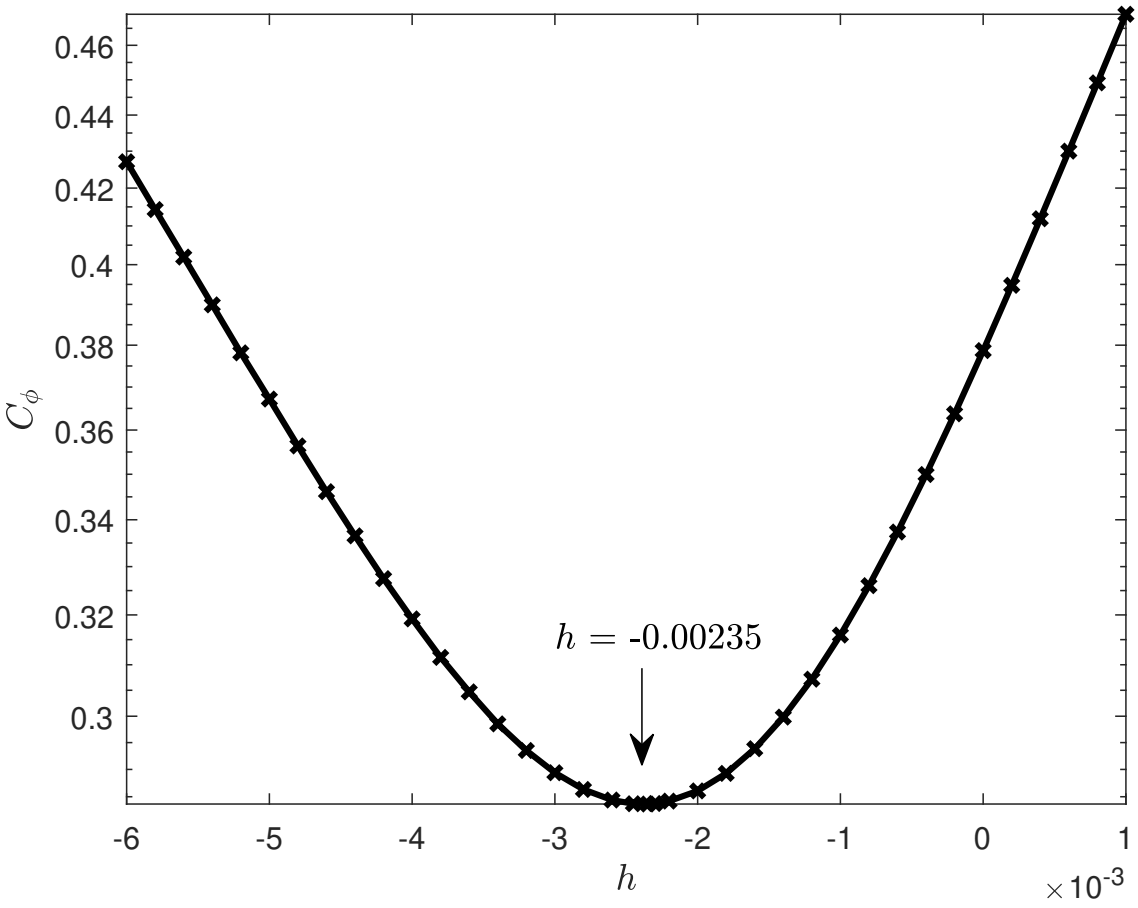


Figure 6.24: The phase cost (6.6) as a function of coupling force coefficient h.

The behavior of the phase of the four beam system model as a function of h is shown in Fig. 6.25 for the $LHLL$ mode.

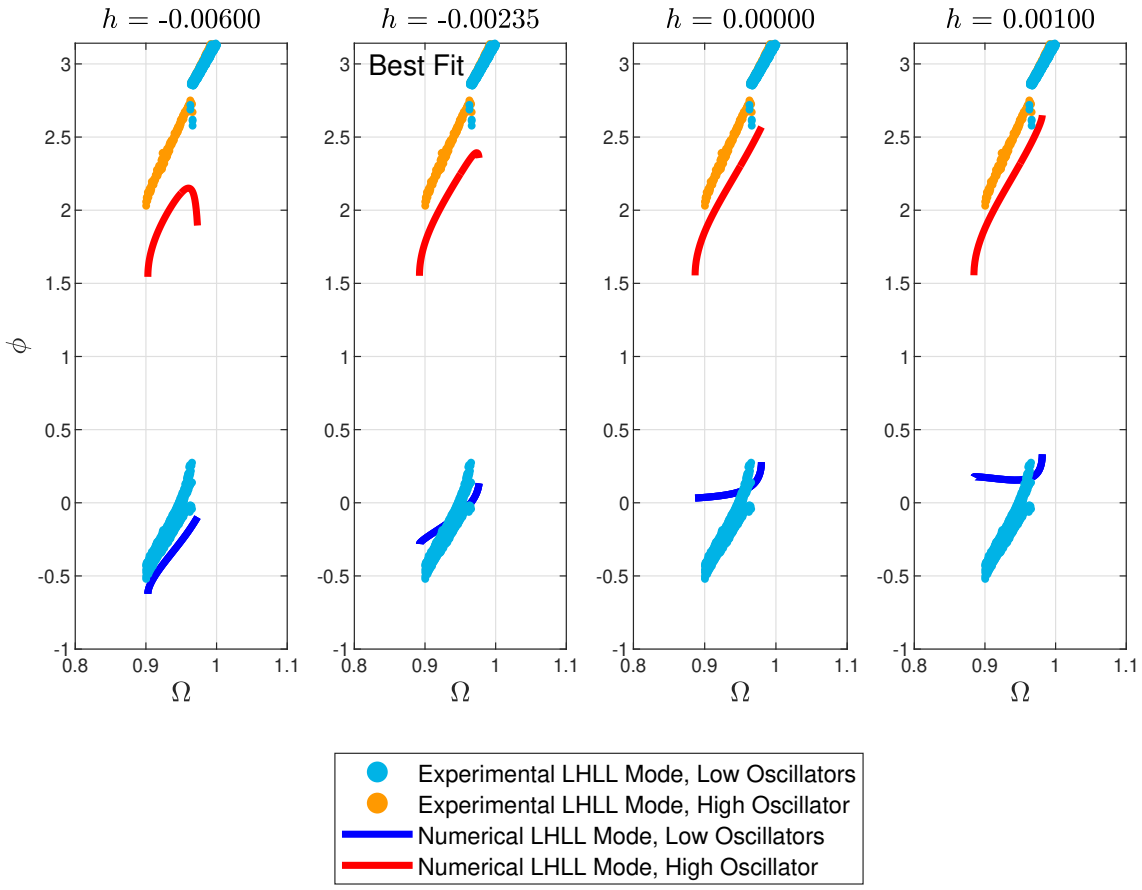


Figure 6.25: The phase response of the $LHLL$ mode from experimental data and from the $N = 4$ system model of (6.5) for four different h values. In the legend, a high amplitude oscillator is denoted as "High Oscillator", and a low amplitude oscillator is denoted as "Low Oscillator". The phase angle, ϕ, is in radians.

The frequency amplitude response of the stable modes of the system model (6.5) obtained with parameters $\alpha = 1$, $\beta = -.2989$, $\eta = 0.0078$, $h = -0.0023$, and $F = 0.0068$ is shown in Fig. 6.26 with the experimental data. While qualitative similarities between the model results and the experimental data are apparent, there is some noticeable disagreement between the model prediction and the experimental response. Alternative system models may lead to improved agreement for the frequency amplitude response,

but this simple model is used here as discussed before.

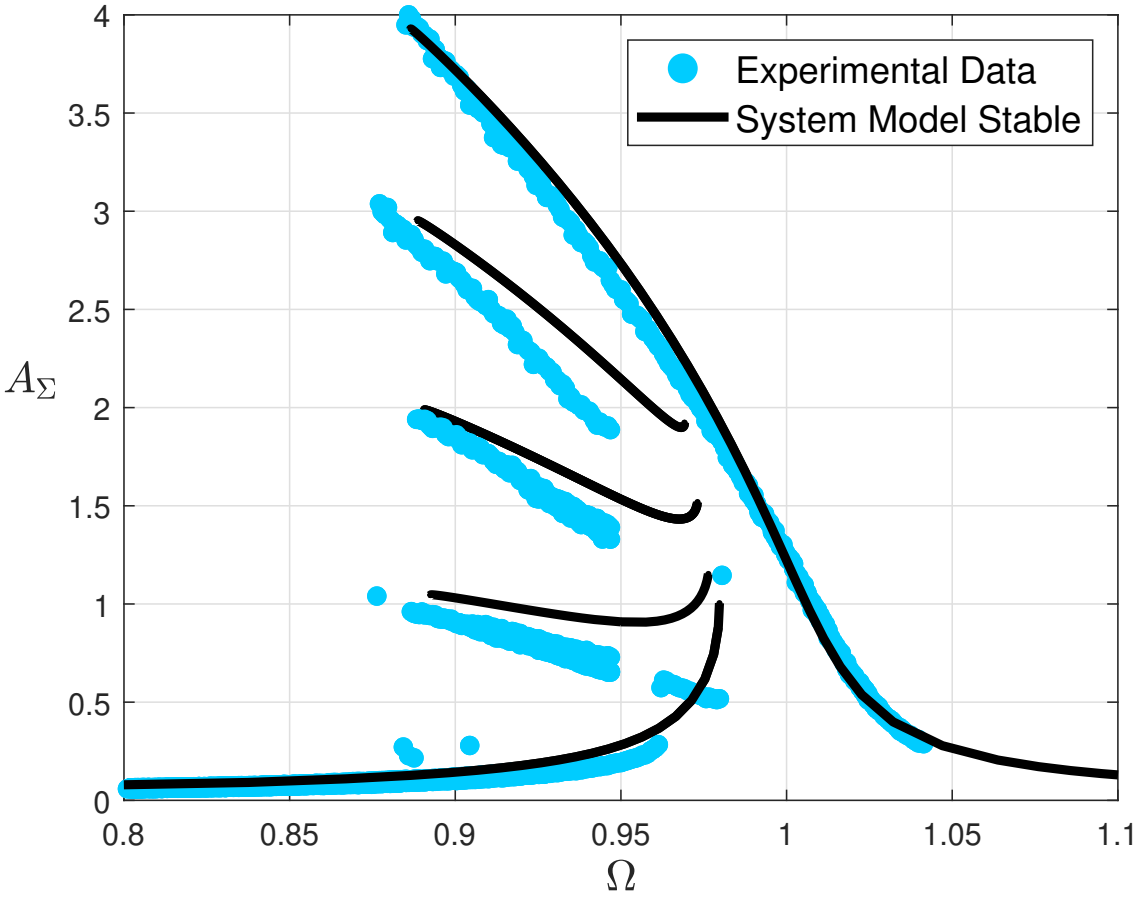


Figure 6.26: Numerical continuation frequency amplitude response of the stable modes of (6.5) with parameters $\alpha = 1, \beta = -.2989, \eta = 0.0078, h = -0.0023$, and $F = 0.0068$ shown with the experimental data.

6.4.3 Experimental Results

A noise trial of the experiment takes the form shown in Fig. 6.27. Initially all four cantilever beams started at rest. A harmonic excitation is introduced at $f_i = 25$ Hz and slowly decreased to the test frequency of $f_i = 23$ Hz. Linear actuators corresponding to Beams 1, 5, and 7 displaced the base magnet of the cantilever beams by 1 cm resulting in

a detuning that transitioned Beams 1, 5, and 7 to a low amplitude oscillation. When the linear actuators returned the base magnets to the original position, the initial condition of the system is such that the system moved towards the $LHLL$ nonlinear mode. Noise is added to the system and sustained for the duration of the trial. Eventually, a noise induced transition is observed from the $LHLL$ mode to the $LLLL$ mode.

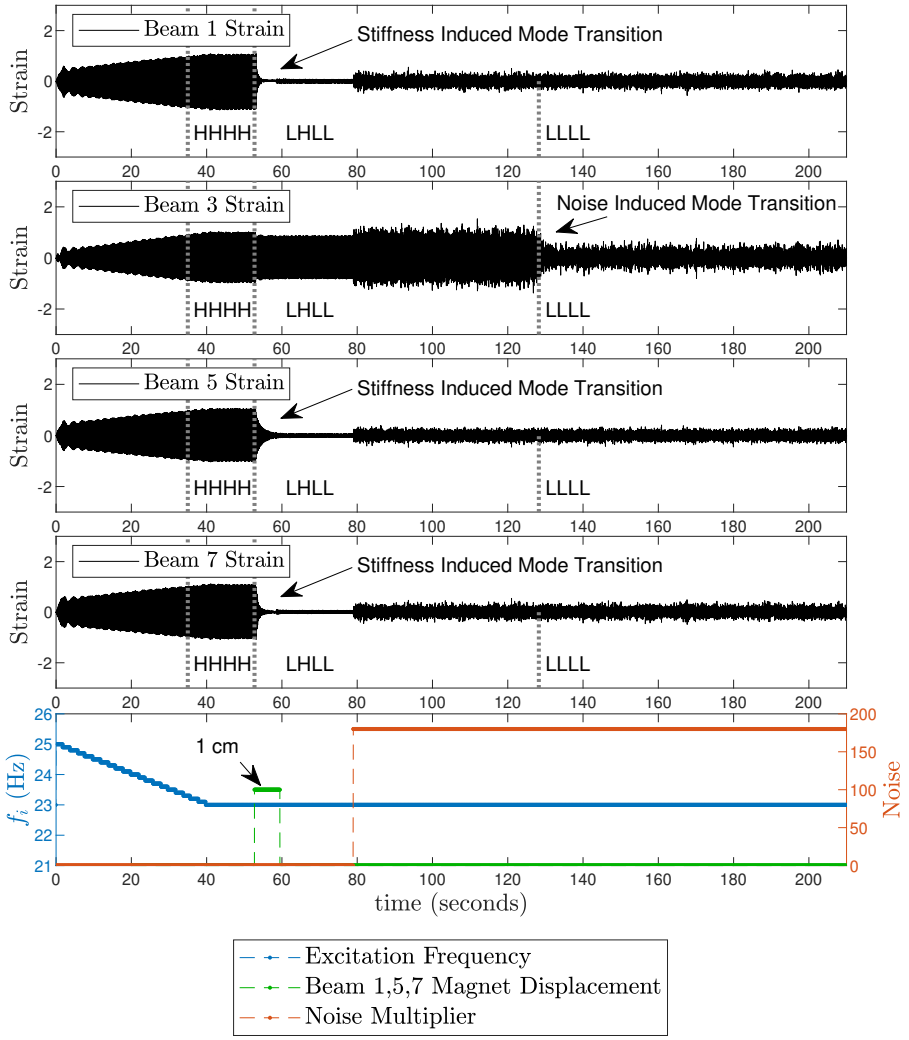


Figure 6.27: Time series representation of a single noise trial. (1-4) strain response of cantilevers 1,3,5,7. (5) Runtime experimental parameters including the excitation frequency, the displacement of magnets, and the noise multiplier. Notice that the strain response increases in all cantilevers into the $HHHH$ mode with decreases in the excitation frequency, the cantilevers transition in the $LHLL$ mode with the magnet movement event, and then the cantilevers transition to the $LLLL$ mode due to the influence of noise.

This procedure is repeated to produce sets of 500 trials at 5 noise intensities, σ. The

distribution of the escape times as a function σ are shown in Fig. 6.28. The probability estimates of remaining in the $LHLL$ mode obtained by using

$$P_{LHLL}(t) = \frac{\sum_{i=1}^{n} \delta_e(t, \tau_i)}{n}$$
$$\delta_e(t, \tau_i) = \begin{cases} 1, & t < \tau_i \\ 0, & t \geq \tau_i \end{cases} \tag{6.10}$$

are shown in Fig. 6.29.

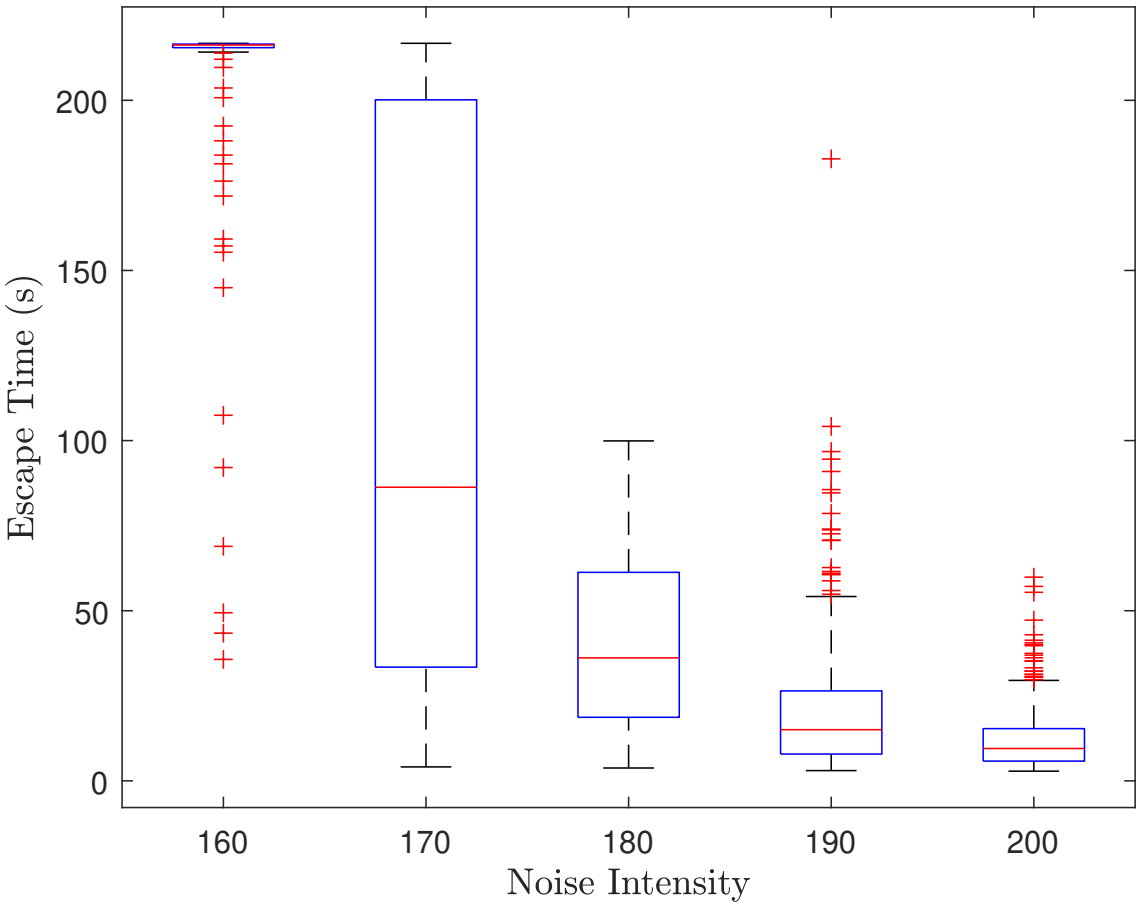


Figure 6.28: Box plots of transitions times out of the $LHLL$ mode for different noise intensities and constant excitation frequency, $f_i = 23$Hz.

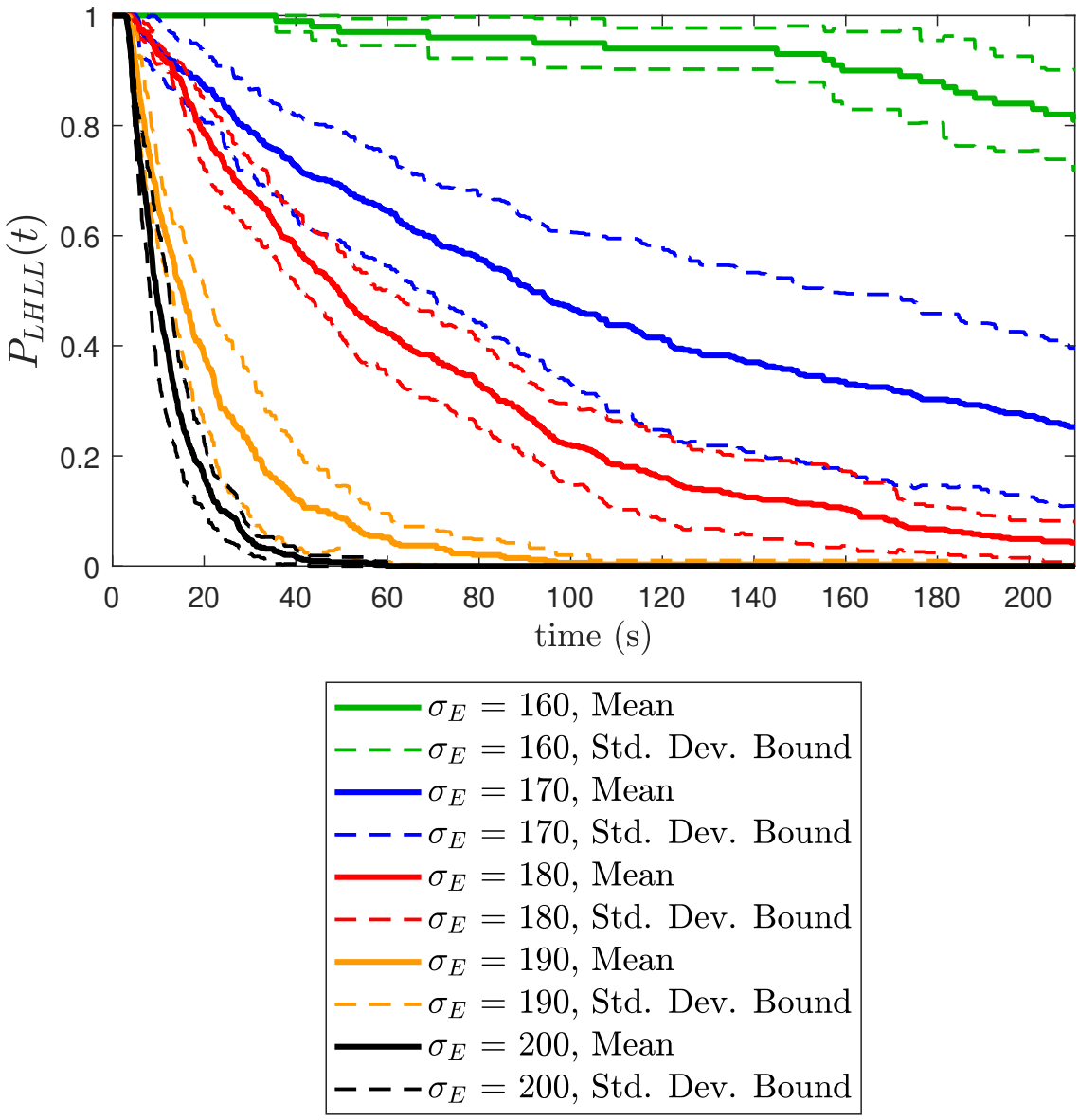


Figure 6.29: Average probability of remaining in the $LHLL$ mode. Each curve corresponds to a different noise intensity and is made up of 10 bins of 50 trials each. The dashed lines indicate $\pm$ one standard deviation bound as an estimate of the error. All curves correspond to the excitation frequency of 23Hz.

Three sets of 500 trials for $\sigma = 200$ are shown for three different excitation frequencies in Fig. 6.30. Notice that the median escape times increase with increasing

excitation frequency in the hysteresis region.

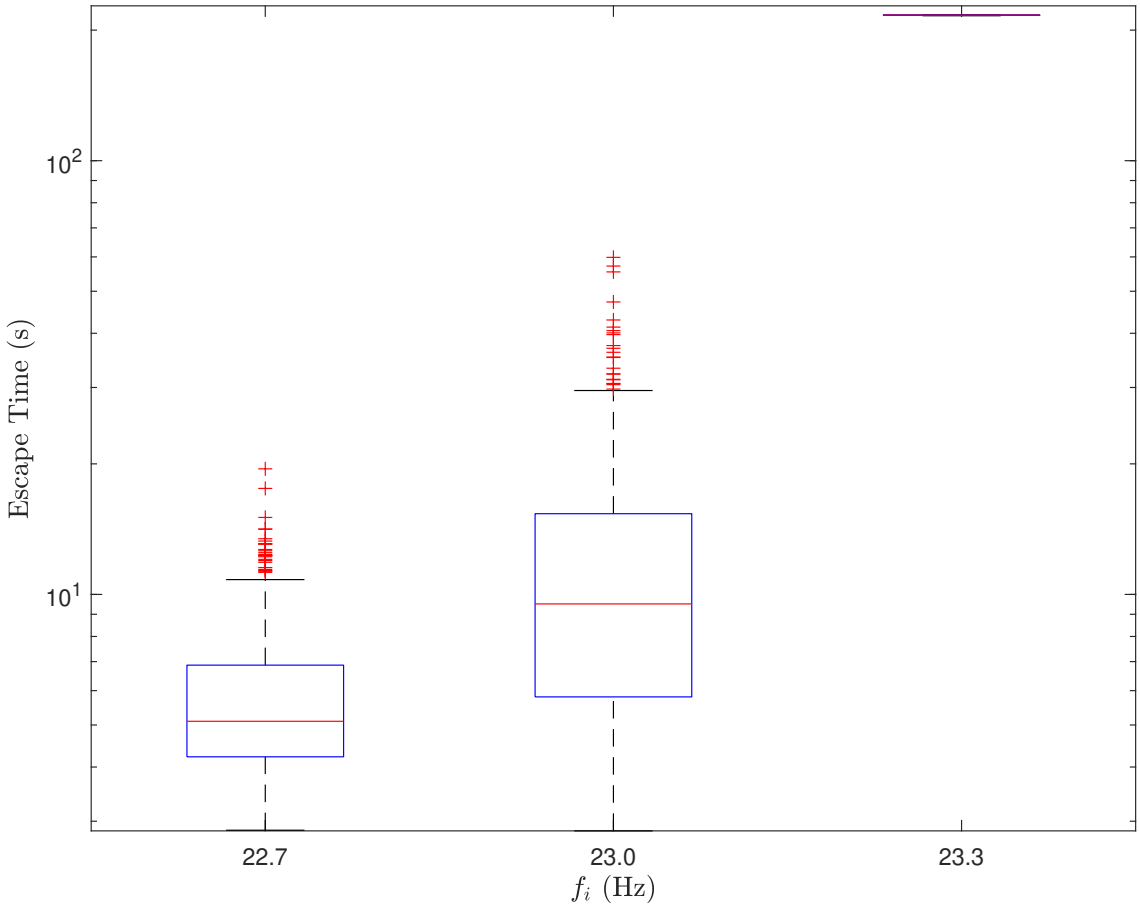


Figure 6.30: Box plots of transitions times out of the $LHLL$ mode for different excitation frequencies and constant noise intensity, $\sigma_E = 200$.

6.4.4 Simulation Results

In this section, two noise models are used for the reduced order model to simulate the stochastic behavior of this system by using the parameters identified in Section 6.4.2. The system of SDEs for a system where all oscillators are influenced by the same noise

is

$$x_k'' + \eta x_k' + (\alpha + (N-1)h)x_k + \beta x_k^3 = \hat{F}_0 \cos(\Omega\tau) + \sum_{l \neq k} h x_l + \sigma dW(\tau) \quad k \in [1, 2, ..., 4] \tag{6.11}$$

Here dW(t) a scalar white noise contribution and σ is the noise multiplier. Equation (6.11) is a good representation of the experimental system because the source of relevant noise in the system comes from a single source, the motor. An alternative system of SDEs that is also used for simulations is

$$x_k'' + \eta x_k' + (\alpha + (N-1)h)x_k + \beta x_k^3 = \hat{F}_0 \cos(\Omega\tau) + \sum_{l \neq k} h x_l + \sigma dW_k(\tau) \quad k \in [1, 2, ..., 4] \tag{6.12}$$

where $dW_k(\tau)$ is the component with index k of a vector of independent white noise quantities $\boldsymbol{dW}(\tau)$. Equation (6.12) is also used for simulations to compare with the results obtained with the methodology in Chapter 4 that is designed with an independent noise assumption. The results for 200 trials of Euler-Maruyama simulations of the noise influenced $LHLL$ mode are shown in Fig. 6.31 for the excitation frequency of $23Hz$ and multiple noise intensities. The Monte Carlo results for (6.11) and (6.12) are not significantly different.

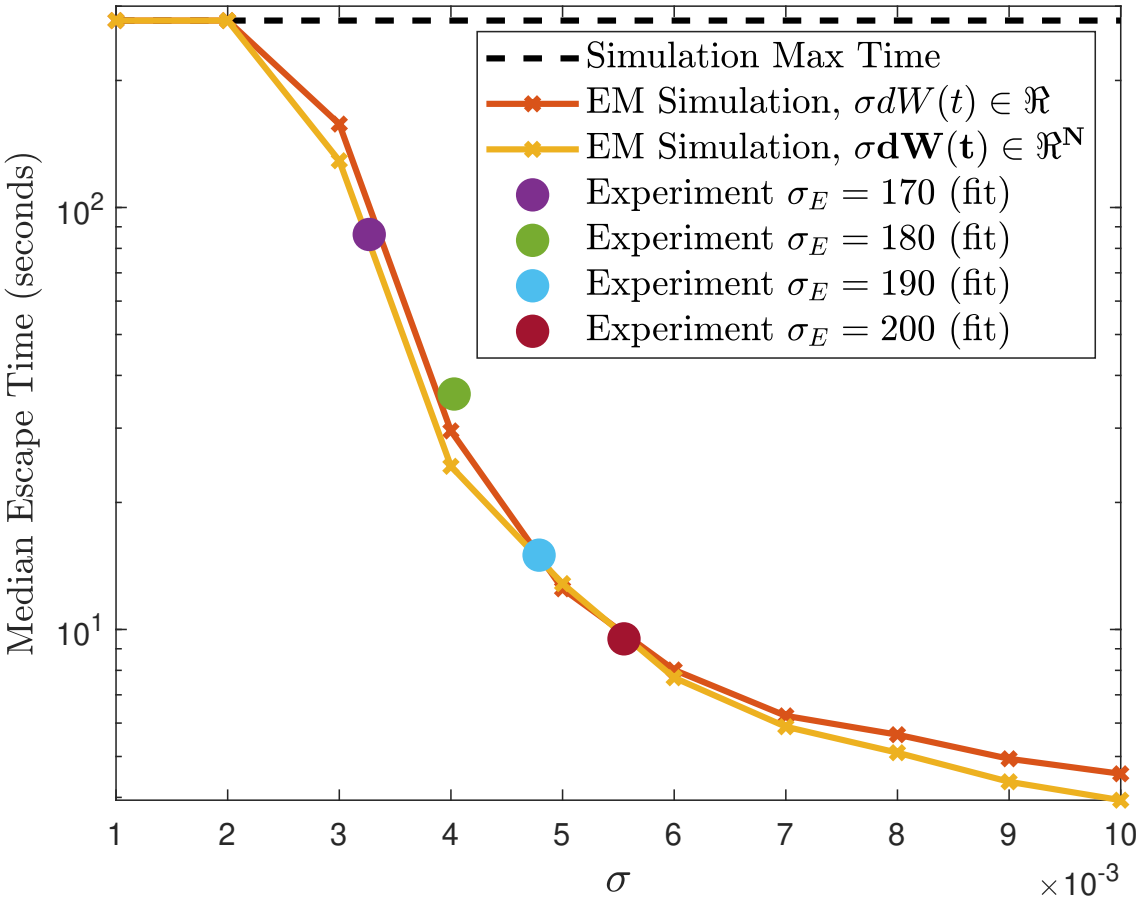


Figure 6.31: The median transition times of transitions out of the $LHLL$ mode for different noise intensities, σ. Each point of the red and yellow curves is the median from 200 numerical results. The experimental points are shown alongside the numerical data. The location of the experimental data with respect to σ is determined by finding a scalar multiplier for σ_E and an offset that best fits the numerical data resulting from (6.11).

The experimental noise intensity, σ_E is scaled by a constant and shifted by an offset to best fit the results with the numerical data, and this quantity is also shown in Fig. 6.31. The probability estimates from the results of (6.11) are qualitatively compared in Fig. 6.32.

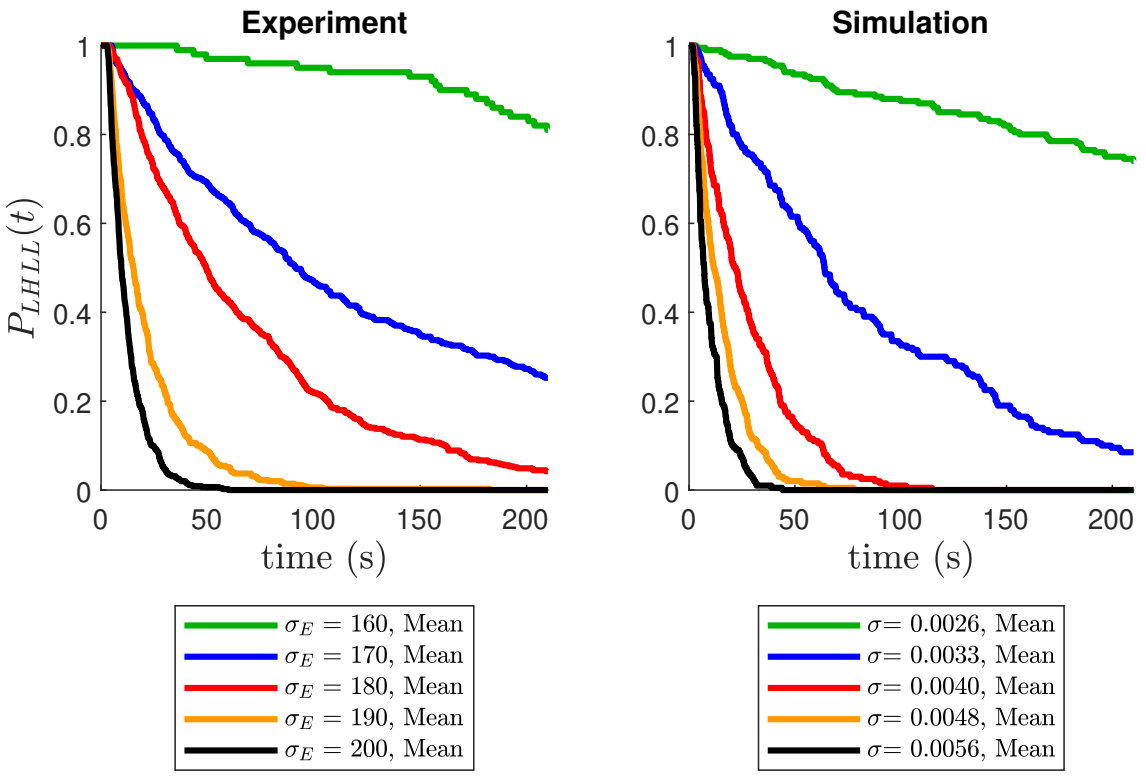


Figure 6.32: The probability of remaining in the $LHLL$ mode for both the experiments and the simulations for different noise intensities.

The probability estimates obtained from the results of (6.12) are used to estimate the quasipotential as in Section 5.6. The stochastic estimate of the quasipotential can be derived as the negative of the slope of $\log(\lambda)$ and $1/\epsilon = 1/\sigma^2$, and this estimate is shown in Fig. 6.33 to be $3.6 * 10^{-}5$.

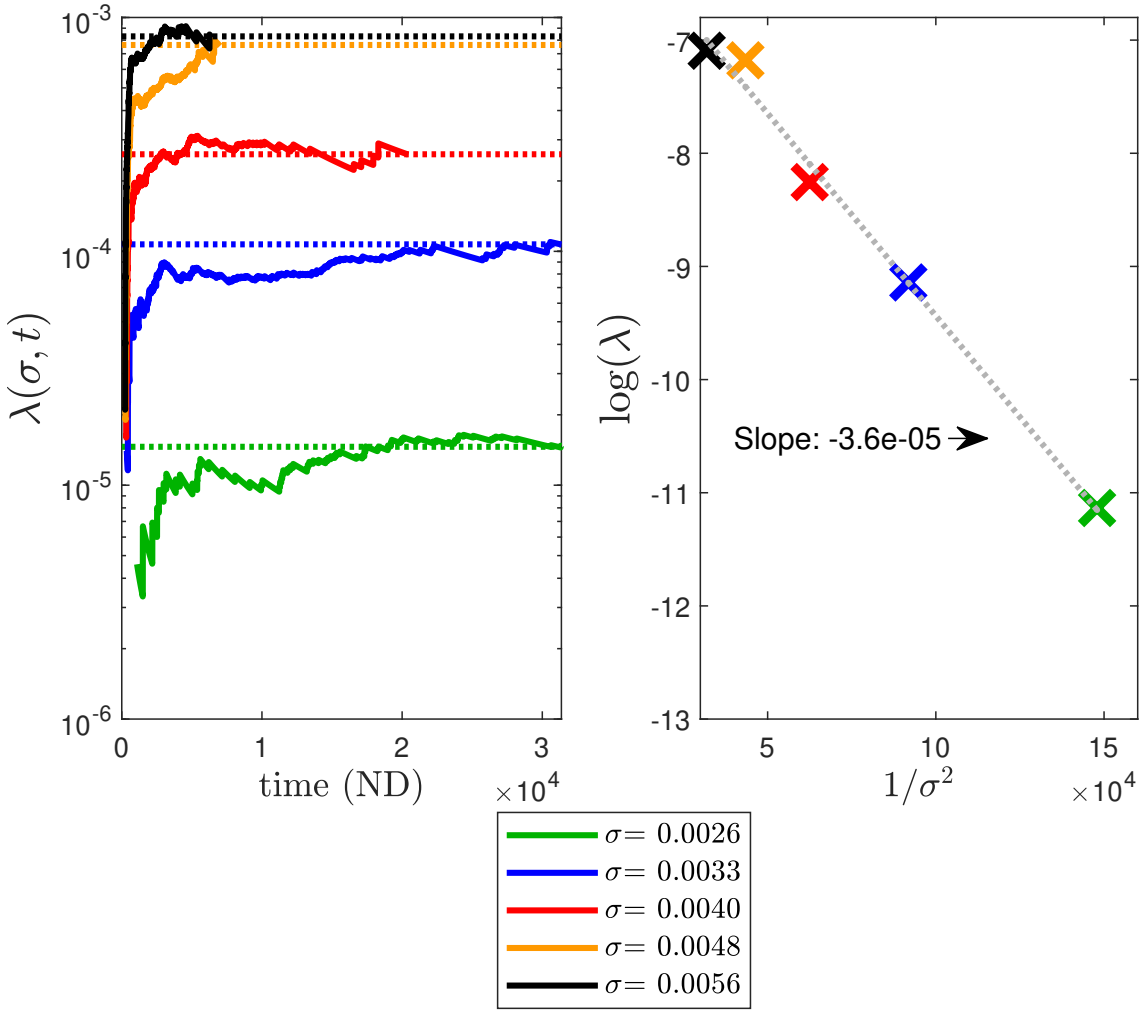


Figure 6.33: (left) The escape rate, λ, estimated from the results in Fig. 6.32 as a function of time. Note it approaches a constant after an initial transient and terminates (no more data) after all trials have transitioned out of the $LHLL$ mode. (right) The slope of the $\log(\lambda)$ and $1/\sigma^2$ that can be used to estimate the quasipotential from simulation results. At the excitation frequency of 23Hz the estimate of the quasipotential is $3.6 * 10^{-5}$.

The simulation results obtained by integrating (6.11) at the constant noise intensity of $\sigma = 0.0056$ are shown for different frequencies of excitation and compared to the experimental results in Fig. 6.34. Notice that increases in frequency in the hysteresis

region lead to increases in the median escape times.

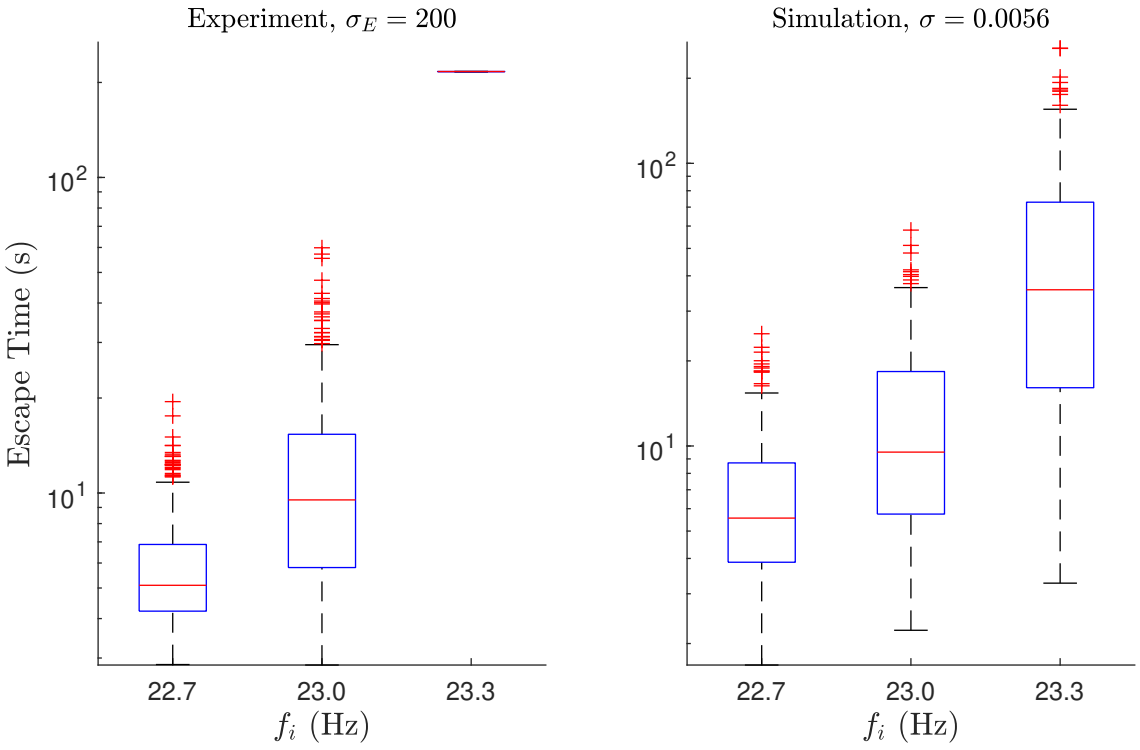


Figure 6.34: Box plots of the transition times from the $LHLL$ mode to the $LLLL$ mode for both the experimental and simulation results for different excitation frequencies, f_i and a constant noise intensity.

The sensitivity of the escape times to the excitation frequency can be explained by observing the behavior of the quasipotential, a quantifier of the difficulty of the escape, as a function of the excitation frequency. By using the method described in Chapter 4, the quasipotential is calculated for the system (6.12) and is shown as a function of frequency in Fig. 6.35. The quasipotential decreases with decreasing frequency leading to lesser escape difficulty and shorter escape times on average. At the $\Omega = 0.92$ which is equivalent to $f_i = 23Hz$ for this system, the quasipotential calculated with the deterministic method of Chapter 4 is $3.1 * 10^{-5}$. The estimate obtained by integrating

(6.12) in Fig. 6.33 has 16% error. Three sources of systemic error include (i) that the method of Chapter 4 assumes $\epsilon \to 0$ while in Fig. 6.33 the noise is finite, (ii) that an exponential relationship between $1/\epsilon$ and λ is assumed, and (iii) numerical errors in the optimization of the methodology in Chapter 4. Statistical errors are also present in the estimate of P_{LHLL} from stochastic simulations. Despite these errors, the estimate is not so far off and one could take away from this that using the method in Chapter 4, which is much less computationally expensive than the Monte Carlo approach, gives an adequate approximation of the quasipotential at small but finite noise intensities.

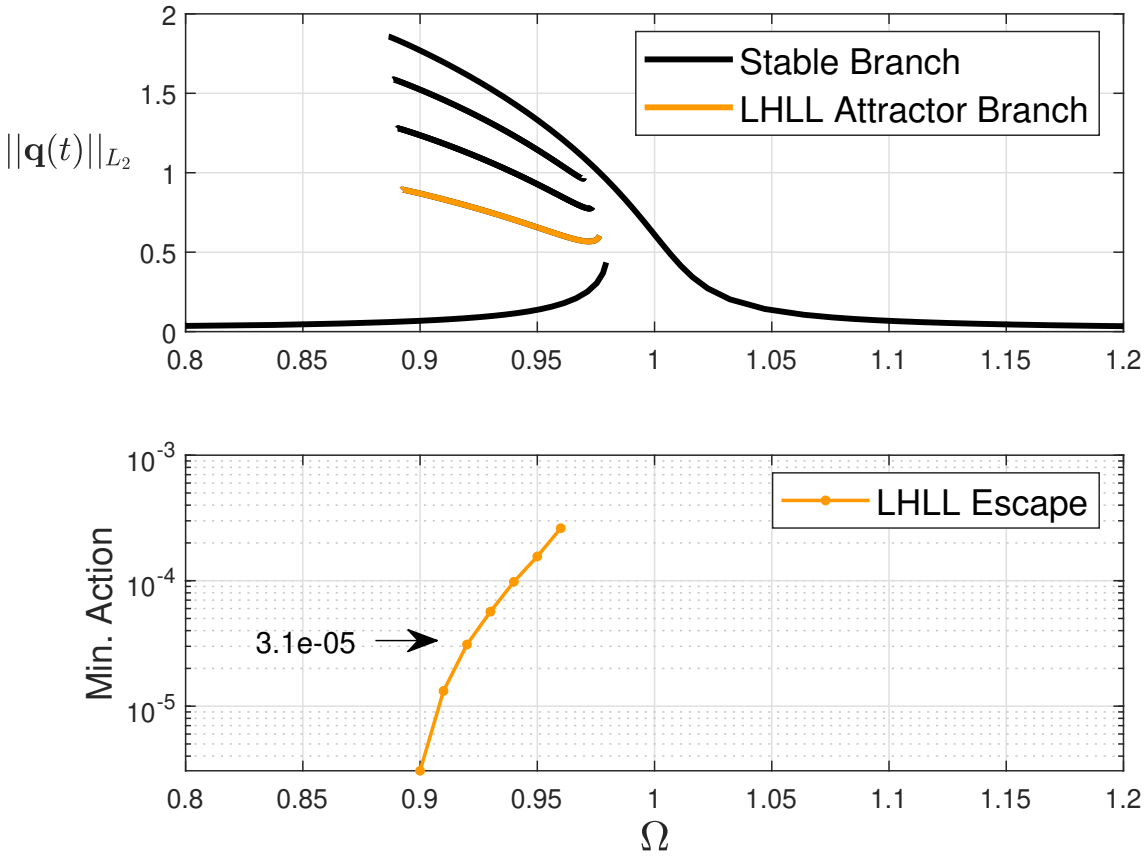


Figure 6.35: (top) L_2 norm of the frequency response of the stable modes of the Four Beam system as a function of excitation frequency. (bottom) The quasipotential (min. action) of escapes from the $LHLL$ mode to as a function of excitation frequency. At $\Omega = 0.92$, the excitation frequency is equivalent to $f_i = 23Hz$, and the corresponding quasipotential value is $3.1 * 10^{-5}$.

6.5 Eight Coupled Cantilever Beams

A study of response localizations in the full array of eight beams is attempted by tuning all eight beams to a first natural frequency of $f_n = 24$ Hz. All beams are highlighted in black in Fig. 6.36 to show they are all tuned beams of interest.

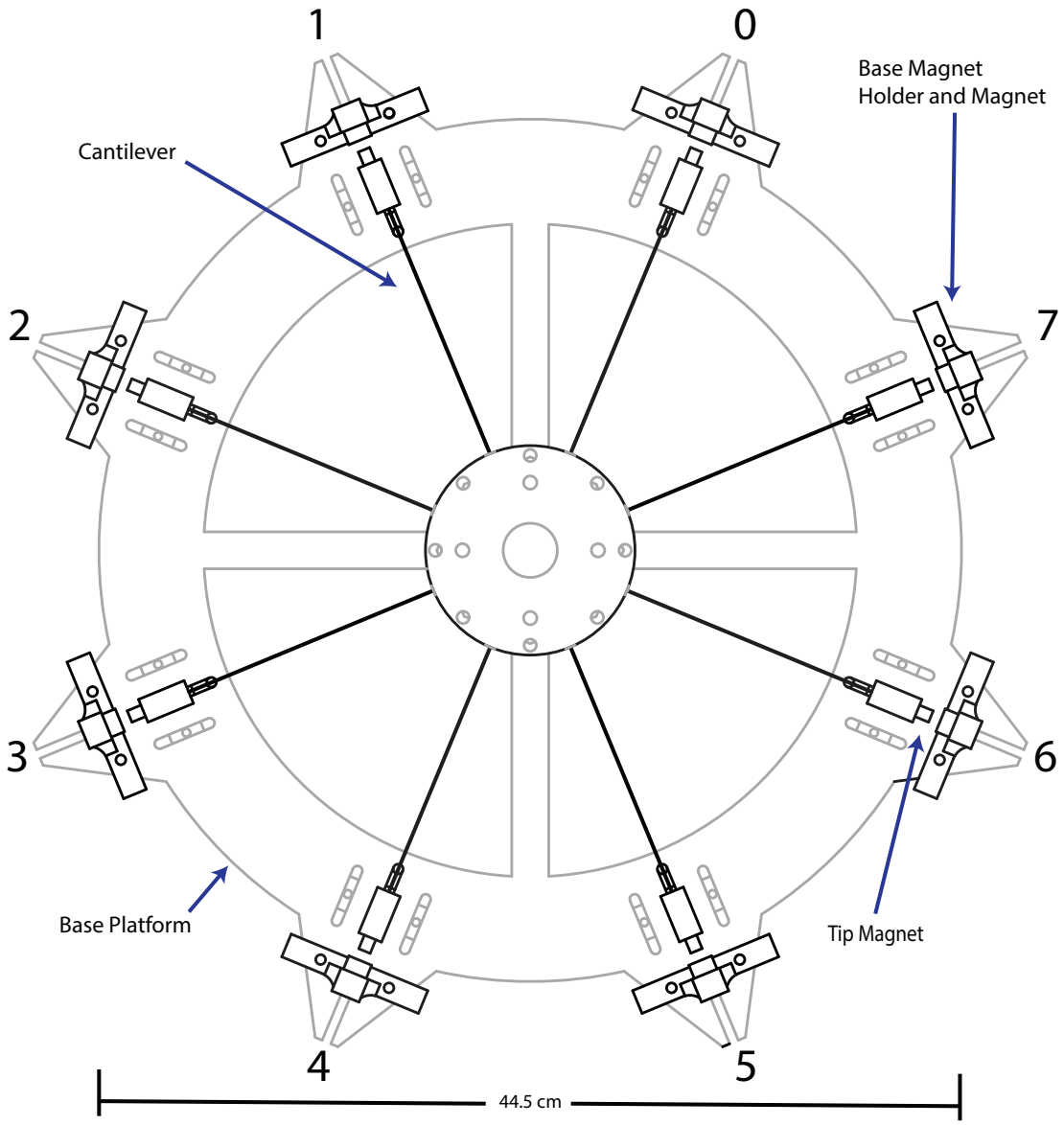


Figure 6.36: Top view schematic of the circular cantilever beam array with all eight beams as tuned beams of interest.

A set of frequencies sweeps are performed for this eight beam system as for the two and four beam systems in Section 6.3.1 and 6.4.1. The sum of the first harmonic amplitudes of the response of the beams are shown as a function of excitation frequency in Fig. 6.37.

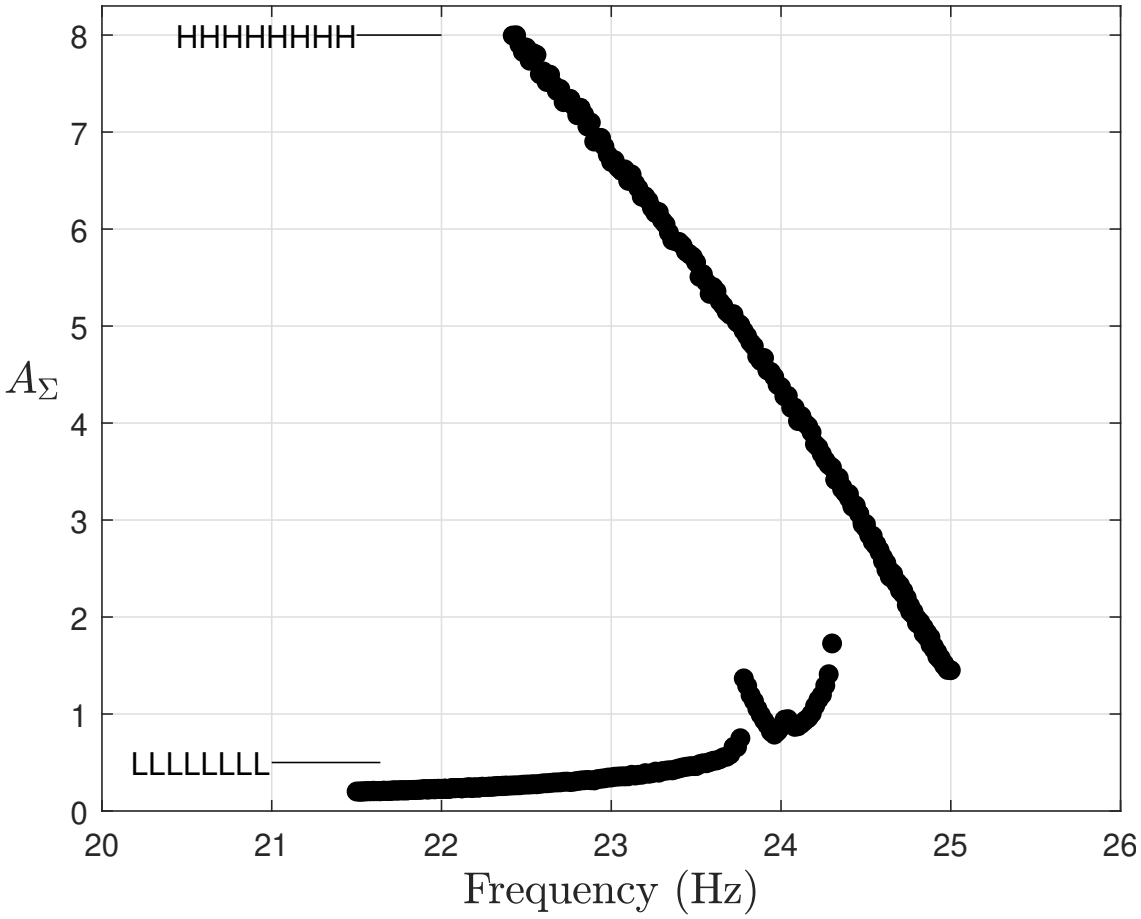


Figure 6.37: The sum of the first harmonic amplitude responses of the eight beam system as a function of frequency. Notice only two unique nonlinear modes labeled in this figure.

There are only two unique responses in the hysteresis region $22.3 \leq f_i \leq 24.3$ Hz. These responses are labeled L^N and H^N with $N = 8$. All beams in the H^N response vibrate at high amplitudes. All beams in the L^N response vibrate at lower amplitudes. No

response localizations are observed despite the use of the detuning system to try to create them as in the two beam and the four beam system. It is possible that with more beams vibrating in this system, there is a larger cumulative coupling force. Consider for example the model (6.5) from Section 6.4; the coupling force is the sum of the displacements of each beam. It is known that response localizations in model nonlinear systems like (6.5) are unstable or do not exist for large coupling forces.

Also note a local maximum in the L^N at $f_i \approx 23.9$ Hz prior to the *jump up* frequency at $f_i \approx 24.3$ Hz. This peak corresponds to certain beams breaking symmetry and vibrating at higher amplitude. This L^N response occurs for sweeps with increasing frequency that started at $f_i = 21.5$ Hz and decreasing frequencies that started at 24Hz. That is, this response near this local maximum is not sensitive to the direction of the frequency sweep. Multiple calibrations and multiple trials of the frequency sweeps were performed to confirm these results. It is possible this local maximum is a symptom of inhomogeneity in the system that calibration of the first natural frequency of the beams does not resolve.

Experiments to study noise influenced transitions out of response localizations were not performed for the eight cantilever beam system because no stable response localizations were observed.

6.6 Discussion

In this chapter, the effect of noise on a circular array of cantilever beams and on coupled softening Duffing oscillators was examined. The experimental system was shown to demonstrate characteristic nonlinear phenomena, including multiple stable responses

under the influence of an external periodic excitation. The experiment was designed with the ability to reliably reproduce the nonlinear modes of interest and to produce large quantity of long duration noise trials. Through these noise trials, evidence was created that shows that noise could create transitions from response localizations into the low amplitude responses, with probabilities that depend on the intensity of the noise and the frequency of the external excitation. The trials were designed such that the one could observe transitions from response localizations into other response localizations or nonlinear modes other than the low amplitude response; nevertheless, in all trials, this system only transitioned from the response localization into the low amplitude response or remained in the initial localized mode.

By itself, the experimental results can provide interesting new insights. This is the first realization of a circular macro cantilever beam array designed to study the influence of noise. It was demonstrated that if beams arranged in this manner experience nonlinear restoring forces, they can experience potentially undesired nonlinear vibration modes. Furthermore, it was demonstrated that for certain designs influenced by noise, with much higher probability, the system will transition out of the response localizations than into these localized responses. This nearly one directional behavior supports the idea that noise from the environment or an open loop control strategy can be useful to keep a design in desirable operating conditions.

The detuning system used in the chapter was designed with the purpose of setting the initial conditions of the experiment. Nevertheless, the effect of inhomogeneity in these systems are inherently a part of the results of this chapter. Magnets were used to calibrate beams of interest to within 0.1 Hz of each other. Other beams were left detuned with

linear natural frequencies far from the excitation bandwidth of interest. A system of linear actuators was used to detune and then retune beams of interest during the operation of the experiment to produce the desired initial conditions; this was possible due to the type of hysteresis that was observed in the response of the beams as a function of the stiffness of the beams. Finally, in the four beam system, it can be observed in the frequency response of Fig. 6.21 that one of the beams has a transition to a high amplitude response before the other beams in the frequency sweep. This behavior may occurs because the beams are not exactly homogeneous despite the calibration. Inhomegeneity was used as a feature of this experiment. Inhomogeneity was used to reduce the dimensionality of the problem when desired, to change the initial conditions of a noise trial, and to demonstrate that models of homogenous systems can be appropriate to model a real physical system that is not perfectly homogeneous.

In order to explain the source of the stochastic nonlinear behavior in the experiment, a nonlinear, N-DOF, lumped mass, spring-mass-damper system model for a cantilever structure with N beams was described. A simple model of the coupling force between the beams was constructed with the assumption that each beam created a proportional force to its displacement that affected each other beam. A coupling coefficient was found by fitting the result of the experimental phase response to the phase response from numerical continuation. Initially, an alternative cost function for the coupling coefficient was used that minimized the error in the frequency amplitude response between the experimental responses and the numerical continuation responses. It was found that the coupling coefficient had minor influences on the amplitude response but significant influence on the phase response.

This system models are a significant approximation of the experimental arrangement, yet the models still provides useful insights into system behavior. In particular, it was demonstrated that the Euler-Maruyama simulations of the system models qualitatively reproduce the relationship between escape times and probability of escape with respect to noise intensity and excitation frequency. Two noise models were used, one with a single noise source, and one with N independent noise sources in Section 6.4.4. The Monte Carlo results were surprisingly similar for both models. It may be that since the model was only applied to with initial conditions in a localized steady state, only the effect of the noise on the high amplitude beam was of importance, and therefore whether the noise source was independent for each beam or not did not have a significant effect. This agrees with results found in Chapter 4, where it was observed that the transitions in the weak noise limit from the localized modes to the low amplitude mode occurred via work performed nearly exclusively to the high amplitude oscillator. The results from the Monte Carlo simulations were also used to approximate the quasipotential. There was a 16% error between the quasipotential found from the Monte Carlo simulations and one generated using the methodology described in Chapter 4. It was shown that the quasipotential varies with frequency of excitation in the four beam system, and that the quasipotential results agree with the qualitative behavior observed as the excitation frequency of the experiment was changed.

The system model has limitations. The agreement in the amplitude response for localized modes between the model and the experiment could be improved. Furthermore, the system model assumes white noise while the actuator in the experiment delivers filtered noise. Considerations of alternative nonlinear terms, coupling terms, and an

improved noise model could improve on the comparisons between the simulation results and the experimental results as a subject of future work.

Chapter 7: Contributions and Future Work

7.1 Summary of Contributions

The effect of noise on response localizations of oscillator arrays has been studied through a combination of experimental studies on cantilever beams and numerical studies on nonlinear oscillators with periodic attractors. This work includes results for four experimental arrangements of a circular oscillator array consisting of 1, 2, 4, and 8 beams, where the single beam experiment can be thought of as representative to nonlinear behavior in an array with negligible coupling forces. The numerical work has analyzed arrays of N coupled Duffing oscillators for $N = 1, 2, 3, 4,$ and 5; this includes arrays with hardening and softening nonlinearities with no coupling, coupling via nearest neighbors linear springs, and coupling via unspecified forces that are linear functions of other beams. The following is a summary of the key contributions from these studies:

A methodology based on the Path Integral Method was proposed to quantify the probability of transitions out of stable periodic solutions of Duffing oscillators and two coupled Duffing oscillators due to short duration white noise in Chapter 3. While it was previously known transitions due to noise in these systems were possible, this work yielded a fast method for quantifying the transitions for systems that experience noise of short duration but large intensities. Such a tool, for example, would be useful in

determining the parameters at which a short term open loop control effort to induce a transition using random perturbations would be useful. The results were compared to an alternative but much more computationally expensive method using the Euler-Maruyama scheme, and the results were shown to be similar.

In Chapter 4, a methodology based on Large Deviation Theory, Optimal Control Theory, and prior work on the Action Plot Method was proposed to quantify the quasipotential and most probable escape paths out of periodic attractors of nonlinear systems in the weak noise limit. This methodology was applied to find the quasipotential and MPEPs of a hardening Duffing oscillator, two coupled hardening Duffing oscillators, and a circular array of $N = 3$ and $N = 5$ hardening Duffing oscillators. The first visualizations of MPEPs of these systems were generated. The respective quasipotential values for the MPEPs were shown as a function of frequency of excitation and coupling strength parameters. Using the quasipotential, it was shown that escape out of response localizations are more likely to transition down into the low amplitude modes near the jump down frequencies and more likely to transition up into higher amplitude modes near the jump up frequencies. Furthermore, it was shown that the quasipotential in this hardening system decreased with increases in coupling strength; one could conclude from this that transitions out of response localizations are more likely within a finite amount of time in a system that has marginally stronger coupling. Furthermore, it was shown that for systems that have nearest neighbor coupling, the quasipotential for escapes out of response localizations of the $N = 3$ system were approximately equal to the quasipotentials of the $N = 5$ system; one could conclude from this that for weakly coupled nearest neighbor systems that have response localizations, it is only the

influence of the nearest neighbors that is not negligible. As a result, low dimensional studies such as the $N = 3$ may provide adequate approximations of the behavior of higher dimensional arrays. The work in this chapter supports and can be used to explain observations in other studies of similar systems including [8, 9] as well as Chapter 5 and 6, wherein the effect of frequency and coupling on these systems have been observed in response to stochastic inputs; that is, for small noise, observed patterns in transition times due to system parameters can be explained by the value of the quasipotential and Large Deviation Theory.

Another contribution of this dissertation is the design of a series of experiments that can produce a high quantity of long duration noise trials of transitions out of stable modes of single cantilever and circular cantilever beam array arrangements. These experiments have produced an enormous amount of highly repeatable empirical evidence demonstrating many difficult to achieve nonlinear modes in circular arrays, as well as noise induced transitions in between these modes. It was observed in Chapter 5 and 6, that transitions times in the experiments are exponentially related to the noise intensity, decrease on average closer to the jump down frequency, and increase on average closer to the jump up frequencies. These patterns were observed in the one cantilever beam experiment and response localizations of the circular oscillator array with two tuned beams and four tuned beams. The system identification approach described in Chapter 5 and Chapter 6 was used to create nonlinear system models of the experimental system. The same qualitative behavior was observed in the experimental system compared to observed behavior during stochastic simulations of the system models. The quasipotential for the system model was also shown to be useful in understanding the transition time

patterns at the finite noise intensities of the simulation and experiments.

7.2 Future Work

As an extension of the work in Chapter 3, results for the one Duffing oscillator case could be used to construct the probability of transitions in higher dimensional systems with independent oscillator assumptions. The independent oscillator assumption will create an error that could be quantified with comparisons to results from Euler-Maruyama simulations of weakly coupled high dimensional systems. Further exploration of these errors could shed interesting insights, including those if the errors are small and within an acceptable range when the system is weakly coupled. Then, the work in Chapter 3 would be practically useful to create fast approximations of probability of transitions in weakly coupled systems of much larger dimensions. Alternatively, it would also be interesting to learn the opposite; that is, that the coupling is essential for probability quantification even when the system is weakly coupled. Additional analysis could be used to explore whether the transition probabilities obtained for a system at the anti-continuum limit ($\nu \to 0$) can bound those for the systems with coupling.

The methodology developed in Chapter 4 was generalized for different stiffness models of coupled second order systems with periodic forcing and these models can be generalized further for mechanical and non-mechanical systems. Simple extensions of this work could be used to explore the quasipotential and most probable escape paths of high dimensional heterogeneous systems. Motivating a future study by the observation there is only a single dominant source of noise in the experiments, the methodology in

Chapter 4 could be adapted for coupled systems subjected to a single noise source. It is unclear whether such a system would exhibit the same patterns observed in Chapter 4, where minimum action paths approached saddle solutions as $t \to \infty$.

The work in Chapter 6 opens the door to many interesting avenues of future work. Without making any changes to the current experimental prototype, one could continue studying the effect of noise on other nonlinear modes of the array other than the localized mode. Furthermore, minor changes to the mechanical design could allow one to study the following:

- Heterogeneous systems via intentional heterogeneous calibration of the cantilever beams
- Coupling strength in the structure via designing different center disks diameters and the inclusion of coupling springs of variable stiffness (see Fig. 6.36)
- Structures that exhibit hardening instead of softening characteristics obtained by varying the base magnet positions or removing the magnets altogether
- Propeller blade structures, instead of cantilever structures, that exhibit dynamics more similar to those of real applications
- Traveling localization dynamics in a circular array with and without the influence of noise via adding impulses to the experimental array.
- Deterministic control strategies by adding control algorithms to the software that programs the FPGA (see Fig. 5.1)
- The influence of random perturbations originating from different distributions by changing the source of noise in the controller.

In addition to these experimental ideas, there is additional analysis that could expand on the data collected in this dissertation. The noise model used in Chapters 5 and 6 assumed white noise; this model and the simulations could be adapted to consider other types of noise. A model to explain the stiffness induced transitions via the change

in positions of the magnets in the detuning system could be developed. Additionally, alternative system identification approaches for both the deterministic system and the random perturbations could also be explored and discussed.

Bibliography

[1] A. Grolet and F. Thouverez, "Free and forced vibration analysis of a nonlinear system with cyclic symmetry: Application to a simplified model," *Journal of Sound and Vibration*, vol. 331, pp. 2911–2928, June 2012.

[2] B. Balachandran, E. Perkins, and T. Fitzgerald, "Response localization in micro-scale oscillator arrays: influence of cubic coupling nonlinearities," *International Journal of Dynamics and Control*, vol. 3, no. 2, pp. 183–188, 2015. Publisher: Springer.

[3] A. Papangelo, F. Fontanela, A. Grolet, M. Ciavarella, and N. Hoffmann, "Multistability and localization in forced cyclic symmetric structures modelled by weakly-coupled Duffing oscillators," *Journal of Sound and Vibration*, vol. 440, pp. 202–211, Feb. 2019.

[4] E. Perkins, M. Kimura, T. Hikihara, and B. Balachandran, "Effects of noise on symmetric intrinsic localized modes," *Nonlinear Dynamics*, vol. 85, no. 1, pp. 333–341, 2016. ISBN: 0924-090X Publisher: Springer.

[5] A. M. Alofi, *Coupled Oscillator Arrays: Dynamics and Influence of Noise*. PhD Thesis, University of Maryland, College Park, 2021.

[6] J. S. Yu, G. Q. Cai, and Y. K. Lin, "A new path integration procedure based on Gauss-Legendre scheme," *International journal of non-linear mechanics*, vol. 32, no. 4, pp. 759–768, 1997. ISBN: 0020-7462 Publisher: Elsevier.

[7] S. Beri, R. Mannella, D. G. Luchinsky, A. Silchenko, and P. V. McClintock, "Solution of the boundary value problem for optimal escape in continuous stochastic systems and maps," *Physical Review E*, vol. 72, no. 3, p. 036131, 2005. Publisher: APS.

[8] B. Balachandran, T. Breunung, G. D. Acar, A. Alofi, and J. A. Yorke, "Dynamics of circular oscillator arrays subjected to noise," *Nonlinear Dynamics*, pp. 1–14, 2022. Publisher: Springer.

[9] A. Alofi, G. Acar, and B. Balachandran, "Noise influenced response movement in coupled oscillator arrays with multi-stability," *Journal of Sound and Vibration*, p. 116951, Apr. 2022.

[10] E. Logan Jr, *Handbook of turbomachinery*. CRC Press, 2003.

[11] Ronidong, "Pratt & Whitney PW4000-112," Jan. 2019.

[12] R. E. Bartels and A. Sayma, "Computational aeroelastic modelling of airframes and turbomachinery: progress and challenges," *Philosophical Transactions of the Royal Society A: Mathematical, Physical and Engineering Sciences*, vol. 365, no. 1859, pp. 2469–2499, 2007. Publisher: The Royal Society London.

[13] S. Beeby and N. M. White, *Energy harvesting for autonomous systems*. Artech House, 2010.

[14] S. Priya and D. J. Inman, *Energy harvesting technologies*, vol. 21. Springer, 2009.

[15] S. P. Beeby, M. J. Tudor, and N. White, "Energy harvesting vibration sources for microsystems applications," *Measurement science and technology*, vol. 17, no. 12, p. R175, 2006. Publisher: IOP Publishing.

[16] P. D. Mitcheson, E. M. Yeatman, G. K. Rao, A. S. Holmes, and T. C. Green, "Energy harvesting from human and machine motion for wireless electronic devices," *Proceedings of the IEEE*, vol. 96, no. 9, pp. 1457–1486, 2008. Publisher: IEEE.

[17] G. W. Taylor, J. R. Burns, S. Kammann, W. B. Powers, and T. R. Welsh, "The energy harvesting eel: a small subsurface ocean/river power generator," *IEEE journal of oceanic engineering*, vol. 26, no. 4, pp. 539–547, 2001. Publisher: IEEE.

[18] Y. Jia, "Review of nonlinear vibration energy harvesting: Duffing, bistability, parametric, stochastic and others," *Journal of Intelligent Material Systems and Structures*, vol. 31, no. 7, pp. 921–944, 2020. Publisher: SAGE Publications Sage UK: London, England.

[19] I. A. Sever, *Experimental validation of turbomachinery blade vibration predictions*. PhD thesis, Imperial College London (University of London), 2004.

[20] M. P. Castanier and C. Pierre, "Modeling and Analysis of Mistuned Bladed Disk Vibration: Current Status and Emerging Directions," *Journal of Propulsion and Power*, vol. 22, pp. 384–396, Mar. 2006.

[21] D. J. Ewins, "The effects of detuning upon the forced vibrations of bladed disks," *Journal of Sound and Vibration*, vol. 9, no. 1, pp. 65–79, 1969. Publisher: Elsevier.

[22] J. A. Kenyon and J. H. Griffin, "Forced Response of Turbine Engine Bladed Disks and Sensitivity to Harmonic Mistuning," *Journal of Engineering for Gas Turbines and Power*, vol. 125, pp. 113–120, Dec. 2002.

[23] Y. Yan, P. Cui, and H. Hao, "Vibration mechanism of a mistuned bladed-disk," *Journal of sound and vibration*, vol. 317, no. 1-2, pp. 294–307, 2008. Publisher: Elsevier.

[24] P. Gardonio and M. Zilletti, "Vibration energy harvesting based on mode localization," *ISMA 2014)(Katholieke Universiteit Leuven, Belgium, 15–17 September 2014)*, 2014.

[25] A. Dick, B. Balachandran, and c. Mote, "Intrinsic localized modes in microresonator arrays and their relationship to nonlinear vibration modes," *Nonlinear Dynamics*, vol. 54, pp. 13–29, Jan. 2008.

[26] G. Kerschen, M. Peeters, J.-C. Golinval, and A. F. Vakakis, "Nonlinear normal modes, Part I: A useful framework for the structural dynamicist," *Mechanical systems and signal processing*, vol. 23, no. 1, pp. 170–194, 2009. Publisher: Elsevier.

[27] T. Ikeda, Y. Harata, and K. Nishimura, "Intrinsic localized modes of harmonic oscillations in nonlinear oscillator arrays," *Journal of Computational and Nonlinear Dynamics*, vol. 8, no. 4, 2013. Publisher: American Society of Mechanical Engineers Digital Collection.

[28] A. V. Srinivasan, "Flutter and Resonant Vibration Characteristics of Engine Blades," *Journal of Engineering for Gas Turbines and Power*, vol. 119, pp. 742–775, Oct. 1997.

[29] E. Lefeuvre, A. Badel, C. Richard, L. Petit, and D. Guyomar, "A comparison between several vibration-powered piezoelectric generators for standalone systems," *Sensors and Actuators A: Physical*, vol. 126, pp. 405–416, Feb. 2006.

[30] J. Emad, A. F. Vakakis, and N. Miller, "Experimental nonlinear localization in a periodically forced repetitive system of coupled magnetoelastic beams," *Physica D: Nonlinear Phenomena*, vol. 137, pp. 192–201, Mar. 2000.

[31] M. Kimura and T. Hikihara, "Coupled cantilever array with tunable on-site nonlinearity and observation of localized oscillations," *Physics Letters A*, vol. 373, pp. 1257–1260, Mar. 2009.

[32] M. Kimura and T. Hikihara, "Experimental manipulation of intrinsic localized modes in macro-mechanical system," *Nonlinear Theory and Its Applications, IEICE*, vol. 3, no. 2, pp. 233–245, 2012.

[33] J. E. Perkins, *Noise-influenced dynamics of nonlinear oscillators*. PhD Thesis, University of Maryland, College Park, 2015.

[34] B. Niedergesäß, A. Papangelo, A. Grolet, A. Vizzaccaro, F. Fontanela, L. Salles, A. J. Sievers, and N. Hoffmann, "Experimental observations of nonlinear vibration localization in a cyclic chain of weakly coupled nonlinear oscillators," *Journal of Sound and Vibration*, vol. 497, p. 115952, 2021.

[35] D. K. Campbell, S. Flach, Y. S. Kivshar, and others, "Localizing energy through nonlinearity and discreteness," *Physics Today*, vol. 57, no. 1, pp. 43–49, 2004. Publisher: American Institute of Physics.

[36] M. Sato, B. E. Hubbard, and A. J. Sievers, "Colloquium: Nonlinear energy localization and its manipulation in micromechanical oscillator arrays," *Reviews of Modern Physics*, vol. 78, pp. 137–157, Jan. 2006.

[37] D. Brake, H. Xu, A. Hollowell, G. Balakrishnan, C. Hains, M. Marconi, and V. Putkaradze, "Intrinsic localized modes in two-dimensional vibrations of crystalline pillars and their application for sensing," *Journal of Applied Physics*, vol. 112, p. 104326, Nov. 2012.

[38] T. Ikeda, Y. Harata, and K. Nishimura, "Intrinsic Localized Modes of Harmonic Oscillations in Pendulum Arrays Subjected to Horizontal Excitation," *Journal of Computational and Nonlinear Dynamics*, vol. 10, Mar. 2015.

[39] A. Grolet, Z. Shami, S. Arabi, and O. Thomas, "Experimental nonlinear localisation in a system of two coupled beams," in *Dynamical systeme theory and applications (DSTA)*, 2019.

[40] P. W. Anderson, "Absence of diffusion in certain random lattices," *Physical review*, vol. 109, no. 5, p. 1492, 1958. Publisher: APS.

[41] V. Agarwal, X. Zheng, and B. Balachandran, "Influence of noise on frequency responses of softening Duffing oscillators," *Physics Letters A*, vol. 382, no. 46, pp. 3355–3364, 2018. ISBN: 0375-9601 Publisher: Elsevier.

[42] V. Agarwal, J. A. Yorke, and B. Balachandran, "Noise-induced chaotic-attractor escape route," *Nonlinear Dynamics*, vol. 102, no. 2, pp. 863–876, 2020. Publisher: Springer.

[43] L. Haitao, Q. Weiyang, L. Chunbo, D. Wangzheng, and Z. Zhiyong, "Dynamics and coherence resonance of tri-stable energy harvesting system," *Smart Materials and Structures*, vol. 25, p. 015001, Nov. 2015. Publisher: IOP Publishing.

[44] T. Irvine, "Bending frequencies of beams, rods, and pipes," vol. 500, no. s50, pp. 31–38, 2012.

[45] M. J. Hochrainer and A. M. Puhwein, "Design and Characterization of a Multi-purpose Duffing Oscillator with Flexible Parameter Selection," in *Special Topics in Structural Dynamics & Experimental Techniques, Volume 5*, pp. 81–88, Springer, 2021.

[46] G. Duffing, "Erzwungene schwingungen bei veränderlicher eigenfrequenz," *Vieweg u. Sohn, Braunschweig*, vol. 7, 1918.

[47] A. Nayfeh and D. Mook, *Nonlinear Oscillations*. Wiley Classics Library, Wiley, 2008.

[48] I. Kovacic and M. J. Brennan, *The Duffing equation: nonlinear oscillators and their behaviour*. John Wiley & Sons, 2011.

[49] C. Hayashi, *Nonlinear oscillations in physical systems*. Princeton University Press, 2014.

[50] B. A. Huberman and J. P. Crutchfield, "Chaotic states of anharmonic systems in periodic fields," *Physical Review Letters*, vol. 43, no. 23, p. 1743, 1979. Publisher: APS.

[51] E. J. Doedel, T. F. Fairgrieve, B. Sandstede, A. R. Champneys, Y. A. Kuznetsov, and X. Wang, "AUTO-07P: Continuation and bifurcation software for ordinary differential equations," tech. rep., 2007.

[52] H. Dankowicz, F. Schilder, M. Li, E. Fotsch, and M. Henderson, "COCO Continuation Core and Toolboxes," *SourceForge, accessed Oct*, vol. 17, p. 2019, 2019.

[53] A. F. Vakais and C. Cetinkaya, "Mode localization in a class of multidegree-of-freedom nonlinear systems with cyclic symmetry," *SIAM Journal on Applied Mathematics*, vol. 53, no. 1, pp. 265–282, 1993. Publisher: SIAM.

[54] G. Kerschen, "Computation of Nonlinear Normal Modes through Shooting and Pseudo-Arclength Computation," in *Modal Analysis of Nonlinear Mechanical Systems* (G. Kerschen, ed.), pp. 215–250, Vienna: Springer Vienna, 2014.

[55] M. Peeters, R. Viguié, G. Sérandour, G. Kerschen, and J.-C. Golinval, "Nonlinear normal modes, Part II: Toward a practical computation using numerical continuation techniques," *Special Issue: Non-linear Structural Dynamics*, vol. 23, pp. 195–216, Jan. 2009.

[56] A. Dick, B. Balachandran, and c. Mote, "Localization in Microresonator Arrays: Influence of Natural Frequency Tuning," *Journal of Computational and Nonlinear Dynamics - J COMPUT NONLINEAR DYN*, vol. 5, Jan. 2010.

[57] U. von Wagner and W. V. Wedig, "On the Calculation of Stationary Solutions of Multi-Dimensional Fokker–Planck Equations by Orthogonal Functions," *Nonlinear Dynamics*, vol. 21, pp. 289–306, Mar. 2000.

[58] W. Martens, U. von Wagner, and V. Mehrmann, "Calculation of high-dimensional probability density functions of stochastically excited nonlinear mechanical systems," *Nonlinear Dynamics*, vol. 67, pp. 2089–2099, Feb. 2012.

[59] A. Förster, L. Panning-von Scheidt, and J. Wallaschek, "Approximate Solution of the Fokker–Planck Equation for a Multidegree of Freedom Frictionally Damped Bladed Disk Under Random Excitation," *Journal of Engineering for Gas Turbines and Power*, vol. 141, Sept. 2018.

[60] S. Ramakrishnan and B. Balachandran, "Energy localization and white noise-induced enhancement of response in a micro-scale oscillator array," *Nonlinear dynamics*, vol. 62, no. 1, pp. 1–16, 2010. Publisher: Springer.

[61] E. Perkins and B. Balachandran, "Noise-enhanced response of nonlinear oscillators," *Procedia Iutam*, vol. 5, pp. 59–68, 2012. Publisher: Elsevier.

[62] E. Perkins, C. Chabalko, and B. Balachandran, "Noise-influenced transient energy localization in an oscillator array," *Nonlinear Theory and Its Applications, IEICE*, vol. 4, no. 3, pp. 232–243, 2013. ISBN: 2185-4106 Publisher: The Institute of Electronics, Information and Communication Engineers.

[63] J. S. Yu and Y. K. Lin, "Numerical path integration of a non-homogeneous Markov process," *International Journal of Non-Linear Mechanics*, vol. 39, no. 9, pp. 1493–1500, 2004.

[64] P. Kumar and S. Narayanan, "Modified path integral solution of Fokker–Planck equation: response and bifurcation of nonlinear systems," *Journal of computational and nonlinear dynamics*, vol. 5, no. 1, 2010.

[65] S. Narayanan and P. Kumar, "Numerical solutions of Fokker–Planck equation of nonlinear systems subjected to random and harmonic excitations," *Probabilistic Engineering Mechanics*, vol. 27, no. 1, pp. 35–46, 2012. ISBN: 0266-8920 Publisher: Elsevier.

[66] J. Cui, W.-A. Jiang, Z.-W. Xia, and L.-Q. Chen, "Non-stationary response of variable-mass Duffing oscillator with mass disturbance modeled as Gaussian white noise," *Physica A: Statistical Mechanics and its Applications*, vol. 526, p. 121018, July 2019.

[67] W. Xie, W. Xu, and L. Cai, "Study of the Duffing–Rayleigh oscillator subject to harmonic and stochastic excitations by path integration," *Special issue for The Beijing-HK Scientific Computing Meetings*, vol. 172, pp. 1212–1224, Jan. 2006.

[68] Z. Ren, W. Xu, and Y. Qiao, "Local averaged path integration method approach for nonlinear dynamic systems," *Applied Mathematics and Computation*, vol. 344, pp. 68–77, 2019. Publisher: Elsevier.

[69] D. J. Higham, "An algorithmic introduction to numerical simulation of stochastic differential equations," *SIAM review*, vol. 43, no. 3, pp. 525–546, 2001. ISBN: 0036-1445 Publisher: SIAM.

[70] U. Von Wagner, "On double crater-like probability density functions of a duffing oscillator subjected to harmonic and stochastic excitation," *Nonlinear Dynamics*, vol. 28, no. 3-4, pp. 343–355, 2002.

[71] W. Xu, Q. He, T. Fang, and H. Rong, "Global analysis of stochastic bifurcation in Duffing system," *International Journal of Bifurcation and Chaos*, vol. 13, no. 10, pp. 3115–3123, 2003. Publisher: World Scientific.

[72] W. Xu, Q. He, T. Fang, and H. Rong, "Stochastic bifurcation in Duffing system subject to harmonic excitation and in presence of random noise," *International Journal of Non-Linear Mechanics*, vol. 39, no. 9, pp. 1473–1479, 2004. ISBN: 0020-7462 Publisher: Elsevier.

[73] Y. Zhang, Y. Jin, P. Xu, and S. Xiao, "Stochastic bifurcations in a nonlinear tri-stable energy harvester under colored noise," *Nonlinear Dynamics*, vol. 99, pp. 879–897, Jan. 2020.

[74] P. Kumar, S. Narayanan, S. Adhikari, and M. Friswell, "Fokker–Planck equation analysis of randomly excited nonlinear energy harvester," *Journal of Sound and Vibration*, vol. 333, pp. 2040–2053, Mar. 2014.

[75] M. I. Freidlin and A. D. Wentzell, "Random perturbations," in *Random perturbations of dynamical systems*, pp. 15–43, Springer, 1998.

[76] W. E, W. Ren, and E. Vanden-Eijnden, "Minimum action method for the study of rare events," *Communications on pure and applied mathematics*, vol. 57, no. 5, pp. 637–656, 2004. Publisher: Citeseer.

[77] M. Heymann and E. Vanden-Eijnden, "Pathways of maximum likelihood for rare events in nonequilibrium systems: application to nucleation in the presence of shear," *Physical review letters*, vol. 100, no. 14, p. 140601, 2008. Publisher: APS.

[78] M. Heymann and E. Vanden-Eijnden, "The geometric minimum action method: A least action principle on the space of curves," *Communications on Pure and Applied Mathematics: A Journal Issued by the Courant Institute of Mathematical Sciences*, vol. 61, no. 8, pp. 1052–1117, 2008. Publisher: Wiley Online Library.

[79] X. Zhou, W. Ren, and W. E, "Adaptive minimum action method for the study of rare events," *The Journal of chemical physics*, vol. 128, no. 10, p. 104111, 2008. Publisher: American Institute of Physics.

[80] X. Zhou and E. Weinan, "Study of noise-induced transitions in the Lorenz system using the minimum action method," *Communications in Mathematical Sciences*, vol. 8, no. 2, pp. 341–355, 2010. Publisher: International Press of Boston.

[81] L. Kikuchi, R. Singh, M. E. Cates, and R. Adhikari, "Ritz method for transition paths and quasipotentials of rare diffusive events," *Phys. Rev. Research*, vol. 2, p. 033208, Aug. 2020. Publisher: American Physical Society.

[82] L. Lin, H. Yu, and X. Zhou, "Quasi-potential calculation and minimum action method for limit cycle," *Journal of Nonlinear Science*, vol. 29, no. 3, pp. 961–991, 2019. Publisher: Springer.

[83] M. Cameron, "Finding the quasipotential for nongradient SDEs," *Physica D: Nonlinear Phenomena*, vol. 241, pp. 1532–1550, Sept. 2012.

[84] D. Dahiya and M. Cameron, "Ordered line integral methods for computing the quasi-potential," *Journal of Scientific Computing*, vol. 75, no. 3, pp. 1351–1384, 2018. Publisher: Springer.

[85] D. Dahiya and M. Cameron, "An ordered line integral method for computing the quasi-potential in the case of variable anisotropic diffusion," *Physica D: Nonlinear Phenomena*, vol. 382, pp. 33–45, 2018. Publisher: Elsevier.

[86] S. Yang, S. Potter, and M. Cameron, "Computing the quasipotential for nongradient SDEs in 3D," *J. Comput. Phys.*, vol. 379, pp. 325–350, 2019.

[87] M. I. Dykman, P. V. E. McClintock, V. N. Smelyanski, N. D. Stein, and N. G. Stocks, "Optimal paths and the prehistory problem for large fluctuations in noise-driven systems," *Phys. Rev. Lett.*, vol. 68, pp. 2718–2721, May 1992. Publisher: American Physical Society.

[88] W. E and E. Vanden-Eijnden, "Towards a Theory of Transition Paths," *Journal of Statistical Physics*, vol. 123, p. 503, May 2006.

[89] N. Lingala, N. S. Namachchivaya, and I. Pavlyukevich, "Random perturbations of a periodically driven nonlinear oscillator: escape from a resonance zone," *Nonlinearity*, vol. 30, no. 4, p. 1376, 2017.

[90] Z. Chen, Y. Li, and X. Liu, "Noise induced escape from a nonhyperbolic chaotic attractor of a periodically driven nonlinear oscillator," *Chaos: An Interdisciplinary Journal of Nonlinear Science*, vol. 26, no. 6, p. 063112, 2016. Publisher: AIP Publishing LLC.

[91] D. G. Luchinsky, S. Beri, R. Mannella, P. V. McClintock, and I. Khovanov, "Optimal fluctuations and the control of chaos," *International Journal of Bifurcation and Chaos*, vol. 12, no. 03, pp. 583–604, 2002. Publisher: World Scientific.

[92] L. Cilenti and B. Balachandran, "Transient probability in basins of noise influenced responses of mono and coupled duffing oscillators," vol. 31, no. 6, p. 063117. Publisher: American Institute of Physics.

[93] L. Socha, *Linearization methods for stochastic dynamic systems*, vol. 730. Springer Science & Business Media, 2007.

[94] H. Cramér, "Mathematical methods of statistics, 1946," *Department of Mathematical SU*, 1946.

[95] R. L. Stratonovich, *Topics in the theory of random noise*, vol. 2. CRC Press, 1967.

[96] L. Cilenti, M. Cameron, and B. Balachandran, "Most probable escape paths in periodically driven nonlinear oscillators," *Chaos: An Interdisciplinary Journal of Nonlinear Science*, vol. 32, p. 083140, Aug. 2022. Publisher: American Institute of Physics.

[97] M. Bardi and I. Capuzzo-Dolcetta, *Optimal control and viscosity solutions of Hamilton-Jacobi-Bellman equations*. Springer Science & Business Media, 2008.

[98] C. Chicone, *Ordinary Differential Equations with Applications*. Springer-Verlag, New York, 1999.

[99] A. Dembo and O. Zeitouni, *Large Deviations Techniques and Applications*. Stochastic Modelling and Applied Probability, New York, NY: Springer, 2 ed., Mar. 1998.

[100] Z. Chen and M. Freidlin, "Smoluchowski–Kramers approximation and exit problems," *Stochastics and Dynamics*, vol. 5, no. 04, pp. 569–585, 2005. Publisher: World Scientific.

[101] M. Freidlin, "Some remarks on the smoluchowski–kramers approximation," *Journal of Statistical Physics*, vol. 117, no. 3/4, pp. 617–634, 2004.

[102] M. I. Dykman and M. A. Krivoglaz, "Theory of fluctuational transitions between stable states of a nonlinear oscillator," *Sov. Phys. JETP*, vol. 50, no. 1, pp. 30–37, 1979.

[103] R. P. Feynman and A. R. Hibbs, *Quantum mechanics and path integrals*. McGraw-Hill, New York, 1965.

[104] D. E. Kirk, *Optimal control theory: an introduction*. Courier Corporation, 2004.

[105] V. I. Arnold, *Mathematical Methods of Classical Mechanics*. Springer-Verlag, New York, 1978.

[106] L. Cilenti, "Influence of noise on a rotating cantilever structure." European Solid Mechanics Conference 2022.

[107] F. J. Massey Jr, "The Kolmogorov-Smirnov test for goodness of fit," *Journal of the American statistical Association*, vol. 46, no. 253, pp. 68–78, 1951. Publisher: Taylor & Francis.